

<https://doi.org/10.15388/vu.thesis.77>
<https://orcid.org/0000-0001-5982-8214>

VILNIUS UNIVERSITY
CENTER FOR PHYSICAL SCIENCES AND TECHNOLOGY

Vidmantas
JAŠINSKAS

Charge Carrier Generation and Motion in Single-Wall Carbon Nanotube/Fullerene Derivative Films

DOCTORAL DISSERTATION

Natural sciences,
Physics (N 002)

VILNIUS 2020

This dissertation was written at the Center for Physical Sciences and Technology between 2015 and 2019.

Academic supervisor — Prof. Habil. Dr. Vidmantas Gulbinas (Center for Physical Sciences and Technology, Natural sciences, Physics – N 002)

This doctoral dissertation will be defended in a public/closed meeting of the Dissertation Defence Panel:

Chairman – Prof. Habil. Dr. Leonas Valkūnas (Center for Physical Sciences and Technology; Natural sciences, Physics – N 002)

Members:

Prof. Dr. Vygintas Jankauskas (Vilnius University; Natural sciences, Physics – N 002),

Dr. Šarūnas Meškiniš (Kaunas University of Technology; Natural sciences, Physics – N 002),

Dr. Ramūnas Nedzinskas (Center for Physical Sciences and Technology; Natural sciences, Physics – N 002),

Prof. Dr. Roland Tomašiūnas (Vilnius University; Technological sciences, Material engineering – T 008).

The dissertation shall be defended at a public meeting of the Dissertation Defence Panel in the auditorium A 101 of the Center for Physical Sciences and Technology at 2 PM on the 24th september 2020.

Address: Saulėtekio al. 3, LT-10257, Vilnius, Lithuania.

Tel. +370 5 264 8884; e-mail: office@ftmc.lt

The text of this dissertation can be accessed at the libraries of the Center for Physical Sciences and Technology and Vilnius University, as well as on the website of Vilnius University: www.vu.lt/lt/naujienos/ivykiu-kalendorius

VILNIAUS UNIVERSITETAS
FIZINIŲ IR TECHNOLOGIJOS MOKSLŲ CENTRAS

Vidmantas
JAŠINSKAS

Krūvininkų generacija ir judėjimas
vienasienių anglies
nanovamzdelių/fulereno darinių
sluoksniuose

DAKTARO DISERTACIJA

Gamtos mokslai,
Fizika (N 002)

VILNIUS 2020

Disertacija rengta 2015 – 2019 metais Fizinių ir technologijos mokslų centre.

Mokslinis vadovas — Prof. habil. dr. Vidmantas Gulbinas (Fizinių ir technologijos mokslų centras; gamtos mokslai, fizika – N 002).

Gynimo taryba:

Pirmininkas – **Prof. habil. dr. Leonas Valkūnas** (Fizinių ir technologijos mokslų centras; gamtos mokslai, fizika – N 002)

Nariai:

Prof. dr. Vygintas Jankauskas (Vilniaus universitetas; gamtos mokslai, fizika – N 002),

Dr. Šarūnas Meškiniš (Kauno technologijos universitetas; gamtos mokslai, fizika – N 002),

Dr. Ramūnas Nedzinskas (Fizinių ir technologijos mokslų centras; gamtos mokslai, fizika – N 002),

Prof. dr. Roland Tomašiūnas (Vilniaus universitetas; technologijos mokslai, medžiagų inžinerija – T 008).

Disertacija ginama viešame Gynimo tarybos posėdyje 2020 m. rugsėjo mėn. 24 d. 14 val. Fizinių ir technologijos mokslų centro A 101 posėdžių salėje.

Adresas: Saulėtekio al. 3, LT-10257, Vilnius, Lietuva.

Tel. +370 5 264 8884; el. paštas: office@ftmc.lt

Disertaciją galima peržiūrėti Vilniaus universiteto ir Fizinių ir technologijos mokslų centro bibliotekose bei VU interneto svetainėje adresu: <https://www.vu.lt/naujienos/ivykiu-kalendorius>

“ipsa scientia potestas est”

CONTENTS

ABBREVIATIONS	8
1. INTRODUCTION.....	9
1.1. HISTORY OF CARBON NANOTUBES	9
1.2. AIM AND OBJECTIVES OF THE DISSERTATION	11
1.3. NOVELTY AND RELEVANCE	12
1.4. STATEMENTS OF THE DISSERTATION	15
1.5. AUTHOR’S CONTRIBUTION	16
2. LITERATURE OVERVIEW	17
2.1. APPLICATION-ORIENTED RESEARCH	17
2.2. WHAT IS THE CARBON NANOTUBE?	19
2.3. PHOTOELECTRONICAL PROPERTIES OF CARBON NANOTUBES	23
2.4. CHARGE TRANSPORT IN CARBON NANOTUBES	26
2.5. PROCESSING OF CARBON NANOTUBES	27
2.5.1. <i>Approaches for Carbon-nanotube-based Device Construction</i>	27
2.5.2. <i>Carbon Nanotubes Bundling and Dispersion</i>	29
2.5.3. <i>Ultrasonication</i>	32
3. MATERIALS AND METHODS	37
3.1. SAMPLE PREPARATION	37
3.1.1. <i>Materials and Mixtures</i>	37
3.1.2. <i>Preparation of Films on the Interdigitated Electrodes (IDE)</i>	39
3.2. INVESTIGATION TECHNIQUES AND EQUIPEMENT	44
3.2.1. <i>Absorption Spectra Measurements</i>	44
3.2.2. <i>Ultrafast Transient Absorption Investigations</i>	44
3.2.3. <i>Steady-state Photocurrent Investigations</i>	44
3.2.4. <i>Transient Photocurrent Investigations</i>	45
3.2.5. <i>Time-delayed Collection-field (TDCF) Technique</i>	47
3.2.6. <i>Time-resolved Electric-field-induced Second Harmonics (TREFISH) Generation Technique</i>	48
4. RESULTS AND DISCUSSION	53
4.1. TRANSIENT PHOTOCONDUCTIVITY OF CARBON NANOTUBE FILMS	55
4.1.1. <i>Steady-state and Transient Photoconductivity</i>	55
4.1.2. <i>Photocurrent Kinetics</i>	58
4.1.3. <i>Saturation of the Photocurrent Components</i>	63
4.1.4. <i>Time-delayed Collection-field Measurements</i>	65

4.1.5.	<i>Decreasing Carrier Mobility</i>	69
4.1.6.	<i>Extracted Charge Saturation at High Excitation Intensities</i>	70
4.2.	ULTRAFAST INITIAL CHARGE CARRIER MOTION DYNAMICS	71
4.2.1.	<i>Adaptation of TREFISH Technique to the Samples on IDEs</i>	73
4.2.2.	<i>Ultrafast Transient Absorption Investigations</i>	83
4.2.3.	<i>TREFISH Measurements</i>	84
4.2.4.	<i>Polarization-dependent TREFISH</i>	89
4.2.5.	<i>Intratubal Drift of Holes</i>	91
4.3.	PERSISTENT BUILT-IN ELECTRIC FIELD IN SWCNT/PCBM BLEND FILMS .	94
4.3.1.	<i>Frozen Polarization</i>	102
4.3.2.	<i>Compensation of the Built-in Field</i>	104
4.4.	GENERALIZED MODEL OF CHARGE CARRIER GENERATION AND MOTION IN SWCNT/PCBM FILMS	106
4.5.	CONCLUSIONS.....	111
5.	REFERENCES.....	114
	EXTRAS.....	131
I.	DISERTACIJOS SANTRAUKA.....	132
I.1.	ĮVADAS	132
I.1.1.	<i>Disertacijos tikslai ir uždaviniai</i>	133
I.1.2.	<i>Darbo naujumas ir aktualumas</i>	133
I.1.3.	<i>Disertacijos ginamieji teiginiai</i>	136
I.1.4.	<i>Autoriaus indėlis</i>	137
I.2.	TYRIMŲ METODIKA.....	138
I.2.1.	<i>Bandinių paruošimas</i>	138
I.2.2.	<i>Eksperimentiniai tyrimo metodai</i>	142
I.3.	SVARBIAUSI REZULTATAI	146
I.4.	IŠVADOS	151
II.	TRUMPOS ŽINIOS APIE DISERTANTĄ	155
III.	LIST OF PUBLICATIONS.....	158
III.1.	PUBLICATIONS RELATED TO THE DISSERTATION	158
III.2.	OTHER PUBLICATIONS	159
III.3.	CONFERENCE PRESENTATIONS	159
IV.	COPIES OF THE PUBLICATIONS	161
	NOTES	190

ABBREVIATIONS

CNT	carbon nanotube
CoMoCAT	cobalt–molybdenum catalyst
CT	charge transfer
CVD	chemical vapor deposition
EFISH	electric-field-induced second harmonic
HiPCO	high pressure CO disproportionation
HOMO	highest occupied molecular orbital
HR-TEM	high-resolution transmission electron microscope
IDE	interdigitated electrodes
I-V	current-voltage
LED	light-emitting diode
LUMO	lowest unoccupied molecular orbital
MEH-PPV	poly[2-methoxy-5-(2-ethylhexyloxy)-1,4-phenylenevinylene]
OD	optical density
P3HT	poly(3-hexylthiophene-2,5-diyl)
PCBM	phenyl-C61-butyric acid methyl ester
PECVD	plasma enhanced chemical vapor deposition
PFO-Bpy	poly[(9,9-dioctyl fluorenyl-2,7-diyl)-alt-co(6,6-2,2-bipyridine)]
PS	polystyrene
RC	resistor–capacitor
SEM	scanning electron microscope
SWCNT	single-wall carbon nanotube
TDCF	time-delayed collection-field
TREFISH	time-resolved electric-field-induced second harmonic
TRMC	time-resolved microwave conductivity

1. INTRODUCTION

1.1. History of Carbon Nanotubes

The carbon nanotube is an intriguing and technologically attractive material. Such and similar promising words are being included in almost every publication related to carbon nanotubes since 1991 when a paper of Sumio Iijima [1] initiated a substantial scientific interest in those nanostructures. Since then, carbon nanotubes became prevalent material for investigations and for attempts to use them in various electronic devices among scientists in the whole world.

For the sake of truth, it should be mentioned that Sumio Iijima wasn't the first and the only one who turned his attention to these elegant nanostructures. A. Oberlin, M. Endo and T. Koyama published an article about filamentous growth of carbon discussing its cylindrical shape and also presented a model for catalytic growth of these fibers in 1976.[2] Russian scientists (or more accurately for those years: the scientists from the Union of Soviet Socialist Republics) also watched and described similar carbon nanotubes using transmission electron microscopy in 1952. The publication of L. V. Radushkevich (*Л. В. Радушкевич*) and V. M. Lukyanovich (*В. М. Лукьянович*) including the images of 50 nm diameter tubes appeared in Soviet Journal of Physical Chemistry (*Журнал физической химии*).[3] This discovery was largely unnoticed because the publication appeared in Russian language and also in the Soviet Union where the so-called Iron Curtain built during the Cold War more or less limited spread of such publications. Despite that fact, their work was even cited by the Pennsylvania State University scientists in 1959.[4] But such nanometer-size objects hardly could attract the attention of scientists those years when there was only the

beginning of the semiconductors era. In the paper, reviewing the history of carbon nanotubes discovery, M. Monthieux and V. Kuznetsov had analyzed publications related to carbon science. They stated that the discovery of the hollow nanometer-size-diameter carbon filaments should also be assigned partially to Radushkevich and Lukyanovich.[5]

But another thing makes carbon nanotubes even more intriguing materials. Imagine a picture. A Medieval Ages battlefield in the Middle East. The Crusader and Muslim armies collide. In the battlefield, the Crusaders cannot understand what the weapons are like that the opponent's warriors wield. Elegant, maneuverable, sharp — it appears to be only designed to slice through everything, and also solid, seemingly unbreakable swords that seem to be far better than their arms. That was the real power of nanotechnology, including the use of carbon nanotubes. This fact has been confirmed nowadays by modern scientists who were investigating an authentic Persian sabre made of so-called Damascus steel.[6,7] As it is visible from these publications, Meyer's team analyzed a genuine Persian sabre manufactured in the seventeenth century (from the Berne Historical Museum's collection, Switzerland). They used a combination of the experimental methods, including high-resolution transmission electron microscopy and X-ray diffraction to study the structure of the samples. It was revealed that the steel contained carbon nanotubes which were discussed as being mainly responsible for the exceptional mechanical properties of the sabres.

As it is evidenced by historical research, the Persians imported such steel, named as Wootz steel, from ancient India. All weapon-making technology and alloy production was kept secret and only passed verbally from generation to generation. However, due to the prohibition of the industry of Wootz steel in India in 1866, its production technology has been lost and today's attempts to completely restore that ancient technology haven't been fully successful yet.[8,9]

But what can we learn from these histories? The first idea is more philosophical and might be summarized as a statement that everything has its consequences. Either it can be related to the prohibition of the industry of Wootz steel in India in 1866 and a consecutive loss of that technology, or it can be concluded as a missed discovery of carbon nanotubes in 1952. The second one is more technological and more related to this work — carbon nanotubes are really technologically applicable. They showed their benefits even many years ago when Persian civilization developed its advanced technology for sabre production without any more profound knowledge of such nanometer-size world. And as history shows — knowledge matters not only for individuals but for societies as well. Nowadays, when we have a broad range of sophisticated scientific instruments, we have plenty of opportunities to conduct point-by-point investigations developing more sophisticated advanced technologies. I hope that this work will also bring a piece of the new knowledge to the common scientific understanding about the photoelectrical processes in the world of nanomaterials.

1.2. Aim and Objectives of the Dissertation

The world of nanomaterials is extremely wide. There are enormous amounts of scientific information that can't be covered in one work, such as a dissertation. And the goal is not about doing that. The dissertation has been oriented to a quite narrow topic of the nanoscience — the photoelectrical processes in the semiconducting carbon nanotubes. Therefore the aim of this dissertation is to investigate the photoelectrical processes in the films, formed from single-wall carbon nanotubes and PCBM mixtures on interdigitated electrodes in a broad time scale. That includes the fast and ultrafast processes, starting from initial exciton formation, charge carriers separation, and

continuing by their migration and recombination; and also particularly slow processes as a formation and decay of a persistent built-in electric field.

To perform such experiments it is necessary to follow several technological steps:

1. To prepare a suspension of homogeneously dispersed carbon nanotubes.
2. To adapt experimental equipment and measurement technique to the new experimental conditions when the samples with interdigitated electrodes are used.
3. Sample formation on interdigitated electrodes from the mixtures made using previously prepared carbon nanotube suspension with controllable amount of PCBM.

1.3. Novelty and Relevance

Many scientific publications are related to single, separated carbon nanotubes, either it is a simple field effect transistor [10–13] and their assembled arrays for computing purposes [14] or more sophisticated device for quantum computing [15] and nanoscale single-wall carbon nanotube-based glucose sensor [16]. That way may be easier in the sense of theoretical prediction and understanding of the processes in such relatively not very complicated molecular systems. However, many practical applications require greater amounts of materials put at one place. Films made of disordered networks of entangled carbon nanotubes are much more complicated to analyze. As a result we can find different scientists having investigated some particular physical properties and also notice that the same processes remain being

determined without reaching a broader consensus across different publications. Photoelectrical applications require a clear understanding of the electronic processes in photoexcited carbon nanotubes, including exciton and charge carrier generation and consecutive motion. The polymer-wrapped semiconducting (6,5)-chirality single-wall carbon nanotubes (SWCNTs) blended with phenyl-C61-butyric acid methyl ester (PCBM) were used as the main materials here. The photogeneration of charge carriers, their drift and recombination in thin films consisting percolating networks of SWCNTs have been investigated by a combination of several experimental techniques.

A combination of the steady-state and transient-photocurrent with the time-delayed collection-field technique enabled us to identify major phases of the photocurrent and to attribute them to the intratube and extratube electron and hole transfer processes. These findings were published in a scientific publication in the journal *Nanoscale* of Royal Society of Chemistry. [17]

Ultrafast all-optical electric-field-strength measurement technique based on the electric-field-induced second harmonic (EFISH) generation was introduced together with the conventional transient photocurrent measurements for the direct tracking of the charge carrier separation and motion dynamics in SWCNTs during the initial ultrashort photocurrent decay phase. The results were also published in *The Journal of Physical Chemistry C*. [18]

Lastly a long-lasting electric-field-induced polarization of SWCNT networks was encountered and tracked. It was revealed that electric voltage applied to the films of SWCNTs and their blends with PCBM creates persistent electric dipoles in SWCNT clusters that partly screens the external electric field and creates a built-in electric field of the opposite direction remaining for several days. These findings led us to another scientific article, published in *Physica Status Solidi (a)*. [19]

The clear identification of several photocurrent phases in disordered SWCNT systems provides broader perspectives for their application in photoelectrical devices while providing new leads for the optimization of photocurrents. The findings based on the direct tracking of ultrafast electronic processes in photoexcited SWCNTs give explicit information about carrier generation and motion mechanisms necessary for their control in the development of more efficient CNT-based systems and devices. This ultrafast photocurrent component, which may be particularly useful in designing new ultrafast photodetectors may be further optimized by increasing nanotube lengths and by making networks with higher degree of nanotube alignment orientation. Additional improvements might be achieved if SWCNTs are better isolated one from another to prevent intertube carrier jumps. The improvement of the SWCNT network percolation, on the other hand, is a crucial requirement for the maximization of the steady-state photocurrents.

The built-in internal electric field, which was here discovered, may play an important role in SWCNT-based electrical and photoelectrical devices, since it may screen the applied electric field, reducing its strength by several times, and causing long-lasting memory effects.

The ultrafast all-optical experimental method used for the direct tracking of the charge carrier separation and motion dynamics needs also a special attention because of the new findings that appeared from the adaptation of the method for the interdigitated comb-like electrodes and led us also to the publication in Optics Letters.[20] A conventional generation of the second harmonics in materials with the disturbed centrosymmetry causes a field-independent background to the electric-field-induced second harmonic (EFISH) signal and limits its applications. Interdigitated electrodes form an optical transmission amplitude diffraction grating. Phase matching of the EFISH radiation creates a specific angular interference pattern, different from both the fundamental and the ordinary second harmonics radiation. This effect

enables a simple geometrical separation of the EFISH signal from a conventional second harmonics background in non-perfectly centrosymmetric, polycrystalline etc. materials, and provides additional experimental possibilities.

The transmission scheme enables a simple changing of the angle between the light polarization and the external electric field if other polarizability tensor elements are addressed. Moreover, this scheme provides possibilities of additional experimental realizations, which are not possible in sandwich-type samples. For example, molecular films may be oriented parallel or perpendicular to the electrodes using conventional orientation techniques, which would enable the investigation of orientation dependent optical properties and processes. These properties may be important and useful to some applications in the light control or other areas of nonlinear optics.

1.4. Statements of the Dissertation

1. Charge carrier photogeneration in films, formed from a mixture of single-wall carbon nanotubes (SWCNTs) and phenyl-C₆₁-butyric acid methyl ester (PCBM), takes place spontaneously without need for assistance of the external electric field. Moreover, the electric field does not increase the generation efficiency at least up to its strength of about $10^4 \text{ V}\cdot\text{cm}^{-1}$.
2. Charge transfer states in SWCNT/PCBM films dissociate into free charge carriers during hundreds of picoseconds, while dominating carrier decay, attributed to geminate recombination, takes place during several microseconds.

3. Charge carrier transfer rate through the interconnected carbon nanotubes network is limited by the carrier jumps between carbon nanotubes, which take significantly more time compared to the intratube carrier drift.
4. Voltage, applied to SWCNT-containing films deposited on interdigitated electrodes, induces formation of a persistent built-in electric field lasting for hours and days.

1.5. Author's Contribution

The author performed most of the experimental investigations including experimental setup preparations and technical arrangements. The computer simulation of the angular intensity dependence of the fundamental, second harmonics and EFISH signal from the films deposited on the interdigitated comb-like electrodes was also done by the author. A part of the sample preparation and photoconductivity measurements was performed by A. Eckstein and V. Bertašius. These results are included in the dissertation as an integral part of the whole experimental data. The debundled samples from a fresh solution (described in the sample preparation section) were prepared by F. Oberndorfer and Dr. T. Hertel using their experimental techniques. The scanning electron microscope images of carbon nanotube samples were produced by Dr. V. Pakštas. The author thanks Dr. M. Gedvilas and Dr. G. Račiukaitis for the laboratory-made interdigitated electrodes used in some experiments. The author also developed the software in the LabView programming environment for experiment's self-acting control which was very beneficial in all photocurrent kinetics and time-delayed collection-field measurements.

2. LITERATURE OVERVIEW

2.1. Application-Oriented Research

As we have learnt from the history of carbon nanotubes, knowledge and advanced technologies are remarkably beneficial. Persian civilization developed its advanced technology of sabre production many years ago, and it was very beneficial them at war times. Currently, almost twenty years have passed away since the publication of Sumio Iijima initiated a huge scientific interest in carbon nanotubes. Because of their unique structure and unusual broadly adjustable electronic and photoelectric properties, carbon nanotubes continue to attract interest and are explored as potentially promising materials for the development of devices based on new operating principles.

Carbon nanotubes have been tested for application in light detectors, [21,22] transistors, [12,13] and phototransistors.[23,24] Devices based on a single nanotube may be a good example paving a way towards a nanotechnology-based electronics.[25] Carbon-nanotube-based field-effect transistors were assembled successfully in one chip and demonstrated their ability to perform computing tasks.[14] In cell biology, functionalized carbon nanotubes have been tested for probing various molecular functions.[26] The character of photoresponse in the infrared spectral region also makes carbon nanotubes particularly well suited for selective infrared light detectors [27]. Due to strong and spectrally tunable absorption bands in visible and infra-red spectral regions and related photoconductivity, as well as high carrier mobility, carbon nanotubes are also promising for the development of materials with enhanced useful electronic properties for more conventional photoelectronic devices.[28] Because of their unique structure and broadly adjustable electronic and photoelectric properties, carbon nanotubes have been attempted

to use in organic solar cells as both electron acceptors and electron donors.[29–32]

There are some interesting investigations on superconductivity in bundles of double-wall carbon nanotubes, showing their resistance drop as a function of temperature and the possible intrinsic superconducting transition below 6.8 K [33]. The temperature dependence of carbon nanotubes film's resistance also attracted scientists' attention to study this physical effect and possible application of multi-wall carbon nanotube networks as a sensing element in small-size temperature sensors [34].

Carbon nanotubes being low-dimensional materials were also tested as mechanical resonators for mass and force sensors. An achieved $4.3 \text{ zN}/\sqrt{\text{Hz}}$ force sensitivity was demonstrated using cryogenically cooled mechanical resonator based on a single carbon nanotube [35]. A strain sensor was fabricated from polymer nanocomposite containing multi-wall carbon nanotubes[36]. Successful music and voice reception has also been demonstrated using an integrated radio receiver in 40-400 MHz range based on a single carbon nanotube serving simultaneously as all essential components of a radio.[37]

For the successful adoption of those nanomaterials for practical use, it is necessary to understand their various physical properties, including geometrical and chemical structure, electronic-band structure, electric and photoelectric properties. Therefore a lot of work and efforts were put into this research area, revealing many interesting possibilities for the use of these nanometer-size structures.

2.2. What Is the Carbon Nanotube?

Before any technological use of a material, it is necessary to understand its various physical properties. One of those is the chemical composition and structure. Doing any more in-depth research, we should have an imagination of what these nanometer-size structures are made of.

The simplest carbon nanotube – single-wall carbon nanotube – can be imagined as a tube thinner than human hair by approximately 50 000 times and rolled-up from a honey-comb lattice of sp^2 -bonded carbon atoms (or simpler – rolled-up graphene sheet). When one would try to do that several times, that carbon nanotube wrapper should notice that the tubes differ depending on the direction which this delicate sheet is rolled at. These various carbon nanotubes are characterized by a so-called chiral vector C_h defined as:

$$C_h = na_1 + ma_2 \quad (1)$$

Here n and m is a pair of integers and a_1, a_2 – basis vectors.[38,39] According to that roll-up direction or consequentially the chiral vector, all single-wall carbon nanotubes are classified into three categories: armchair ($n = m$), zigzag ($m = 0$) and chiral ($n \neq m \neq 0$) type carbon nanotubes.[38,40,41] Chiral carbon nanotubes can be left-handed as well as right-handed also.[42] **Figure 2.1** represents that nomenclature based on the direction which a graphene sheet is rolled at.

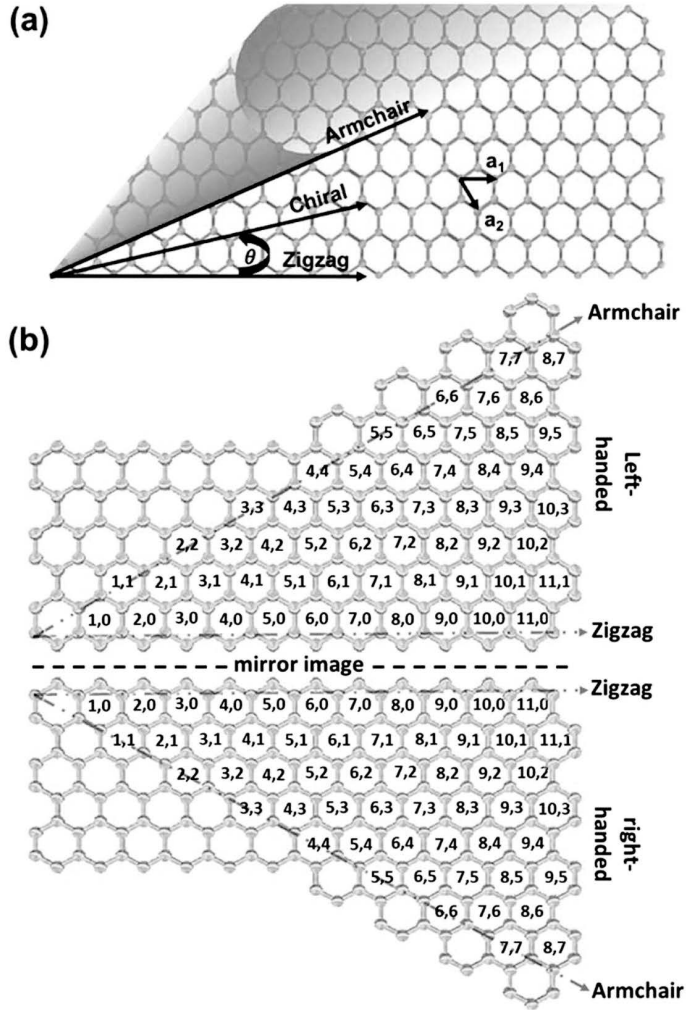


Figure 2.1. Structure and chirality of single-wall carbon nanotube (adapted from ref.[41])

The diameter of single-wall carbon nanotube can be easily calculated from the chiral vector using the formula: [38]

$$d = \sqrt{3}a_{C-C} \frac{\sqrt{m^2 + nm + n^2}}{\pi} \quad (2)$$

Here $a_{C-C} = 1.42 \text{ \AA}$ which is the nearest neighbor carbon-carbon distance.

Another characterization of carbon nanotubes is by the number of walls. They are classified as single-wall and multi-wall carbon nanotubes. In scientific literature, a particular case of multi-wall carbon nanotubes – double-wall carbon nanotubes are also being distinguished.

As one may notice from **Figure 2.1**, there is an infinite number of possible ways of how a carbon nanotube can be rolled-up. But it is actually hardly possible to bend one or two benzene rings into a tube. Therefore one may fancy a question, what the smallest diameter of carbon nanotube is still really possible. There is an excellent theoretical work of Sawada and Hamada, which covers this question.[43] According to the authors, two competitive energies – bending and binding take place during the carbon nanotube formation. They conclude that there is a threshold of approximately 4 Å of nanotube diameter when the binding energy is still able to compensate the bending energy. Below this threshold, carbon atoms are more likely to rest in the graphene sheet rather than form a tube. This prediction was checked experimentally by Guan, Suenaga and Iijima more than a decade later.[44] They attempted to produce the smallest carbon nanotube. Therefore, they synthesized double-wall carbon nanotubes and measured with better than 0.14 nm resolution 0.4-0.5 nm diameter inner-shell nanotubes showing that such carbon nanotubes with the chiral index (3,3), (4,3) or (5,1) are still possible. But they also state that these extremely thin carbon nanotubes are rather unstable and extremely sensitive to environmental conditions and impact and therefore being available as the inner shells of multi-wall carbon nanotubes. This claim also fits well to the results when other scientists investigated oxidative properties of single-wall carbon nanotubes and found the smaller ones being easier to decompose.[45]

Before Guan, Suenaga and Iijima experiments, other scientists also put effort to produce the smallest carbon nanotube. Qin with colleagues reported the discovery of the smallest possible carbon nanotube of 4 Å in diameter in 2000.[46] Zhao with colleagues claimed having found a 3 Å diameter

armchair (2,2) carbon nanotube in 2004.[47] These all were found as the most inner layer of a multi-wall carbon nanotube using HR-TEM technique. However, Guan, Suenaga and Iijima argue that the image simulation has revealed substantial deviation from the actual diameters in the simple measurements of diameters with a ruler from HR-TEM images.[44] Therefore they claim that such simple measurements aren't reliable and suggest using an improved HR-TEM equipped with a post-specimen aberration corrector.[44] The above mentioned theoretical work [43] can also give us some clues about the existence of polyacenes and other polycyclic aromatic hydrocarbons as small molecules rather than being bent into rings or tubules. Above the nanotube diameter threshold, the dependence curve of the difference of the cohesive energies between the sheet and the tube upon the tube diameter is shallow but also exhibits a maximum at about 10 Å.[43] If one ever had a question why the single-wall carbon nanotubes are said to be of 1 nm in diameter, this fact gives some explanation. In addition to the smallest possible carbon nanotube prediction, on the other side, it is also estimated theoretically and experimentally that the critical diameter for single-wall carbon nanotubes at the atmospheric pressure lies between 4.2 and 6.9 nm.[48] Bigger tubules are expected to collapse, forming ribbons. These facts also serve as clues to answering the question — why the absolute majority of investigated single-wall carbon nanotubes presented in the published scientific literature are the carbon nanotubes of approximately 1 nm diameter as well.

2.3. Photoelectronical Properties of Carbon Nanotubes

A substantial property of single-wall carbon nanotubes (SWCNTs) is their chirality, defining the symmetry of the arrangement of the carbon atoms. Depending on chirality, carbon nanotubes may exhibit innate metallic or semiconductor properties. These properties can be also modulated, including full transition from metal to semiconductor, using strong magnetic [49–51] and electric [52–54] fields or mechanical deformations [55,56] as well as chemical doping [57,58].

From all types of carbon nanotubes, semiconducting SWCNTs stand out as being particularly interesting for electronic applications. Photoelectrical applications need a solid understanding of the electronic processes in photoexcited carbon nanotubes, particularly exciton and charge carrier generation and motion. Much work has been done to reveal various photoelectrical properties of carbon nanotubes however several important points continue to be lacking till the complete picture of the processes in SWCNT-containing materials.

Several studies have explored the photoconductivity of single carbon nanotubes [13] and of thin films [28,59] without reaching a broader consensus. The mechanism of charge carrier generation is thus still not fully understood and requires further investigation.

Initially, carbon nanotube photoconductivity was discussed in terms of excitonic and interband transitions.[60] However, high binding energies of excitons in SWCNTs, reaching hundreds of milielectronvolts,[61,62] called direct carrier photogeneration into question. Nonetheless, spontaneous carrier photogeneration in SWCNTs has been reported by several authors [63–66], and it remains unclear if the spontaneous carrier generation may also occur in

“perfect” nanotube or if it requires defects or impurities. Adsorbed oxygen was demonstrated to significantly enhance the photocurrent,[28] and charge separation was also suggested to occur by electron transfer to metal electrodes.[59] The local electric field was suggested to cause free carrier photogeneration in inhomogeneously doped single semiconducting nanotubes.[67]

Efficient charge photogeneration was also demonstrated to take place at the interfaces between carbon nanotubes and fullerenes or fullerene derivatives, raising interest to the potential of such systems for solar cell fabrication.[21,29,30] In most of these systems, single-wall carbon nanotubes (SWCNTs) and fullerene derivatives are believed to form type-II heterojunctions,[21] thus establishing a clear reference for the mechanism of carrier generation.

The dynamics associated with charge carrier generation and the motion of charges away from their initial generation site are still largely unexplored. Conventional electrical methods have insufficient time-resolution to address initial carrier generation and motion phases. Time-resolved microwave conductivity enabled contactless probing of the carrier motion dynamics and provided valuable information about the carrier trapping and recombination processes.[66,68] However, its time-resolution was also too low to address the generation dynamics.

Transient absorption spectroscopy revealed that charge-carrier generation by electron transfer between SWCNTs and fullerene occurs on a femtosecond timescale.[64,69,70] Electron transfer to conjugated polymer (P3HT) was found taking place with a similar rate.[71] However, conventional transient absorption was unable to separate between free and localized charge carriers.

Attempts to address the carrier dynamics with another ultrafast technique, time-resolved THz spectroscopy, revealed the generation of localized and

delocalized charge carriers, and their localization during the thermalization process, but the free charge carrier response was not identified.[71]

Time-resolved microwave conductivity (TRMC) investigations have demonstrated spontaneous carrier photogeneration in the suspensions of SWCNTs, [66] and at the heterojunctions of SWCNTs and fullerene layers. [68,72,73]

Quasiparticle (e.g. trions) formation is very favorable in low dimensional materials. It is unclear how, or even if, trions (irrespective of polarity) will influence microwave conductivity in such measurements. Authors argue, that it is reasonable to expect that trions may behave as “heavy” electrons and holes, i.e., charges with comparatively high effective masses and, thus, lower mobilities. Therefore these particles and quasiparticles are indistinguishable in TRMC experiments.

Purely optical transient absorption investigations also revealed spontaneous carrier generation in semiconducting (6,5)-SWCNTs.[74] However, the observed carrier recombination was much faster — on a sub-nanosecond timescale. Therefore it remains unclear, whether both studies probed different processes, or the experimental conditions were too different to allow a detailed comparison.

Although these investigations clarified some aspects of the charge carrier generation in carbon nanotube systems, the elementary steps following photon absorption leading to the generation of free charge carriers thus still remain somewhat vague, and it is not clear what processes determine carrier generation efficiency, its dependence on the material chemical composition, morphology and external conditions. The information obtained from different samples and different investigation techniques is still insufficient to draw a general photoconductivity picture.

2.4. Charge Transport in Carbon Nanotubes

Application of the nanomaterials in electronic devices requires a clear understanding of their various physical properties, especially charge transport properties, which are particularly important for any electronic material. Charge transport through the bundles of SWCNTs[75–78] as well as its dependence on the temperature,[75,76] doping,[77] and intertube interactions[76,78] have been addressed in a number of publications. Charge carrier photogeneration and their transport through the SWCNT network can be considered as a very fast or ultrafast process.[79] Intratube charge carrier mobility reaches thousands of $\text{cm}^2\text{V}^{-1}\text{s}^{-1}$, [10,11,80] which makes them interesting for fast electronics. However, charge carrier motion in carbon nanotube films is extremely dispersive. The intratube carrier transport takes place on a ps timescale, [79] while intertube carrier jumps are much slower occurring on a timescale of tens of microseconds. *Gadermaier et al.* reported an effective lifetime of 43 ms of the trapped charges in single-wall carbon nanotubes.[81]

Much slower electronic processes in carbon nanotube films were also reported. Gravity-induced self-charging of paper-like carbon nanotube-polyaniline supercapacitors lasting for hours was reported by *Gao et al.* and attributed to the motion of electrolyte ions.[82] Slow processes also cause a well-known persistent photoconductivity phenomenon. It was observed in some materials [83,84] including carbon nanotube structures. [28,85,86] Persistent photoconductivity of modified carbon nanotube film lasting for more than 30 min was reported by *Khairoutdinov et al.*[85] The slow processes were attributed to the photoinduced electron transfer from attached molecular substituents to carbon nanotubes. *Allen et al.* have demonstrated

that the slow processes lasting for tens of minutes influence carrier mobility in a nanotube field-effect transistor.[87]

2.5. Processing of Carbon Nanotubes

2.5.1. Approaches for Carbon-nanotube-based Device Construction

There are, in principle, two main concepts to produce nanomaterials for organic and hybrid devices – the top-down and bottom-up approaches. The top-down method refers to slicing, etching or/and milling techniques applied to synthesized bulk material as a way to get nano-sized particles while following a bottom-up approach the nanoparticles are getting constructed from raw materials by self-assembly processes during chemical synthesis itself.[88] In the case of carbon nanotubes, only the bottom-up methods can be applied because, due to their peculiar structure, there is no crystal that could be chopped or milled obtaining separate carbon nanotubes.

Since 1991 when Sumio Iijima published his article about helical microtubules of graphitic carbon [1] and initiated a massive interest among researchers in carbon nanotube science, much time has already passed. Scientists tried many methods, including the most popular arc-discharge, laser ablation and chemical vapor deposition (CVD) techniques, to synthesize single-wall or multi-wall carbon nanotubes. More sophisticated methods, e.g. plasma enhanced chemical vapor deposition (PECVD), high pressure CO disproportionation (HiPCO) or molten salt technique, were also developed. Their work was later described in reviews [41,89,90] and books [91–93] dedicated to carbon nanotube synthesis, properties and possible applications.

There are also two main concepts to construct devices from nanomaterials – the grow-in-place and grow-then-place approaches.[90] Both of them can be

applied to carbon nanotubes. The grow-in-place technique usually consists of preparing the substrate with a catalyst present in the locations where the nanoparticles or, in our case, carbon nanotubes would be synthesized. The main advantages of this technique are:

- Catalyst can be placed into the desired position, which makes easy to control the position of nanotube growth.
- There exist proven recipes to obtain vertically aligned carbon nanotubes if such a result is desired.
- Good electrical and physical contact between substrate and carbon nanotubes.

The major disadvantage of the grow-in-place method is the risk of damaging pre-existing structures on substrates, especially significant when using organic materials as other functional layers.

The grow-then-place technique consists of preparing nanoparticles, e.g. carbon nanotubes in our case first and then transferring them onto the substrate. Using this approach no restrictions on the process or temperature for carbon nanotubes synthesis appear as well as there is also a great ability to purify, functionalize, chirality or conductivity select or pretreat carbon nanotubes in other ways.[90]

The major disadvantage of the grow-then-place technique is the still insufficient level of repeatability and control to transfer carbon nanotubes to specific regions of a substrate with high accuracy.[90] The requirement of the exact positioning of carbon nanotubes on a substrate vanishes using the technological approach of the layered device structure.

2.5.2. Carbon Nanotubes Bundling and Dispersion

When one wants to produce a high-quality layer for an electronic device using a solution-based technique, one of the requirements is to have starting materials being homogeneous as much as possible. It was noticed, that producing a bulk amount of carbon nanotubes they bunch together and that fact converts into a challenge later when trying to disperse them into solution.[94] Several factors promote their tendency to form bundle aggregates. Firstly they usually have a huge aspect ratio, i.e. they are long enough but extremely thin. That feature leads to becoming entwined, interwoven, formed loops around each other and therefore entangled physically. Secondly, attractive Van der Waal's forces between neighboring carbon nanotube surfaces also glue them together and decrease the dispersibility. [94]

The fact is that many potential applications of carbon nanotubes require that carbon nanotubes be dispersed and processed in liquids such as organic solvents, polymer melts or other solutions. A 2005 NASA-NIST workshop addressed this issue and made a clear distinction between “nanodispersion” of individual carbon nanotubes and “macrodispersion” of carbon nanotube bundles. [95] They defined macrodispersion as the dispersion of tiny carbon nanotube bundles and nanodispersion as the dispersion where the bundles are completely split into individual, non-bundled carbon nanotubes.

Mastering the preparation of carbon nanotube dispersion is critical because the functionality of many applications depends on whether carbon nanotubes are separate or bundled and also the degree of bundling as well. For example, the percolation threshold for polymer/carbon nanotube nanocomposites depends inversely on the average aspect ratio of the dispersed entities.[95] Many methods are used to disperse carbon nanotubes and in the meantime to

prevent their re-aggregation. These methods can be categorized into three broad groups:[95]

1. Carbon nanotubes can be functionalized first and as a consequence made soluble in some particular solvents;
2. Mechanical mixing or ultrasonication used to break the bundles apart followed by an introduction of a wrapping agent such as a surfactant or polymer that leads to the dispersion stabilization;
3. Direct dissolution of carbon nanotubes.

The first method is promoted when chemically functionalized carbon nanotubes are desirable in the application. In other cases, the second or third method has to be chosen, because the functionalization of the carbon nanotube sidewalls tends to change for sure their electrical, chemical and other properties. [96]

The simplest way to determine the efficiency of the method is by using the optical absorbance spectroscopy to measure the fraction of carbon nanotubes remaining in dispersion after centrifugation.[97,98] Trying to describe it quantitatively a set of dimensionless parameters were introduced to characterize the degree of carbon nanotube dispersion.[95]

Spontaneous dispersion of single-wall carbon nanotubes in superacids such as chlorosulphonic acid was reported.[99] Authors declare that at higher weight concentrations (up to 0.5wt% of carbon nanotubes), the components of dispersion form liquid-crystal phases that can be processed further into layers of controlled morphology.

Another approach towards a direct dissolution of carbon nanotubes is by forming chemical compounds, named as polyelectrolytes. It was shown that single-wall carbon nanotubes are able to form polyelectrolyte salts with alkali metals such as lithium, sodium, potassium – carbon nanotubides.[100–104]

Consequently, these compounds become soluble in polar organic solvents without any ultrasonication or other mechanical intervention, thus forming thermodynamically stable nanodispersion of separate nanotubes.[101]

The last-mentioned method involves the use of chemical compounds instead of pure carbon nanotubes. Therefore more chemical technology steps must be included, which may affect the properties of the device. The use of very aggressive liquids such as superacids is also not a very convenient way in most cases when organic materials and technologies are involved. There is also an interesting method in the second category. It is also called as polymer-sorting of carbon nanotubes when a particular polymer is introduced in suspension besides the sonication or another mechanical mixing, and this polymer wraps the carbon nanotubes selectively.[105–107] Two aspects make it technologically attractive. First, the selection of the one chirality pure carbon nanotubes, for example, fluorene- and carbazole-based copolymers are known for high selectivity of (6, 5) chirality single-wall carbon nanotubes which are semiconductors by their electric properties and therefore potentially applicable for electronics. And second, the enhanced dispersibility of such polymer-wrapped carbon nanotubes in common organic solvents.[105,106] A disadvantage of this method is an additional material being introduced into suspension which can't be fully eliminated later and consequently must be taken into account modeling the properties of the device.

There are also more sophisticated and particular-application-oriented methods to make stable dispersion. In particular a recent book of O.V.Kharissova and B.I.Kharisov [108] covers many of these methods more in detail and also offers an extensive list of references to guide a further study.

2.5.3. Ultrasonication

Ultrasonication is a simple, effective and therefore widely and very often used method to disperse nanoparticles in various solutions during technological steps. It is so widely accepted method that in a vast number of scientific publications, there are only a couple of sentences or even words dedicated to describing that technological step in experimental sections. However, this is rather a many-sided method, which can incorporate additional effects or alter some properties of the materials being processed. Therefore we will do a slightly deeper sight into that part of the science of sonic waves.

Despite the fact that the ultrasonication method is popular and widely used, a good dispersion of nanoparticles is not always achieved, due to the physical processes in the experimental setup – incoming ultrasonic waves in liquid are usually reflected and damped at the gas/liquid interface. Sonication baths and tip sonicators are the most popular realizations of technological setup. While bath-sonication setups involve more different medium and therefore suffer more wave reflections from the interfaces, tip sonicators are used to deliver ultrasonic waves directly into the solution.

The ultrasonication method almost completely lies on the physical process named acoustic cavitation. Acoustic cavitation can be defined as bubble activity induced by sound waves in liquids and gases.[109] It is distinguished between inertial and noninertial cavitation. Inertial cavitation is when in a liquid medium, an ultrasound-induced bubble rapidly expands, very often growing to more than twice in one or two acoustic cycles, and then violently collapses. Noninertial or sometimes called stable cavitation occurs at lower acoustic pressures and contrary to inertial cavitation, the bubble does not collapse violently but rather keeps pulsating.

The energy density of sound waves are relatively low, but the bubbles produced by the cavitation process can act as energy concentrators causing high energy densities at micron and submicron length scales. Consequently, the nearly adiabatic bubble collapse leads to almost nine orders of magnitude of enhancement in the energy per molecule, producing internal gas pressures of hundreds to thousands of atmospheres and temperatures of thousands of degrees Kelvin.[109] Release of such energies to a small volume causes many physical and chemical effects, including the initiation of chemical reactions, production of free radicals, acoustic noise (produced by bubble pulsations), visible light emission (named as sonoluminescence), heating of the liquid and also physical damage of the solid surfaces in the proximity of such collapsing bubbles.[109–112]

For the case of carbon nanotubes, the ultrasonication method is a classical debundling method used to disperse them in various solvents.[108] Taking into account the above-mentioned effects the cavitation process produces the strong shear force, leading to the exfoliation of carbon nanotube bundles, providing homogeneity of nanosuspension.[113]

One can get a question, which parameters to choose for ultrasonication process, e.g. sonication energy, sonication time. The evaluation of the role of sonication energy on carbon nanotube dispersions in the presence of sodium dodecylbenzene sulfonate was revealed, that the concentration of dispersed carbon nanotubes depends on the sonication energy, but not output power of the sonicator alone or the sonication time.[114] It was also noticed that the optimal energy depends on carbon nanotube diameter, and it was independent on amounts of carbon nanotubes, surface functional groups, and carbon nanotube length.[114]

Another study [115] reveals the differences between noninertial (stable) cavitation and inertial cavitation using broadband acoustic emission

monitoring and H₂O₂ production in aqueous solutions. Stable cavitation favors chemical reactions and modification of carbon nanotubes. Inertial cavitation leads to carbon nanotube length reduction and exfoliation. The inertial cavitation was found to be responsible for effective carbon nanotube dispersion.[115] The authors also highlight that careful control of acoustic cavitation rather than a blind application of input power is essential in the large volume production of nanomaterial dispersions with tailored properties.[115]

When the ultrasonication appears as not so simple but rather a many-sided method for dissolution of carbon nanotubes, maybe there are better approaches for this task. A group of scientists performed a study attempting to clarify the best method of dispersing carbon nanotubes. They compared eleven different dispersion methods applied for both long and short single-wall carbon nanotubes as well as for short multi-wall carbon nanotubes also.[116] These methods can be classified into three general mechanisms: turbulent flow (Nanomizer, high pressure jet-mill), cavitation (probe sonicator), and mechanical force with a grinding media involved (ball-mill, paint shaker, ball collision-mill, bead-mill) and without any grinding media (cone-mill, high shear batch disperser, thin-film spin mixer, rotor-mill). The study showed that the electrical conductivity of composites measured using the four-probe method varied by a factor of ~4 among the different methods and the highest conductivity was observed for the samples when their preparation involved turbulent flows (**Figure 2.2**). SEM and laser diffraction experiments also showed more homogeneous samples and smaller particle sizes in dispersion for turbulent flow methods.

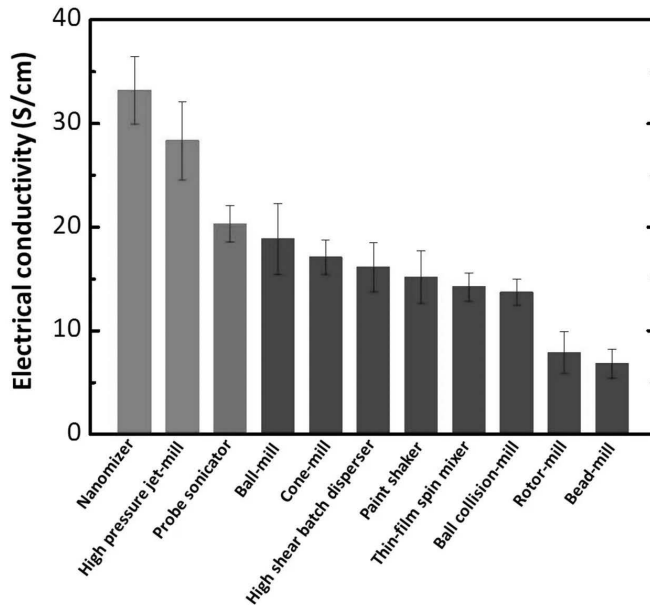


Figure 2.2. The electrical conductivity of 10 wt% single-wall carbon nanotubes/fluorinated rubber composites (adapted from ref.[116])

The authors also state that the effect of the dispersion is an interplay between the level of bundles exfoliation and the level of damage introduced to the carbon nanotubes — both of them increase with dispersion time. Once a relatively fine mesh structure is achieved, the advantage gained by further exfoliation decreases while the damage monotonically increases.[116] They also propose to quantify the level of exfoliation as the cubic inverse of the particle size measured by the laser diffraction method.

Direct monitoring of the dispersion process of carbon nanotubes by light scattering and optical absorption methods, using continuous sonication as a dispersion method, was performed by another group of scientists.[117] They also highlight the significance of the process monitoring and the ability to find the optimal dispersion parameters.

Summarizing the above-mentioned information about the ultrasonication method, we can state that ultrasonication is a simple, not expensive and, in most cases, effective dispersion method. But on the other hand, it is also a many-sided method involving a number of side effects that must be taken into account while performing technological steps. The monitoring of the dispersion process and selection of optimal technological conditions are essential for reproducibility.

3. MATERIALS AND METHODS

3.1. Sample Preparation

3.1.1. Materials and Mixtures

Single-wall carbon nanotubes (SWCNTs) used for sample preparation were purified from commercially available CoMoCAT type SWCNT soot (99%, Sigma Aldrich). According to the technical bulletin, these SWCNTs were produced by a catalytic chemical vapor deposition (CVD) process, using a flow of pure carbon monoxide at a pressure of 1-10 atm. The SWCNTs growth performed by carbon monoxide disproportionation process (i.e. decomposition of CO into carbon and CO₂) at a temperature of 700-950°C when a cobalt–molybdenum catalyst was used. Average diameter of carbon nanotubes, as indicated in datasheet, is 0.78 nm, while their average length — ~1 μm. This SWCNT soot is highly enriched by (6,5)-chirality SWCNTs (up to 41 % of CNTs).

Semiconducting (6,5)-chirality SWCNTs were purified (enrichment up to 96 – 97 % of CNTs) from this material by means of selective wrapping with poly[(9,9-dioctyl fluorenyl-2,7-diyl)-alt-co(6,6-2,2-bipyridine)] (PFO-Bpy) copolymer as described in ref.[105].

Briefly, the selective purification of (6,5)-SWCNTs was achieved through ultrasound-assisted SWCNT wrapping with PFO-Bpy copolymer, centrifugation and filtration-assisted polymer depletion. The PFO-Bpy-stabilized (6,5)-SWCNTs were resuspended in chlorobenzene (>98%, Fluka) and then used for further sample preparation. Chemical structure of this copolymer is represented in **Figure 3.1(a)**. As it was mentioned before, charge photogeneration was demonstrated to take place at

the interfaces between carbon nanotubes and fullerenes or fullerene derivatives, forming charge transfer complexes.[21,29,30] In our experiments phenyl-C₆₁-butyric acid methyl ester (PCBM) was used aiming to form a charge transfer complex with PCBM as electron acceptor and SWCNT – as donor. Diagram of HOMO and LUMO energy levels of the used materials was estimated using published scientific data and is represented in **Figure 3.1(b)**,[118–120]

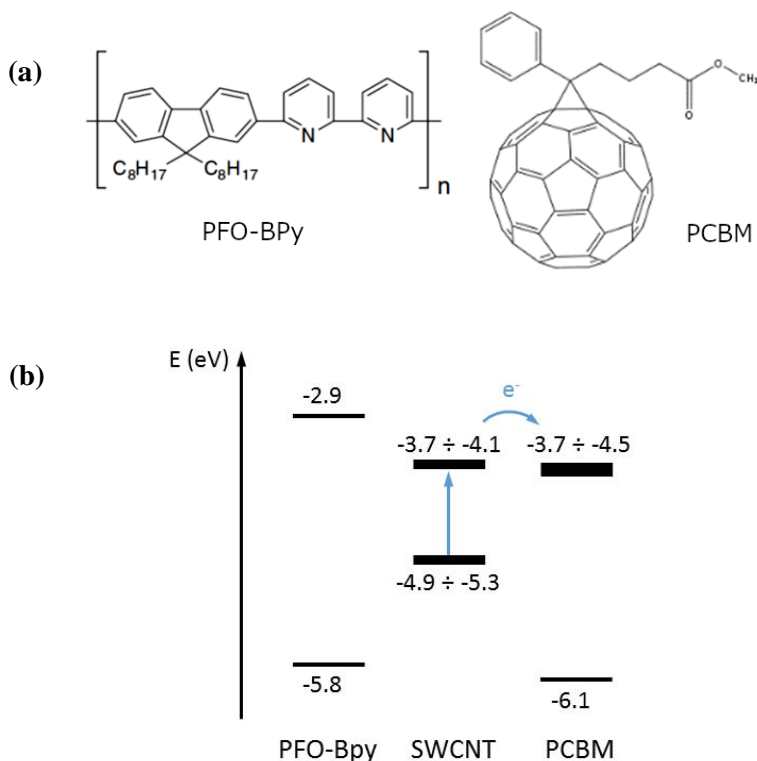


Figure 3.1. (a) Chemical structure of additional materials used for sample preparation; (b) schematic diagram of HOMO and LUMO energy levels

To obtain SWCNTs and phenyl-C₆₁-butyric acid methyl ester (PCBM) mixtures, that chlorobenzene suspension with polymer-wrapped SWCNTs were mixed with PCBM solutions of different concentrations. The PCBM to

SWCNT weight ratio x/y in different films is indicated using the designation PCBM/SWCNT (x/y). Since repetitive purification process tends to a partial loss of CNTs, x/y ratios were estimated from the film absorption spectra using published SWCNT photo-absorption cross sections.[121,122] Designation SWCNT/PFO-Bpy corresponds to the sample used in some measurements that was prepared almost identically to the sample PCBM/SWCNT (120/1) with only PCBM replaced by additional PFO-Bpy copolymer.

3.1.2. Preparation of Films on the Interdigitated Electrodes (IDE)

In electrical or photoelectrical measurements, very significant parts of the experimental setup are electrodes and electrical-wire connections. Usual experimental realizations for these measurements use sandwich-type samples containing an active layer between transparent or semitransparent electrodes. Herein a new experiment-realization scheme, based on the interdigitated comb-like electrodes, was introduced. It is also worth to mention that this method solves some problems and setup limitations which occur when the layered sandwich-type samples are being investigated.

Firstly, when the ultrafast electric-field-induced second harmonics (EFISH) technique is used, the experimental realizations of these measurements in thin films are not optimal in the sandwich-type samples because of the electric field-strength vectors mismatch. The application of the EFISH technique also becomes very difficult or impossible if the films are polycrystalline or at least partly ordered. That causes difficulty in distinguishing EFISH signal from the conventional, often much stronger second harmonics generation.

Another problem of the thin film investigation is a rather complicated and time-consuming fabrication of multilayered samples. It practically precludes

fast characterization of materials. In the case of very thin, monolayer Langmuir-Blodgett or self-assembled films, formation of the top electrodes becomes a complex, often insolvable problem.

Our technique based on the interdigitated comb-like electrodes (IDE) solves the above mentioned problems and additionally provides several completely new experimental possibilities. Although manufacturing of the electrode arrays requires high precision technologies, the preparation of the samples on already manufactured electrode-arrays becomes easy and fast. It is enough to form a thin layer of material on the electrode arrays. This technique is particularly convenient for the solution processed films, which may be formed by using spin coating, dip coating or doctor blade techniques. The comb-like electrodes may be reused if the deposited film can be washed off. It also solves the top electrode problem enabling the application of the EFISH technique to monolayer or other ultrathin films.

This scheme also enables a simple changing of the angle between the light polarization and the external electric field if other polarizability tensor elements are addressed.

Moreover, this scheme provides possibilities of additional experimental realizations, which are not possible in sandwich-type samples. For example, molecular films may be oriented parallel or perpendicular to the comb of electrodes using conventional orientation techniques, which would enable the investigation of orientation dependent optical properties and processes.

Two types of the interdigitated comb-like electrodes were used in the experiments — laboratory-made and commercially available.

The commercially available interdigitated comb-like electrodes (IDEs) from *Micrux Technologies* were used in the photoelectrical measurements. These metal-based electrodes are fabricated by thin-film technologies on a glass substrate. One separate electrode consists of a thin, 50 nm thickness binding

layer made of titanium and then covering 150 nm thick platinum layer over that.

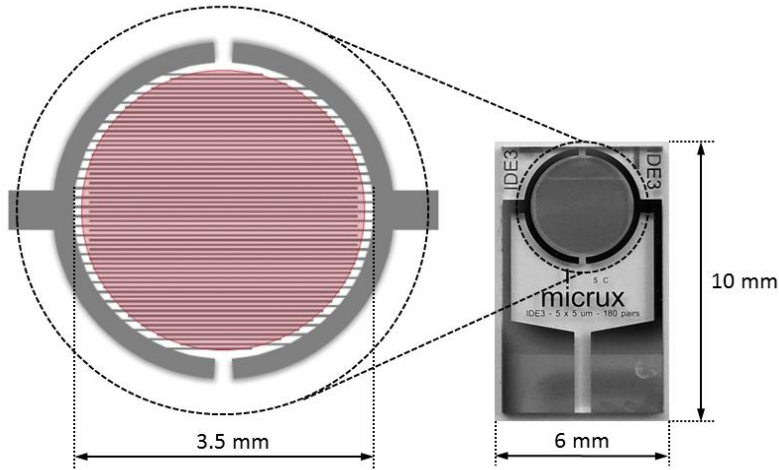


Figure 3.2. Commercially available interdigitated comb-like electrodes (IDE) from *Micrux Technologies*

The electrode plates consist of two individually addressable microelectrode array strips with an interdigitated approach. The plate contains a round active cell of 3.5 mm diameter (area of 9.6 mm^2) formed from 180 pairs of the electrode strips of the $5 \mu\text{m}$ width and $5 \mu\text{m}$ interelectrode distances. The unusable area of the plate is protected by a SU-8 resin protective layer.

The laboratory-made interdigitated comb-like electrodes were used in the investigation of the second harmonics generation. These electrodes were fabricated by the direct laser ablation technique from the thin chromium layer deposited on a transparent glass plate. This technique enables fabrication of interdigitated electrodes with electrode widths and interelectrode distances as narrow as about $1 \mu\text{m}$. The electrode widths and gaps between electrodes were made equal to $4 \mu\text{m}$ and the electrode length was 2 mm. Their height, measured with a profilometer, was about 70 nm.

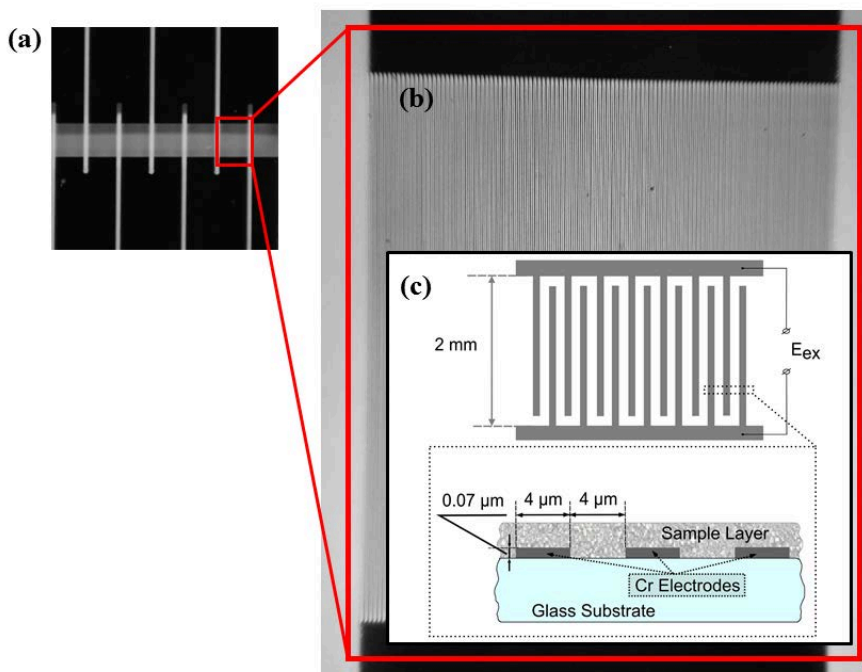


Figure 3.3. (a) Arrays of laboratory-made interdigitated electrodes, their magnified microscope view (b) and schematic representation (c)

The films on IDEs were prepared by the drop-cast method using controlled amounts ($2 \mu\text{l}$) of mixtures. This method enables preparation of films of several hundred micrometer thick. SWCNTs in the films tend to aggregate into bundles forming an entangled-network pattern.

Investigation of SWCNT films, containing assembled or bundled SWCNTs at different levels, enabled us to distinguish between intratube and intertube carrier motions. In this case, two types of the samples were prepared — from fresh solution and from solution aged more than a year when SWCNT aggregation took place more significantly. For the sake of simplicity, these samples will be referred to as *fresh* and *aged* respectively.

SEM images of corresponding *fresh* and *aged* films on interdigitated electrodes are shown in **Figure 3.4**. *Aged* films contain clearly visible

aggregates with densely packed SWCNTs, while in *fresh* films carbon nanotubes are more separated, tending to form a net-like structure.

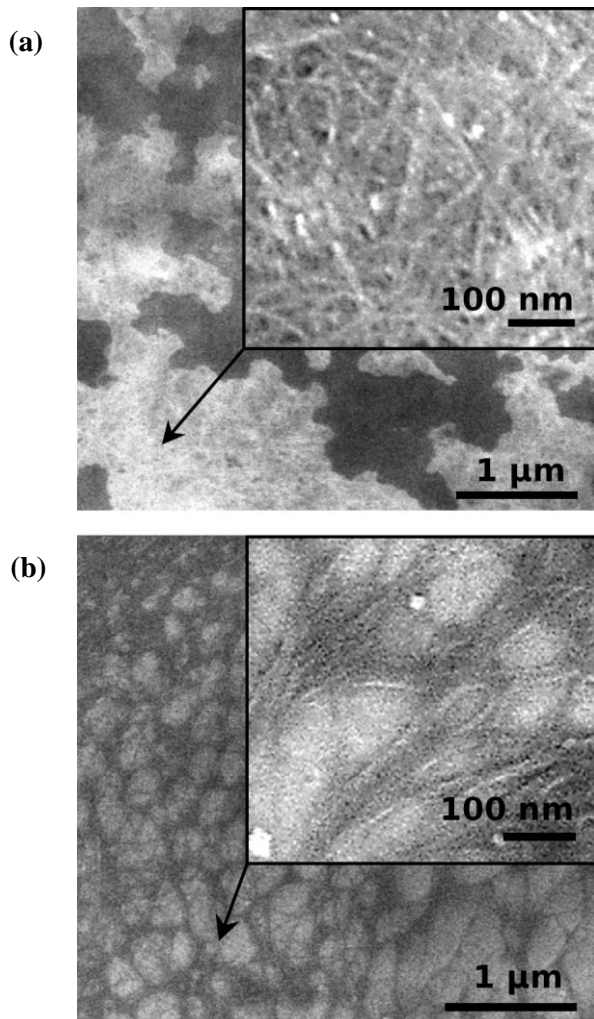


Figure 3.4. SEM images of the samples from *aged* (a) and *fresh* (b) solution

3.2. Investigation Techniques and Equipment

3.2.1. Absorption Spectra Measurements

Absorption spectra measurements were performed in transmission mode using the *Jasco V-670* spectrophotometer. In the case that the interdigitated comb-like electrodes were used for sample preparation, the referencing background signal was obtained from the measurements of the empty electrode plate.

3.2.2. Ultrafast Transient Absorption Investigations

Ultrafast transient absorption investigations were performed by means of a pump-probe spectrometer based on a *Pharos* femtosecond laser (*Light Conversion*) generating 1030 nm, 250 fs duration pulses at 5 kHz repetition rate. Parametric generator *Orpheus* (*Light Conversion*) was used to produce excitation pulses at 1000 nm, and light continuum generated in a sapphire plate was used as a probe light.

3.2.3. Steady-state Photocurrent Investigations

The steady-state photocurrent was measured using a *Keithley 6487* picoammeter. The steady state voltage up to 5 V was applied to interdigitated comb-like electrodes forming the electric field between neighboring electrodes. The field strength was position dependent; it was up to about four times larger in close proximity of the electrodes than in the

middle between them. The samples were illuminated with the green light-emitting diode (LED) with the light intensity of $300 \mu\text{W}\cdot\text{cm}^{-2}$. The photocurrent was determined by subtracting the current measured in dark from the current under illumination.

3.2.4. Transient Photocurrent Investigations

Transient photocurrent investigations were performed with an *Agilent Technologies DSO 5054A* oscilloscope and the arbitrary function generator *Tektronix AFG 3101* under the sample illumination with pulsed laser light. A graphical representation of the electrical circuit is given in **Figure 3.5**. An investigated sample represented here as parallel-connected capacitor and resistor. Two types of lasers were used for sample excitation: picosecond laser with pulses of ~ 150 ps duration at 532 nm or 1064 nm wavelength at the 5 Hz repetition rate, and a femtosecond Ti:sapphire laser, producing 800 nm light pulses of ~ 130 fs duration at 430 Hz repetition rate. The femtosecond Ti:sapphire laser was equipped with an optical parametric amplifier *Topas-C* for the excitation at 1000 nm. Synchronization scheme of electrical and optical pulses is represented in **Figure 3.6**.

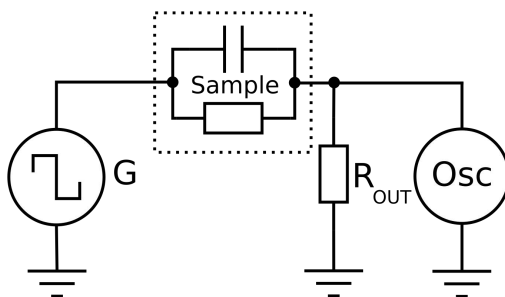


Figure 3.5. Scheme of electrical measurements setup (G – arbitrary function generator, Osc – oscilloscope, R_{OUT} – oscilloscope load resistance)

The transient photocurrent was measured in the current mode using the 50Ω input of an oscilloscope (load resistance R_{OUT}) and in the integrating regime using $1 \text{ M}\Omega$ oscilloscope input when sample and oscilloscope capacitances served as the integrating capacitor. The integrating regime enables the measurement of very weak photocurrents on long timescales and it also has a better time resolution. The voltage is proportional to the charge extracted from the sample, while the photocurrent strength can be evaluated as a time derivative of the extracted charge transients.

The extracted charge in the current mode can be defined as:

$$Q_{extr}(t) = \int_0^t I(t') dt' \quad (3)$$

Time resolution of the current-mode measurements was about 10 ns, mainly determined by the oscilloscope input resistance and the sample capacitance, which, depending on the PCBM/SWCNT film composition ranged between 3 nF and 20 nF.

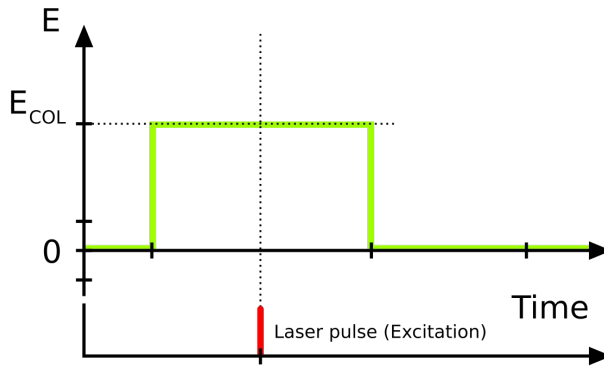


Figure 3.6. Experimental time arrangement for the transient photocurrents measurements

Time resolution of the integrating regime was about 2 ns and was mainly limited by the oscilloscope bandwidth – nevertheless it was better than that of

the current regime. A more convenient measurement of weak currents at long timescales is another advantage of the integrating regime, therefore it was mainly used.

The integrated kinetics were corrected for the limited recharging time of the integrating capacitor using the procedure described by Kettlitz et al. in ref.[123], otherwise it would cause a decrease of the extracted charge values during tens of microseconds.

In order to improve the accuracy and exclude the influence of some slow sample photomodification processes the measurements were performed by computer which controlled the collection and averaging of experimental data from many laser pulses as well as from many cycles in variation of experimental parameters.

3.2.5. Time-delayed Collection-field (TDCF) Technique

Time-delayed collection-field (TDCF) technique is a good tool aiming to separate the charge carrier generation and extraction phases as well as to investigate the carrier recombination dynamics. TDCF investigations were performed with the same experimental setup as the transient photocurrent measurements. An adjustable voltage was kept applied to the sample during the optical excitation (generation voltage E_{GEN}) and after a tunable delay-time a collection voltage (E_{COL}) was switched on, as shown in **Figure 3.7**. Charge extraction kinetics was measured using an integrating measurement mode as described in transient photocurrent investigations section. The photocurrent appears together with the current in darkness, therefore the time-delayed charge extraction kinetics were evaluated as the difference between the charge extraction kinetics with and without the optical excitation.

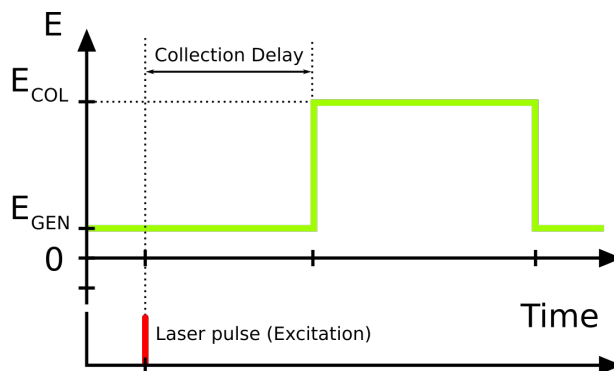


Figure 3.7. Experimental time arrangement for the TDCF measurements

3.2.6. Time-resolved Electric-field-induced Second Harmonics (TREFISH) Generation Technique

Optical harmonics generation in addition of being primary important effect in nonlinear optics and laser technology is a powerful tool for investigation of optical and electronic properties of materials. Huge possibilities to create different organic compounds give us opportunities to have many materials suitable for optics, organic electronics or optoelectronics. Electric-field-induced second harmonics (EFISH) generation has been recognized as an important nonlinear technique for investigation of nonlinear effects in centrosymmetric medium, polarizability and charge carrier mobility measurements. Theory of harmonics generation was investigated as soon as laser was created.[124,125] According to literature, there are five ways for second harmonic generation: electric dipole, magnetic dipole coupling, electric quadrupole, magnetic dipole and electric dipole coupling mechanisms.[125] The last four among them are suitable for centrosymmetric

materials. But these are higher order multipole processes and their transition moments are small compared with the electric dipole transitions.[126,127]

Model of electric dipole mechanism requires medium to be polar. Electric-field-induced second harmonics (EFISH) generation technique fulfills that condition. When acted on by the electric field, the naturally isotropic medium polarizes according to that electric field direction. If material has the center of symmetry, this material loses it at these conditions.[126] This process is especially important to isotropic medium which isn't able to generate second harmonic from the only laser irradiation.

EFISH generation effect has been applied successfully for the investigation of the internal electric field dynamics in field effect transistors [128], organic diodes [129], light emitting diodes [130] and solar cells [131–133]. In combination with ultrafast spectroscopy methods it enabled investigation of ultrafast charge carrier dynamics in organic materials and photoelectrical devices.

Usual experimental realizations for EFISH measurements use special cells for liquids [134] and gases [135] and "sandwich" type samples in a form of thin layers between semitransparent electrodes for solids [129–133]. In case if one of the electrodes is nontransparent metal, the EFISH measurements in thin films are usually performed in reflection mode.

The realization of experiment in reflection mode isn't optimal. If the incoming laser beam is perpendicular to the sample surface, electric field strength vectors of the laser radiation and of the applied external voltage are perpendicular. Consecutively, the EFISH generation in isotropic materials is not possible. Usually in measurements, performed in reflection mode, electric field strength vectors of incoming laser radiation (E_{OPT}) and applied external electric field (E_{EXT}) are arranged to form an acute angle (see **Figure 3.8**). Therefore, the p-polarized light beam propagating at a small angle to the film

surface is usually used. However, a refractive index of the investigated material reduces the angle of refraction. In this case only a small projection of the electric field of light to the normal to a surface contributes to the EFISH generation. It would be ideal that this angle were equal to zero. When these electric field strength vectors are parallel, we can suspect that EFISH generation were maximal in this particular case. But it is difficult to form a big enough angle of incidence and realize this scheme for EFISH measurements in reflection mode because of the impact of refractive index.

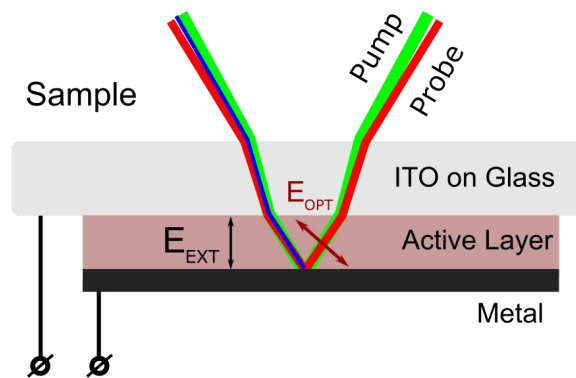


Figure 3.8. Sample structure and arrangement of electric fields in reflection measurement-mode

The ultrafast carrier motion dynamics was investigated using a time-resolved electric-field-induced second harmonic generation (TREFISH) technique. This all-optical investigation technique has demonstrated its usefulness for investigations of ultrafast carrier motion dynamics in conjugated polymers [136] and blends for organic solar cells [137] and was described in detail earlier.[136,138]

Briefly, this is a pump-probe-type technique which is based on the EFISH generation phenomenon — that facilitates the measurement of electric field dynamics directly inside the investigated material. An applied voltage charges the sample capacitance prior to optical excitation. When the sample is excited

with an ultrashort light pulse, the induced photocurrent reduces the electric field by discharging the sample's capacitance and subsequent probe pulse, delayed by a variable delay time, probes the electric field kinetics.

The electric field strength is determined from the EFISH signal as:

$$F = F_0 \left(\frac{I_{2H}}{I_{2H}^0} \right)^2 \quad (4)$$

where F_0 is the applied electric field, I_{2H} and I_{2H}^0 are the second harmonic intensities with and without excitation, respectively. The square root of the EFISH intensity depends linearly on the applied voltage, thus enabling a straightforward determination of the electric field strength from the EFISH signal.

But on the contrary to previous successful applications,[136,138] in our case there is a difference in applying this method because of the sample architecture – our samples consist of films, formed on interdigitated comb-like electrodes (IDEs). This change in the sample structure and experimental setup brought us some additional effects which will be more discussed later in the results section. The experiments are performed in transmission mode, therefore, in our case, sample is positioned perpendicularly to incoming laser radiation and the polarisation of the probe laser light is adjusted so that the electric field strength vectors of incoming laser radiation (E_{OPT}) and applied external electric field (E_{EXT}) would be parallel. A schematic representation of the experimental setup, adapted to transmission-mode TREFISH measurements, is reproduced in **Figure 3.9**.

A femtosecond Ti:sapphire laser equipped with an optical parametric amplifier Topas-C was used as a light source. The samples were excited at 1000 nm, and fundamental laser radiation at 800 nm was used as a probe light to probe the second harmonic generation efficiency. To minimize irreversible

sample damage from a current breakdown, the voltage was applied in the form of short $20 \mu\text{s}$ square pulses (*Tektronix* AFG 2021 arbitrary function generator equipped with the high-speed high-voltage linear amplifier *Falco Systems* WMA-320) synchronized with laser pulses. Synchronization scheme is similar to that, used in transient photocurrent measurements (**Figure 3.6**). The electric-field-induced second harmonic (EFISH) intensity was measured by the photomultiplier. An optical chopper, periodically interrupting a pump light beam, was used to register the second harmonic intensities with and without excitation. Adjusting mirror **M4** and optical slit **S1** (**Figure 3.9**) were introduced into setup due to peculiarities of EFISH generation from the samples, formed on interdigitated comb-like electrodes.

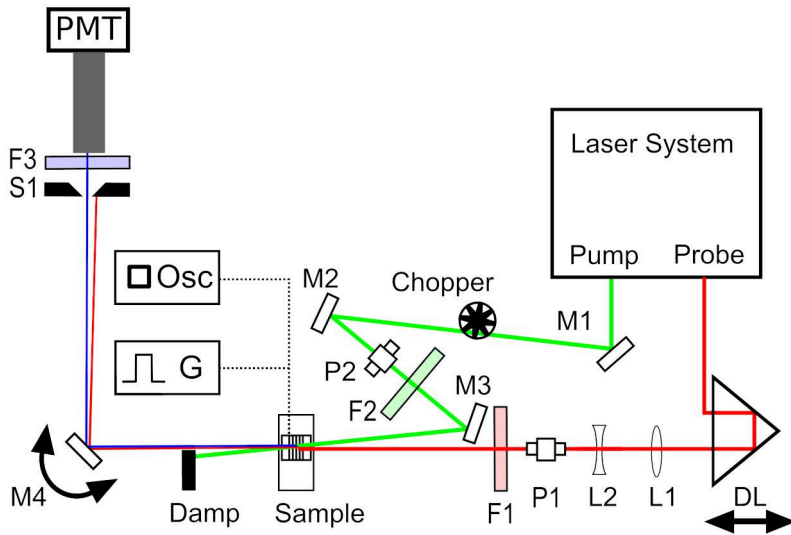


Figure 3.9. Adapted experimental setup for the TREFISH measurements in transmission mode (M – mirrors, L – lenses, DL – optical delay line, F – optical filters, P – polarisation adjusting plates, S – optical slit, PMT – photomultiplier tube)

4. RESULTS AND DISCUSSION

To obtain a clearer picture of photoelectrical processes in SWCNT layers, we started with conventional transient and steady-state photocurrent experimental methods as well as time-delayed-collection field technique to investigate the charge carriers generation, motion and recombination processes in layers of aggregated polymer-wrapped (6,5)-SWCNTs mixed with phenyl-C61-butyric acid methyl ester (PCBM) deposited on the interdigitated comb-like electrodes (IDE) from Micrux Technologies.

To reveal the information about the light absorbance or, in other words, which of the compounded materials is going to be acted by which wavelength of light, we measured the absorption spectra of the samples. **Figure 4.1** shows the absorption spectra of the samples with different PCBM/SWCNT mass ratios. Designation SWCNT/PFO-Bpy in **Figure 4.1 (b)** corresponds to the sample, almost identical to the sample PCBM/SWCNT (120/1) with only PCBM replaced by additional PFO-Bpy. Absorption at 1000 nm and 580 nm corresponds to the two low energy dipole-allowed exciton transitions in (6,5)-SWCNTs. The absorbance between 400 nm and 500 nm in samples with high PCBM concentrations is mostly due to PCBM, while both PCBM and (6,5)-SWCNTs absorb at 300-400 nm. An observed 7 nm red-shift of the exciton band in the blends may be due to the increased dielectric screening in SWCNTs by PCBM molecules nearby.[72]

Comparison of the spectra obtained from *aged* and *fresh* samples revealed that there is no clear difference between spectra of the two sample types. Relative intensities of polymer and SWCNTs absorption bands give estimate of the SWCNTs to PFO-Bpy mass ratios of about 1 to 20.

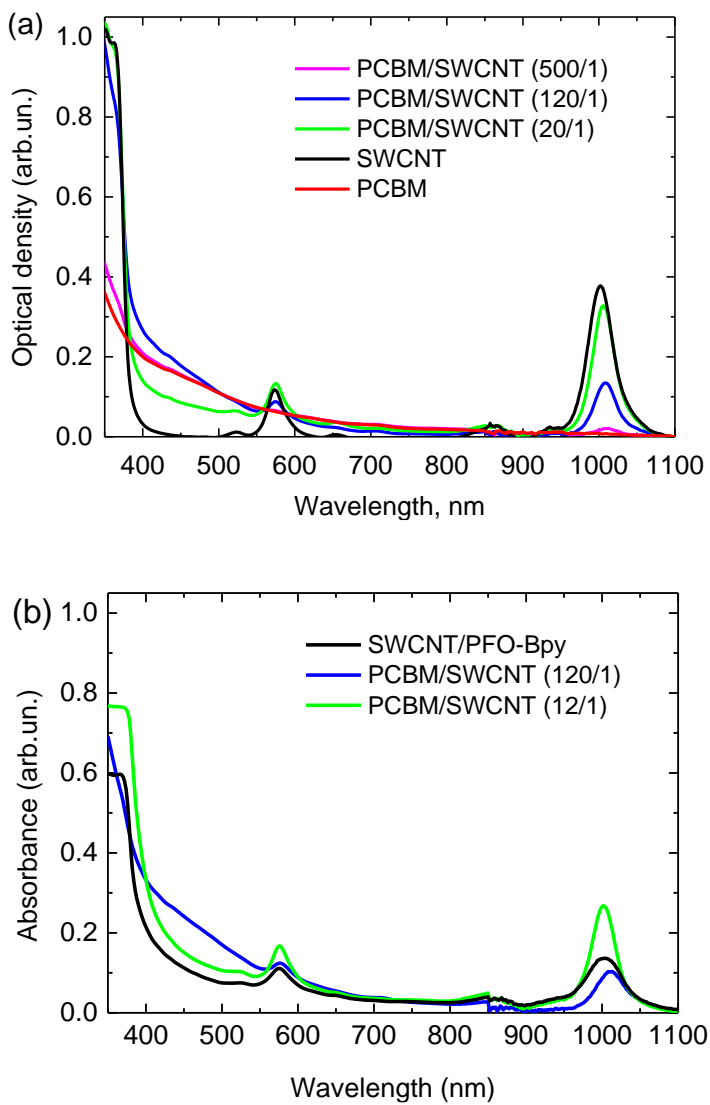


Figure 4.1. Absorption spectra of films on the comb-like electrodes with different PCBM to SWCNT mass ratios – (a) *aged* and (b) *fresh* samples. The absorbance of electrodes was compensated

4.1. Transient Photoconductivity of Carbon Nanotube films

4.1.1. Steady-state and Transient Photoconductivity

For the initial characterization of the photoconductivity properties of the samples, we measured steady-state photocurrents in the samples with different PCBM to SWCNT mass ratios. For these measurements, samples were illuminated by an incandescent halogen lamp jointly with band-pass filters serving for selection a specific excitation-wavelength range. Sample architecture with the investigated film deposited on the IDE enabled an investigation of the carrier drift along the film plane (lateral motion). A sizeable photocurrent was observed only under excitation at SWCNT absorption bands, while the photocurrent was absent or very low under excitation in-between SWCNT exciton bands at about 450 nm and 700 nm. Taking into account the PCBM absorption profile, this suggests that the excitation of PCBM produces no or only a very weak photocurrent.

For further steady-state investigations and for better comparison of the results with the transient photocurrent measurements (performed under 532 nm laser illumination) we thus illuminated samples with an LED in the narrower, 520-530 nm, range, at the vibronic band of the second electronic transition of (6,5)-SWCNT.

Figure 4.2 shows the dependence of the steady-state photocurrent on the PCBM/SWCNT mass ratio for the excitation intensity of $300 \mu\text{W}\cdot\text{cm}^{-2}$. The absorbance of samples at the excitation wavelength decreased with the PCBM/SWCNT mass ratio, and therefore the photocurrent in the **Figure 4.2** is normalized to the absorbed light intensity. The normalized photocurrent was very low in the pure SWCNT sample. It increased with the PCBM content,

but started to decrease again at a PCBM/SWCNT mass ratio exceeding one hundred.

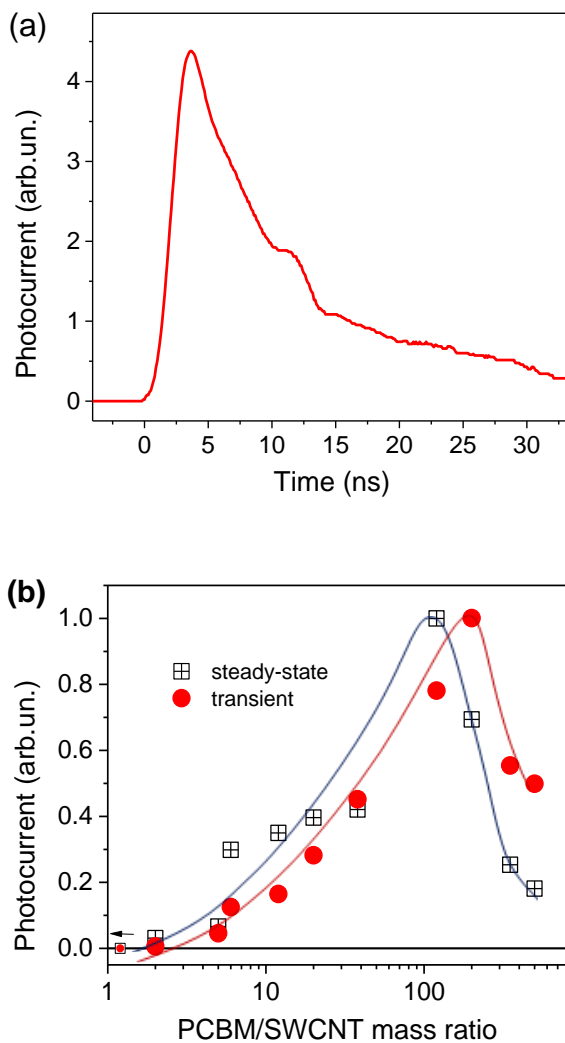


Figure 4.2. (a) Typical transient photocurrent kinetics; (b) dependence of the steady-state and transient photocurrent on the relative PCBM/SWCNT mass ratio concentration. Smaller symbols show photocurrent values in the sample without PCBM

For transient photocurrent measurements, pulsed excitation of our samples with 532 nm picosecond laser pulses at the 5 Hz repetition rate created short

photocurrent pulses limited by the time resolution of our experimental setup (see **Figure 4.2(a)**) containing a very weak photocurrent tail lasting for tens of nanoseconds.

The amplitude of the photocurrent pulse showed a similar dependence on the PCBM/SWCNT mass ratio to that observed with the steady excitation. The only difference is the slight shift in the peak position (see **Figure 4.2(b)**). The non-monotonic photocurrent dependence on the PCBM content suggests that at least two competing processes determine the photocurrent intensity.

The increase of the photocurrent with the PCBM content at low concentrations is easy to rationalize — PCBM molecules act as electron acceptors from excited SWCNTs and facilitate the charge carriers generation.[73,139] Thus electrons are created in PCBM while the holes – in SWCNTs. Photocurrent is determined by the efficiency of the charge carrier generation and by mobilities of the created charge carriers. According to that interpretation the charge-carriers-generation efficiency is expected to saturate when carbon nanotubes are covered with a sufficient amount of PCBM molecules to ensure an efficient electron capture. The small residual photocurrent in samples without PCBM is probably created by impurities, defects or carriers transfer to metal contacts.

The decrease of the photocurrent at a high PCBM content is most likely related to the increase in the dark-state resistance of the samples from $\sim 8\text{ k}\Omega$ of a pure SWCNT film to $\sim 200\text{ k}\Omega$ of the films with the highest PCBM content. This suggests that PCBM molecules covering SWCNTs electrically isolate them from the metal electrodes and possibly one from another also preventing hole motion.

A less significant decrease of the transient photocurrent at high PCBM content in comparison with the steady-state photocurrent is in line with the following explanation. Charge carriers, moving inside isolated SWCNTs, create a

displacement photocurrent which significantly contributes to the transient photoelectrical signal while it does not contribute to the steady-state photocurrent.

4.1.2. Photocurrent Kinetics

To further explore the lateral photoconductivity properties of SWCNT/PCBM films deposited on interdigitated electrodes (IDE), we investigated the photocurrent kinetics using the integrating measurement regime. In this case, we used a 1 M Ω oscilloscope input, and measured the voltage kinetics on a capacitor formed by the sample and oscilloscope capacitances. This regime is more favorable to the measurement of very weak photocurrents on long timescales and it also has a better time resolution.

Figure 4.3 shows the charge extraction kinetics from the samples with a different PCBM content. These measurements revealed that the charge extraction kinetics have three growth components:

- 1) the initial ultrafast component present in all samples and shorter than the time resolution of our setup (~ 2 ns). It reveals the presence of a strong but short-lasting photocurrent;
- 2) the second component, also present in all samples, which reveals the photocurrent lasting for several microseconds;
- 3) the longest, tens of microseconds, component which was observed only in the samples with a high PCBM content.

We can attribute the third photocurrent component to the drift of electrons through the PCBM. The PCBM molecules, at their high content, are likely to form a continuous film enabling the drift of electrons, while at their low

content, these molecules are likely to rest in a form of isolated clusters, probably adsorbed partly to SWCNTs, and also do not form a continuous path for electrons.

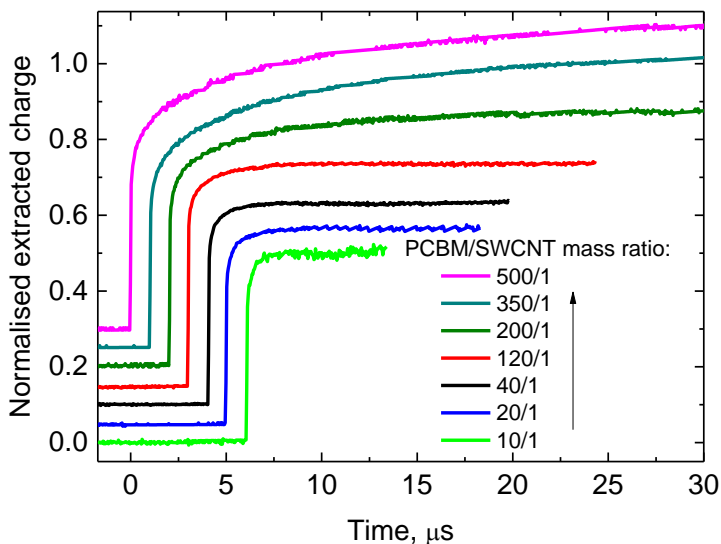


Figure 4.3. Charge extraction kinetics from the samples with different PCBM to SWCNT mass ratios measured under excitation at 1064 nm with $16 \mu\text{J}\cdot\text{cm}^{-2}$ energy pulses under 2 V applied voltage. For a clearer presentation they are normalized to the equal intensity of the fast growth component and shifted vertically and horizontally.

The estimation of the PCBM film thickness supports this attribution. The absorbance of the samples with the highest PCBM content is of about 0.15 OD at 450 nm, which translates to the PCBM layer thickness of about 20 nm. The same estimation for three films with the lowest PCBM content gives their thicknesses below 1 nm, thus insufficient for the formation of the continuous film enabling lateral electron motion.

Electron extraction times are also in a good agreement with the reported electron mobility values in PCBM layers ranging from $0.001 \text{ cm}^2\cdot\text{V}^{-1}\text{s}^{-1}$ to

$0.1 \text{ cm}^2 \cdot \text{V}^{-1} \cdot \text{s}^{-1}$. [140–143] This gives the electron extraction time between $1 \mu\text{s}$ and $100 \mu\text{s}$ at the applied voltage of 2 V , which is in a good agreement with the experimentally obtained slow charge extraction times of tens of microseconds. As the PCBM is out of the scope of this work we will not analyze further in detail the motion of electrons through PCBM.

The first two (accordingly, the ultrafast and the intermediate, several microseconds) photocurrent components are present in all samples, including those without PCBM, therefore they should be attributed to the carriers motion through the network of interconnected SWCNTs.

Investigation of films prepared from fresh nanotube suspension and from aged suspension with a high amount of more closely assembled or bundled SWCNTs enabled us to distinguish between intratube and intertube carrier motions. Transient photocurrent kinetics were measured in films made from *fresh* and *aged* solutions of SWCNTs with different PCBM to SWCNTs mass ratios. **Figure 4.4** compares these kinetics of the cumulated charge measured in integrating regime. All samples exhibit an ultrafast increase of the cumulated charge indicating that decay of the photocurrent is too fast to be resolved by our setup with its time resolution of about 2 ns , as it was noticed before. The subsequent kinetics strongly varies from sample to sample. PCBM/SWCNT (12/1) and SWCNT/PFO-Bpy films prepared from a fresh solutions show only a fast growth of the cumulated charge and subsequent slow decay caused by recharging of the sample capacitance with its rate being determined by the sample resistance.

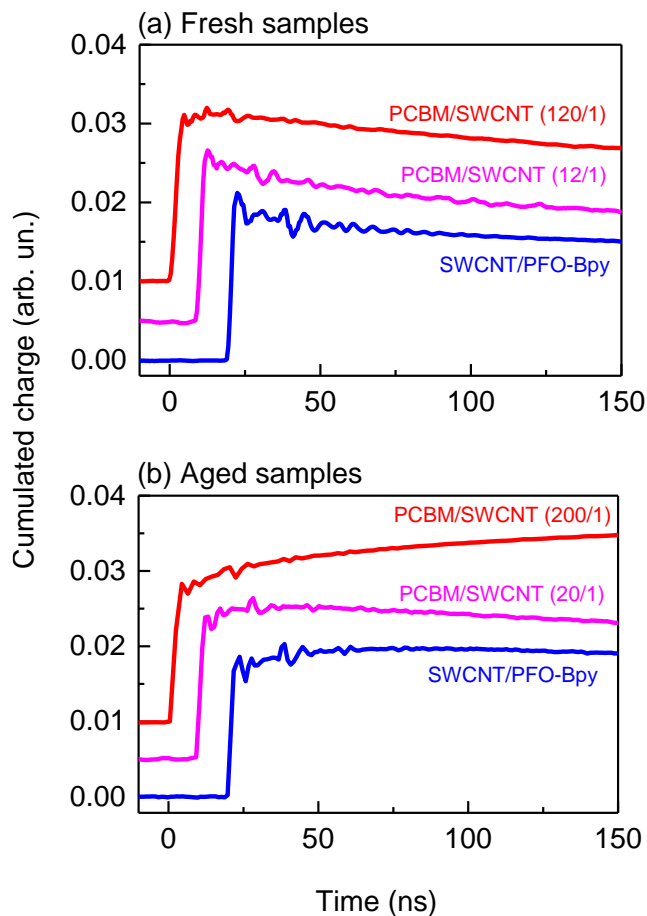


Figure 4.4. Kinetics of the cumulated charge for *fresh* (a) and *aged* (b) samples with different SWCNT to PCBM mass ratios measured at 5 V applied voltage. For better presentation, the curves are offset vertically and horizontally. Decay on a hundreds of nanoseconds timescale is caused by the sample recharging.

The photoconductivity of SWCNT/PCBM blends was previously attributed to charge carrier generation by electron transfer from photoexcited SWCNTs to adjacent PCBM molecules.[21,144] Despite relatively high content of PFO-Bpy copolymer in our samples, PCBM molecules apparently made close complexes with SWCNTs enabling efficient electron transfer. In contrast,

oxygen or other impurities were suggested to play the role of electron acceptor in samples without PCBM.[28] The photocurrent was shown to be dominated by the hole motion within the SWCNTs network. Thus, the hole drift in PCBM/SWCNT (12/1) and SWCNT/PFO-Bpy films continues for less than 2 ns.

The sample, indicated as PCBM/SWCNT (120/1), which was prepared from fresh solution shows an additional weak increase of the cumulated charge during tens of ns. This increase is more expressed for all films prepared from aged solutions. The tens of nanoseconds component was previously attributed to intertube carrier migration within aggregates. The relative intensity and the decay rate of this photocurrent component vary somewhat from sample to sample, which is not surprising, taking into account that drop-casting is prone to the variability of the film microstructure, thus causing different percolation between SWCNTs. The absence of this component in some films made from fresh SWCNTs solutions suggests that SWCNTs in these films are less aggregated and thus less percolated, which is in agreement with the SEM images presented in **Figure 3.4** in the materials section. These observations are in agreement with the earlier conclusion that the carrier generation and drift inside individual nanotubes take less than 2 ns at the electric field strengths used here. PCBM/SWCNT (200/1) film also shows a weak, hundreds of nanoseconds component. This component is probably also present in PCBM/SWCNT (120/1) sample only upstaged by the sample recharging. This slow photocurrent component observed in samples with a high PCBM content was also attributed previously to the electron motion within PCBM.

4.1.3. Saturation of the Photocurrent Components

The charge extraction kinetics of the PCBM/SWCNT sample with the mass ratio of 120/1, measured under photoexcitation at 1064 nm at different applied voltages and at different excitation intensities are presented in **Figure 4.5**. Since PCBM does not absorb at 1064 nm, we can unambiguously attribute the photocurrent to the excitation of SWCNTs at the low energy wing of the first sub-band exciton. We found that the extracted charge was proportional to the applied voltage, but the shape of the extraction kinetics within the experimental accuracy was independent of the applied voltage.

The dependence of the charge extraction kinetics on the excitation intensity (presented in **Figure 4.5(b)**) is more complex. The $1.25 \mu\text{J}\cdot\text{cm}^{-2}$ curve multiplied by 4 coincides with the $5 \mu\text{J}\cdot\text{cm}^{-2}$ curve, which shows that the extracted charge increases linearly with the excitation intensity and the shape of the charge extraction kinetics does not change up to about $5 \mu\text{J}\cdot\text{cm}^{-2}$. This suggests that carrier dynamics at low excitation densities is not affected by the nongeminate electron-hole recombination or other nonlinear processes. At higher intensities, the extracted charge starts to saturate. The intermediate component saturates completely starting with the $20 \mu\text{J}\cdot\text{cm}^{-2}$ excitation intensity, while the ultrafast component does not reach complete saturation.

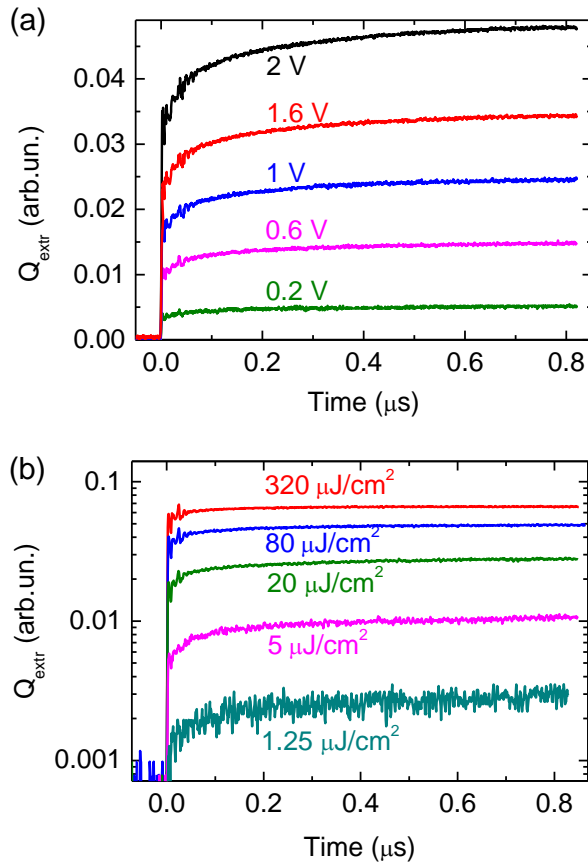


Figure 4.5. Charge extraction kinetics from the PCBM/SWCNT (120/1) sample measured under excitation at 1064 nm at **(a)** different applied voltages, and **(b)** at different excitation intensities

The estimation based on the evaluation of the total number of SWCNTs per square area unit of the film using the published SWCNT photoabsorption cross-sections [121,122] and absorbed photon density suggest that the saturation of the extracted charge starts at the excitation intensity creating approximately one charge pair per nanotube.

4.1.4. Time-delayed Collection-field Measurements

Time-delayed collection-field (TDCF) investigations (see methods section for details) were performed aiming to separate the charge carrier generation and extraction phases as well as to investigate the carrier recombination dynamics. For these measurements an adjustable generation-voltage was applied, during of which the photoexcitation of the sample was performed, and then after a tunable delay-time the collection-voltage was switched on. Typical TDCF carrier extraction transients, measured in the integrating mode are presented in **Figure 4.7(a)**.

Figure 4.6 shows the dependence of the total extracted charge (determined from the plateau of the charge extraction transients) on generation and collection voltages at the collection delay of 300 ns. The total extracted charge increases linearly with the collection voltage, which shows that the carrier extraction is the major factor determining the photocurrent dependence on the applied voltage.

The extracted charge shows no saturation, indicating that the used voltage was not nearly high enough to extract all photogenerated charge carriers. On the other hand, the extracted charge (except for some random scattering) was independent of the generation voltage when the collection voltage was maintained at 3 V. This unambiguously shows that the external electric field is not necessary and does not influence the carrier photogeneration, at least up to its strength of about $10^4 \text{ V}\cdot\text{cm}^{-1}$. This conclusion is in a good agreement with the published data on the spontaneous carrier generation in carbon nanotubes in solutions [66] and at the SWCNT/fullerene interfaces.[68,72,73]

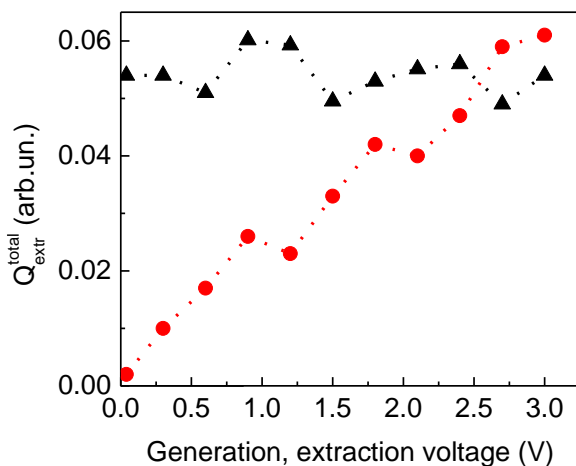


Figure 4.6. Dependences of the total extracted charge from the sample PCBM/SWCNT (120/1) by the collection voltage of 3 V delayed by 300 ns on the generation voltage (triangles) and on the extraction voltage when the generation voltage was 0 V (circles).

Figure 4.7(a) shows the time-delayed carrier extraction kinetics at different collection delay-times measured in PCBM/SWCNT (120/1) sample at the 0 V generation and 2 V extraction voltages. Zero time corresponds to the optical excitation pulse. The kinetics resemble those obtained under the steady state applied voltage, but the contribution of the ultrafast component is smaller and it decreases with the extraction delay-time. The intermediate component also becomes slower at longer delays. Variation of the charge carrier extraction kinetics with the collection delay time indicates that besides the decay in carrier density, their mobility also decreases, which may be attributed to the carrier localization at low energy sites, typical for disordered materials.[145]

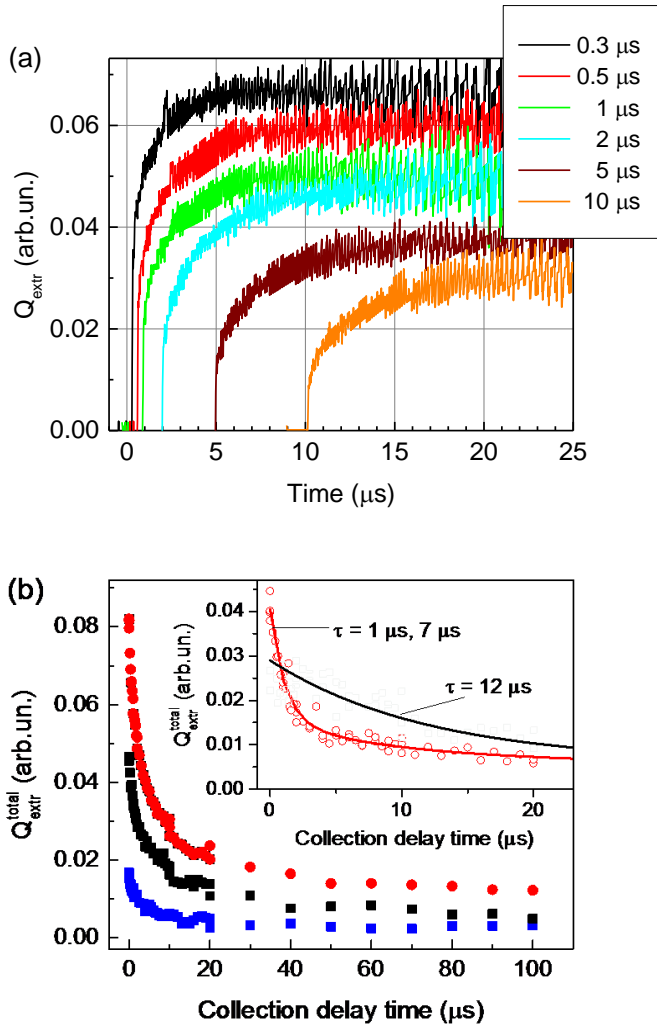


Figure 4.7. (a) TDCF charge extraction kinetics at different delay times between optical excitation and electrical collection-voltage pulses; (b) dependence of the total TDCF extracted charge on the extraction delay time at $320 \mu\text{J}\cdot\text{cm}^{-2}$ (red dots), $80 \mu\text{J}\cdot\text{cm}^{-2}$ (black dots) and $20 \mu\text{J}\cdot\text{cm}^{-2}$ (blue dots) excitation intensities. Insert shows the same dependence for the ultrafast (red symbols) and slow (black symbols) extraction components. Lines in insert show approximation of the dependences with exponential or biexponential decay functions.

Figure 4.7(b) shows the dependence of the total extracted charge on the collection delay time at the 0 V generation and 2 V collection voltages

measured in the same PCBM/SWCNT (120/1) sample at the at three different excitation intensities: $320 \mu\text{J}\cdot\text{cm}^{-2}$, $80 \mu\text{J}\cdot\text{cm}^{-2}$ and $20 \mu\text{J}\cdot\text{cm}^{-2}$. It shows that the charge carrier concentration decreases rapidly during the first several microseconds, but almost stabilizes after several tens of microseconds. By normalizing the delay dependences of the carrier extraction kinetics we see that their shapes remained identical even when the excitation intensity increased by a factor of 16, indicating that the bimolecular recombination did not play any important role (**Figure 4.8**).

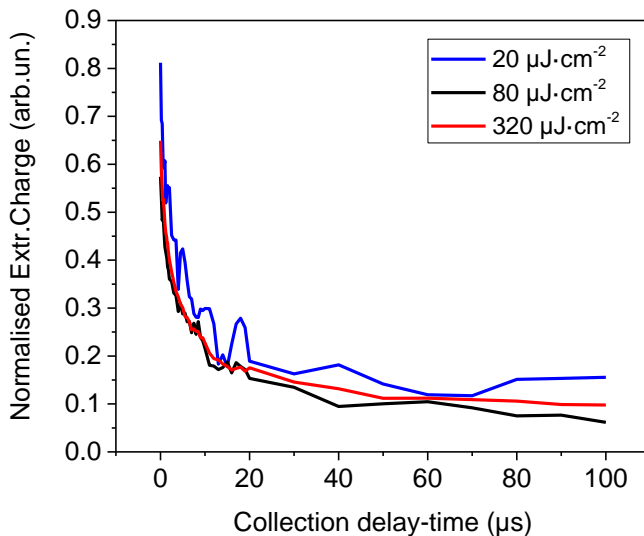


Figure 4.8. Normalized charge carrier extraction kinetics

The inset in **Figure 4.7(b)** shows the dependence of charges extracted during the ultrafast and intermediate phases, which indicates that the concentration of charge carriers responsible for the ultrafast photocurrent phase decays much faster than that responsible for the intermediate phase.

It also should be noted that the decay of the charge carrier density determined from TDCF measurements is much slower than the decay of the photoconductance of SWCNT/fullerene systems determined by means of the

time-resolved microwave conductivity (TRMC) technique,[66,68,72] where it was found to be determined by the second order recombination.[68] This difference further supports the conclusion that the bimolecular recombination in our systems is insignificant and the carrier decay is determined by the geminate charge pair recombination.

Suppression of the bimolecular recombination is most probably related to the structure of our samples. SWCNTs form a weakly percolated network, where the carrier migration between nanotubes is slow, the electron migration within the thin disordered PCBM film is also slow and therefore the recombination of nongeminate electrons and holes is inefficient.

4.1.5. Decreasing Carrier Mobility

Our findings confirm that photocurrents in the polymer-wrapped SWCNT/PCBM system are created by spontaneous electron transfer from photoexcited SWCNTs to PCBM. We distinguish a fast carrier motion in the interconnected-SWCNTs network and a slow one within the PCBM phase.

To this end, we next compare charge extraction kinetics measured under the applied constant voltage and by means of the TDCF technique. The charge extraction kinetics at the constant applied voltage lasting for several microseconds is determined by the product of the time-dependent carrier concentration and carrier mobility. On the other hand, TDCF measurements show much slower carrier concentration decay lasting for hundreds of microseconds, thus indicating that the charge extraction kinetics at the constant applied voltage is mainly determined by the decreasing carrier mobility.

In order to understand the mechanism of the carrier mobility decrease we again consider the spatial structure of our samples. As discussed before, SWCNTs and their bundles may be considered as dispersed in the isolating PCBM matrix or air. Under these conditions the drift distance of photogenerated holes is limited by the SWCNT length, or by dimensions of their bundles forming a percolated pathway. Carriers drifting inside such a SWCNT network are expected to have different mobilities depending on the length scale. The mobility is high for the intratube hole motion,[146] but it may drop significantly when carriers reach tube ends where continued drift requires them to jump to another tube. However, this mobility decay mechanism is important only to the one-directional carrier drift, but plays no role in TRMC measurements where carriers move forth and back, or in TDCF investigations where charge carriers during the delay time before collection pulse move only by diffusion.

4.1.6. Extracted Charge Saturation at High Excitation Intensities

Finally we will briefly discuss saturation of the extracted charge at high excitation intensities. It may be caused by two types of processes: the nonlinear charge carrier and/or exciton recombination; or the electric field screening. The saturation can hardly be caused by the bimolecular carrier recombination because the recombination kinetics determined by TDCF technique is identical at excitation intensities differing up to 16 times (**Figure 4.8**). Exciton-exciton annihilation, which was shown to be very effective in SWCNTs,[147] would cause proportional saturation of both ultrafast and intermediate photocurrent components, which is not the case. Thus, although we cannot completely exclude these processes, their role in the photocurrent saturation is apparently not dominating.

The electric field screening is another common process limiting photocurrents in photoconducting organic layers. In homogeneous materials, space charges created by drifting carriers may screen the electric field in the bulk material and reduce the current. A significant field screening is expected when the photogenerated charge becomes comparable to the charge on electrodes, i.e. to the product of the sample capacitance and the applied voltage. In the integrating regime, it causes the voltage drop comparable to the applied voltage. In our samples the voltage drop was more than ten times lower than the applied voltage even at the highest used excitation intensities, which excludes the total macroscopic field screening. However, the screening mechanism in our samples containing photoconducting SWCNTs dispersed in the PCBM matrix may be more complex. In addition to the macroscopic screening, drifting charge carriers may screen the electric field just locally, inside individual SWCNTs or their bundles, when charge carriers accumulate at their edges. This mechanism may cause photocurrent saturation at lower extracted charge values in agreement with the photocurrent dependences on the excitation intensity presented before in **Figure 4.5**.

4.2. Ultrafast Initial Charge Carrier Motion Dynamics

As it was shown above, we applied conventional electrical experimental methods to investigate the charge-carrier generation, motion and recombination processes in films composed of aggregates of (6,5)-SWCNTs wrapped with PFO-Bpy copolymer. Addition of the fullerene derivative PCBM was found to greatly enhance the carrier generation efficiency in such samples.

At this point our findings have confirmed that photocurrents in the polymer-wrapped SWCNT/PCBM system are created by spontaneous electron transfer from the photoexcited SWCNTs to PCBM. Electrical investigations with about 2 ns time resolution also revealed photocurrent generation and decay on a sub-microsecond timescale. It was distinguished a fast intertube carrier migration in the SWCNT network and a slow one within the PCBM phase. The above mentioned results were also published in scientific article – see ref. [17]. However, the intratube charge-carrier generation and motion were too fast to resolve using conventional electrical methods. Thus, the properties and motion peculiarities of the intratube charge-carrier generation and motion require further analysis using better time-resolution techniques.

To investigate the ultrafast carrier generation and motion dynamics, we used an all-optical method based on the time-resolved electric-field-induced second harmonics (TREFISH) generation. This experimental method is sensitive to charge carrier motion with a very high time resolution of about 1 ps. And as it was mentioned earlier in the methods section, this all-optical investigation technique has demonstrated its usefulness for investigations of ultrafast carrier motion dynamics in conjugated polymers [136] and blends for organic solar cells [137] and was described in detail earlier.[136,138]

But in our case, there is a difference in applying this method because of the sample architecture. In opposite to previously used layered sandwich-type samples, our samples consist of films formed on interdigitated comb-like electrodes (IDEs). That change in the sample structure and experimental setup bring us some additional effects and requires further analysis.

4.2.1. Adaptation of TREFISH Technique to the Samples on IDEs

The time-resolved electric-field-induced second harmonics (TREFISH) generation experimental technique is a pump-probe-type measurement method, based on the phenomenon of the even optical harmonics generation in centrosymmetric systems in presence of external electric fields. The simple electric-field-induced second harmonics (EFISH) generation technique is recognized as a method for the investigation of molecular hyperpolarizability and nonlinear optical properties of materials.[148,149] This experimental method has been also successfully applied for investigation of the internal electric field distribution and its dynamics in organic materials and photoelectric devices. [136,137,150]

As it was mentioned before, usual experimental realizations for electric-field-induced second harmonics (EFISH) measurements use special cells for liquids [134] and gases [135] and sandwich-type samples in a form of thin layers between semitransparent electrodes are usually used for the investigation of solids.[130,131] In the most cases, when one of the electrodes is made of a nontransparent metal, the EFISH measurements are performed in the reflection mode.

Therefore before applying the time-resolved electric-field-induced second harmonics (TREFISH) generation technique, we first have to consider the peculiarities of EFISH generation in the experimental setup where the interdigitated comb-like electrodes are introduced.

The interdigitated comb-like electrodes for the adaptation experiment were fabricated by the direct laser ablation technique from the thin chromium layer deposited on a transparent glass plate. The electrode widths and gaps between electrodes were made equal to 4 μm and the electrode length was 2 mm. Their

height measured with a profilometer was about 70 nm. A schematic view of the electrodes is shown in **Figure 4.9(a)**.

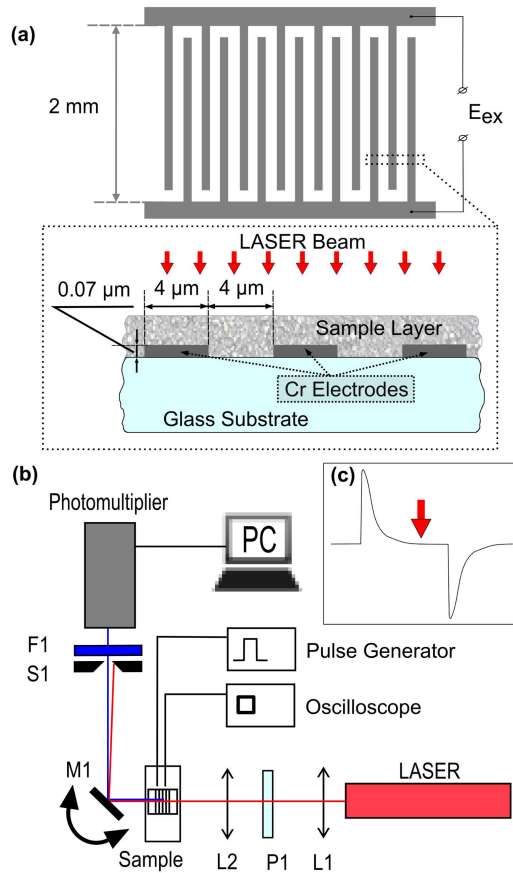


Figure 4.9. (a) Interdigitated comb-like electrodes (schematic sketch of the top-view and of the side-view, E_{ex} – external voltage), (b) Experimental setup (L1, L2 – lenses, P1 - half-wave plate for polarization rotation, M1 – adjustable mirror, S1 – slit, F1 – short-pass filter ($\lambda = 400$ nm)), (c) arrangement of synchronization of laser (arrow) and electric pulses.

A prepared sample is positioned perpendicularly to incident laser radiation in transmission measurement-mode. It is not surprising that such comb-like electrodes behave as a binary transmission amplitude diffraction grating for the incident laser radiation.

The organic films were prepared by casting drops of mixtures of organic materials on the electrodes. The film thickness was measured with a profilometer. It had been tested a wide range of organic materials in that experimental setup but the material with the highest achieved intensities of electric-field-induced second harmonics (EFISH) was chosen for further analysis. These intensities were obtained by using a well-known material – poly[2-methoxy-5-(2-ethylhexyloxy)-1,4-phenylenevinylene] (MEH-PPV, from Sigma-Aldrich). Chloroform (99.0-99.4 %, from Sigma-Aldrich) was used as a solvent. Mixtures were prepared by dissolving 10 mg of polymer in 1 ml of chloroform. Typical capacitance of the samples was about 100 pF.

The experimental setup for the EFISH investigation is presented in **Figure 4.9(b)**. It consists of the femtosecond laser system *Quantronix Integra-C* (femtosecond regenerative multi-pass Ti:Sapphire amplifier), optical elements (filters, lenses, etc.), the electrical pulse generation and detection system based on a photomultiplier. The laser produced 800 nm wavelength light pulses of about 130 fs duration at the 1 kHz repetition rate.

The EFISH generation in the MEH-PPV film of about 700 nm thickness was very weak when it was measured in the direction of the directly propagating fundamental laser radiation beam. We have changed the detection direction by precisely turning the angle of the mirror M1 as indicated in **Figure 4.9(b)**. The EFISH signal was also very weak or absent in angular positions of the diffracted fundamental laser radiation and of its second harmonics, generated with an additional crystal positioned before our sample or by the non-ideally centrosymmetric sample accordingly. However, at certain angular positions the EFISH signal was significantly stronger. **Figure 4.10** presents this angular distribution.

It should be noticed that the experimenter must pay attention to its setup when moving from layered samples to comb-like electrodes because of the

diffraction and interference occurrence in the comb-like electrode system. In opposite to previous work related to EFISH investigations using layered sandwich-type samples, [136–138] the EFISH radiation has only a very weak intensity in the direction of the directly propagating beam (0^{th} order maximum). But instead of that it has two strong maxima situated between the 0^{th} and 1^{st} order conventional second harmonics maxima and two weak maxima between the 1^{st} order maxima of the fundamental and the second harmonics beams. This unusual angular distribution may be explained considering phase relationships of EFISH electromagnetic waves generated in neighboring grating gaps (the gaps between electrodes).

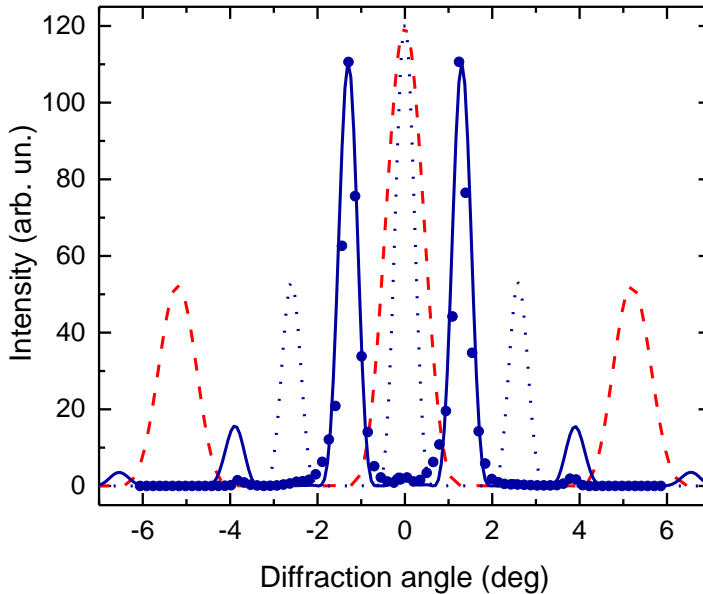


Figure 4.10. Angular dependences of the intensity of the EFISH radiation: experimentally measured data (points); calculated by using **Eq. (10)** (solid blue line). Calculated Fraunhofer diffraction of light from interdigitated electrodes grating: fundamental harmonic (dashed red line) and its second harmonic (dotted blue line).

In the case of the electric dipole approximation, the nonlinear polarization creating the EFISH signal can be stated as: [151]

$$P_z^{EFISH} = \sum_{jkl} \chi_{zjkl}^{(3)}(2\omega, 0, \omega, \omega) E_j(0) E_k(\omega) E_l(\omega) \quad (5)$$

where $\chi_{zjkl}^{(3)}(2\omega, 0, \omega, \omega)$ is the nonlinear optical susceptibility tensor, E is the electric field strength, ω is the angular frequency of the electric field.

For the linearly polarized light with the electric field vector perpendicular to the electrodes and parallel to the external electric field, when tensor components $j = k = l = z$, the electric field strength for the electromagnetic wave can be expressed as:

$$E_z = E_0 \exp(i(kr - \omega t)) \quad (6)$$

For centrosymmetric materials all the other susceptibility components except for $\chi_{zzzz}^{(3)}$ should be equal to zero. Taking into account that the direction of the applied electric field in the neighboring gaps between electrodes is opposite, the external electric field may be expressed as:

$$E_z(0, n) = (-1)^n E_z(0) \quad (7)$$

where $n = 1, 2, 3$ is a gap number. Consequently:

$$P_z^{EFISH}(\omega, n) = \chi_{zzzz}^{(3)}(2\omega, 0, \omega, \omega) (-1)^n E_z(0) E_0^2 \times \exp(i(2kr - 2\omega t)) \quad (8)$$

Replacing $(-1)^n = \exp(i\pi n)$ we obtain

$$P_z^{EFISH}(\omega, n) = P_{0,z} \exp(i(2kr - 2\omega t + \pi n)) \quad (9)$$

where P_0 is the polarization amplitude. Accordingly, this oscillating polarization creates the EFISH electric field with the amplitude E_0^{EFISH} and also with the phases differing in neighboring gaps by π .

Consequently the EFISH radiation from all the gaps interferes destructively in the directly propagating beam direction (0th diffraction order) because of the equal amount of the waves with opposite phases, while the constructive interference appears and creates the EFISH maxima in the middle between the diffraction maxima of the convenient second harmonics light.

According to the diffraction model of two subgratings, developed by Yang et al. [152,153], the far-field intensity distribution created by this process can be expressed as follows:

$$I(\theta) = \left(\frac{\sin(0.5ka \sin(\theta))}{0.5ka \sin(\theta)} \right)^2 \left(\frac{\sin(mk(a+b) \sin(\theta))}{m \sin(k(a+b) \sin(\theta))} \right)^2 \times \left(\cos \left(k(a+b) \cos \frac{\theta}{2} \sin \frac{\theta}{2} + \frac{\pi}{2} \right) \right)^2 \quad (10)$$

where:

k — the wave number of the EFISH;

a — the width of one gap of the grating;

b — the width of one electrode;

m — the number of the EFISH generating gaps;

θ — the diffraction angle, measured from the normal of the grating surface.

This expression correctly reproduced positions of the angular maxima of the EFISH radiation, but their widths were narrower.

We have also simulated the angular dependence of the fundamental, second harmonics and EFISH signal by using the freely available finite-difference time-domain simulation software *OptiFDTD* from *Optiwave Systems Inc.* For

the EFISH calculation, we artificially constructed a phase shift by π between electromagnetic waves originating from the neighboring grating gaps, as follows from **Eq. (9)**. The simulation results are also presented in **Figure 4.10**.

Simulations perfectly reproduce positions and widths of the major EFISH maxima confirming the validity of the used approach. On the other hand, both experimentally measured and simulated angular dependences show a weak 0th order diffraction maximum, which, according to the theoretical description, should be absent, while the measured and calculated second order EFISH maxima have very different intensities. The 0th order maximum apparently appears because of a non-ideal diffraction grating; the gap widths and shapes are not ideally uniform, therefore the destructive interference is not perfect. The signal in the calculated pattern appears because of the limited number of gaps used for calculations. Lower experimentally obtained intensities of the 2nd order EFISH peaks are also apparently caused by deviation of the experimentally used grating from the ideal grating used in the calculations; non-ideal experimental grating is closer to the sinusoidal amplitude grating, which gives no second order peaks.

In order to get more information about properties of the EFISH generation using the interdigitated comb-like electrodes we investigated dependences of the EFISH intensity on the sample parameters and experimental conditions. We chose MEH-PPV and also Polystyrene polymers and their mixtures at different stoichiometric ratios as model materials. The investigation results are presented in **Figure 4.11**.

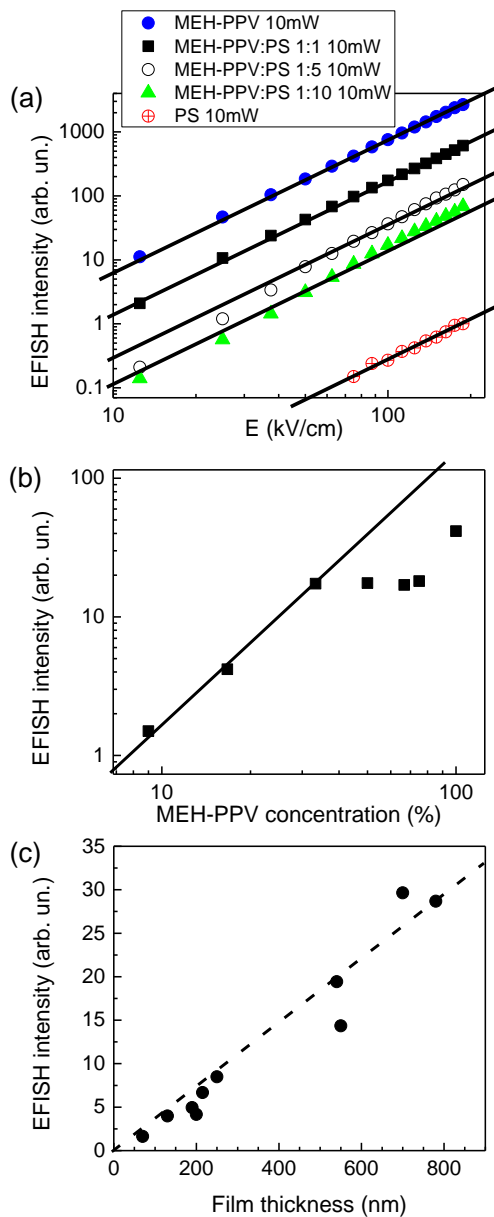


Figure 4.11. (a) EFISH intensity dependence on the external electric field strength E for different polymeric films (lines show square dependences), (b) EFISH intensity dependence on the MEH-PPV weight concentration in the MEH-PPV:PS mixture (line shows square dependence), (c) EFISH intensity dependence on the polymer layer thickness (line is guide for eyes).

As expected, the intensity of the EFISH signal in all investigated materials is proportional to the square of the fundamental light intensity. The EFISH signal in pure materials is also proportional to the square of the applied electric field strength (**Figure 4.11(a)**).

However, in mixtures with the low MEH-PPV concentration the EFISH signal shows a stronger field dependence (experimental points deviate from the line showing square dependence) with the power index of about 2.3-2.5.

The stronger field dependences show that some additional field-dependent process takes place. The field-assisted charge carrier photogeneration, which is quite efficient in MEH-PPV,[154] is the most relevant process. The charge carrier accumulation in MEH-PPV chains isolated by the nonconductive polystyrene matrix may additionally enhance their role. In pure polystyrene, charge carriers cannot be generated, while from the pure MEH-PPV they are easily extracted.

The EFISH intensity strongly depends on the stoichiometric ratio of the film formed on combs. Even a small amount of MEH-PPV (9%) increases the EFISH signal about a hundred times. With a further increase in the MEH-PPV concentration, the EFISH intensity strongly increases and partly saturates after reaching about 30%. Polystyrene is transparent for both the fundamental laser radiation and its second harmonics, consequently the light-matter interaction is nonresonant, and therefore the EFISH signal is weak. Since MEH-PPV has an absorption band in the 400-600 nm region, therefore the EFISH interaction with MEH-PPV is resonant and much stronger. The EFISH intensity is expected to be quadratic versus concentration of resonantly interacting molecules.[134] Indeed, the quadratic dependence up to about 30% of the MEH-PPV concentration is observed (line in **Figure 4.11(b)**). Deviation from the quadratic dependence at higher concentrations most probably appears because of absorption of the EFISH light by MEH-PPV.

Figure 4.11(c) shows the dependence of the EFISH intensity on the thickness of MEH-PPV/PS film with the 1:10 stoichiometric ratio. The EFISH intensity increased approximately linearly with the film thickness. At low film thickness and low dye concentration we expected a quadratic dependence. However, several factors may cause deviation from this dependence: the EFISH light absorption, inhomogeneous electric field distribution, and finally the Maker fringe pattern [134] in thick layers.

In conclusion, the presented experimental data, which are also published in ref.[20], demonstrate the potential of the EFISH generation with interdigitated comb-like electrodes as a convenient tool for the characterization of nonlinear optical and other properties of thin molecular films. That change in sample structure and experimental setup also bring some additional useful effects:

- Firstly, this experimental scheme enables a simple changing of the angle between the light polarization and the external electric field if other polarizability tensor elements are addressed.
- Secondly, the EFISH radiation creates an angular interference pattern with the zero intensity in the direction of the directly propagating excitation beam and with maxima in the positions different from diffraction angles of both the fundamental and second harmonics radiation. Consequently this unusual angular dependence enables background-free EFISH measurements, easy separation of the EFISH signal from the ordinary second harmonics generation in non-perfectly centrosymmetric, polycrystalline etc. materials.

These properties may also be important to some applications in the light control or other areas of nonlinear optics.

4.2.2. Ultrafast Transient Absorption Investigations

Before investigation of the ultrafast charge carrier motion we have applied another ultrafast technique — transient absorption measurements, to obtain additional information about the excited state dynamics. **Figure 4.12** shows the absorption bleaching relaxation measured for the *fresh* samples with and without PCBM at the maximum of the S_{11} absorption band (1000 nm) under excitation at 1000 nm.

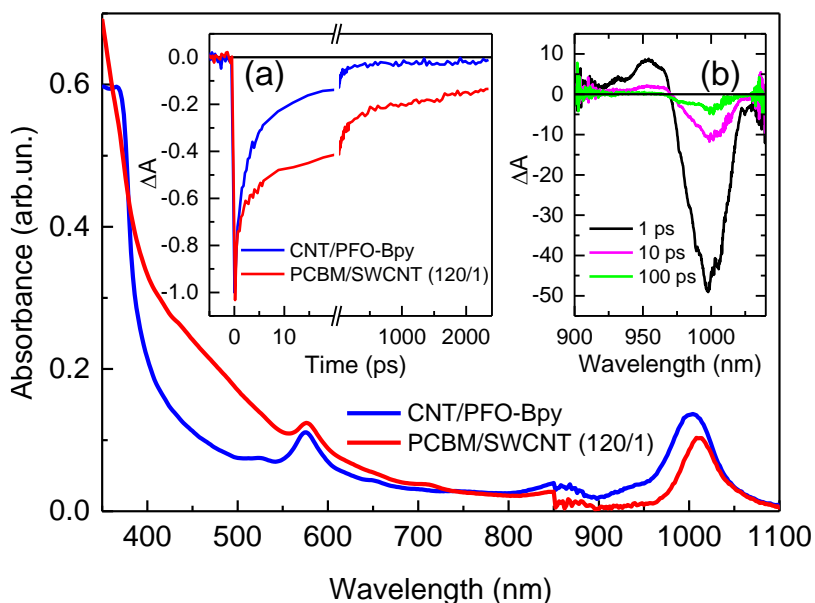


Figure 4.12. Steady state absorption spectra of fresh SWCNT/PFO-Bpy and PCBM/SWCNT (120/1) samples. Insert (a) shows absorption bleaching kinetics measured at 1000 nm for both samples, and insert (b) shows the transient differential absorption spectra of the SWCNT/PFO-Bpy sample at different delay times. Excitation wavelength was 1000 nm

The excitation relaxation kinetics is very similar to that reported previously.[70,155] The dominating exciton decay in film without PCBM

takes place during tens of picoseconds. A weak long-living component shall be attributed to a low efficiency generation of free charge carriers responsible for a weak photoconductivity of this film. Fresh PCBM/SWCNT (120/1) film shows only partial relaxation on the subnanosecond-nanosecond time scale. The strong long-living component shall be unambiguously attributed to the efficient ultrafast electron transfer from excited SWCNT to PCBM and generation of free charge carriers preventing recovery of the SWCNT absorption.[70] The partial relaxation of the absorption bleaching on the subnanosecond-nanosecond time scale shall be attributed to the charge carrier recombination.

4.2.3. TREFISH Measurements

The all-optical TREFISH technique was used to address the kinetics of carrier motion inside individual single-wall carbon nanotubes that cannot be resolved by conventional transient photocurrent measurements. Since we used samples formed on interdigitated comb-like electrodes, measurements were performed in transmission mode and the samples were positioned perpendicularly to the incident probing laser light. We combined the ultrafast measurements with conventional transient photocurrent investigations to address all pathways from photon absorption to final hole motion phases inside individual nanotubes and their aggregates.

Before analyzing experimental results we should shortly discuss electronic processes in SWCNT/PCBM system which we expect to take place on an ultrafast timescale. To analyze the ultrafast electric field kinetics we consider four excited state species, which may be created by the sample photoexcitation: neutral excitons, charge transfer (CT) states with a hole located in a SWCNT and an electron in the adjacent PCBM, as well as free

electrons in the PCBM phase with holes in the SWCNTs. All these species contribute to displacement or conductivity currents and, thus change the applied electric field. We can describe the change of the electric field as:

$$\begin{aligned} \Delta F(t) = & \frac{F_0}{2 \varepsilon \varepsilon_0} [n_{ex}(t)\Delta\alpha_{ex} + n_{CT}(t)\Delta\alpha_{CT}] + \\ & + \frac{e}{\varepsilon \varepsilon_0} [n_{el}(t)l_{el}(t) + n_h(t)l_h(t)] \end{aligned} \quad (11)$$

where the first and the second terms describe electric field changes caused by the displacement current from photogenerated neutral and CT excitons, while the third and the fourth terms describe changes created by the drift of photogenerated electrons and holes, respectively. Here, $n_{ex}(t)$, $n_{CT}(t)$, $n_{el}(t)$ and $n_h(t)$ are densities of the species described above, $\Delta\alpha_{ex}$ and $\Delta\alpha_{CT}$ are differences between polarizabilities of related excitons and neutral SWCNT segments, e is the electron charge, and $l_{el}(t)$ and $l_h(t)$ are electron and hole drift distances.

Figure 4.13 shows the dependences of the electric field strength on the delay-time between the excitation and probe pulses in aged and in fresh samples with different PCBM concentrations measured by the TREFISH technique. Horizontal lines show corresponding EFISH intensity before sample excitation. Vertical dashed lines show excitation time. Bars indicate values of the electric field changes relatively to the applied electric field (due to the different optical densities of the samples, the changes in the electric field strength in each sample should not be compared directly)

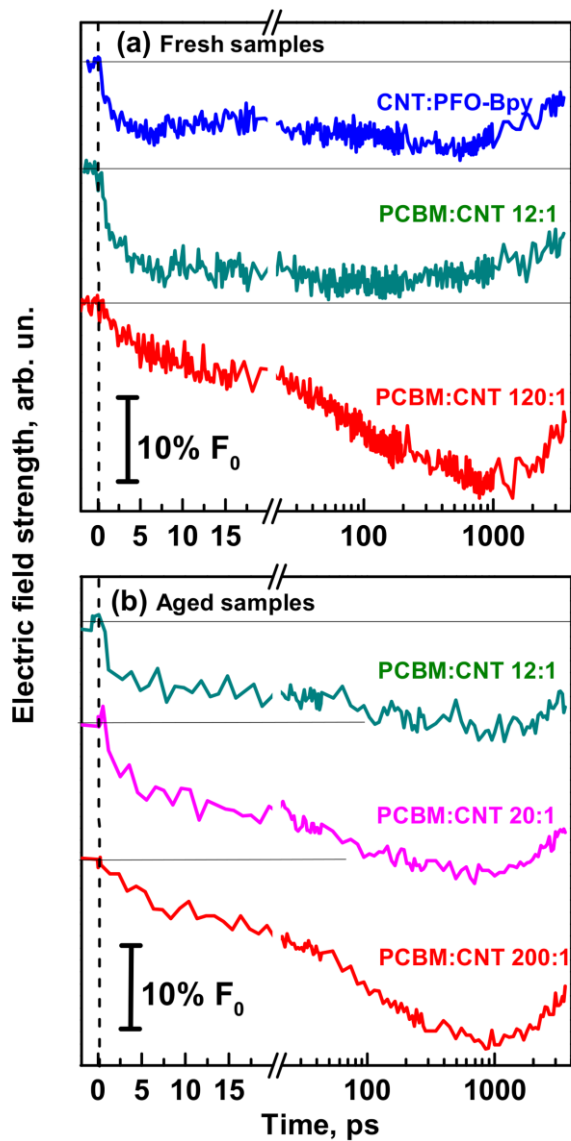


Figure 4.13. Electric field kinetics for *fresh* (a) and *aged* (b) samples measured by the TREFISH method at an applied voltage of 40V after excitation at 1000 nm.

According to transient absorption investigations, only neutral excitons and low concentration of charge carriers are generated in samples without PCBM.

Neutral and CT excitons usually have higher polarizabilities than corresponding nonexcited species, therefore they reduce the electric field inside the investigated material by increasing its dielectric constant and consequently capacity of the charged sample. Neutral excitons, which are generated during the excitation pulse duration, get polarized by the electric field instantaneously and screen the electric field practically instantaneously. We observe such ultrafast electric field drop in samples without or with low PCBM concentration.

The electric field is expected to recover again when excitons relax on tens of picosecond time scale. We observe such partial recovery of the electric field in SWCNT/PFO-Bpy sample during 5-20 ps. At longer times the recovery is apparently compensated by the photocurrent created by the photogenerated charge carriers.

As determined from the transient photocurrent measurements, PCBM increases the carrier generation efficiency, and it is larger by over an order of magnitude in samples with a high PCBM content if compared to the samples without PCBM. Therefore charge carrier contribution to the electric field dynamics in samples with PCBM is much larger overwhelming the electric field dynamics caused by the exciton decay. Surprisingly, we also do not see any instantaneous electric field drop in samples with a very high PCBM content (samples 120/1, 200/1). This suggests that neutral excitons responsible for the ultrafast field drop are not generated, or are very rapidly quenched in these samples. Such rapid quenching by electron transfer from excited CNTs to fullerenes is in agreement with the transient absorption kinetics and was also observed in similar systems taking place during hundreds of fs.[70] The absence of the fast electric field drop also suggests that polarizability of the CT excitons created by electron transfer to PCBM is low, much lower than that of neutral excitons. The low polarizability is expected because electrons in CT states are localized on comparatively small PCBM molecules, while the

Coulomb interaction also causes localization of a hole. Similar carrier localization was discussed for AuCl₃ doped SWCNTs.[156,157]

The subsequent electric field dynamics on the picosecond time scale is determined by the free carrier generation and motion processes. In cells with the highest PCBM content, where exciton contribution is insignificant, these processes completely determine the field dynamics during initial nanosecond. Unfortunately, carrier generation and motion processes cannot be separated one from another in our experiments - the slower one limits the field decrease rate. We can thus only establish upper limits for the either one being about 200-1000 ps. Assuming carrier motion is the rate-limiting process we can estimate the intratube hole mobility of about 10 cm²/Vs. This value is about two orders of magnitude lower than the intratube mobility values reported in the prior literature [11,158–160] and thus hardly can be correct. Consequently, more likely the electric field decay is limited by carrier generation, i.e. splitting of CT states into free charge carriers, which lasts for about 1000 ps.

It is important to remark that we do not see any significant differences between the ultrafast electric field dynamics in films made from fresh and aged SWCNT solutions. This is in contrast to the different photocurrent kinetics on a nanosecond time scale, attributed to different sample morphology causing different intertube carrier motion (see **Figure 4.4**). Therefore we attribute the ultrafast electric field dynamics to electronic processes within individual nanotubes. This also confirms our earlier conclusion that intertube hole motion takes place on a nanosecond timescale.

The electric field slightly recovers again during several nanoseconds after optical excitation. We attribute this recovery to the charge carrier recombination observed also in transient absorption measurements. Similar recombination rate was also determined for charge carriers generated at the SWCNT/C₆₀ interface. This process is most likely dominated by carriers

generated in SWCNTs oriented nearly perpendicularly to the direction of the electric field, where diffusion of holes against the electric field back to electrons located on PCBM is associated with only a small energy barrier. This recovery is slightly weaker in aged films. We attribute this difference to a manifestation of intertube carrier motion: some carriers, which would have recombined in isolated SWCNTs, may jump to neighboring nanotubes and avoid geminate recombination.

It should be also noted, that the neutral excitons, do not contribute to the transient photocurrent measured by oscilloscope. This is because of limited time-resolution of the oscilloscope, which cannot detect species with lifetimes of tens of picoseconds. On the other hand, we do not observe any signatures of the electron motion in ultrafast TREFISH investigations. The electron motion gives a sizable contribution to the photocurrent at very high PCBM concentration and this contribution is associated with a photocurrent on a much slower, sub-microsecond time scale. Thus, we can ignore the electron contribution considering picosecond electric field dynamics.

4.2.4. Polarization-dependent TREFISH

Lastly, we report the dependence of the electric field kinetics on the excitation light polarization which provides additional information about charge carrier motion. **Figure 4.14** presents data for fresh samples without PCBM and PCBM/SWCNT (12/1). The ratio between the electric field drops created by excitation light polarized perpendicularly and in parallel to the electric field direction equals to about 0.6 at the initial time and increases to about 0.8 at a long time. The influence of the excitation light polarization on the EFISH signal value shall be identical to the influence of the excitation light polarization on the value of the transient absorption signal in polarized

transient absorption measurements, and to the anisotropy of fluorescence created by linearly polarized light. From this analogy, we expect this ratio being equal to 0.33 for randomly oriented linear stick-like particles if intertube exciton and carrier migrations do not take place.

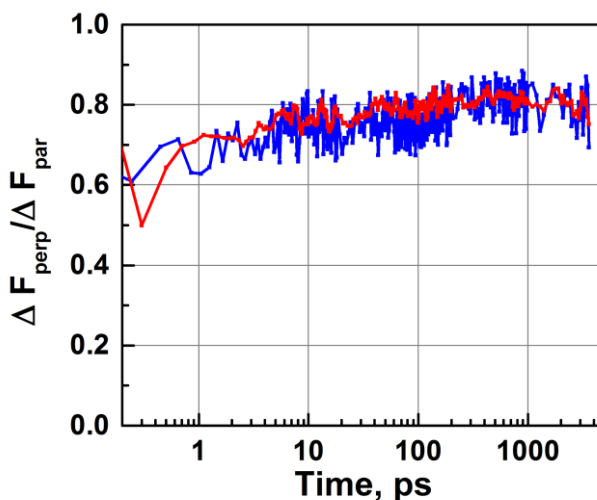


Figure 4.14. Time dependence of the ratio of the excitation induced EFISH drop under parallel and perpendicular to the electric field direction excitation pulse polarizations for the samples prepared from fresh solutions without PCBM (blue) and PCBM/SWCNT (12/1) (red)

Since the initial electric field drop in these samples is mainly caused by neutral excitons, the larger ratio of about 0.6 is apparently caused by depolarization of excitons due to their diffusion along bent SWCNTs to slightly differently oriented SWCNTs segments or to neighboring SWCNTs faster than the time resolution of our measurements.

Additional depolarization on a subnanosecond timescale reflects slower exciton migration phase and probably also hole motion along bent SWCNT. Within experimental accuracy, the depolarization kinetics for samples without and with PCBM are identical, which confirms that PCBM is essential for the charge carrier generation, but does not influence the motion of generated

holes. The depolarization kinetics for the samples prepared from aged samples were within experimental accuracy identical, therefore not presented.

4.2.5. Intratubal Drift of Holes

The intratubal hole drift may be rather complex. Charge carriers were suggested to be delocalized inside of SWCNTs, with the delocalization length of about 100 nm [71] limited by defects and impurities. Nanotube wrapping with polymer may cause additional disorder, thus the delocalization length is expected to be shorter.

Initial dynamics of the carriers inside of the delocalization region should be considered as an instantaneous polarization of the hole density distribution causing displacement current, while carrier localization in low energy sites and jumps over barriers limit the intratubal carrier mobility.[161] Thus, carrier motion within the SWCNT network is also expected to have a hierarchical character — instantaneous hole polarization followed by a fast intratubal drift and slow intertube jumps.

Very fast (<2 ns) initial carrier extraction and linear scaling of the ultrafast extraction component with the applied voltage suggest that it may have a displacement origin. Then the photocurrent on the tens of ns time scale might be attributed to the intratubal carrier drift accounting barriers and traps and photocurrent during several microseconds to intertube hole motion. However, this assignment is questionable because of large contribution of the ultrafast component to the total extracted charge. Even for 100 nm carrier delocalization length, the field-induced displacement of the delocalised hole density distribution may be expected to be of tens of nanometers at most, which is about 100 times shorter than the carrier drift distance along the entire

nanotube length. Thus the contribution of the displacement current to the total extracted charge is expected to be of about 1% or less. More likely that the ultrafast carrier extraction phase accounts for the carrier drift inside the entire SWCNT length. This drift may also be very fast. Literature data report up to thousands of cm^2/Vs charge carrier mobility within individual SWCNTs.[10,11,80] Taking into account the applied electric field strength and several micrometer SWCNT length, the hole drift inside a single SWCNT is expected to take place on a picosecond, or several nanoseconds time scales. In this case the intermediate carrier extraction phase during tens and hundreds of nanoseconds shall be attributed to the intertube hole drift within SWCNT bundles. The intertube mobility in polymer wrapped SWCNTs has been reported to be in the 1-10 cm^2/Vs range,[162] which gives intertube hole jump times of tens and hundreds of nanoseconds, in a close agreement with this assignment. The weak photocurrent lasting up to several microseconds shall be attributed to the hole drift at larger distances within a poorly percolated nanotube network.

This assertion is further supported by the excitation polarization investigations. Simple evaluation shows that extracted charge related to the displacement current shall be about three times larger under parallel to the electric field excitation polarization than under perpendicular (in analogy with the fluorescence anisotropy). Relatively low initial difference between charge values extracted under different excitation polarizations presented in **Figure 4.15** therefore shows that holes have moved to somehow differently oriented nanotube segments already during the ultrafast photocurrent phase. Subsequent polarization memory loss taking place during the intermediate charge extraction phase shall be assigned to intertube hole jumps.

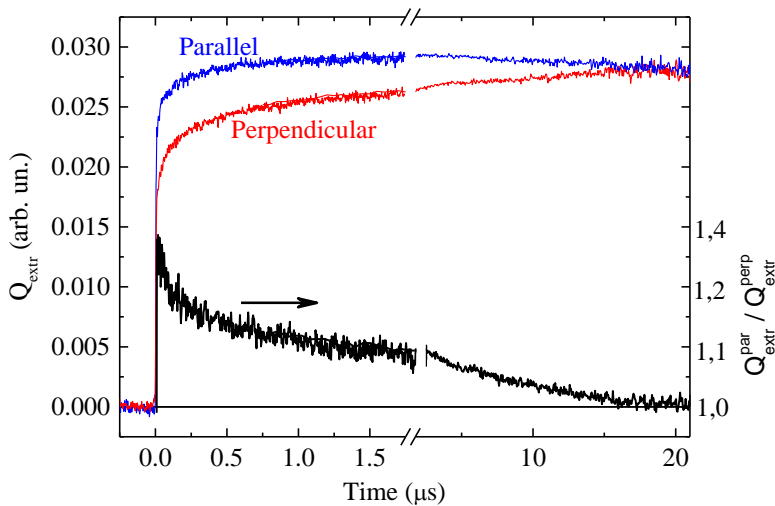


Figure 4.15. Charge extraction kinetics from PCBM/SWCNT (120/1) sample under excitation by 1064 nm light polarised parallel and perpendicular to the applied electric field direction. Bottom curve shows their ratio

According to this attribution, majority of holes remain located on the same SWCNTs where they were generated causing the ultrafast photocurrent phase. A fraction of holes jump to neighbouring SWCNTs creating photocurrent on nanosecond - several microsecond time scale. Consequently carrier decay with about 1 μ s time constant revealed by TDCF measurements shall be attributed to the geminate recombination of holes remaining on the same SWCNT where they were generated and electrons located on PCBM molecules adsorbed to these SWCNTs. At longer delay times, only holes transferred to different SWCNTs survive and their recombination takes place during tens and hundreds of microseconds.

4.3. Persistent Built-in Electric Field in SWCNT/PCBM Blend Films

As we have seen before, photogeneration of charge carriers and their transport through the SWCNT percolating network can be considered as very fast or ultrafast process. During these investigations, we also noticed that the applied electric field creates also some changes of the photoelectrical properties lasting for hours to days. Such electrically poled films showed photocurrent and photovoltage without applied external voltage indicating that the persistent built-in electric field was created. The persistent built-in electric field may be an interesting phenomenon for the application of carbon nanotubes systems as memory elements or for photodetectors operating without applied voltage.

The persistent built-in electric field was formed by poling the samples using a relatively high voltage applied to the sample. The poling of the samples used for steady-state investigations was performed by applying the steady-state voltage (up to 7 V) or 20 μs voltage pulses (up to 40 V) at 1 kHz repetition rate. Steady-state electrical and photoelectrical properties of pristine and poled SWCNT films were investigated by measuring current-voltage characteristics (I-V curves) under application of a small external voltage, which does not change substantially the sample poling. **Figure 4.16(a)** shows I-V curves measured in the dark and under 1 Sun ($\sim 0.1 \text{ W/cm}^2$) illumination for the nonpoled SWCNT/PCBM (1/120) sample and that poled for 20 min by steady state 5 V voltage. As expected, the dark I-V curves for the nonpoled sample cross the (0,0) point. The I-V curve for the poled sample measured in the dark is less steep indicating that the poling reduces the sample conductivity.

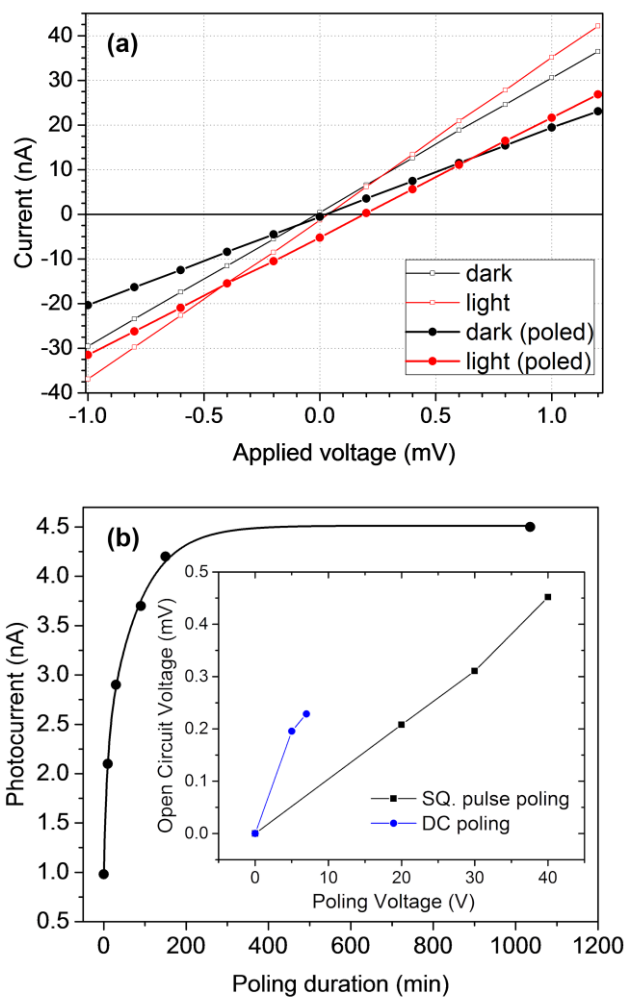


Figure 4.16. (a) I-V curves measured in dark and under illumination by about 0.1 W/cm^2 white light for nonpoled SWCNT/PCBM (1/120) sample and that poled for 20 min by the steady-state 5 V voltage; (b) dependence of the closed-circuit photocurrent on the poling time (20 V square-pulsed voltage of $20 \mu\text{s}$ duration at 1 kHz repetition rate); inset shows a built-in voltage created by 10 min poling using constant or pulsed voltage

According to the poling mechanism discussed below, a fraction of equilibrium charge carriers are dragged into isolated sites making them immobile. Illumination of both poled and nonpoled samples increases steepness of I-V

curves almost identically for both samples showing that photoconductivity of the films does not change substantially with the sample poling. In contrast to the equilibrium charge carriers, the carriers photogenerated after the termination of the poling voltage were not affected by poling. However, illumination of the poled sample also shifts the I-V curve down revealing the photocurrent at zero applied voltage (close-circuit current) and a built-in open-circuit voltage of about 0.2 mV.

Inset in **Figure 4.16(b)** shows the dependences of the built-in voltage on the constant or pulsed voltage used for the sample poling. In the case of the sample poling by pulsed voltage, the investigated parameters show nearly linear voltage dependences in the whole examined voltage range. In the case of the constant poling voltage, the curve starts to saturate at approximately 6 V, while further voltage increase usually caused sample degradation due to sample heating and thus irreversible changes. Square 20 μ s 20 V pulses at 1 kHz repetition rate created approximately equivalent sample poling as steady-state voltage of 5 V, but pulsed voltage caused no sample degradation up to 40 V. Therefore, in further experiments, the sample poling was performed by 20 μ s pulses at 1 kHz repetition rate. **Figure 4.16(b)** shows the dependence of the close-circuit photocurrent on the poling duration. Initially, the photocurrent increases rapidly with the poling time, but the full saturation of the photocurrent was reached after several hours.

We further investigated the poling dynamics and decay of the created built-in field. To address fast phases of the built-in field formation and decay, the samples were similarly poled by the train of 20 μ s electrical pulses at 1 kHz repetition rate, but to avoid the effect of the slow poling component, every second pulse was of the opposite polarity. Thus, the time-averaged sample poling was absent, and the poling by any individual pulse was identical to that created by a single pulse (see **Figure 4.17(b)**). We probed the dynamics of the internal electric field induced by poling by measuring photocurrent created by

130 fs, 1000 nm optical pulses synchronized with the electrical pulses. The photoresponse kinetics was obtained from multiple pulses by changing optical probing time relatively to the rising front of the electrical pulse. The optical probing time was varied during the entire electrical pulse and during the interval between electrical pulses which allowed to probe both polarization formation and its decay. The optical excitation created pulses of photocurrent lasting for less than ten nanoseconds, but we considered only their peak values, that we termed — photoresponses.

The curves in **Figure 4.17(c)** show the photoresponse dependences on the probing time for different samples, represented schematically in **Figure 4.17(a)**. The photoresponse dependences were qualitatively similar for all investigated samples. The zero time corresponds to the probing immediately after the application of the electrical pulse (see inset in **Figure 4.17(c)**). The photoresponse then was maximal and decreased with the probing delay indicating that the created polarization screened the applied electric field. After termination of the electrical pulse, the photoresponse changed its polarity and initially was approximately equal to the drop of the photoresponse during the electrical pulse action. Moreover, the decay kinetics of the photoresponse during the electrical pulse action and after its termination was very similar. It shows that the negative photoresponse observed after the termination of the electrical pulse originates from the built-in internal electric field of the opposite direction created by the sample polarization, which is also responsible for the screening of the applied electric field. The electric field kinetics resembles that of sample connected in series with capacitor. However sample capacitance and external load give RC time constant of several nanoseconds only, which shows that internal processes in SWCNT film are responsible for the observed dynamics.

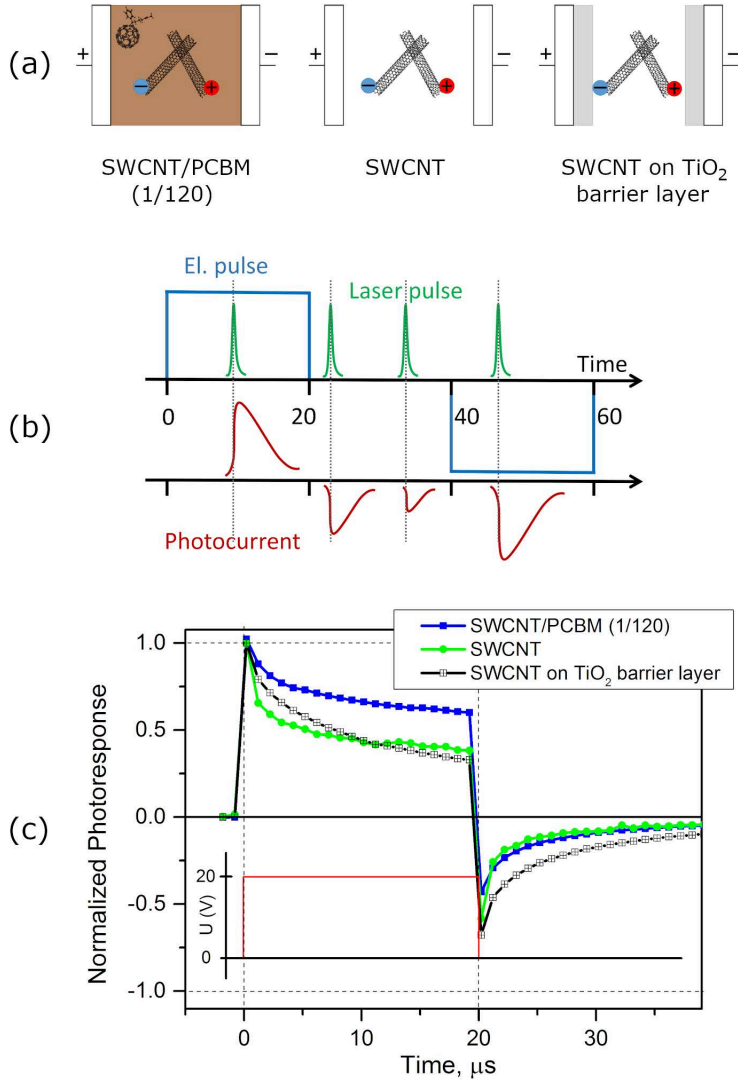


Figure 4.17. (a) schematic representation of the sample structure; (b) synchronization scheme of the electrical pulses, laser pulses, and measured photoresponses; (c) photoresponse as the function of the delay time between the rising front of the electrical poling pulse (20 V) and photoexcitation pulse; inset illustrates the presence of that 20 μs duration electrical pulse

For the SWCNT/PCBM (1/120) film the photoresponse decreased by about 40 % during the 20 μs electrical pulse action. For a pure SWCNT film, the

photoresponse decrease was even stronger, by about 60%. The built-in field was also correspondingly stronger. Films with other SWCNT to PCBM ratio were also investigated. The tendency of the decrease of the built-in field in samples with larger PCBM content was observed, however, a clear dependence was not established because of the weak differences and of the limited sample fabrication reproducibility. It should be also noted, that the absolute photoresponse values for the pure SWCNT films were more than ten times lower than for the blends with PCBM because of the less efficient charge carrier photogeneration. The absolute photoresponse value was not important for probing of the built-in field values relatively to the applied field, however samples with PCBM were more convenient for investigation of the weak built-in fields.

To verify the role of internal processes the electrodes comb was also covered with TiO₂ layer forming additional capacitor connected in series with the SWCNT film. The thin TiO₂ layer did not block the charge transport completely but increased the sample resistance from several to tens and hundreds of kilohms. As **Figure 4.17(c)** shows, the sample with TiO₂ layer showed a qualitatively similar electric field dynamics to these without it. The electric field screening and the residual built-in field were of similar values confirming that the internal processes within a SWCNT film were mainly responsible for the built-in field. Large additional resistance just slightly slowed down formation and relaxation of the built-in field.

We further examined the built-in field decay on a minutes and hours timescale. But the photoresponse created by a single electrical pulse was too weak at long delay times. Therefore we have examined the decay of the photoresponse created by a train of 20 μ s electrical pulses of the same polarity applied at 1 kHz repetition rate for 10 min. The slow polarization decay component lasting for hours was observed in all investigated samples.

We chose the SWCNT/PCBM (1/120) film for a more detail investigation of the built-in field decay, because of its stronger photoresponse. We examined the decay kinetics both on short and long timescales at different temperatures. **Figure 4.18** shows the merged data for both decay components on a wide timescale in a log-log representation. The photoresponse values created by a single pulse and by train of pulses were appropriately normalized. We clearly observe two polarization decay phases.

The fast decay phase continues for hundreds of microseconds, and the photoresponse drops almost by two orders of magnitude during this time. As the insert in **Figure 4.18** shows, the fast phase is also strongly nonexponential, and polarization decreases several times during the initial several microseconds. This decay phase closely resembles the recombination kinetics of photogenerated charge carriers determined by the delayed-collection-field (TDCF) technique described earlier in this work (**Figure 4.7** and **Figure 4.8**). Therefore, this phase should be attributed to the motion of equilibrium charge carriers present in SWCNT layer. The carrier motion is limited by intertube jumps in a disordered SWCNT network causing a strongly nonexponential decay. The fast phase shows a very weak temperature dependence (see insert in **Figure 4.18**), similarly as the transient photocurrent. It indicates that the initial carrier motion is governed by the carrier tunneling between carbon nanotubes and their clusters, rather than by thermally activated jumps.

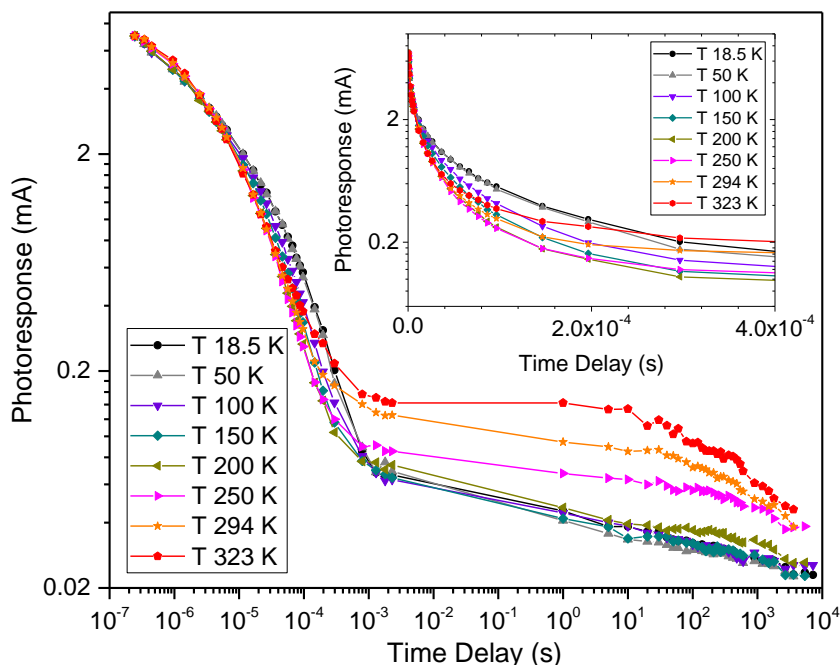


Figure 4.18. Kinetics of the photoresponse decay after termination of the electrical poling pulse on a wide log-log scale measured for the SWCNT/PCBM (1/120) blend film at different temperatures; inset highlights the fast decay phase

The slow polarization component is about hundred times weaker than the fast one. It starts to dominate at about 1 ms and its relaxation continues for hours. This phase shows a strong temperature dependence.

The polarization decay shows a complex temperature dependence. The fast polarization phase and its decay during the initial several microseconds are insensitive to temperature. The decay slightly slows down at low temperature on a timescale of tens of microseconds. The slow polarization component is also almost independent of temperature below 200 K, but increases more than three times in the 200 – 323 K range. Such weak temperature dependence is surprising taking into account that the dark conductivity of the film decreases more than ten times at low temperatures (see **Figure 4.19(a)**).

4.3.1. Frozen Polarization

We can further increase the slow polarization component at some particular temperature by performing the film poling at a higher temperature. The samples were heated to the desired poling temperature, then the poling voltage was applied. After some poling time the samples were cooled down still keeping the poling voltage applied until the desired measurement temperature was reached. Then the poling voltage was disconnected and the photoresponse decay kinetics was measured. As **Figure 4.19(b)** shows, only the polarization intensity increases by the sample poling at the higher temperature, while its decay kinetics remains approximately unchanged.

The two phases of photoresponse decay should be attributed to different processes. The field screening may be caused by charge carriers as well as by ions. Most likely SWCNT films possess equilibrium holes, since SWCNT in the ambient atmosphere become p-doped because of adsorbed oxygen molecules, which withdraw electrons.[163–165]

The SWCNT films are composed of single SWCNT and their bundles, which are partly interconnected, but pathways for charge transport apparently contain dead ends. Under applied electric field a fraction of drifting charge carriers stack on the dead ends of their pathways causing the appearance of electrical dipoles created by the stacked holes and the immobile negatively charged oxygen molecules. The created dipoles cause the screening of the applied external electric field. After the voltage cutoff, created dipoles gradually decay when charge carriers drift back to their initial positions. Consequently, screening of the electric field and decay of the built-in field reveal very slow charge carrier drift tails, which contribute to the current very little, and therefore cannot be observed, for example, by investigating transient photocurrent kinetics.

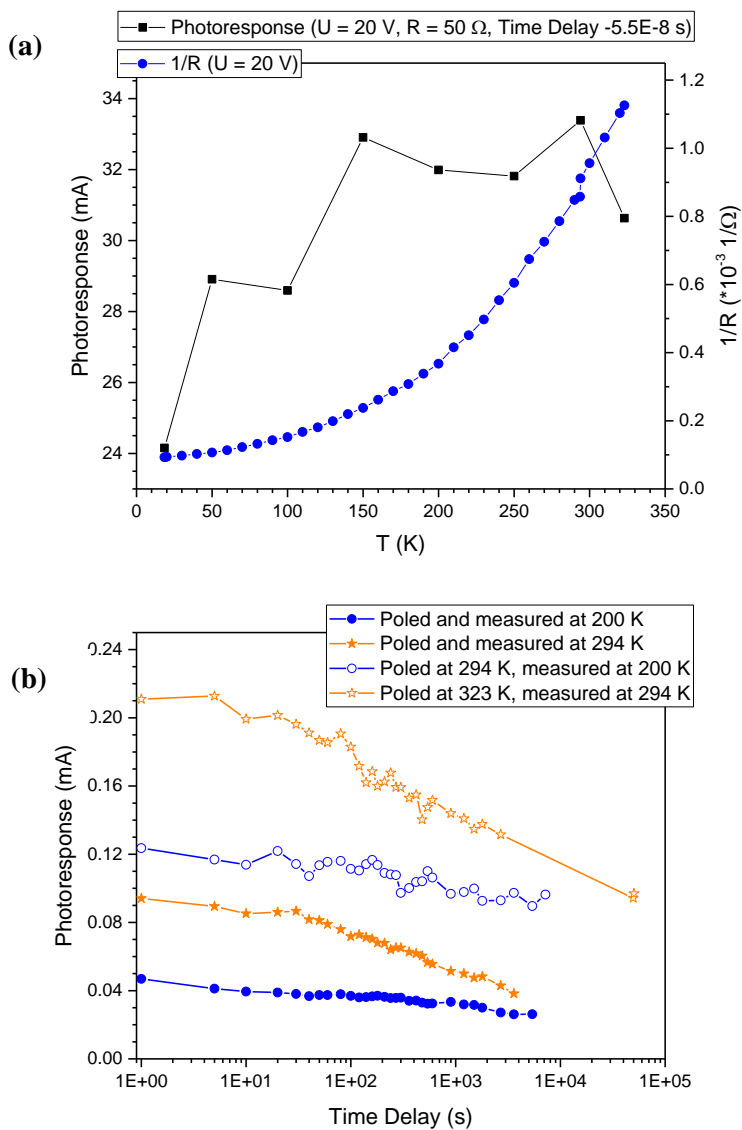


Figure 4.19. (a) dependences on the temperature of the steady-state sample conductivity (blue) and of the photoresponses while 20 V poling voltage is applied (black); (b) slow phase of the photoresponse decay kinetics for SWCNT/PCBM (1/120) sample at frozen and non-frozen poling conditions

As it was mentioned, this dynamics resembles recombination dynamics of photogenerated charge carriers measured by TDCF technique. Indeed, these

processes are expected to be similar because both of them are determined by carriers traveling back to their counter-charges at zero applied electric field. Electrons and holes can hardly cause processes lasting for hours and days, therefore we attribute the long-lasting built-in electric field to the motion of ions. A similar attribution was made analyzing the environmental influence on the electrical conductivity of SWCNT films where such long-lasting processes were assigned to adsorbed oxygen.[166] As the temperature dependences in **Figure 4.18** show, this motion requires thermal assistance of about 200 K (16 meV), which, according to Arrhenius equation, converts into 5 – 10 meV activation energy.

4.3.2. Compensation of the Built-in Field

To obtain additional information about the properties of the built-in electric field we attempted to compensate it by applying an external voltage. To better reveal a weak photocurrent at long times, we performed these investigations in the integrating regime using a high load resistance of 100 k Ω . In these measurements, the sample capacitance served as an integrating capacitor and the measured voltage was proportional to the integrated photocurrent.

Figure 4.20 shows the integrated photocurrent kinetics at different applied voltages for the poled sample. We were unable to compensate the transient photocurrent during the entire time range. At high applied voltage (100 mV), when the applied field strongly dominated over the built-in field, the voltage growth was relatively slow and continued for more than 1 μ s. While at zero applied voltage, when only the built-in electric field was present, the voltage drop was faster than could be resolved by our measurements. It shows that the photocurrent created by the built-in field endures much shorter than the photocurrent created by an external applied voltage.

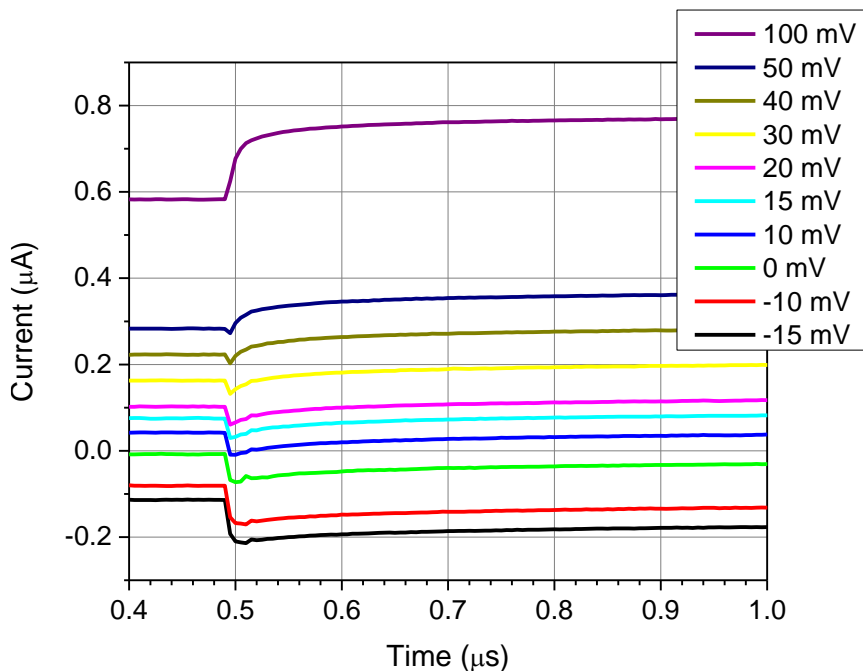


Figure 4.20. Transient integrated photocurrent kinetics of the SWCNT/PCBM (1/120) blend film at small applied voltages

When the applied and built-in fields were of similar strength but of opposite directions, the photocurrent kinetics was more complex, apparently determined by the competition of the two photocurrent components. Such curve shape suggests that the internal-net electric field, in this case, was inhomogeneous and even of different directions in different spatial regions. The regions in the vicinities of poling-induced dipoles with dominating built-in field were surrounded by the regions weakly affected by the induced dipoles. Consequently, charge carriers photogenerated in the vicinity of induced dipoles moved only over short distances towards charges forming the induced dipoles, thus creating only short photocurrent pulse. The charge carriers, photogenerated in the regions dominated by the external electric field, moved over larger distances and correspondingly longer time.

4.4. Generalized Model of Charge Carrier Generation and Motion in SWCNT/PCBM Films

A combination of several experimental techniques – conventional transient photocurrent, time-resolved electric-field-induced second harmonics (TREFISH) generation, and transient absorption – enabled us to track directly the carrier generation and motion in individual polymer-wrapped SWCNTs and their aggregates.

Charge carrier generation takes place spontaneously by the electron transfer from the excited SWCNT to PCBM. Our investigations revealed, that directly photogenerated delocalized neutral excitons feature high polarizability and significantly screen an applied electric field. The neutral excitons are quenched on a femtosecond timescale by electron transfer to adjacent PCBM creating strongly localized weakly polarizable charge transfer (CT) states. The CT states dissociate into free charge carriers during hundreds of picoseconds and limit the photocurrent dynamics, while the hole transfer along individual nanotubes is much faster.

A much slower intertube hole motion in SWCNT aggregates takes place during tens of nanoseconds. These photogenerated holes create a transient photocurrent in the interconnected SWCNT network, which is controlled by the morphology of the network, rather than by the carrier recombination or extraction.

The transient photocurrent shows three characteristic decay regimes. An ultrafast phase, lasting less than 2 ns is attributed to the hole transfer within single SWCNTs while hole jumps between SWCNTs take several microseconds. The slowest photocurrent component is observed only at high PCBM concentrations and is attributed to the electron transfer via PCBM.

Electrons and holes residing on the same nanotube recombine within about 1 μs . On the contrary, carriers located on different SWCNTs can survive hundreds of microseconds.

Scheme in **Figure 4.21** summarizes the above-discussed processes. Five photoinduced processes were found to take place on that (ps to μs) time scale in individual SWCNTs and their bundles:

- a) relaxation of neutral exciton in isolated SWCNT,
- b) creation of CT exciton by electron transfer to PCBM and simultaneous hole localization next to electron,
- c) dissociation of CT exciton to free charge carriers,
- d) recombination of a fraction of photogenerated charge carriers and eventual interchain hole transfer.
- e) further hole motion through SWCNT percolating network and the electron motion through PCBM phase

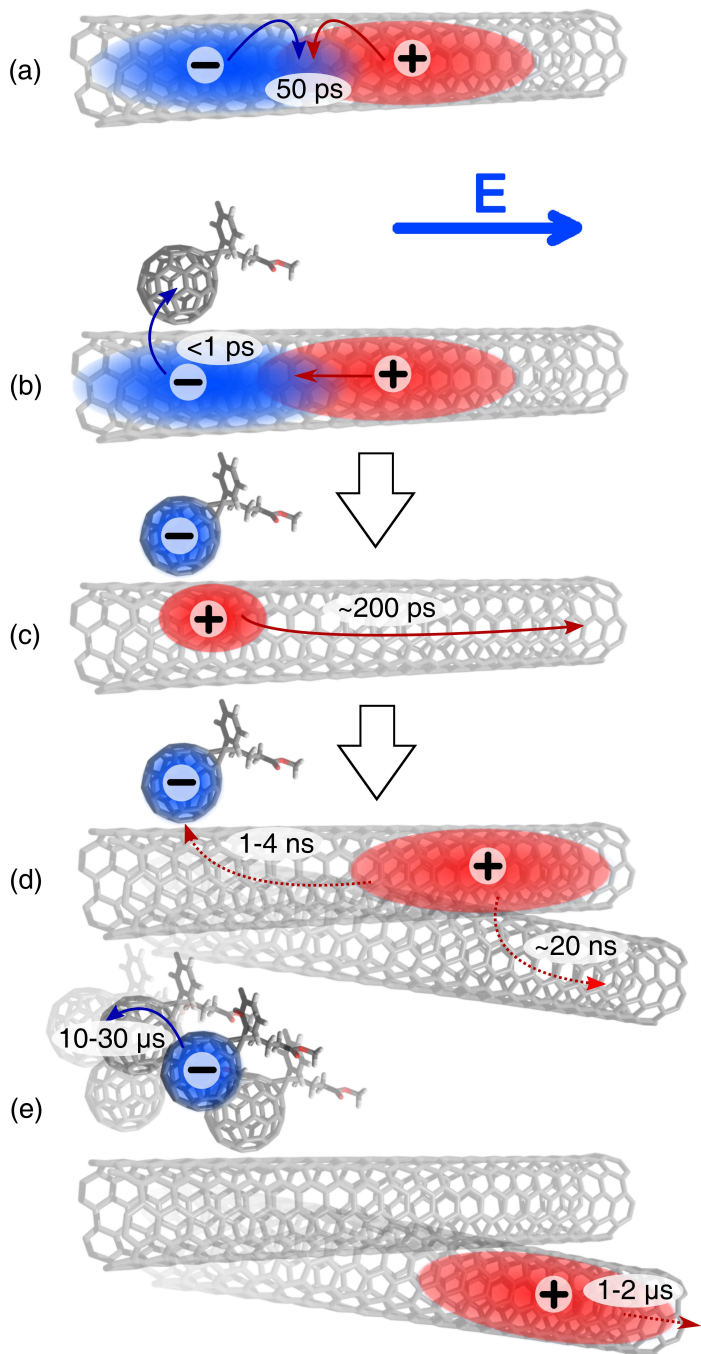


Figure 4.21. Schematic illustration of the processes in excited SWCNTs and their films

In addition to these processes, the voltage applied to SWCNT and SWCNT/PCBM blend films deposited on interdigitated electrodes induces the formation of persistent electric dipoles in SWCNT clusters. As a result, the applied electric field is screened, which causes persistent photoconductivity lasting for hours and days after the voltage was switched off. **Figure 4.22** schematically represents these processes.

The fast ($\sim 10 \mu\text{s}$) component of the decay of the persistent photoconductivity was attributed to the charge carrier displacement, while the slow component lasting for several days is likely to result from the displacement of ions. The slow component becomes weaker at low temperatures indicating that the field-induced ion displacement requires thermal activation.

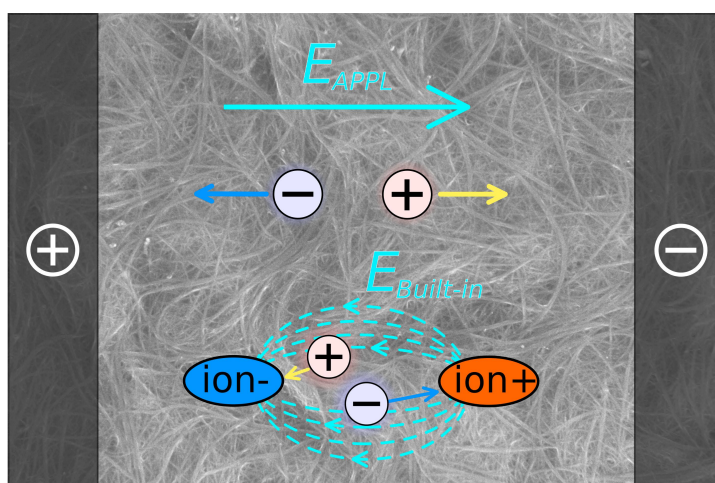


Figure 4.22. Schematic illustration of the built-in electric field formation and photoelectrical processes in SWCNT films

The built-in field compensation experiment revealed that when the applied and built-in fields were of similar strength but of opposite directions, the photocurrent kinetics was apparently determined by the competition of the two photocurrent components. Such curve shape suggests that the internal-net electric field, in this case, was inhomogeneous and even of different directions

in different spatial regions. These regions in the vicinities of poling-induced dipoles with dominating built-in field were surrounded by the regions weakly affected by the induced dipoles, where the electric field created by applied voltage was dominating (see **Figure 4.22**).

According to that assumption, charge carriers photogenerated in the vicinity of induced dipoles moved only over short distances towards charges forming the induced dipoles, thus creating only short photocurrent pulse. While the charge carriers, photogenerated in the regions dominated by the external electric field, moved over larger distances and correspondingly longer time.

4.5. CONCLUSIONS

Summarising the investigated photoelectrical processes in the SWCNT and their blend films in a broad time scale, we can make such major conclusions:

1. Photocurrent in SWCNT/PCBM films is determined by the efficiency of the charge carrier generation and by mobilities of the created charge carriers. The hole drift distance through the SWCNT network is mainly limited by the gaps in the nanotube percolation network. The PCBM molecules, at their high content, tend to form a continuous film enabling uninterrupted drift of electrons, while at low content, they are likely to rest in a form of isolated clusters, partly adsorbed to SWCNTs, and do not form a continuous path for electrons. On the other hand, PCBM molecules, at their high content, electrically isolate SWCNTs from the metal electrodes and one from another also preventing hole motion through SWCNT network.
2. Charge carrier generation efficiency increases with the PCBM content, but saturates when a sufficient amount of PCBM molecules cover carbon nanotubes ensuring an efficient electron transfer. Photocurrent saturation at high excitation intensities takes place when excitation densities reach generation of more than one charge pair per nanotube.
3. The time-resolved electric-field-induced second harmonics (TREFISH) experimental technique has been adapted for samples deposited on interdigitated comb-like electrodes (IDEs). This experimental geometry requires simple sample preparation and enables investigation of ultrafast carrier motion dynamics in a wide range of organic and inorganic amorphous materials. The unusual angular dependence of EFISH radiation

enables background-free EFISH measurements and easy separation of the EFISH signal from the ordinary second harmonics generation.

4. Combination of several experimental techniques – conventional transient photocurrent, time-resolved EFISH generation, and transient absorption – enables direct tracking of the carrier generation and motion in individual SWCNTs and in their aggregates with PCBM. Directly photogenerated delocalized neutral excitons feature high polarizability and significantly screen the applied electric field. The neutral excitons are quenched on a femtosecond timescale by electron transfer to adjacent PCBM molecules creating strongly localized weakly polarizable charge transfer (CT) states, which dissociate into free charge carriers during hundreds of picoseconds. A much slower intertube hole motion in SWCNT aggregates takes place during tens of nanoseconds.
5. The charge carrier dynamics in SWCNT/PCBM films at the used experimental conditions is not affected by the nongeminate electron-hole recombination or by other nonlinear processes. Kinetics of the transient photocurrents shows that the extracted charge is proportional to the applied voltage, but the shape of the extraction kinetics within the experimental accuracy is independent of the applied voltage. The extracted charge increases linearly with the excitation intensity and the shape of the charge extraction kinetics does not change up to about $5 \mu\text{J}\cdot\text{cm}^{-2}$. The bimolecular recombination in our systems is insignificant, and the carrier decay is determined by the geminate charge pair recombination. Majority of holes on a picosecond timescale remain located on the same SWCNTs where they were generated causing the ultrafast photocurrent phase. A fraction of holes jump to neighbouring SWCNTs creating photocurrent on nanosecond - several microsecond time scale. Consequently carrier decay with about $1 \mu\text{s}$ time-constant is caused by the geminate recombination of holes remaining on the same SWCNT where they were generated and of

electrons located on PCBM molecules adsorbed to these SWCNTs. At longer delay times, only holes transferred to different SWCNTs survive and their recombination takes place during tens and hundreds of microseconds.

6. Time-delayed collection-field (TDCF) measurements show that the external electric field does not influence the carrier photogeneration at the used experimental conditions, at least up to its strength of about $10^4 \text{ V}\cdot\text{cm}^{-1}$.
7. The voltage applied to SWCNT and SWCNT/PCBM blend films deposited on interdigitated electrodes induces the formation of persistent electric dipoles in SWCNT clusters. These dipoles screen the applied electric field and also cause persistent photoconductivity lasting for hours and days since the voltage was switched off.
8. A temperature dependence of the voltage-induced built-in field kinetics suggests that the two different processes contribute to the built-in field formation. The rapidly decreasing built-in field component shows a very weak temperature dependence, which indicates that the initial carrier motion responsible for the short-lived built-in field component is governed by the carrier tunnelling between carbon nanotubes and their clusters, rather than by thermally activated jumps. The slow component, which is about 100 times weaker, starts to dominate at about 1 ms. This phase shows a strong temperature dependence and requires a thermal assistance to overcome 5 – 10 meV barriers. The long-lived built-in electric field component is attributed to the motion of ions.

5. REFERENCES

1. S. Iijima, "Helical microtubules of graphitic carbon," *Nature* **354**(6348), 56–58 (1991).
2. A. Oberlin, M. Endo, and T. Koyama, "Filamentous growth of carbon through benzene decomposition," *Journal of Crystal Growth* **32**(3), 335–349 (1976).
3. Л. В. Радужкевич and В. М. Лукъянович, "О структуре углерода, образующегося при термическом разложении окиси углерода на железном контакте," *Журнал физической химии* **т.26**(вип. 1), 88–95 (1952).
4. P. L. Walker, J. F. Rakszawski, and G. R. Imperial, "Carbon Formation from Carbon Monoxide-Hydrogen Mixtures over Iron Catalysts.I. Properties of Carbon Formed," *J. Phys. Chem.* **63**(2), 133–140 (1959).
5. M. Monthieux and V. L. Kuznetsov, "Who should be given the credit for the discovery of carbon nanotubes?," *Carbon* **44**(9), 1621–1623 (2006).
6. M. Reibold, P. Paufler, A. A. Levin, W. Kochmann, N. Pätzke, and D. C. Meyer, "Carbon nanotubes in an ancient Damascus sabre," *Nature* **444**(7117), 286–286 (2006).
7. M. Reibold, P. Paufler, A. A. Levin, W. Kochmann, N. Pätzke, and D. C. Meyer, "Discovery of Nanotubes in Ancient Damascus Steel," in *Physics and Engineering of New Materials*, D. T. Cat, A. Pucci, and K. Wandelt, eds., Springer Proceedings in Physics (Springer Berlin Heidelberg, 2009), pp. 305–310.
8. O. D. Sherby and J. Wadsworth, "Ancient blacksmiths, the Iron Age, Damascus steels, and modern metallurgy," *Journal of Materials Processing Technology* **117**(3), 347–353 (2001).
9. U. S. Dixit, M. Hazarika, and J. P. Davim, *A Brief History of Mechanical Engineering*, Softcover reprint of the original 1st ed. 2017 edition (Springer, 2018).
10. S. Rosenblatt, Y. Yaish, J. Park, J. Gore, V. Sazonova, and P. L. McEuen, "High Performance Electrolyte Gated Carbon Nanotube Transistors," *Nano Lett.* **2**(8), 869–872 (2002).

11. X. Zhou, J.-Y. Park, S. Huang, J. Liu, and P. L. McEuen, "Band Structure, Phonon Scattering, and the Performance Limit of Single-Walled Carbon Nanotube Transistors," *Phys. Rev. Lett.* **95**(14), 146805 (2005).
12. R. S. Park, M. M. Shulaker, G. Hills, L. Suriyasena Liyanage, S. Lee, A. Tang, S. Mitra, and H.-S. P. Wong, "Hysteresis in Carbon Nanotube Transistors: Measurement and Analysis of Trap Density, Energy Level, and Spatial Distribution," *ACS Nano* **10**(4), 4599–4608 (2016).
13. C. Qiu, Z. Zhang, M. Xiao, Y. Yang, D. Zhong, and L.-M. Peng, "Scaling carbon nanotube complementary transistors to 5-nm gate lengths," *Science* **355**(6322), 271–276 (2017).
14. M. M. Shulaker, G. Hills, N. Patil, H. Wei, H.-Y. Chen, H.-S. P. Wong, and S. Mitra, "Carbon nanotube computer," *Nature* **501**(7468), 526–530 (2013).
15. T. Cubaynes, M. R. Delbecq, M. C. Dartailh, R. Assouly, M. M. Desjardins, L. C. Contamin, L. E. Bruhat, Z. Leghtas, F. Mallet, A. Cottet, and T. Kontos, "Highly coherent spin states in carbon nanotubes coupled to cavity photons," *npj Quantum Inf* **5**(1), 1–5 (2019).
16. K. Yum, T. P. McNicholas, B. Mu, and M. S. Strano, "Single-Walled Carbon Nanotube-Based Near-Infrared Optical Glucose Sensors toward In Vivo Continuous Glucose Monitoring," *J Diabetes Sci Technol* **7**(1), 72–87 (2013).
17. A. Eckstein, V. Bertašius, V. Jašinskas, I. Namal, T. Hertel, and V. Gulbinas, "Carrier photogeneration, drift and recombination in a semiconducting carbon nanotube network," *Nanoscale* **9**(34), 12441–12448 (2017).
18. V. Jašinskas, F. Oberndorfer, V. Pakštas, T. Hertel, and V. Gulbinas, "Direct Tracking of Ultrafast Carrier Motion Dynamics in Semiconducting Single-Wall Carbon Nanotubes," *J. Phys. Chem. C* **122**(28), 16424–16430 (2018).
19. V. Jašinskas, F. Oberndorfer, T. Hertel, and V. Gulbinas, "Electronic and Ionic Electric Field Screening and Persistent Built-In Electric Field in Carbon Nanotube/PCBM Films," *physica status solidi (a)* **217**(6), 1900673 (2020).
20. V. Jašinskas, M. Gedvilas, G. Račiukaitis, and V. Gulbinas, "Background-free electric field-induced second harmonic generation

- with interdigitated combs of electrodes," *Opt. Lett.* **41**(12), 2759–2762 (2016).
21. M. S. Arnold, J. D. Zimmerman, C. K. Renshaw, X. Xu, R. R. Lunt, C. M. Austin, and S. R. Forrest, "Broad Spectral Response Using Carbon Nanotube/Organic Semiconductor/C60 Photodetectors," *Nano Lett.* **9**(9), 3354–3358 (2009).
 22. S. Liang, Z. Ma, G. Wu, N. Wei, L. Huang, H. Huang, H. Liu, S. Wang, and L.-M. Peng, "Microcavity-Integrated Carbon Nanotube Photodetectors," *ACS Nano* **10**(7), 6963–6971 (2016).
 23. C. Biswas, H. Jeong, M. S. Jeong, W. J. Yu, D. Pribat, and Y. H. Lee, "Quantum Dot–Carbon Nanotube Hybrid Phototransistor with an Enhanced Optical Stark Effect," *Adv. Funct. Mater.* **23**(29), 3653–3660 (2013).
 24. M. Spina, B. Náfrádi, H. M. Tóháti, K. Kamarás, E. Bonvin, R. Gaal, L. Forró, and E. Horváth, "Ultrasensitive 1D field-effect phototransistors: CH₃NH₃PbI₃ nanowire sensitized individual carbon nanotubes," *Nanoscale* **8**(9), 4888–4893 (2016).
 25. M. Freitag, Y. Martin, J. A. Misewich, R. Martel, and Ph. Avouris, "Photoconductivity of Single Carbon Nanotubes," *Nano Lett.* **3**(8), 1067–1071 (2003).
 26. C. Ménard-Moyon, K. Kostarelos, M. Prato, and A. Bianco, "Functionalized Carbon Nanotubes for Probing and Modulating Molecular Functions," *Chemistry & Biology* **17**(2), 107–115 (2010).
 27. Q. Zeng, S. Wang, L. Yang, Z. Wang, T. Pei, Z. Zhang, L.-M. Peng, W. Zhou, J. Liu, W. Zhou, and S. Xie, "Carbon nanotube arrays based high-performance infrared photodetector [Invited]," *Optical Materials Express* **2**(6), 839 (2012).
 28. I. A. Levitsky and W. B. Euler, "Photoconductivity of single-wall carbon nanotubes under continuous-wave near-infrared illumination," *Appl. Phys. Lett.* **83**(9), 1857–1859 (2003).
 29. M. J. Shea and M. S. Arnold, "1% solar cells derived from ultrathin carbon nanotube photoabsorbing films," *Appl. Phys. Lett.* **102**(24), 243101 (2013).

30. D. J. Bindl, M.-Y. Wu, F. C. Prehn, and M. S. Arnold, "Efficiently Harvesting Excitons from Electronic Type-Controlled Semiconducting Carbon Nanotube Films," *Nano Lett.* **11**(2), 455–460 (2011).
31. M. P. Ramuz, M. Vosgueritchian, P. Wei, C. Wang, Y. Gao, Y. Wu, Y. Chen, and Z. Bao, "Evaluation of Solution-Processable Carbon-Based Electrodes for All-Carbon Solar Cells," *ACS Nano* **6**(11), 10384–10395 (2012).
32. M. Lanzi, L. Paganin, and D. Caretti, "New photoactive oligo- and poly-alkylthiophenes," *Polymer* **49**(23), 4942–4948 (2008).
33. W. Shi, Z. Wang, Q. Zhang, Y. Zheng, C. Jeong, M. He, R. Lortz, Y. Cai, N. Wang, T. Zhang, H. Zhang, Z. Tang, P. Sheng, H. Muramatsu, Y. A. Kim, M. Endo, P. T. Araujo, and M. S. Dresselhaus, "Superconductivity in Bundles of Double-Wall Carbon Nanotubes," *Scientific Reports* **2**, 625 (2012).
34. A. Di Bartolomeo, M. Sarno, F. Giubileo, C. Altavilla, L. Iemmo, S. Piano, F. Bobba, M. Longobardi, A. Scarfato, D. Sannino, A. M. Cucolo, and P. Ciambelli, "Multiwalled carbon nanotube films as small-sized temperature sensors," *Journal of Applied Physics* **105**(6), 064518 (2009).
35. S. L. de Bonis, C. Urgell, W. Yang, C. Samanta, A. Noury, J. Vergara-Cruz, Q. Dong, Y. Jin, and A. Bachtold, "Ultrasensitive Displacement Noise Measurement of Carbon Nanotube Mechanical Resonators," *Nano Letters* **18**(8), 5324–5328 (2018).
36. N. Hu, Y. Karube, C. Yan, Z. Masuda, and H. Fukunaga, "Tunneling effect in a polymer/carbon nanotube nanocomposite strain sensor," *Acta Materialia* **56**(13), 2929–2936 (2008).
37. K. Jensen, J. Weldon, H. Garcia, and A. Zettl, "Nanotube Radio," *Nano Lett.* **7**(11), 3508–3511 (2007).
38. M. S. Dresselhaus, G. Dresselhaus, and R. Saito, "C60-related tubules," *Solid State Communications* **84**(1), 201–205 (1992).
39. M. S. Dresselhaus, G. Dresselhaus, and R. Saito, "Carbon fibers based on C60 and their symmetry," *Phys. Rev. B* **45**(11), 6234–6242 (1992).
40. R. Saito, M. Fujita, G. Dresselhaus, and M. S. Dresselhaus, "Electronic structure of graphene tubules based on C60," *Phys. Rev. B* **46**(3), 1804–1811 (1992).

41. A. S. R. Bati, L. Yu, M. Batmunkh, and J. G. Shapter, "Synthesis, purification, properties and characterization of sorted single-walled carbon nanotubes," *Nanoscale* **10**(47), 22087–22139 (2018).
42. Ge. G. Samsonidze, A. Grüneis, R. Saito, A. Jorio, A. G. Souza Filho, G. Dresselhaus, and M. S. Dresselhaus, "Interband optical transitions in left- and right-handed single-wall carbon nanotubes," *Phys. Rev. B* **69**(20), 205402 (2004).
43. S. Sawada and N. Hamada, "Energetics of carbon nano-tubes," *Solid State Communications* **83**(11), 917–919 (1992).
44. L. Guan, K. Suenaga, and S. Iijima, "Smallest Carbon Nanotube Assigned with Atomic Resolution Accuracy," *Nano Lett.* **8**(2), 459–462 (2008).
45. Y. Miyata, T. Kawai, Y. Miyamoto, K. Yanagi, Y. Maniwa, and H. Kataura, "Chirality-Dependent Combustion of Single-Walled Carbon Nanotubes," *J. Phys. Chem. C* **111**(27), 9671–9677 (2007).
46. L.-C. Qin, X. Zhao, K. Hirahara, Y. Miyamoto, Y. Ando, and S. Iijima, "The smallest carbon nanotube," *Nature* **408**(6808), 50–50 (2000).
47. X. Zhao, Y. Liu, S. Inoue, T. Suzuki, R. O. Jones, and Y. Ando, "Smallest Carbon Nanotube Is 3 Å in Diameter," *Phys. Rev. Lett.* **92**(12), 125502 (2004).
48. J. A. Elliott, J. K. W. Sandler, A. H. Windle, R. J. Young, and M. S. P. Shaffer, "Collapse of Single-Wall Carbon Nanotubes is Diameter Dependent," *Phys. Rev. Lett.* **92**(9), 095501 (2004).
49. M. F. Lin and K. W.-K. Shung, "Magnetoconductance of carbon nanotubes," *Phys. Rev. B* **51**(12), 7592–7597 (1995).
50. F. L. Shyu, C. P. Chang, R. B. Chen, C. W. Chiu, and M. F. Lin, "Magnetoelectronic and optical properties of carbon nanotubes," *Phys. Rev. B* **67**(4), 045405 (2003).
51. L. Rosales, M. Pacheco, Z. Barticevic, C. G. Rocha, and A. Latgé, "Magnetic-field effects on transport in carbon nanotube junctions," *Phys. Rev. B* **75**(16), 165401 (2007).
52. X. Zhou, H. Chen, and O.-Y. Zhong-can, "Can electric field induced energy gaps in metallic carbon nanotubes?," *J. Phys.: Condens. Matter* **13**(27), L635–L640 (2001).

53. C.-W. Chen, M.-H. Lee, and S. J. Clark, "Band gap modification of single-walled carbon nanotube and boron nitride nanotube under a transverse electric field," *Nanotechnology* **15**(12), 1837–1843 (2004).
54. T. H. Cho, W. S. Su, T. C. Leung, W. Ren, and C. T. Chan, "Electronic and optical properties of single-walled carbon nanotubes under a uniform transverse electric field: A first-principles study," *Phys. Rev. B* **79**(23), 235123 (2009).
55. T. W. Tomblor, C. Zhou, L. Alexseyev, J. Kong, H. Dai, L. Liu, C. S. Jayanthi, M. Tang, and S.-Y. Wu, "Reversible electromechanical characteristics of carbon nanotubes under local-probe manipulation," *Nature* **405**(6788), 769–772 (2000).
56. Y. Okuno, Y. Saito, S. Kawata, and P. Verma, "Tip-Enhanced Raman Investigation of Extremely Localized Semiconductor-to-Metal Transition of a Carbon Nanotube," *Phys. Rev. Lett.* **111**(21), 216101 (2013).
57. C. Zhou, J. Kong, E. Yenilmez, and H. Dai, "Modulated Chemical Doping of Individual Carbon Nanotubes," *Science* **290**(5496), 1552–1555 (2000).
58. R. Chegel, "Tuning electronic properties of carbon nanotubes by Boron and Nitrogen doping," *Physica B: Condensed Matter* **499**, 1–16 (2016).
59. S. Lu and B. Panchapakesan, "Photoconductivity in single wall carbon nanotube sheets," *Nanotechnology* **17**(8), 1843–1850 (2006).
60. A. Fujiwara, Y. Matsuoka, H. Suematsu, N. Ogawa, K. Miyano, H. Kataura, Y. Maniwa, S. Suzuki, and Y. Achiba, "Photoconductivity in Semiconducting Single-Walled Carbon Nanotubes," *Jpn. J. Appl. Phys.* **40**(11B), L1229 (2001).
61. F. Wang, G. Dukovic, L. E. Brus, and T. F. Heinz, "The Optical Resonances in Carbon Nanotubes Arise from Excitons," *Science* **308**(5723), 838–841 (2005).
62. J. Maultzsch, R. Pomraenke, S. Reich, E. Chang, D. Prezzi, A. Ruini, E. Molinari, M. S. Strano, C. Thomsen, and C. Lienau, "Exciton binding energies in carbon nanotubes from two-photon photoluminescence," *Phys. Rev. B* **72**(24), 241402 (2005).

63. M. C. Beard, J. L. Blackburn, and M. J. Heben, "Photogenerated Free Carrier Dynamics in Metal and Semiconductor Single-Walled Carbon Nanotube Films," *Nano Lett.* **8**(12), 4238–4242 (2008).
64. G. Soavi, F. Scotognella, D. Brida, T. Hefner, F. Späth, M. R. Antognazza, T. Hertel, G. Lanzani, and G. Cerullo, "Ultrafast Charge Photogeneration in Semiconducting Carbon Nanotubes," *J. Phys. Chem. C* **117**(20), 10849–10855 (2013).
65. Y. Kumamoto, M. Yoshida, A. Ishii, A. Yokoyama, T. Shimada, and Y. K. Kato, "Spontaneous Exciton Dissociation in Carbon Nanotubes," *Phys. Rev. Lett.* **112**(11), 117401 (2014).
66. J. Park, O. G. Reid, J. L. Blackburn, and G. Rumbles, "Photoinduced spontaneous free-carrier generation in semiconducting single-walled carbon nanotubes," *Nature Communications* **6**, 8809 (2015).
67. M. Barkelid and V. Zwiller, "Photocurrent generation in semiconducting and metallic carbon nanotubes," *Nature Photonics* **8**(1), 47–51 (2014).
68. A. J. Ferguson, A.-M. Dowgiallo, D. J. Bindl, K. S. Mistry, O. G. Reid, N. Kopidakis, M. S. Arnold, and J. L. Blackburn, "Trap-limited carrier recombination in single-walled carbon nanotube heterojunctions with fullerene acceptor layers," *Phys. Rev. B* **91**(24), 245311 (2015).
69. S. D. Stranks, C. Weisspfennig, P. Parkinson, M. B. Johnston, L. M. Herz, and R. J. Nicholas, "Ultrafast Charge Separation at a Polymer–Single-Walled Carbon Nanotube Molecular Junction," *Nano Lett.* **11**(1), 66–72 (2011).
70. A.-M. Dowgiallo, K. S. Mistry, J. C. Johnson, and J. L. Blackburn, "Ultrafast Spectroscopic Signature of Charge Transfer between Single-Walled Carbon Nanotubes and C60," *ACS Nano* **8**(8), 8573–8581 (2014).
71. L. Perfetti, T. Kampfrath, F. Schapper, A. Hagen, T. Hertel, C. M. Aguirre, P. Desjardins, R. Martel, C. Frischkorn, and M. Wolf, "Ultrafast Dynamics of Delocalized and Localized Electrons in Carbon Nanotubes," *Phys. Rev. Lett.* **96**(2), 027401 (2006).
72. D. J. Bindl, A. J. Ferguson, M.-Y. Wu, N. Kopidakis, J. L. Blackburn, and M. S. Arnold, "Free Carrier Generation and Recombination in Polymer-Wrapped Semiconducting Carbon Nanotube Films and Heterojunctions," *J. Phys. Chem. Lett.* **4**(21), 3550–3559 (2013).

73. R. Ihly, K. S. Mistry, A. J. Ferguson, T. T. Clikeman, B. W. Larson, O. Reid, O. V. Boltalina, S. H. Strauss, G. Rumbles, and J. L. Blackburn, "Tuning the driving force for exciton dissociation in single-walled carbon nanotube heterojunctions," *Nature Chemistry* **8**(6), 603–609 (2016).
74. G. Soavi, F. Scotognella, D. Viola, T. Hefner, T. Hertel, G. Cerullo, and G. Lanzani, "High energetic excitons in carbon nanotubes directly probe charge-carriers," *Sci Rep* **5**(1), 1–5 (2015).
75. M. Salvato, M. Cirillo, M. Lucci, S. Orlanducci, I. Ottaviani, M. L. Terranova, and F. Toschi, "Charge Transport and Tunneling in Single-Walled Carbon Nanotube Bundles," *Phys. Rev. Lett.* **101**(24), 246804 (2008).
76. B. Gao, D. C. Glattli, B. Plaçais, and A. Bachtold, "Cotunneling and one-dimensional localization in individual disordered single-wall carbon nanotubes: Temperature dependence of the intrinsic resistance," *Phys. Rev. B* **74**(8), 085410 (2006).
77. R. S. Lee, H. J. Kim, J. E. Fischer, A. Thess, and R. E. Smalley, "Conductivity enhancement in single-walled carbon nanotube bundles doped with K and Br," *Nature* **388**(6639), 255–257 (1997).
78. T. Kim, G. Kim, W. I. Choi, Y.-K. Kwon, and J.-M. Zuo, "Electrical transport in small bundles of single-walled carbon nanotubes: Intertube interaction and effects of tube deformation," *Applied Physics Letters* **96**(17), 173107 (2010).
79. T. Hertel, R. Fasel, and G. Moos, "Charge-carrier dynamics in single-wall carbon nanotube bundles: a time-domain study," *Appl Phys A* **75**(4), 449–465 (2002).
80. M. Shim, A. Javey, N. W. Shi Kam, and H. Dai, "Polymer Functionalization for Air-Stable n-Type Carbon Nanotube Field-Effect Transistors," *J. Am. Chem. Soc.* **123**(46), 11512–11513 (2001).
81. C. Gadermaier, E. Menna, M. Meneghetti, W. J. Kennedy, Z. V. Vardeny, and G. Lanzani, "Long-Lived Charged States in Single-Walled Carbon Nanotubes," *Nano Lett.* **6**(2), 301–305 (2006).
82. D. Gao, R. Liu, W. Yu, Z. Luo, C. Liu, and S. Fan, "Gravity-Induced Self-Charging in Carbon Nanotube/Polymer Supercapacitors," *J. Phys. Chem. C* **123**(9), 5249–5254 (2019).

83. H. J. Queisser and D. E. Theodorou, "Decay kinetics of persistent photoconductivity in semiconductors," *Phys. Rev. B* **33**(6), 4027–4033 (1986).
84. N. B. Pendyala and K. S. R. K. Rao, "Observation of persistent photoconductivity in flower shaped PbS dendrite structures," *Solid State Communications* **149**(43), 1928–1931 (2009).
85. R. F. Khairoutdinov, L. V. Doubova, R. C. Haddon, and L. Saraf, "Persistent Photoconductivity in Chemically Modified Single-Wall Carbon Nanotubes," *J. Phys. Chem. B* **108**(52), 19976–19981 (2004).
86. J.-L. Zhu, G. Zhang, J. Wei, and J.-L. Sun, "Negative and positive photoconductivity modulated by light wavelengths in carbon nanotube film," *Applied Physics Letters* **101**(12), 123117 (2012).
87. C. S. Allen, G. Liu, Y. Chen, A. W. Robertson, K. He, K. Porfyrakis, J. Zhang, G. A. D. Briggs, and J. H. Warner, "Optically enhanced charge transfer between C60 and single-wall carbon nanotubes in hybrid electronic devices," *Nanoscale* **6**(1), 572–580 (2013).
88. S. Roy, C. K. Ghosh, and C. K. Sarkar, eds., *Nanotechnology: Synthesis to Applications*, 1 edition (CRC Press, 2017).
89. W. Zhou, X. Bai, E. Wang, and S. Xie, "Synthesis, Structure, and Properties of Single-Walled Carbon Nanotubes," *Advanced Materials* **21**(45), 4565–4583 (2009).
90. A. A. Rashad, R. Noaman, S. A. Mohammed, and E. Yousif*, "Synthesis of Carbon Nanotube : A Review," *Journal of Nanoscience and Technology* 155–162 (2016).
91. M. Endo, S. Iijima, and M. S. Dresselhaus, *Carbon Nanotubes*, 1 edition (Pergamon, 1997).
92. M. S. Dresselhaus, G. Dresselhaus, and P. Avouris, eds., *Carbon Nanotubes: Synthesis, Structure, Properties, and Applications*, Topics in Applied Physics (Springer-Verlag, 2001).
93. Y. Li and S. Maruyama, eds., *Single-Walled Carbon Nanotubes: Preparation, Properties and Applications*, Topics in Current Chemistry Collections (Springer International Publishing, 2019).
94. J. Hilding, E. A. Grulke, Z. G. Zhang, and F. Lockwood, "Dispersion of Carbon Nanotubes in Liquids," *Journal of Dispersion Science and Technology* **24**(1), 1–41 (2003).

95. M. J. Green, "Analysis and measurement of carbon nanotube dispersions: nanodispersion versus macrodispersion," *Polymer International* **59**(10), 1319–1322 (2010).
96. J. L. Hudson, M. J. Casavant, and J. M. Tour, "Water-Soluble, Exfoliated, Nonroping Single-Wall Carbon Nanotubes," *J. Am. Chem. Soc.* **126**(36), 11158–11159 (2004).
97. V. C. Moore, M. S. Strano, E. H. Haroz, R. H. Hauge, R. E. Smalley, J. Schmidt, and Y. Talmon, "Individually Suspended Single-Walled Carbon Nanotubes in Various Surfactants," *Nano Lett.* **3**(10), 1379–1382 (2003).
98. Z. Sun, V. Nicolosi, D. Rickard, S. D. Bergin, D. Aherne, and J. N. Coleman, "Quantitative Evaluation of Surfactant-stabilized Single-walled Carbon Nanotubes: Dispersion Quality and Its Correlation with Zeta Potential," *J. Phys. Chem. C* **112**(29), 10692–10699 (2008).
99. V. A. Davis, A. N. G. Parra-Vasquez, M. J. Green, P. K. Rai, N. Behabtu, V. Prieto, R. D. Booker, J. Schmidt, E. Kesselman, W. Zhou, H. Fan, W. W. Adams, R. H. Hauge, J. E. Fischer, Y. Cohen, Y. Talmon, R. E. Smalley, and M. Pasquali, "True solutions of single-walled carbon nanotubes for assembly into macroscopic materials," *Nature Nanotech* **4**(12), 830–834 (2009).
100. F. Liang, A. K. Sadana, A. Peera, J. Chattopadhyay, Z. Gu, R. H. Hauge, and W. E. Billups, "A Convenient Route to Functionalized Carbon Nanotubes," *Nano Lett.* **4**(7), 1257–1260 (2004).
101. A. Pénicaud, P. Poulin, A. Derré, E. Anglaret, and P. Petit, "Spontaneous Dissolution of a Single-Wall Carbon Nanotube Salt," *J. Am. Chem. Soc.* **127**(1), 8–9 (2005).
102. A. Pénicaud, P. Poulin, E. Anglaret, P. Petit, O. Roubeau, S. Enouz, and A. Loiseau, "Dissolution Douce of Single Walled Carbon Nanotubes," *AIP Conference Proceedings* **786**(1), 266–270 (2005).
103. S. Fogden, C. A. Howard, R. K. Heenan, N. T. Skipper, and M. S. P. Shaffer, "Scalable Method for the Reductive Dissolution, Purification, and Separation of Single-Walled Carbon Nanotubes," *ACS Nano* **6**(1), 54–62 (2012).
104. C. Jiang, A. Saha, and A. A. Martí, "Carbon nanotubides: an alternative for dispersion, functionalization and composites fabrication," *Nanoscale* **7**(37), 15037–15045 (2015).

105. H. Ozawa, N. Ide, T. Fujigaya, Y. Niidome, and N. Nakashima, "One-pot Separation of Highly Enriched (6,5)-Single-walled Carbon Nanotubes Using a Fluorene-based Copolymer," *Chem. Lett.* **40**(3), 239–241 (2011).
106. F. Lemasson, N. Berton, J. Tittmann, F. Hennrich, M. M. Kappes, and M. Mayor, "Polymer Library Comprising Fluorene and Carbazole Homo- and Copolymers for Selective Single-Walled Carbon Nanotubes Extraction," *Macromolecules* **45**(2), 713–722 (2012).
107. F. Bottacchi, L. Petti, F. Späth, I. Namal, G. Tröster, T. Hertel, and T. D. Anthopoulos, "Polymer-sorted (6,5) single-walled carbon nanotubes for solution-processed low-voltage flexible microelectronics," *Appl. Phys. Lett.* **106**(19), 193302 (2015).
108. O. V. Kharissova and B. I. Kharisov, *Solubilization and Dispersion of Carbon Nanotubes* (Springer International Publishing, 2017).
109. L. A. Crum, T. J. Mason, J. L. Reisse, and K. S. Suslick, eds., *Sonochemistry and Sonoluminescence*, Nato Science Series C: (Springer Netherlands, 1999).
110. V. Kamath, A. Prosperetti, and F. N. Egolfopoulos, "A theoretical study of sonoluminescence," *The Journal of the Acoustical Society of America* **94**(1), 248–260 (1993).
111. D. F. Gaitan, L. A. Crum, C. C. Church, and R. A. Roy, "Sonoluminescence and bubble dynamics for a single, stable, cavitation bubble," *The Journal of the Acoustical Society of America* **91**(6), 3166–3183 (1992).
112. T. G. Leighton, *The Acoustic Bubble* (Academic Press, 2012).
113. V. A. Tarasov, M. A. Komkov, N. A. Stepanishchev, V. A. Romanenkov, and R. V. Boyarskaya, "Modification of polyester resin binder by carbon nanotubes using ultrasonic dispersion," *Polym. Sci. Ser. D* **8**(1), 9–16 (2015).
114. K. Yang, Z. Yi, Q. Jing, R. Yue, W. Jiang, and D. Lin, "Sonication-assisted dispersion of carbon nanotubes in aqueous solutions of the anionic surfactant SDBS: The role of sonication energy," *Chin. Sci. Bull.* **58**(17), 2082–2090 (2013).
115. A. Sesis, M. Hodnett, G. Memoli, A. J. Wain, I. Jurewicz, A. B. Dalton, J. D. Carey, and G. Hinds, "Influence of Acoustic Cavitation on the

- Controlled Ultrasonic Dispersion of Carbon Nanotubes," *J. Phys. Chem. B* **117**(48), 15141–15150 (2013).
116. H. Yoon, M. Yamashita, S. Ata, D. N. Futaba, T. Yamada, and K. Hata, "Controlling exfoliation in order to minimize damage during dispersion of long SWCNTs for advanced composites," *Scientific Reports* **4**, 3907 (2014).
 117. M. (Dawn) Yang, M. Li, S. Luo, and R. Liang, "Real-time monitoring of carbon nanotube dispersion using dynamic light scattering and UV-vis spectroscopy," *Int J Adv Manuf Technol* **82**(1), 361–367 (2016).
 118. C.-Q. Sheng, P. Wang, Y. Shen, Y.-J. Li, W.-H. Zhang, F.-Q. Xu, J.-F. Zhu, G.-Q. Lai, and H.-N. Li, "Electronic structure of PCBM," *Chinese Phys. B* **21**(1), 017102 (2012).
 119. X. Zhang and X.-D. Li, "Effect of the position of substitution on the electronic properties of nitrophenyl derivatives of fulleropyrrolidines: Fundamental understanding toward raising LUMO energy of fullerene electron-acceptor," *Chinese Chemical Letters* **25**(4), 501–504 (2014).
 120. A. T. Mallajosyula, W. Nie, G. Gupta, J. L. Blackburn, S. K. Doorn, and A. D. Mohite, "Critical Role of the Sorting Polymer in Carbon Nanotube-Based Minority Carrier Devices," *ACS Nano* **10**(12), 10808–10815 (2016).
 121. F. Schöppler, C. Mann, T. C. Hain, F. M. Neubauer, G. Privitera, F. Bonaccorso, D. Chu, A. C. Ferrari, and T. Hertel, "Molar Extinction Coefficient of Single-Wall Carbon Nanotubes," *J. Phys. Chem. C* **115**(30), 14682–14686 (2011).
 122. S. R. Sanchez, S. M. Bachilo, Y. Kadria-Vili, C.-W. Lin, and R. B. Weisman, "(n,m)-Specific Absorption Cross Sections of Single-Walled Carbon Nanotubes Measured by Variance Spectroscopy," *Nano Lett.* **16**(11), 6903–6909 (2016).
 123. S. W. Kettlitz, J. Mescher, N. S. Christ, M. Nintz, S. Valouch, A. Colsmann, and U. Lemmer, "Eliminating RC-Effects in Transient Photocurrent Measurements on Organic Photodiodes," *IEEE Photonics Technology Letters* **25**(7), 682–685 (2013).
 124. E. Adler, "Nonlinear Optical Frequency Polarization in a Dielectric," *Phys. Rev.* **134**(3A), A728–A733 (1964).

125. H. Hoshi, T. Yamada, K. Ishikawa, H. Takezoe, and A. Fukuda, "Second-harmonic generation in centrosymmetric molecular films: Analysis under anisotropic conditions," *Phys. Rev. B* **52**(16), 12355–12365 (1995).
126. S. Kielich, "Optical second-harmonic generation by electrically polarized isotropic media," *IEEE Journal of Quantum Electronics* **5**(12), 562–568 (1969).
127. T. Manaka, C.-Q. Li, X.-M. Cheng, and M. Iwamoto, "Spectroscopic consideration of the surface potential built across phthalocyanine thin films on a metal electrode," *J. Chem. Phys.* **120**(16), 7725–7732 (2004).
128. T. Manaka, E. Lim, R. Tamura, and M. Iwamoto, "Direct imaging of carrier motion in organic transistors by optical second-harmonic generation," *Nature Photonics* **1**(10), 581–584 (2007).
129. S. Nishi, D. Taguchi, T. Manaka, and M. Iwamoto, "Analysis of current-voltage characteristics of Au/pentacene/fluorine polymer/indium zinc oxide diodes by electric-field-induced optical second-harmonic generation," *Journal of Applied Physics* **117**(24), 245502 (2015).
130. D. Taguchi, L. Zhang, J. Li, M. Weis, T. Manaka, and M. Iwamoto, "Analysis of Carrier Transients in Double-Layer Organic Light Emitting Diodes by Electric-Field-Induced Second-Harmonic Generation Measurement," *J. Phys. Chem. C* **114**(35), 15136–15140 (2010).
131. D. Taguchi, T. Shino, L. Zhang, J. Li, M. Weis, T. Manaka, and M. Iwamoto, "Direct Probing of Photovoltaic Effect Generated in Double-Layer Organic Solar Cell by Electric-Field-Induced Optical Second-Harmonic Generation," *Appl. Phys. Express* **4**(2), 021602 (2011).
132. X. Chen, D. Taguchi, M. Weis, T. Manaka, and M. Iwamoto, "Analyzing Photo Induced Internal Electric Field in Pentacene/C60 Double-Layer Organic Solar Cells under Various External Voltages by Electric-Field-Induced Optical Second Harmonic Generation Measurement," *Jpn. J. Appl. Phys.* **51**(4R), 041605 (2012).
133. X. Chen, D. Taguchi, K. Lee, T. Manaka, and M. Iwamoto, "Analysis of Anomalous Discharging Processes in Pentacene/C60 Double-Layer Organic Solar Cell," *Jpn. J. Appl. Phys.* **51**(2S), 02BK01 (2012).
134. C. S. Liu, R. Glaser, P. Sharp, and J. F. Kauffman, "The Slope Ratio Method: A Simple and Accurate Method to Extract the First

- Hyperpolarizability from EFISH Measurements," *J. Phys. Chem. A* **101**(38), 7176–7181 (1997).
135. R. S. Finn and J. F. Ward, "DC-Induced Optical Second-Harmonic Generation in the Inert Gases," *Phys. Rev. Lett.* **26**(6), 285–289 (1971).
136. A. Devižis, A. Serbenta, K. Meerholz, D. Hertel, and V. Gulbinas, "Ultrafast Dynamics of Carrier Mobility in a Conjugated Polymer Probed at Molecular and Microscopic Length Scales," *Phys. Rev. Lett.* **103**(2), 027404 (2009).
137. D. A. Vithanage, A. Devižis, V. Abramavičius, Y. Infahsaeng, D. Abramavičius, R. C. I. MacKenzie, P. E. Keivanidis, A. Yartsev, D. Hertel, J. Nelson, V. Sundström, and V. Gulbinas, "Visualizing charge separation in bulk heterojunction organic solar cells," *Nature Communications* **4**, 2334 (2013).
138. A. Devižis, K. Meerholz, D. Hertel, and V. Gulbinas, "Ultrafast charge carrier mobility dynamics in poly(spirobifluorene-co-benzothiadiazole): Influence of temperature on initial transport," *Phys. Rev. B* **82**(15), 155204 (2010).
139. C. Li, Y. Chen, Y. Wang, Z. Iqbal, M. Chhowalla, and S. Mitra, "A fullerene–single wall carbon nanotube complex for polymer bulk heterojunction photovoltaic cells," *J. Mater. Chem.* **17**(23), 2406–2411 (2007).
140. T. J. Savenije, J. E. Kroeze, M. M. Wienk, J. M. Kroon, and J. M. Warman, "Mobility and decay kinetics of charge carriers in photoexcited PCBM/PPV blends," *Phys. Rev. B* **69**(15), 155205 (2004).
141. S. M. Tuladhar, D. Poplavskyy, S. A. Choulis, J. R. Durrant, D. D. C. Bradley, and J. Nelson, "Ambipolar Charge Transport in Films of Methanofullerene and Poly(phenylenevinylene)/Methanofullerene Blends," *Advanced Functional Materials* **15**(7), 1171–1182 (2005).
142. C. S. Ponseca, H. Němec, N. Vukmirović, S. Fusco, E. Wang, M. R. Andersson, P. Chabera, A. Yartsev, and V. Sundström, "Electron and Hole Contributions to the Terahertz Photoconductivity of a Conjugated Polymer:Fullerene Blend Identified," *J. Phys. Chem. Lett.* **3**(17), 2442–2446 (2012).
143. A. Devižis, D. Hertel, K. Meerholz, V. Gulbinas, and J.-E. Moser, "Time-independent, high electron mobility in thin PC61BM films: Relevance

- to organic photovoltaics," *Organic Electronics* **15**(12), 3729–3734 (2014).
144. C. M. Isborn, C. Tang, A. Martini, E. R. Johnson, A. Otero-de-la-Roza, and V. C. Tung, "Carbon Nanotube Chirality Determines Efficiency of Electron Transfer to Fullerene in All-Carbon Photovoltaics," *J. Phys. Chem. Lett.* **4**(17), 2914–2918 (2013).
 145. H. Bässler, "Charge Transport in Disordered Organic Photoconductors a Monte Carlo Simulation Study," *physica status solidi (b)* **175**(1), 15–56 (1993).
 146. T. Hertel, S. Himmelein, T. Ackermann, D. Stich, and J. Crochet, "Diffusion Limited Photoluminescence Quantum Yields in 1-D Semiconductors: Single-Wall Carbon Nanotubes," *ACS Nano* **4**(12), 7161–7168 (2010).
 147. Y.-Z. Ma, L. Valkunas, S. L. Dexheimer, S. M. Bachilo, and G. R. Fleming, "Femtosecond Spectroscopy of Optical Excitations in Single-Walled Carbon Nanotubes: Evidence for Exciton-Exciton Annihilation," *Phys. Rev. Lett.* **94**(15), 157402 (2005).
 148. J. W. Perry, "Nonlinear Optical Properties of Molecules and Materials," in *Materials for Nonlinear Optics*, ACS Symposium Series No. 455 (American Chemical Society, 1991), **455**, pp. 67–88.
 149. Ch. Bosshard, G. Knöpfle, P. Prêtre, and P. Günter, "Second-order polarizabilities of nitropyridine derivatives determined with electric-field-induced second-harmonic generation and a solvatochromic method: A comparative study," *Journal of Applied Physics* **71**(4), 1594–1605 (1992).
 150. Yu. D. Glinka, T. V. Shahbazyan, I. E. Perakis, N. H. Tolk, X. Liu, Y. Sasaki, and J. K. Furdyna, "Ultrafast dynamics of interfacial electric fields in semiconductor heterostructures monitored by pump-probe second-harmonic generation," *Appl. Phys. Lett.* **81**(20), 3717–3719 (2002).
 151. A. Alejo-Molina, K. Hingerl, and H. Hardhienata, "Model of third harmonic generation and electric field induced optical second harmonic using simplified bond-hyperpolarizability model," *J. Opt. Soc. Am. B, JOSAB* **32**(4), 562–570 (2015).
 152. X. Yang, L. T. Wood, and J. H. Miller, "Diffraction from tunable periodic structures: application for the determination of electro-optic coefficients," *Appl. Opt., AO* **40**(31), 5583–5587 (2001).

153. X. Yang, M. Aspelmeyer, L. T. Wood, and J. H. Miller, "Diffraction from tunable periodic structures. II. Experimental observation of electric field-induced diffraction peaks," *Appl. Opt.*, AO **41**(28), 5845–5850 (2002).
154. M. G. Harrison, J. Grüner, and G. C. W. Spencer, "Analysis of the photocurrent action spectra of MEH-PPV polymer photodiodes," *Phys. Rev. B* **55**(12), 7831–7849 (1997).
155. D. J. Styers-Barnett, S. P. Ellison, B. P. Mehl, B. C. Westlake, R. L. House, C. Park, K. E. Wise, and J. M. Papanikolas, "Exciton Dynamics and Biexciton Formation in Single-Walled Carbon Nanotubes Studied with Femtosecond Transient Absorption Spectroscopy," *J. Phys. Chem. C* **112**(12), 4507–4516 (2008).
156. K. H. Eckstein, H. Hartleb, M. M. Achsnich, F. Schöppler, and T. Hertel, "Localized Charges Control Exciton Energetics and Energy Dissipation in Doped Carbon Nanotubes," *ACS Nano* **11**(10), 10401–10408 (2017).
157. S. M. Kim, K. K. Kim, Y. W. Jo, M. H. Park, S. J. Chae, D. L. Duong, C. W. Yang, J. Kong, and Y. H. Lee, "Role of Anions in the AuCl₃-Doping of Carbon Nanotubes," *ACS Nano* **5**(2), 1236–1242 (2011).
158. W. Fu, Z. Xu, X. Bai, C. Gu, and E. Wang, "Intrinsic Memory Function of Carbon Nanotube-based Ferroelectric Field-Effect Transistor," *Nano Letters* **9**(3), 921–925 (2009).
159. G. Pennington and N. Goldsman, "Semiclassical transport and phonon scattering of electrons in semiconducting carbon nanotubes," *Phys. Rev. B* **68**(4), 045426 (2003).
160. T. Dürkop, B. M. Kim, and M. S. Fuhrer, "Properties and applications of high-mobility semiconducting nanotubes," *J. Phys.: Condens. Matter* **16**(18), R553 (2004).
161. C. Gómez-Navarro, P. J. D. Pablo, J. Gómez-Herrero, B. Biel, F. J. Garcia-Vidal, A. Rubio, and F. Flores, "Tuning the conductance of single-walled carbon nanotubes by ion irradiation in the Anderson localization regime," *Nature Materials* **4**(7), 534 (2005).
162. M. Held, S. P. Schießl, D. Miebler, F. Gannott, and J. Zaumseil, "Polymer/metal oxide hybrid dielectrics for low voltage field-effect transistors with solution-processed, high-mobility semiconductors," *Appl. Phys. Lett.* **107**(8), 083301 (2015).

163. S.-H. Jhi, S. G. Louie, and M. L. Cohen, "Electronic Properties of Oxidized Carbon Nanotubes," *Phys. Rev. Lett.* **85**(8), 1710–1713 (2000).
164. J. Zhao, A. Buldum, J. Han, and J. P. Lu, "Gas molecule adsorption in carbon nanotubes and nanotube bundles," *Nanotechnology* **13**(2), 195–200 (2002).
165. D. Kang, N. Park, J. Ko, E. Bae, and W. Park, "Oxygen-induced p-type doping of a long individual single-walled carbon nanotube," *Nanotechnology* **16**(8), 1048–1052 (2005).
166. A. Roch, M. Greifzu, E. R. Talens, L. Stepien, T. Roch, J. Hege, N. Van Nong, T. Schmiel, I. Dani, C. Leyens, O. Jost, and A. Leson, "Ambient effects on the electrical conductivity of carbon nanotubes," *Carbon* **95**, 347–353 (2015).

EXTRAS

I. DISERTACIJOS SANTRAUKA

I.1. ĮVADAS

Anglies nanovamzdeliai yra technologiškai patraukli ir daug žadanti medžiaga. Tokie ir panašūs motyvuojuojantys žodžiai yra įtraukiami į daugumą publikacijų, susijusių su anglies nanovamzdelių tyrimais, nuo pat 1991 m., kai japonų mokslininko Sumio Iijima [1] paskelbtas straipsnis sukėlė didelį susidomėjimą tomis nanostruktūromis pasaulio mokslininkų tarpe. Nuo pastarosios publikacijos pasirodymo, anglies nanovamzdeliai tapo plačiai tyrinėjami pasaulio mokslininkų, publikuota šimtai straipsnių, bandyta juos pritaikyti įvairiuose prietaisuose.

Anglies nanovamzdeliai pademonstravo savo naudingas savybes dar prieš daugelį metų, kai persų civilizacija sukūrė metalo apdirbimo technologijas, skirtas taip vadinamo *Damasko* plieno gamybai, neturėdamos jokių išsamesnių žinių apie tokį nanometrų dydžio pasaulį. Tačiau kaip rodo istorija – žinios yra svarbios ne tik pavieniams žmonėms, bet ištisoms visuomenėms taip pat. Šiais laikais, kai turime platų modernių mokslinių instrumentų asortimentą, turime daug platesnes galimybes atlikti tyrimus nuosekliau, kurdami naujas sudėtingesnes pažangias technologijas. Tikiuosi, kad šis darbas taip pat prisidės prie mokslinių žinių apie fotoelektrinius procesus nanomedžiagų pasaulyje багаžo didinimo.

I.1.1. Disertacijos tikslai ir uždaviniai

Nanomedžiagų ir nanotechnologijų pasaulis yra nepaprastai platus. Kadangi tos tematikos jau senokai plėtojamoms, yra sukaupta labai daug mokslinės informacijos. Tokios plačios ir išsamios informacijos neįmanoma aprėpti viename darbe – o ir tikslas nėra toks. Ši disertacija orientuota į gana siaurą nanomokslo temą – fotoelektrinių procesų dinamiką puslaidininkiniuose anglies nanovamzdeliuose. Taigi disertacijos tikslas yra ištirti fotoelektrinius procesus anglies nanovamzdelių sluoksniuose plačiame laiko intervale. Tai apima greitus ir ypač greitus procesus, pradedant po optinio sužadavimo sekančiu eksitono susiformavimu, krūvininkų atskyrimu ir tęsiant tolesnę jų migraciją ir rekombinaciją. Disertacijoje nagrinėjamas laiko intervalas taip pat apima ir ypač lėtus procesus, tokius kaip ilgai išliekančio vidinio elektrinio lauko formavimasis ir nykimas.

I.1.2. Darbo naujumas ir aktualumas

Daugelyje mokslinių publikacijų nagrinėjami pavieniai, atskiri anglies nanovamzdeliai. Kaip pavyzdys galėtų būti tiek paprastas lauko efekto tranzistorius, [10–13] tiek jų rinkiniai viename luste, skirti skaičiavimo tikslams [14], arba jau sudėtingesnis įtaisas, skirtas kvantiniam skaičiavimui, [15] o taip pat ir vienasienio anglies nanovamzdelio pagrindu pagamintas gliukozės jutiklis [16]. Teorinis vykstančių procesų ir eksperimentiškai išmatuotų duomenų nagrinėjimas tokiose santykinai nelabai sudėtingose molekulinėse sistemose yra paprastesnis ir lengviau įgyvendinamas. Tačiau daugelis praktinių taikymų reikalauja didesnio kiekio vienoje vietoje esančios medžiagos. Tokiu atveju dažniausiai prietaisus bandoma konstruoti naudojant

daugiasluoksnę technologiją. Tačiau tokiuose sluoksniuose, sudarytuose iš netvarkingai išsidėsčiusių ir tarpusavyje persipynusių anglies nanovamzdelių tinklų, vykstančius fizikinius procesus analizuoti yra daug sunkiau. Mokslinėje literatūroje galime rasti įvairių publikacijų, kuriose mokslininkai skelbia apie tam tikras iširtas fizikines savybes. Tačiau taip pat galima pastebėti, kad tie patys ar labai panašūs procesai visai kitaip aprašomi kitose publikacijose.

Fotoelektriniam taikymams reikalingas aiškus supratimas apie fotoelektroninius procesus anglies nanovamzdelių sluoksniuose, įskaitant eksitonų susidarymą ir krūvininkų generavimą, o taip pat ir jų tolesnį dreifą. Šioje disertacijoje buvo tiriami sluoksniai, suformuoti iš PFO-Bpy polimerais apgaubtų puslaidininkinių (6,5) chiralizmo vienasienių anglies nanovamzdelių (SWCNT), bei jų mišinių su [6,6]-fenil-C61-butano rūgšties metilo esteriu (PCBM). Krūvininkų fotogeneravimas, jų dreifas ir rekombinacija plonose plėvelėse, sudarytose iš tarpusavyje persipynusių SWCNT tinklų, iširti derinant kelis eksperimentinius metodus.

Stacionarios ir nestacionarios fotosrovės eksperimentinių matavimo metodų derinimas su uždelsto ištraukimo lauko (TDCF) metodu leido nustatyti pagrindines fotosrovės komponentes ir priskirti jas atitinkamiems elektronų ir skylių judėjimo procesams anglies nanovamzdelių viduje ir jų išorėje.

Tyrimuose taip pat buvo panaudotas ultraspartus optinis elektrinio lauko stiprio matavimo metodas, pagrįstas elektros lauku indukuotos antrosios harmonikos (EFISH) generavimu. Šis metodas, derinamas su įprastais nestacionarios fotosrovės matavimais, leido tiesiogiai stebėti krūvininkų atskyrimą ir jų dinamiką SWCNT pradinėse nestacionarios fotosrovės fazėse.

Galiausiai buvo pastebėta ilgalaikė elektriniu lauku indukuota poliarizacija SWCNT perkoliaciniuose tinkluose. Atskleista, kad išoriniu elektros lauku veikiant SWCNT ir jų mišinių su PCBM plėveles, jose esančiuose SWCNT

klasteriuose susidaro elektriniai dipoliai, kurie iš dalies ekranuoja išorinį elektrinį lauką ir sukuria vidinį priešingos krypties elektrinį lauką, išliekanti iki keletos dienų po išorinio elektrinio lauko veikimo nutraukimo.

Aiškus fotosrovės komponenčių identifikavimas SWCNT sistemose suteikia platesnes perspektyvas jų pritaikymui ir optimizavimui fotoelektriniuose prietaisuose. Rezultatai, išplaukiantys iš ypač greitų elektroninių procesų tyrimų fotosužadintuose SWCNT, suteikia informacijos apie krūvininkų generavimą ir dinamikos mechanizmus, reikalingus jų valdymui, kuriant efektyvesnes anglies nanovamzdelių pagrindu veikiančias sistemas ir įrenginius. Ši ypač greita fotosrovės komponentė, kuri gali būti naudinga kuriant naujus ypač greitus fotodetektorius, gali būti toliau optimizuojama keičiant nanovamzdelių ilgį bei sukuriant perkoliacinius tinklus su didesne orientuotų anglies nanovamzdelių dalimi. Didesnė greitaveika gali būti pasiekta, jei SWCNT būtų labiau izoliuoti vienas nuo kito, išvengiant tarpvamzdelinių krūvininkų šuolių. Kita vertus, SWCNT tinklo perkoliacijos pagerinimas yra esminis reikalavimas, norint maksimaliai padidinti stacionarias fotosroves.

Minėtas ilgai išliekantis vidinis elektrinis laukas taip pat gali atlikti svarbų vaidmenį SWCNT pagrindu sukonstruotuose elektriniuose ir fotoelektriniuose įrenginiuose. Jis gali ekranuoti pridėtą išorinį elektrinį lauką, kelis kartus sumažindamas jo stiprumą ir sukelti ilgalaikius atminties efektus.

Ultraspartus optinis elektrinio lauko matavimo eksperimentinis metodas, kuris buvo naudojamas tiesioginiam krūvininkų atskyrimo ir dinamikos stebėjimui, reikalauja atskiro paminėjimo, atsižvelgiant į naujus efektus, išryškėjusius pritaikant metodą bandiniams ant šukų tipo elektrodų. Elektriniu lauku indukuotos antrosios harmonikos (EFISH) generacijos metodas yra galingas instrumentas optiniams netiesiškumams, medžiagų poliarizacijai, vidiniams elektriniams laukams ir kitoms fotoninių medžiagų ir prietaisų savybėms tirti.

Įprastas antrosios harmonikos generavimas medžiagose, nepasižyminčiose centrosimetrija, sukuria nuo elektrinio lauko nepriklausantį foną ir riboja EFISH taikymą. Šukų tipo elektrodai suformuoja amplitudinę difrakcinę gardelę lazerio spinduliuotei. Tačiau EFISH spinduliuotė sukuria interferencinį vaizdą, neturintį centrinio maksimumo tiesiogiai sklindančio žadinimo spindulio kryptimi, ir sukuria interferencinius maksimumus vietose, besikiriančiose ir nuo pagrindinės, ir nuo įprastos antros harmonikos interferencinių maksimumų pozicijų. Šis efektas suteikia galimybę paprastai realizuoti geometrinį EFISH signalo, kuris įprastai būna ypač silpnas, išskyrimą iš bendro stipraus fono, o taip pat suteikia ir papildomų eksperimentinių galimybių.

Patobulinta eksperimento schema leidžia paprasčiau ir platesniame intervale keisti kampą tarp šviesos poliarizacijos ir išorinio elektrinio lauko, jei tiriami kiti poliarizacijos tenzorius elementai. Be to, ši schema suteikia papildomų technologinių galimybių, kurios neįmanomos daugiasluoksniuose bandiniuose. Pavyzdžiui, molekulės sluoksniuose gali būti orientuotos lygiagrečiai arba statmenai elektrodams, naudojant įprastus orientavimo metodus, taip sudarant galimybes tirti nuo orientacijos priklausomas optines savybes ir procesus. Šios savybės gali būti svarbios ir naudingos kai kurioms šviesos valdymo bei kitoms netiesinės optikos sritims.

I.1.3. Disertacijos ginamieji teiginiai

1. Krūvininkų fotogeneracija vienasienių anglies nanovamzdelių (SWCNT) ir [6,6]-fenil-C₆₁-butano rūgšties metilo esterio (PCBM) mišinių netvarkiuose sluoksniuose vyksta spontaniškai, nereikalaujant išorinio elektrinio lauko. Be to, elektrinis laukas nepadidina

- fotogeneravimo efektyvumo, bent jau iki maždaug $10^4 \text{ V}\cdot\text{cm}^{-1}$ elektrinio lauko stiprio.
2. Krūvio pernašos (CT) būsenos SWCNT/PCBM sluoksniuose skyla į laisvus krūvininkus per šimtus pikosekundžių. Tuo tarpu krūvininkų skaičiaus mažėjimą lemia geminalinė rekombinacija, vykstanti keletą mikrosekundžių po fotosužadavimo.
 3. Krūvininkų pernašos sparta persipynusiu anglies nanovamzdelių tinklu yra apribota krūvininkų šuolių tarp anglies nanovamzdelių, kurie yra žymiai lėtesni nei krūvininkų dreifas vamzdelio viduje.
 4. Prijungta elektrine įtampa veikiant ant šukų tipo elektrodų suformuotus anglies nanovamzdelių turinčius sluoksnius, skatinamas vidinio priešingos krypties elektrinio lauko formavimasis, kuris išlieka iki kelių dienų po minėtos įtampos atjungimo.

I.1.4. Autoriaus indėlis

Autorius atliko didžiąją dalį eksperimentinių tyrimų, įskaitant įrangos parengimo darbus ir techninius sprendimus. Autorius taip pat atliko pagrindinės ir antrosios harmonikų bei EFISH signalo intensyvumo erdvinio pasiskirstymo kompiuterinį modeliavimą bandiniuose, suformuotuose naudojant šukų tipo elektrodus. Dalį bandinių paruošimo darbų ir fotolaidumo matavimų atliko A. Eckstein ir V. Bertašius. Šie rezultatai yra įtraukti į disertaciją kaip neatsiejama visų eksperimentinių duomenų dalis. Bandinius, apibūdinamus kaip pagamintus naudojant šviežią tirpalą (aprašytus mėginių paruošimo skyriuje) paruošė F. Oberndorfer ir T. Hertel, naudodamiesi savo technologiniais metodais. Bandinių vaizdinimas skenuojančiu elektroniniu mikroskopu atliktas V. Pakšto, o už šukų tipo elektrodų, naudotų kai kuriuose

matavimuose, gamybą autorius dėkingas M. Gedvilui ir G. Račiukaičiui. Autorius taip pat sukūrė programinę įrangą LabView aplinkoje, skirtą eksperimento valdymui, duomenų surinkimui ir apdorojimui. Ši programinė įranga buvo naudojama visoms fotosrovės kinetikoms ir uždelsto ištraukimo lauko (TDCF) tyrimams.

I.2. TYRIMŲ METODIKA

I.2.1. Bandinių paruošimas

Puslaidininkiniai vienasieniai anglies nanovamzdeliai (SWCNT), naudojami bandinių paruošimui, buvo išgryninti iš CoMoCAT būdu susintetinto SWCNT mišinio (99,9%, Sigma Aldrich), selektyviai apvyniojant (6,5) chiraliskumo anglies nanovamzdelius poli [(9,9 dioktilfluorenil-2,7-diil)–alt–ko(6,6-2,2-bipiridino)] (PFO-Bpy) kopolimeru, kaip aprašyta [105]. PFO-Bpy kopolimeru stabilizuoti (6,5)-SWCNT buvo suspenduoti chlorbenzene (> 98%, Fluka) ir panaudoti tolesniam mėginių paruošimui.

Norint gauti SWCNT ir [6,6]-fenil-C₆₁-butano rūgšties metilo esterio (PCBM) mišinius, ši chlorbenzeno suspensija su polimeru apvyniotais (6,5)-SWCNT buvo sumaišyta su skirtingos koncentracijos PCBM tirpalais. PCBM ir SWCNT masės santykis x/y skirtinguose bandiniuose nurodomas naudojant žymėjimą PCBM/SWCNT (x/y). Kadangi anglies nanovamzdelių gryninimo bei puslaidininkinių vamzdelių išskyrimo iš mišinio technologija pasižymi anglies nanovamzdelių praradimu proseso metu, x/y santykis suformuotose pėvelėse buvo įvertintas pagal sluoksnio absorbcijos spektrus, naudojant mokslinėje literatūroje paskelbtus SWCNT fotoabsorbcijos skerspjūvius. [121,122]

Matavimams, kurie toliau aprašomi, paprastai naudojami daugiasluoksniai arba, taip vadinami, sumuštinio tipo bandiniai, turintys aktyvųjį sluoksnį tarp elektrodų iš kurių bent vienas yra optiškai skaidrus. Čia buvo naudojama eksperimento realizavimo schema, kai bandiniai formuojami ant metalinių šukų tipo elektrodų, suformuotų ant optiškai skaidraus padėklo. Verta paminėti tokio metodo skirtumus, lyginant su daugiasluoksnių bandinių tyrimo metodika.

Pirma, kai naudojamas elektriniu lauku indukuotos antros harmonikos (EFISH) generacijos metodas, eksperimento sąlygos šiems eksperimentams nėra optimalios daugiasluoksnių tipo mėginiuose dėl elektrinio lauko stiprio vektorių nesutapimo. Taikyti šį metodą taip pat tampa labai sunku arba net neįmanoma, jei plėvelės yra polikristalinės arba sudarytos iš orientuotų ar dalinai orientuotų struktūrų. Dėl pastarosios priežasties tampa sunku išskirti EFISH signalą iš įprastos, dažnai daug stipresnės antrosios harmonikos generacijos.

Kita plonų plėvelių tyrimo problema yra susijusi su gana sudėtinga ir daug laiko reikalaujančia daugiasluoksnių bandinių gamyba. Tai praktiškai apriboja greitą medžiagų charakterizavimą. Ypač plonų, monosluoksnių „Langmuir Blodgett“ arba saviorganizaciniais metodais suformuotų plėvelių atveju viršutinių elektrodų formavimas tampa sudėtinga, dažnai neišsprendžiama problema.

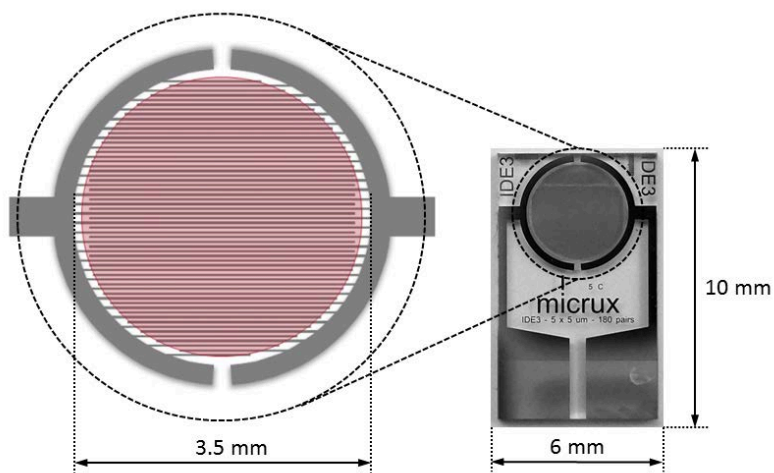
Mūsų technika, formuojant bandinius ant šukų tipo elektrodų (IDE), išsprendžia aukščiau paminėtas problemas ir papildomai suteikia keletą visiškai naujų eksperimentinių galimybių. Nors pačių elektrodų gamybai reikalingos labai tikslios technologijos, tolesnis bandinių paruošimas ant jau pagamintų elektrodų yra lengvas ir greitas. Pakanka suformuoti ploną medžiagos sluoksnį ant elektrodų. Ši technika yra ypač patogi formuojant plonas plėveles iš tirpalo. Šukų tipo elektrodai gali būti naudojami

pakartotinai, jei suformuotą ir ištirtą sluoksnį įmanoma nuplauti. Šis metodas taip pat išsprendžia viršutinio elektrodo problemą, leidžiančią išvengti kylančių problemų formuojant elektrodus monosluoksninėms ar kitoms ypač plonomis plėvelėms.

Ši eksperimento realizavimo metodika taip pat leidžia paprasčiau ir platesniame intervale keisti kampą tarp šviesos poliarizacijos ir išorinio elektrinio lauko, jei tiriami kiti poliarizacijos tenzorius elementai.

Prie metodo privalumų priskirtinos papildomų eksperimentinių realizacijų galimybės, kurios sunkiai įmanomos daugiasluoksniuose bandiniuose. Pavyzdžiui, molekulės plėvelėse gali būti orientuotos lygiagrečiai arba statmenai elektrodams, naudojant įprastus orientavimo metodus. Šiuo atveju šukų tipo elektrodų naudojimas leidžia ištirti nuo molekulių orientacijos priklausomas optines ir fotoelektrines savybes bei procesus.

Eksperimentams buvo naudojami dviejų tipų elektrodai – laboratorijoje gaminti ir prekyboje esantys. Fotoelektriniuose matavimuose buvo naudojami prekyboje esantys „*Micrux Technologies*“ šukų tipo elektrodai (**I.2.1 pav.**). Šie elektrodai yra gaminami plonų plėvelių technologijomis ant stiklo pagrindo. Vieną atskirą elektrodą sudaro plonas 50 nm storio rišantis titano sluoksnis, ant kurio užneštas 150 nm storio platinos sluoksnis.



I.2.1 pav. Šukų tipo elektrodų (IDE) plokštelė iš *Micrux Technologies*

Šukų tipo elektrodus sudaro du atskiri elektrodų strypelių masyvai, suformuoti ant plokštelės taip, kad aktyvioje zonoje elektrodų strypeliai iš skirtingų masių eina pakaitomis. Aktyvi zona yra apskrita 3,5 mm skersmens (9,6 mm² ploto), suformuota iš 180 porų elektrodų juostelių, kurių kiekvienos plotis 5 μm ir tarp gretimų juostelių yra 5 μm atstumas. Nenaudojamas plotas yra apsaugotas SU-8 dervos apsauginiu sluoksniu.

Tiriami sluoksniai ant šukų tipo elektrodų buvo paruošti lašinimo būdu, naudojant kontroliuojamą kiekį (2 μl) paruoštos suspensijos. SWCNT yra linkę kauptis į gniužulus, atitinkančius susipainiojusio tinklo modelį. Ištyrus skirtingo SWCNT susipainiojimo lygio plėveles, galima išskirti skirtingas krūvininkų judėjimo fazes. Todėl buvo paruošti dviejų tipų bandiniai – iš šviežio tirpalo ir iš tirpalo, pagaminto anksčiau kaip prieš metus. Paprastumo dėlei šie mėginiai vadinami atitinkamai *šviežiais* ir *senais*. Senos plėvelės turi aiškiai matomus klasterius su persipynusiais SWCNT, o šviežiuose bandiniuose susidaro labiau tinklinę struktūrą primenantis persipynusių anglies nanovamzdelių sluoksnis.

I.2.2. Eksperimentiniai tyrimo metodai

SUGERTIES SPEKTROSKOPIJA

Sugerties spektrai buvo matuojami pralaidumo režimu, naudojant Jasco V-670 spektrofotometrą. Kai bandiniai paruošti naudojant šukų tipo elektrodus, foninis signalas nustatytas matuojant „tuščią“ elektrodų plokštelę.

ULTRASPARČIOJI SUGERTIES ŽADINIMO – ZONDAVIMO SPEKTROSKOPIJA

Ultrasparčios sugerties žadinimo – zondavimo spektroskopijos tyrimai buvo atlikti naudojant „Pharos“ femtosekundinį lazerį (*Light Conversion*), generuojantį 1030 nm bangos ilgio, 250 fs trukmės impulsus 5 kHz pasikartojimo dažniu. 1000 nm bangos ilgio žadinimo impulsams generuoti buvo naudojamas parametrinis generatorius „Orpheus“ (*Light Conversion*). Zondavimui panaudotas baltos šviesos kontinuumas, kuriamas safyro plokštelėje.

STACIONARIOS FOTOSROVĖS MATAVIMAI

Stacionarios fotosrovės buvo išmatuotos naudojant *Keithley 6487* pikoampermetrą. Iki 5 V pastovi įtampa buvo prijungama prie šukų tipo elektrodų su ant jų suformuota tiriamą plėvelę. Lauko stiprumas bandinyje stipriai priklausė nuo vietos – jis buvo maždaug keturis kartus didesnis arti elektrodų nei per vidurį tarp jų. Bandiniai buvo apšviesti žalia fotodiodo šviesa, kurio šviesos stipris buvo $300 \mu\text{W}\cdot\text{cm}^{-2}$. Fotosrovė buvo nustatyta atimant tamsoje išmatuotą bandiniu tekančią srovę iš apšviečiant išmatuotos srovės.

NESTACIONARIOS FOTOSROVĖS MATAVIMAI

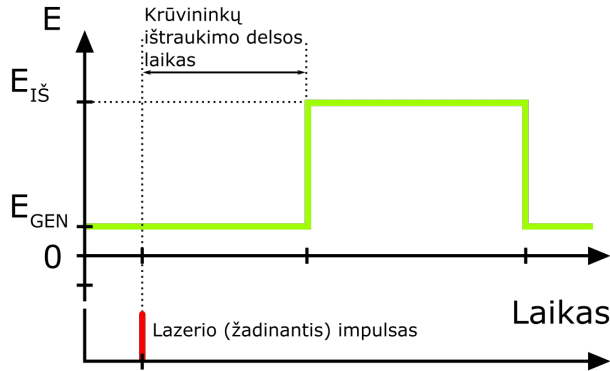
Nestacionarios fotosrovės tyrimai buvo atlikti naudojant „*Agilent Technologies DSO 5054A*“ osciloskopą ir elektrinių signalų generatorių „*Tektronix AFG 3101*“, bandinį žadinant impulsine lazerio šviesa. Bandinių fotosužaditimui buvo naudojami dviejų tipų lazeriai: pikosekundinis lazeris, kurio impulsai buvo ~ 150 ps trukmės, esant 532 nm arba 1064 nm bangos ilgiui, ir 5 Hz pasikartojimo dažniui, bei femtosekundinis Ti:Safyro lazeris, generuojantis 800 nm bangos ilgio ~ 130 fs trukmės šviesos impulsus, esant 430 Hz pasikartojimo dažniui. Femtosekundinis Ti:Safyro lazeris buvo naudojamas kartu su optiniu parametriniu stiprintuvu „*Topas-C*“ (*Light Conversion*), kuris buvo naudojamas 1000 nm bangos ilgio šviesos generacijai.

Nestacionarioji fotosrovė buvo matuojama srovės režimu naudojant 50Ω varžos osciloskopo įvestį ir integravimo režimu naudojant $1 \text{ M}\Omega$ varžos osciloskopo įvestį, kai bandinio ir osciloskopo elektrinės talpos veikė kaip integravimo kondensatorius. Integruojantis režimas leidžia išmatuoti labai silpnas fotosrovės ilgesnėje laiko skalėje, o taip pat turi geresnę laiko skiriamąją gebą. Įtampa šiuo atveju yra proporcinga iš bandinio ištrauktam krūviui, o fotosrovės stipris gali būti vertinamas kaip ištraukto krūvio kinetikos laiko išvestinė.

UŽDELSTO IŠTRAUKIMO LAUKO (TDCF) METODAS

Uždelsto ištraukimo lauko (TDCF) technika yra geras įrankis, siekiant atskirti krūvininko susidarymo ir ištraukimo fazes, taip pat ištirti krūvininkų rekombinacijos dinamiką. TDCF tyrimai buvo atlikti panašiu būdu, kaip ir nestacionarios fotosrovės matavimai. Nustatyta įtampa ant bandinio buvo palaikoma optinio sužadavimo metu (generavimo el. laukas E_{GEN}), o po derinamo delsos laiko buvo įjungiama krūvio ištraukimo įtampa (ištraukimo

el. laukas E_{IS}), (**I.2.2 pav.**). Krūvio ištraukimo kinetika buvo išmatuota naudojant integruojantį matavimo režimą, kaip aprašyta nestacionarios fotosrovės tyrimų skiltyje. Fotosrovė šiuo atveju sumuojasi su tamsoje tekančia srove, todėl uždelsto krūvio ištraukimo kinetika įvertinta kaip skirtumas tarp krūvio ištraukimo kinetikų, išmatuotų su optiniu žadinimu ir be jo.



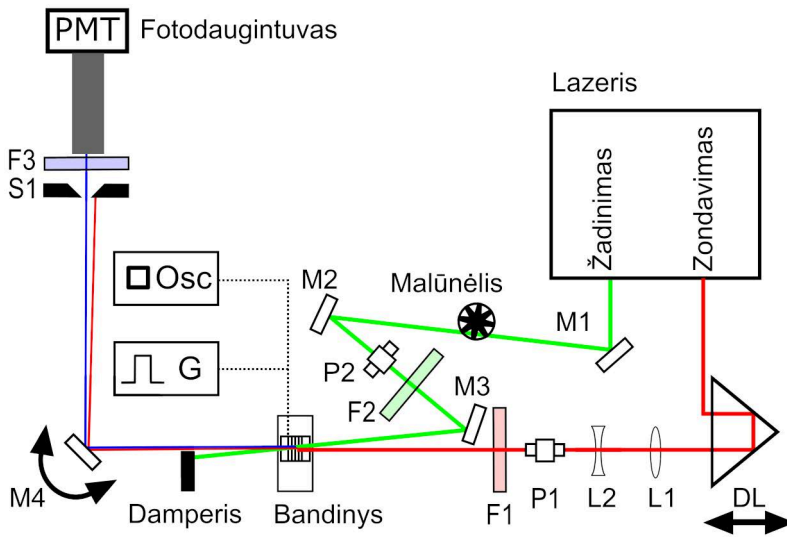
I.2.2 pav. Laiko sinchronizacijos schema TDCF matavimams

LAIKINĖS SKYROS ELEKTRINIŲ LAUKŲ INDUKUOTOS ANTROS HARMONIKOS (TREFISH) GENERACIJOS MATAVIMAI

EFISH (*electric-field-induced second harmonics (angl.)*) – elektriniu lauku indukuota antroji harmonika) efektas buvo sėkmingai pritaikytas tiriant vidinio elektrinio lauko dinamiką lauko efekto tranzistoriuose [128], organiniuose dioduose [129], šviesos dioduose [130] ir saulės elementuose [131–133]. Metodą derinant kartu su ultrasparčios spektroskopijos metodais, atsirado galimybė tirti greitą krūvininkų dinamiką organinėse medžiagose ir fotoelektriniuose prietaisuose.

Ultrasparti krūvininkų judėjimo dinamika buvo ištirta naudojant laikinės skyros elektriniu lauku indukuotos antros harmonikos (TREFISH) generavimo metodą. Ši visiškai optinė tyrimo metodika buvo pritaikyta tiriant

krūvininkų dinamiką konjuguotuose polimeruose [136] bei jų mišiniuose, naudojamuose organiniams saulės elementams [137] ir buvo išsamiau aprašyta mokslinėje literatūroje anksčiau. [136,138] TREFISH eksperimento matavimų schema, šio mokslinio darbo metu pritaikyta bandiniams su šukų tipo elektrodais, parodyta **I.2.3 pav.**



I.2.3 pav. TREFISH matavimų schema pralaidumo režimu (F – optiniai filtrai, L – lęšiai, M – veidrodėliai, P – poliarizacijos derinimo plokštės, S – optinis plyšys, DL – optinio vėlinimo linija, Osc – osciloskopas, G – el. impulsų generatorius)

Trumpai tariant, TREFISH yra žadinimo – zondavimo tipo technika, pagrįsta EFISH fenomenu, kas suteikia galimybę atlikti elektrinio lauko dinamikos matavimą optiniais metodais tiesiogiai tiriamosios medžiagos viduje. Prijungta įtampa įkrauna bandinio talpą prieš optinį sužadimą. Kai bandinys sužadamas ultratrumpu šviesos impulsu, sugeneruoti krūvininkai ekranuoja elektrinį lauką, taip jį susilpnindami bandinio viduje. Bandiniu pratekanti fotosrovė taip pat iškrauna prieš tai įkrautą bandinio talpą. Po kontroliuojamo delso laiko paleistas zonduojantis lazerio spindulys naudojamas elektrinio lauko kinetikai tirti, pasinaudojant EFISH generacijos efektu.

I.3. SVARBIAUSI REZULTATAI

Stacionarios fotosrovės matavimai parodė, kad PCBM molekulių fotosužadınimas SWCNT/PCBM mišinio sluoksniuose sukuria tik labai silpnas fotosroves, priešingai, nei žadinant SWCNT.

Uždelsto ištraukimo lauko (TDCF) matavimai atskleidė, kad elektriniu lauku ištrauktas sugeneruotas krūvis didėja proporcingai pridėtam elektriniam laukui, kas rodo, jog krūvininkų ištraukimas yra pagrindinis faktorius, apsprendžiantis fotosrovės priklausomybę nuo pridėtos išorinės elektros įtampos. Šie rezultatai taip pat rodo, kad krūvininkų generacija SWCNT/PCBM kompleksuose vyksta spontaniškai ir išorinio elektrinio lauko vaidmuo krūvininkų generavime nėra reikšmingas.

Kelių eksperimentinių metodų derinys – įprastinės nestacionarios fotosrovės, laikinės skyros elektrinio lauko indukuotos antros harmonikos (TREFISH) generacijos ir ultrasparčios sugerties žadinimo-zondavimo spektroskopijos – leido tiesiogiai sekti krūvininkų generaciją ir judėjimą PFO-Bpy kopolimeru apgaubtuose anglies nanovamzdeliuose ir iš jų susiagregavusiuose klasteriuose.

Krūvininkų generacija vyksta spontaniškai, elektronams peršokant iš sužadinto SWCNT į PCBM molekulę. Mūsų tyrimai atskleidė, kad tiesiogiai fotogeneruoti delokalizuoti neutralūs eksitonai pasižymi dideliu poliarizuojamumu ir reikšmingai ekranuoja išorinį elektrinį lauką. Neutralūs eksitonai yra gesinami femtosekundinėje laiko skalėje, perduodant elektroną į adsorbuotą PCBM molekulę, taip sukuriant lokalizuotas silpnai poliarizuotas krūvio pernašos (CT) būsenas. CT būsenos skyla į laisvus krūvininkus per šimtus pikosekundžių ir šis procesas yra vienas iš fotosrovės dinamiką

ribojančių faktorių. Tuo tarpu skylių judėjimas išilgai atskirų nanovamzdelių yra daug greitesnis.

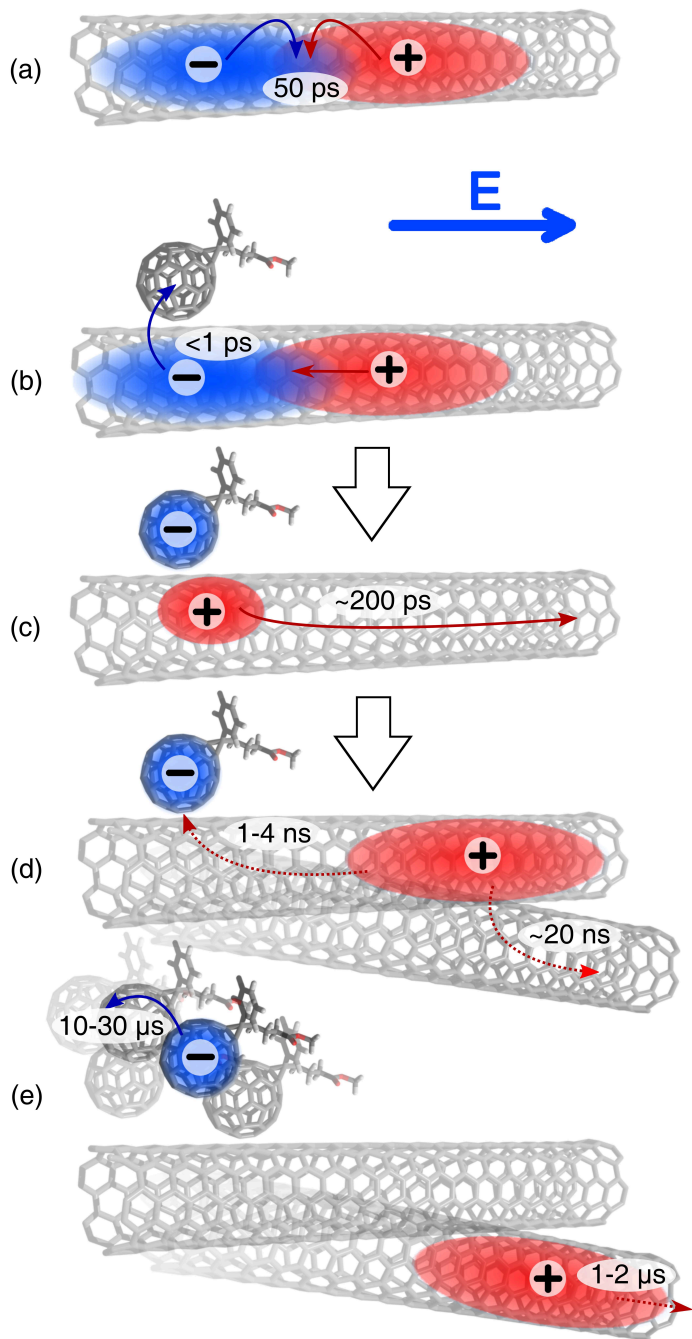
Skylių pernaša tarp susiagregavusių SWCNT yra daug lėtesnė nei judėjimas anglies nanovamzdelio viduje ir vyksta dešimtimis nanosekundžių. Šios fotogeneruotos skylės sukuria nestacionarią fotosrovę perkoliaciniame SWCNT tinkle, kurią labiau apsprendžia paties tinklo morfologija, nei krūvininkų rekombinacija ar ištraukimas.

Nestacionarios fotosrovės kinetika parodo tris charakteringus jos vystymosi etapus. Itin greita fazė, trunkanti mažiau nei 2 ns, priskiriama skylių judėjimui pavieniuose anglies nanovamzdeliuose, o skylių šuoliai tarp anglies nanovamzdelių gali trukti keletą mikrosekundžių. Skylių judėjimas izoliuotų anglies nanovamzdelių viduje sukuria poslinkio sroves, kurios matomos nestacionarios fotosrovės kinetikose, tačiau nekuria stacionarios fotosrovės. Lėčiausias foto srovės komponentas stebimas tik esant didelėms PCBM koncentracijoms ir yra priskiriamas elektronų judėjimui per PCBM molekules. Tame pačiame anglies nanovamzdeliulyje esantys elektronai ir skylės rekombinuoja maždaug per 1 μ s. Tuo tarpu, krūvininkai, esantys skirtinguose SWCNT, gali išgyventi šimtus mikrosekundžių.

Taip pat paminėtina, kad fotogeneruotų krūvininkų tankio mažėjimo sparta, nustatyta TDCF matavimais yra daug lėtesnė negu mokslinėje literatūroje publikuota laikinės skyros mikrobangų laidumo (TRMC) metodais nustatyta fotolaidumo mažėjimo sparta SWCNT/fulerenų kompleksuose.[66,68,72] Publikuotuose tyrimų rezultatuose kaip fotolaidumo mažėjimą lemiantis faktorius nurodomi antros eilės rekombinacijos procesai.[68] Šis skirtumas gali būti paaiškintas, kad bimolekulinė rekombinacija mūsų SWCNT/PCBM kompleksuose yra nereikšminga ir krūvininkų nykimas yra apsprendžiamas geminalinės krūvininkų poros rekombinacija.

Aukščiau aptarti procesai apibendrinti **I.3.1 pav.** pateiktoje schemoje. Nustatyta, kad atskiruose SWCNT ir jų klasteriuose dėstant pagal laiko skalę (nuo ps iki μ s) vyksta penki fotoindukuoti procesai:

- a) neutralaus eksitono relaksacija izoliuotame SWCNT,
- b) krūvio pernašos (CT) eksitono susidarymas perduodant elektroną iš anglies nanovamzdelio į adsorbuotą PCBM molekulę ir tuo pat metu lokalizuojant skylę šalia elektrono,
- c) CT eksitono skilimas į laisvus krūvininkus,
- d) dalies fotogeneruotų krūvininkų rekombinacija ir galimas skylių perkėlimas į kitas grandines.
- e) tolesnis skylės judėjimas SWCNT perkoliaciniu tinklu bei elektronų pernaša per medžiagų mišinį sudarančių PCBM fazę.

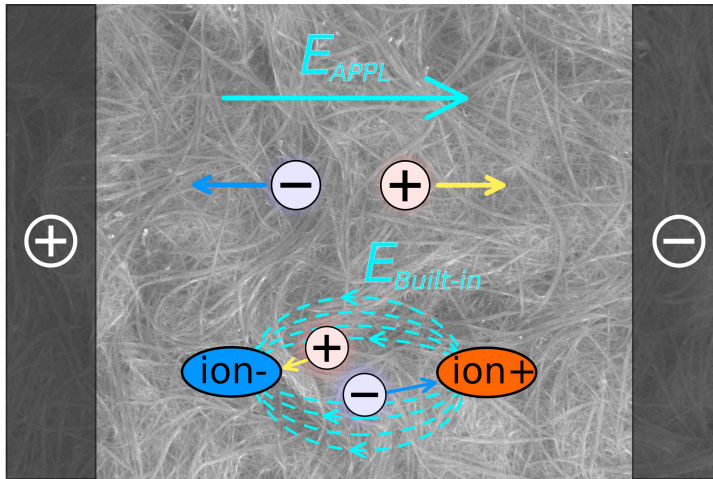


I.3.1 pav. Schema, vaizduojanti svarbiausius procesus fotosužadintuose anglies nanovamzdeliuose ir jų sluoksniuose

Be šių procesų, taip pat aptikta, kad išorinis elektrinis laukas, kuriuo veikiami SWCNT ir SWCNT/PCBM mišinių sluoksniai, suformuoti ant šukų tipo elektrodų, skatina ilgai išliekančių elektrinių dipolių susidarymą SWCNT klasteriuose. Dėl šių poliarizacijos reiškinių, pridėtas išorinis elektrinis laukas yra ekranuojamas, ir tai taip pat sukuria ilgai išliekantį sluoksnio fotolaidumą, pasireiškiantį valandas ir dienas po to, kai buvo atjungta nagrinėjamos medžiagos sluoksnį veikianti elektrinė įtampa.

Greitoji ($\sim 10 \mu\text{s}$) ilgai išliekančio fotolaidumo nykimo komponentė buvo priskirta kaip esanti susijusi su krūvininkų poslinkiu, o lėta, kelias dienas trunkanti komponentė labiausiai tikėtina atsiranda dėl jonų poslinkio. Lėta komponentė sukurama silpnesnė žemoje temperatūroje, o tai rodo, kad pridėto elektrinio lauko sukeltas jonų poslinkis reikalauja šiluminio aktyvavimo.

Išoriniu elektriniu lauku indukuoto ilgai išliekančio vidinio lauko kompensavimo eksperimentas atskleidė, kad kai išorinis ir vidinis elektriniai laukai buvo panašaus stiprumo, bet priešingų kryptių, fotosrovės kinetiką, nulėmė dvi konkuruojančios fotosrovės komponentės. Tokia kreivės forma leidžia manyti, kad sukurtas elektrinis laukas medžiagos sluoksnyje buvo nevienalytis ir net skirtingų kryptių atskirose erdvinėse srityse. Regionai, kuriuose buvo elektriniu polinimu sukurtų dipolių, turinčių dominuojantį vidinį lauką, buvo apsupti regionų, kuriuos silpnai veikė sukurtieji dipoliai, ir kur dominavo tuo metu prijungtos įtampos sukuriamas elektrinis laukas (žr. **I.3.2 pav.**).



I.3.2 pav. Vidinio elektrinio lauko formavimosi ir fotoelektrinių procesų SWCNT sluoksniuose schema

Remiantis šia prielaida, krūvininkai, sugeneruoti ir esantys sukurtų vidinių dipolių aplinkoje, judėjo tik nedideliais atstumais link dipolius sudarančių krūvių, sukurdami tik trumpą fotosrovės impulsą. Tuo tarpu krūvininkai, sugeneruoti regionuose, kuriuose dominuoja prijungtas išorinis elektrinis laukas, judėjo didesniais atstumais ir atitinkamai ilgesnį laiką.

I.4. IŠVADOS

Apibendrinami ištirtus fotoelektrinius procesus PFO-Bpy kopolimeru apgaubtų (6,5) chiralizmo puslaidininkinių anglies nanovamzdelių ir jų mišinių su PCBM sluoksniuose plačiame laiko intervale, galime padaryti tokias pagrindines išvadas:

1. Fotosrovę SWCNT/PCBM mišinių sluoksniuose apsprendžia krūvininkų generavimo efektyvumas ir sukurtų krūvininkų judris. Skylių dreifo nuotolį SWCNT perkoliaciniu tinklu daugiausia riboja tarpų dydis tarp

gretimų anglies nanovamzdelių. Esant dideliam PCBM kiekiui mišinyje, PCBM molekulės susijungia į ištisinę plėvelę, leidžiančią nepertraukiamai judėti elektronams. O esant mažam jų kiekiui, PCBM molekulės greičiausiai suformuoja atskirus izoliuotus klasterius, taip pat iš dalies yra adsorbuotos ant SWCNT ir nesuformuoja ištisinio nepertraukiamo kelio elektronams. Kita vertus, didelis PCBM kiekis mišinyje elektriškai izoluoja anglies nanovamzdelius nuo metalinių elektrodų ir vienas nuo kito, kas taip pat neleidžia skylėms nepertraukiamai judėti SWCNT tinklu.

2. Krūvininkų generavimo efektyvumas didėja, didėjant PCBM kiekiui mišinyje, tačiau pasiekama sotis, kai pakankamas PCBM molekulių kiekis atsorbuojamas ant anglies nanovamzdelių, užtikrinant efektyvų elektronų perdavimą. Fotosrovės įsotinimas esant dideliame žadinimo intensyvumui atsiranda, kai žadinimo intensyvumas pasiekia daugiau nei vieną fotogeneruotų krūvininkų porą viename nanovamzdelyje.
3. Laikinės skyros elektriniu lauku indukuotos antrosios harmonikos (TREFISH) eksperimentinė technika buvo pritaikyta tirti bandiniams, suformuotiems iš SWCNT/PCBM medžiagų mišinio ant šukų tipo elektrodų (IDE). Mėginio paruošimas yra paprastas ir greitas, bei leidžiantis ištirti labai greitą krūvininkų dinamiką plačiame organinių ir neorganinių amorfinių medžiagų diapazone. Dėl neįprasto elektriniu lauku indukuotos antrosios harmonikos (EFISH) spinduliuotės intensyvumo kampinio pasiskirstymo galima atlikti EFISH matavimus lengvai geometriškai išskiriant EFISH signalą nuo įprastos antrosios harmonikos generacijos.
4. Įprastinės nestacionarios fotosrovės, laikinės skyros elektriniu lauku indukuotos antrosios harmonikos (TREFISH) generacijos ir ultrasparčios sugerties žadinimo-zondavimo spektroskopijos metodų naudojimas leido

tiesiogiai sekti ir išskirti krūvininkų generaciją ir judėjimą anglies nanovamzdeliuose ir jų agregatuose su PCBM. Fotogeneruoti delokalizuoti neutralūs eksitonai pasižymi dideliu poliarizuojamumu ir reikšmingai ekranuoja pridėtą išorinį elektrinį lauką. Neutralūs eksitonai yra gesinami femtosekundinėje laiko skalėje, perduodant elektronus į ant SWCNT adsorbuotas PCBM molekules. Taip sukuriama stipriai lokalizuota silpnai polarizuojama krūvio pernašos (CT) būsenos, kurios šimtų pikosekundžių metu skyla į laisvus krūvininkus. Daug lėtesnis skylių judėjimas tarp anglies nanovamzdelių SWCNT agregatuose vyksta dešimtimis nanosekundžių.

5. Naudojamomis eksperimentinėmis sąlygomis, krūvininkų dinamikai SWCNT/PCBM plėvelėse negeminalinė elektronų-skylių rekombinacija ar kiti netiesiniai procesai nedaro reikšmingos įtakos. Nestacionarių fotosrovių kinetika rodo, kad ištrauktas krūvis yra proporcingas pridėtai įtampai, tačiau ekstrahavimo kinetikos forma eksperimento tikslumu nuo šios įtampos nepriklauso. Ištrauktas krūvis tiesiškai didėja didėjant žadinimo intensyvumui, o krūvio ištraukimo kinetika nesikeičia iki maždaug $5 \mu\text{J}\cdot\text{cm}^{-2}$. Bimolekulinė rekombinacija mūsų sistemose nėra reikšminga, o krūvininkų mažėjimą lemia geminalinė krūvininkų poros rekombinacija. Pikosekundžių laiko skalėje didžioji dalis sugeneruotų skylių lieka tuose pačiuose anglies nanovamzdeliuose, kur jos buvo sukurtos, ir kuria ypač greitą fotosrovės fazę. Dalis skylių peršoka į kaimyninius SWCNT, sukurdamos fotosrovę nanosekundės-kelių mikrosekundžių laiko skalėje. Todėl krūvininkų skaičiaus mažėjimą maždaug ties $1 \mu\text{s}$ laiko konstanta sukelia skylių, esančių tame pačiame SWCNT, kur jos buvo sukurtos, ir elektronų, esančių ant šių SWCNT adsorbuotų PCBM molekulių, rekombinacija. Ilgesniuose laiko intervaluose išlieka tik skylės, peršokusios į kitus anglies

nanovamzdelius, ir jų rekombinacija vyksta dešimtis ir šimtus mikrosekundžių.

6. Uždelsto ištraukimo lauko (TDCF) matavimai rodo, kad pridėtas išorinis elektrinis laukas nedaro įtakos krūvininkų fotogeneracijai esamomis eksperimentinėmis sąlygomis, bent jau iki jo stiprio maždaug $10^4 \text{ V}\cdot\text{cm}^{-1}$.
7. Išorinė įtampa, kuria veikiami SWCNT ir SWCNT/PCBM mišinių sluoksniai, suformuoti ant šukų tipo elektrodų (IDE), skatina ilgai išliekančių elektrinių dipolių susidarymą SWCNT klasteriuose. Šie dipoliai ekranuoja pridėtą elektrinį lauką ir taip pat sukelia ilgai išliekančios fotosrovės efektą, kuris pasireiškia valandas ir dienas jau po išorinės įtampos išjungimo.
8. Temperatūrinė elektriniu lauku indukuoto ilgai išliekančio vidinio lauko kinetikos priklausomybė rodo, kad du skirtingi procesai prisideda prie vidinio lauko formavimosi. Sparčiai mažėjančioji vidinio lauko komponentė rodo labai silpną temperatūrinę priklausomybę. Tokia priklausomybė rodo, jog pradinį krūvininkų judėjimą, atsakingą už trumpalaikę vidinio lauko komponentę, apsprendžia krūvininkų tuneliavimas tarp anglies nanovamzdelių ir jų grupių, o ne termiškai aktyvuojami šuoliai. Lėtoji komponentė, kuri yra apie 100 kartų silpnesnė, pradeda dominuoti maždaug ties 1 ms nuo polinančio elektrinio lauko išjungimo. Šiai fazei būdinga stipri temperatūrinė priklausomybė ir jai reikalinga šiluminė aktyvacija, atitinkanti 5–10 meV barjerus. Ši ilgai išliekanti vidinio elektrinio lauko komponentė priskiriama jonų judėjimui.

II. TRUMPOS ŽINIOS APIE DISERTANTĄ

Disertantas Vidmantas Jašinskas gimė 1983 metais Rietave, Rūtos ir Juozo Jašinskių šeimoje. 1990 metais pradėjo lankyti Rietavo L. Ivinskio vardo vidurinę mokyklą (dabar gimnazija), kurią su pagyrimu baigė 2002 metais. Tolesnį savo mokslinį kelią disertantas ėjo Vilniaus universitete.

IŠSILAVINIMAS

2012 m	Medžiagų Technologijų Magistras (Vilniaus universitetas, Fizikos fakultetas) Magistro studijų programa: „Optoelektronikos Medžiagos ir Technologijos“ Mokslinio tiriamojo darbo tema: „Anglies nanodarinių sluoksnių formavimas elektroforezės būdu“ <i>Darbo vadovas:</i> doc. Algirdas P. Smilga
2010 m	Fizikos Bakalauras (Vilniaus universitetas, Fizikos fakultetas) Bakalauro studijų programa: „Fizika“ Mokslinio tiriamojo darbo tema: „Anglies nanovamzdelių orientavimas“ <i>Darbo vadovas:</i> doc. Algirdas P. Smilga

DOKTORANTŲ VASAROS MOKYKLOS

2019 m	<ul style="list-style-type: none">• “Extreme Light Infrastructure Summer School (ELISS 2019).” Dolní Břežany, Čekijos respublika.
--------	---

- | | |
|--------|---|
| 2018 m | <ul style="list-style-type: none"> • “International School on Light Sciences and Technologies (ISLiST 2019). Light in Sources, Health and Medicine”. Santander, Ispanija. (ECTS kreditai: 1) |
| 2017 m | <ul style="list-style-type: none"> • “International School on Light Sciences and Technologies (ISLiST 2018). Light in communications and sensing”. Santander, Ispanija. (ECTS kreditai: 1) |
| 2016 m | <ul style="list-style-type: none"> • “Advanced materials and Technologies. International conference – school”. Palanga, Lietuva. • “International School on Light Sciences and Technologies (ISLiST 2017). Light for energy and environment”. Santander, Ispanija. (ECTS kreditai: 1) • “Advanced materials and Technologies. International conference – school”. Palanga, Lietuva. • “International School on Light Sciences and Technologies (ISLiST 2016). Light in medicine”. Santander, Ispanija. (ECTS kreditai: 1) |

PRANEŠIMAI KONFERENCIJOSE

- | | |
|--------|---|
| 2019 m | <ul style="list-style-type: none"> • “13th International Conference on Optical Probes of Organic and Hybrid Optoelectronic Materials and Applications”. Vilnius, Lietuva. <p style="margin-left: 20px;">Stendinis pranešimas: “Persistent built-in photoactivity of single-wall carbon nanotube films”.</p> |
| 2018 m | <ul style="list-style-type: none"> • “8th Conference of PhD Students and Young Researchers FizTeCh2018”. Vilnius, Lietuva. |

2017 m	<p>Žodinis pranešimas: “Ilgai išliekantis indukuotas elektrinis laukas anglies nanovamzdelių sluoksniuose”.</p> <ul style="list-style-type: none"> • “7th Conference of PhD Students and Young Researchers FizTeCh2017”. Vilnius, Lietuva.
	<p>Žodinis pranešimas: “Carrier photogeneration, drift and recombination in a semiconducting carbon nanotube network”.</p> <ul style="list-style-type: none"> • “Lietuvos Nacionalinė Fizikos Konferencija LNFK42”. Vilnius, Lietuva. <p>Stendinis pranešimas: “Carrier photogeneration, drift and recombination in a semiconducting carbon nanotube network”.</p>
2016 m	<ul style="list-style-type: none"> • “6th Conference of PhD Students and Young Researchers FizTeCh2016”. Vilnius, Lietuva. <p>Žodinis pranešimas: “Second harmonic generation in polymers induced by periodic electric field”.</p>
2016 m	<ul style="list-style-type: none"> • “Advanced materials and Technologies. International conference – school”. Palanga, Lietuva. <p>Stendinis pranešimas: “Background-free electric field-induced second harmonic generation with interdigitated combs of electrodes”.</p>

GAUTAS FINANSAVIMAS

2019 m	<ul style="list-style-type: none"> • “ISLiST-2019 Full International Student Grant” (Universidad Internacional Menéndez Pelayo, Ispanija) dalyvavimui tarptautinėje mokykloje “International School on Light Sciences and Technologies” (Santander, Ispanija).
--------	---

- Lietuvos Mokslo Tarybos parama doktorantų akademinėms išvykoms. Parama skirta dalyvavimui vasaros mokykloje “Extreme Light Infrastructure Summer School ELISS 2019” (Dolní Břežany, Čekijos respublika).
- 2018 m
- “ISLiST-2018 Full International Student Grant” (Universidad Internacional Menéndez Pelayo, Ispanija) dalyvavimui tarptautinėje mokykloje “International School on Light Sciences and Technologies” (Santander, Ispanija).
- 2017 m
- “ISLiST-2017 Full International Student Grant” (Universidad Internacional Menéndez Pelayo, Ispanija) dalyvavimui tarptautinėje mokykloje “International School on Light Sciences and Technologies” (Santander, Ispanija).

III. LIST OF PUBLICATIONS

III.1. Publications Related to the Dissertation

- **Vidmantas Jašinskas**, Mindaugas Gedvilas, Gediminas Račiukaitis, and Vidmantas Gulbinas, *"Background-free electric field-induced second harmonic generation with interdigitated combs of electrodes"*, Opt. Lett. **41**, 2759-2762 (2016). DOI: [10.1364/OL.41.002759](https://doi.org/10.1364/OL.41.002759)
- Angela Eckstein, Valentas Bertašius, **Vidmantas Jašinskas**, Imge Namal, Tobias Hertel and Vidmantas Gulbinas. *"Carrier photogeneration, drift and recombination in a semiconducting carbon nanotube network"*, Nanoscale, 2017, 9, 12441. DOI: [10.1039/C7NR03813E](https://doi.org/10.1039/C7NR03813E)

- **Vidmantas Jašinskas**, Florian Oberndorfer, Vidas Pakštas, Tobias Hertel, and Vidmantas Gulbinas. "*Direct tracking of ultrafast carrier motion dynamics in semiconducting single-wall carbon nanotubes*", The Journal of Physical Chemistry C, 2018, 122 (28), 16424-16430. DOI: [10.1021/acs.jpcc.8b04672](https://doi.org/10.1021/acs.jpcc.8b04672)
- **Vidmantas Jašinskas**, Florian Oberndorfer, Tobias Hertel, and Vidmantas Gulbinas. "*Electronic and ionic electric field screening and persistent built-in electric field in carbon nanotube/PCBM films*", Phys. Status Solidi (a), 2020, 1900673. DOI: [10.1002/pssa.201900673](https://doi.org/10.1002/pssa.201900673)

III.2. Other Publications

- Rokas Jasiūnas, Rokas Gegevičius, Marius Franckevičius, **Vidmantas Jašinskas**, and Vidmantas Gulbinas. "*Energy barriers restrict charge carrier motion in MAPI perovskite films*", Adv. Optical Mater., 2020, 2000036. DOI: [10.1002/adom.202000036](https://doi.org/10.1002/adom.202000036)

III.3. Conference Presentations

INTERNATIONAL CONFERENCES

- **Vidmantas Jašinskas**, Mindaugas Gedvilas, Gediminas Račiukaitis, Vidmantas Gulbinas. "*Background-free electric field-induced second harmonic generation with interdigitated combs of electrodes*", International conference – school "Advanced materials and Technologies". Palanga, Lithuania, 2016.

- **Vidmantas Jašinskas**, Florian Oberndorfer, Tobias Hertel and Vidmantas Gulbinas. “*Persistent built-in photoactivity of single-wall carbon nanotube films*”, 13th International Conference on Optical Probes of Organic and Hybrid Optoelectronic Materials and Applications OP2019. Vilnius, Lithuania, 2019.

LOCAL CONFERENCES

- **Vidmantas Jašinskas**, Mindaugas Gedvilas, Gediminas Račiukaitis, Vidmantas Gulbinas. „*Second harmonic generation in polymers induced by periodic electric field*”, 6th Conference of PhD Students and Young Researchers FizTeCh2016. Vilnius, Lithuania, 2016.
- **Vidmantas Jašinskas**, Valentas Bertašius, Angela Eckstein, Imge Namal, Tobias Hertel, Vidmantas Gulbinas. “*Carrier photogeneration, drift and recombination in a semiconducting carbon nanotube network*”, Lietuvos Nacionalinė Fizikos Konferencija LNFK42. Vilnius, Lithuania, 2017.
- **Vidmantas Jašinskas**, Valentas Bertašius, Angela Eckstein, Imge Namal, Tobias Hertel, Vidmantas Gulbinas. “*Carrier photogeneration, drift and recombination in a semiconducting carbon nanotube network*”, 7th Conference of PhD Students and Young Researchers FizTeCh2017”. Vilnius, Lithuania, 2017.
- **Vidmantas Jašinskas**, Florian Oberndorfer, Tobias Hertel, Vidmantas Gulbinas. „*Ilgai išliekantis indukuotas elektrinis laukas anglies nanovamzdelių sluoksniuose*“, 8th Conference of PhD Students and Young Researchers FizTeCh2018. Vilnius, Lithuania, 2018.

IV. Copies of the Publications

1

Background-free electric field-induced second harmonic generation with interdigitated combs of electrodes

Vidmantas Jašinskas, Mindaugas Gedvilas, Gediminas Račiukaitis,
and Vidmantas Gulbinas

Background-free electric field-induced second harmonic generation with interdigitated combs of electrodes

VIDMANTAS JAŠINSKAS, MINDAUGAS GEDVILAS, GEDIMINAS RAČIUKAITIS,
VIDMANTAS GULBINAS*

Center for physical sciences and technology, Savanoriu Ave. 231, LT-02300 Vilnius, Lithuania
*Corresponding author: vidmantas.gulbinas@ftmc.lt

Received XX Month XXXX; revised XX Month, XXXX; accepted XX Month XXXX; posted XX Month XXXX (Doc. ID XXXXX); published XX Month XXXX

The electric field-induced second harmonic (EFISH) generation is a powerful tool for the investigation of optical nonlinearities, material polarization, internal electric fields and other properties of photonic materials and devices. A conventional generation of the second harmonics (SH) in materials with the disturbed centrosymmetry causes a field-independent background to EFISH and limits its applications. Here we suggest and analyze the application of the interdigitated combs of electrodes for the EFISH generation in thin films. Interdigitated electrodes form an optical transmission amplitude diffraction grating. Phase matching of the EFISH radiation creates unusual diffraction fringes with the zero intensity along the zeroth order direction, and with the diffraction angles different from diffraction angles of incident fundamental laser radiation and its second harmonics. It enables a simple geometrical separation of the EFISH signal from a conventional SH background, simplifies the sample preparation and provides additional experimental possibilities. We demonstrate applicability of the suggested technique for characterization of submicrometer thickness organic films of transparent and resonantly interacting polymers and of their mixtures.

OCIS codes: (190.2620) Harmonic generation and mixing; (230.1950) Diffraction gratings; (160.2100) Electro-optical materials; (240.310) Thin films.

DOI:

The electric field-induced second harmonic (EFISH) generation is recognized as an important technique for the investigation of molecular hyperpolarizability and nonlinear optical properties of materials [1, 2]. In addition to those conventional applications, the EFISH generation effect has been recently successfully applied to the investigation of the internal electric field distribution and its dynamics in field-effect transistors [3], light emitting diodes [4]

and solar cells [5]. In combination with ultrafast spectroscopy methods it enabled the investigation of ultrafast charge carrier dynamics in organic materials and photoelectric devices [6-8].

Theory of the harmonics generation was developed as soon as the laser was created [9, 10]. There are five well known mechanisms of the second harmonic (SH) generation based on: electric dipole, magnetic dipole, electric quadrupole as well as magnetic dipole and electric dipole couplings [10]. The last four of them are applicable to centrosymmetric materials, but these couplings are very weak and consequently the SH generation efficiencies are very low in comparison with the electric dipole mechanism [11, 12]. However, the electric dipole mechanism requires the medium to be non-centrosymmetric. The EFISH generation technique fulfills this condition even for centrosymmetric materials. When acted upon by a static electric field, naturally the isotropic medium polarizes along the direction of the applied field and loses the centrosymmetry [11].

Usual experimental realizations for EFISH measurements use special cells for liquids [13] and gases [14]. "Sandwiched" samples in a form of thin layers between semitransparent electrodes are widely used for the investigation of solids by the EFISH technique [4, 5]. If one of the electrodes is a nontransparent metal, the EFISH measurements are performed in the reflection mode. These experimental realizations of the EFISH measurements in thin films are not optimal. If the incoming laser beam is perpendicular to the sample surface, electric field vectors of the laser radiation and of the applied external voltage are perpendicular, thus the EFISH generation in isotropic materials is not possible. Therefore, the P-polarized light beam propagating at a small angle to the film surface is usually used. However, a refractive index of the investigated material reduces the angle of refraction and only a small projection of the electric field of light to the normal to a surface contributes to the EFISH generation. Another problem of the thin film investigation is a rather complicated and time consuming fabrication of multilayered samples. It practically precludes fast characterization of materials. In the case of very thin, monolayer Langmuir-Blodgett or self-assembled films, formation of top electrodes becomes a complex, often insolvable

problem. The application of the EFISH technique becomes very difficult or impossible if the films are polycrystalline or at least partly ordered causing the conventional, often much stronger SH generation.

Here we introduce an EFISH realization scheme, based on the application of interdigitated combs of electrodes, and analyze its properties. This technique solves the above mentioned problems and additionally provides several completely new experimental possibilities. A similar electrode comb has been used by Yang et al. to manipulate a diffraction pattern by using the linear electro-optic effect [15, 16]. Here we demonstrate an unusual angular distribution of the EFISH light, which is advantageous to investigations and may be also of interest in some nonlinear optical or light control applications. The theoretical description of the EFISH generation with combs of electrodes is introduced in the work and it is in good agreement with the experimental results.

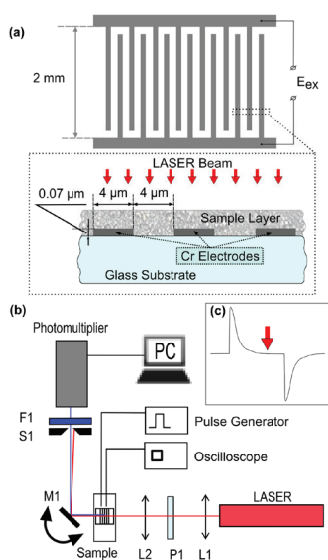


Fig. 1. (a) Interdigitated combs of electrodes (schematic sketch of the top-view and of the side-view, E_{ex} – external electric field), (b) Experimental setup (L1, L2 – lenses, P1 – half-wave plate for polarization rotation, M1 – adjustable mirror, S1 – slit, F1 – short-pass filter ($\lambda = 400$ nm)), (c) arrangement of synchronization of laser (arrow) and electric pulses.

The combs of electrodes were fabricated by the direct laser ablation technique from the thin chromium layer deposited on a transparent glass plate. This technique enables fabrication of combs with electrodes and interelectrode distances as narrow as about 1 μm. Slightly finer electrodes, if necessary, may be

fabricated by using nanolithography processing techniques. A schematic view of the electrodes comb is shown in Fig. 1(a).

The electrode widths and gaps between electrodes were equal to 4 μm and the electrode length was 2 mm. Their height measured with a profilometer was about 70 nm. The electrodes behave as a binary transmission amplitude diffraction grating for the incident laser radiation. Typical capacitance of the samples was about 100 pF.

The organic films were prepared by casting drops of mixtures of organic materials on the electrodes or by spin – coating technique. The film thickness was measured with a profilometer. We have tested a wide range of organic materials. Here we present experimental results with the highest achieved intensities of EFISH, which were obtained by using well known materials – poly[2-methoxy-5-(2-ethylhexyloxy)-1,4-phenylenevinylene] (MEH-PPV, from Sigma-Aldrich) and polystyrene ($M_p \sim 200000$, from Fluka). Chloroform (99.0 – 99.4 %, from Sigma-Aldrich) was used as a solvent. Mixtures were prepared by dissolving 10 mg of polymer in 1 ml of chloroform.

The experimental setup for the EFISH investigation is presented in Fig. 1(b). It consists of the femtosecond laser system Quamtronic Integra-C (femtosecond regenerative multi-pass Ti:Sapphire amplifier), optical elements (filters, lenses, etc.), the electrical pulse generation and detection system based on a photomultiplier. The laser produced 800 nm wavelength light pulses of about 130 fs duration at the 1 kHz repetition rate.

The EFISH generation in the MEH-PPV film of about 700 nm thickness was very weak when it was measured in the direction of the directly propagating fundamental laser radiation beam. We have changed the detection direction by precisely turning the angle of the mirror M1 as shown in Fig. 1(b). The EFISH signal was also very weak or absent in angular positions of the diffracted fundamental laser radiation and of its SH, generated with an additional crystal positioned before our sample or by the nonideally centrosymmetric sample. However, at certain angular positions the EFISH signal was much stronger. Fig. 2 shows this angular distribution.

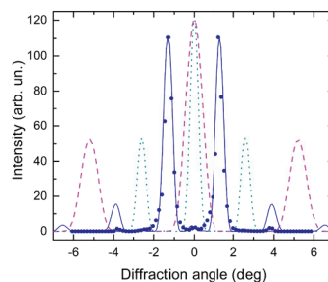


Fig. 2. (Color online) Angular dependences of the intensity of the EFISH radiation: experimentally measured data (points); calculated by using Eq. (4) (solid blue line). Calculated Fraunhofer diffraction of light from interdigitated electrodes grating: fundamental harmonic (dashed magenta line); SH (dotted green line).

Indeed the EFISH radiation has only a very weak intensity in the direction of the directly propagating beam (0th order maximum), but it has two strong maxima situated between the 0th and 1st order conventional SH maxima and two weak maxima between the 1st order maxima of the fundamental and the SH beams. This unusual angular distribution may be explained by considering phase relationships of EFISH electromagnetic waves generated in neighboring grating gaps (the gaps between electrodes).

In the case of the electric dipole approximation, the nonlinear polarization creating the EFISH signal can be stated as: [17]

$$P_z^{EFISH} = \sum_{jkl} \chi_{zjkl}^{(3)}(2\omega, 0, \omega, \omega) E_j(0) E_k(\omega) E_l(\omega) \quad (1)$$

where $\chi_{zjkl}^{(3)}(2\omega, 0, \omega, \omega)$ is the nonlinear optical susceptibility tensor, E is the electric field strength, ω is the angular frequency of the electric field.

For the linearly polarized light with the electric field vector perpendicular to the electrodes and parallel to the external electric field, when tensor components $j = k = l = z$, the electric field strength for the electromagnetic wave can be expressed as:

$$E_z = E_0 \exp(i(kr - \omega t)).$$

For centrosymmetric materials all the other susceptibility components except for $\chi_{zzz}^{(3)}$ should be equal to zero. Taking into account that the direction of the applied electric field in the neighboring gaps between electrodes is opposite, the external electric field may be expressed as:

$$E_z(0, n) = (-1)^n E_z(0), \text{ where } n = 1, 2, 3, \dots \text{ is a gap number.}$$

Consequently:

$$P_z^{EFISH}(\omega, n) = \chi_{zzz}^{(3)}(2\omega, 0, \omega, \omega) (-1)^n E_z(0) E_0^2 e^{i(2kr - 2\omega t)} \quad (2)$$

Replacing $(-1)^n = \exp(i\pi n)$ we obtain

$$P_z^{EFISH}(\omega, n) = P_{0,z} \exp(i(2kr - 2\omega t + \pi n)) \quad (3)$$

where P_0 is the polarization amplitude. Accordingly, this oscillating polarization creates the EFISH electric field with the amplitude E_0^{EFISH} and with the phases differing in neighboring gaps by π .

Consequently the EFISH radiation from all the gaps interferes destructively in the directly propagating beam direction (0th diffraction order) because of the equal amount of the waves with opposite phases, while the constructive interference appears and creates the EFISH maxima in the middle between the diffraction maxima of the SH light.

According to the diffraction model of two subgratings, developed by Yang et al. [15, 16], the far-field intensity distribution created by this process can be expressed as follows:

$$I(\Theta) = \left(\frac{\sin(0.5 \cdot ka \sin \Theta)}{0.5 \cdot ka \sin \Theta} \right)^2 \left(\frac{\sin(mk(a+b) \sin \Theta)}{\sin(k(a+b) \sin \Theta)} \right)^2 \quad (4)$$

$$\times \left(\cos \left(k(a+b) \cos \frac{\Theta}{2} \sin \frac{\Theta}{2} + \frac{\pi}{2} \right) \right)^2$$

where k is the wave number of the EFISH, a is the width of one gap of the grating, b is the width of one electrode, m is the number of the EFISH generating gaps, Θ is the diffraction angle measured from the normal of the grating surface. This expression

correctly reproduced positions of the angular maxima of the EFISH radiation, but their widths were narrower.

We have also simulated the angular dependence of the fundamental, SH and EFISH signal by using the freely available finite-difference time-domain simulation software OptiFDTD from Optiwave Systems Inc. For the EFISH calculation, we artificially constructed a phase shift by π between electromagnetic waves originating from the neighboring grating gaps, as follows from Eq. (3). Modelling results are presented in Fig. 2. Simulations perfectly reproduce positions and widths of the major EFISH maxima confirming the validity of the used approach. On the other hand, both experimentally measured and simulated angular dependences show a weak 0th order diffraction maximum, which, according to the theoretical description, should be absent, while the measured and calculated second order EFISH maxima have very different intensities. The 0th order maximum apparently appears because of a non-ideal diffraction grating; the gap widths and shapes are not ideally uniform, therefore the destructive interference is not perfect. The signal in the calculated pattern appears because of the limited number of gaps used for calculations. Lower experimentally obtained intensities of the 2nd order EFISH peaks are also apparently caused by deviation of the experimentally used grating from the ideal grating used in the calculations; non-ideal experimental grating is closer to the sinusoidal amplitude grating, which gives no second order peaks.

In order to get more information about properties of the EFISH generation with the interdigitated combs of electrodes we investigated dependences of the EFISH intensity on the sample parameters and experimental conditions. We chose MEH-PPV and Polystyrene polymers and their mixtures at different stoichiometric ratios as model materials. The investigation results are presented in Fig. 3.

As expected, the intensity of the EFISH signal in all investigated materials is proportional to the square of the fundamental light intensity (not presented). The EFISH signal in pure materials is also proportional to the square of the applied electric field strength (Fig. 3(a)).

However, in mixtures with the low MEH-PPV concentration the EFISH signal shows a stronger field-dependence (experimental points deviate from the line showing square dependence) with the power index of about 2.3-2.5. The stronger field-dependences show that some additional field-dependent process takes place. The field-assisted charge carrier photogeneration, which is quite efficient in MEH-PPV [18], is the most relevant process. The charge carrier accumulation in MEH-PPV chains isolated by the nonconductive polystyrene matrix may additionally enhance their role. In pure polystyrene, charge carriers cannot be generated, while from pure MEH-PPV they are easily extracted.

The EFISH intensity strongly depends on the stoichiometric ratio of the film formed on combs. Even a small amount of MEH-PPV (9%) increases the EFISH signal about 100 times. With a further increase in the MEH-PPV concentration, the EFISH intensity strongly increases and partly saturates after reaching about 30%. Polystyrene is transparent for both the fundamental laser radiation and its SH, consequently the light-matter interaction is nonresonant, therefore the EFISH signal is weak. Since MEH-PPV has an absorption band in the 400-600 nm region, therefore the EFISH interaction with MEH-PPV is resonant and much stronger. The EFISH intensity is expected to be quadratic versus concentration of resonantly interacting

molecules [13]. Indeed, the quadratic dependence up to about 30% of the MEH-PPV concentration is observed (line in Fig. 3(b)). Deviation from the quadratic dependence at higher concentrations most probably appears because of absorption of the EFISH light by MEH-PPV.

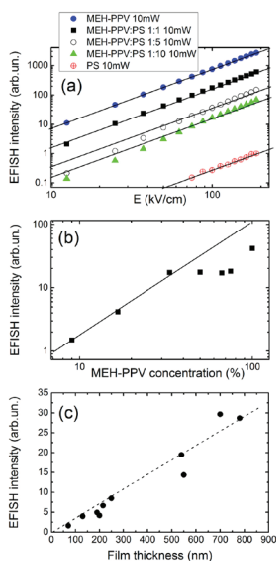


Fig. 3. (a) EFISH intensity dependence on the external electric field strength E for different polymeric films (lines show square dependences). (b) EFISH intensity dependence on the MEH-PPV weight concentration in the MEH-PPV:PS mixture (line shows square dependence). (c) EFISH intensity dependence on the polymer layer thickness (line is guide for eyes).

Figure 3(c) shows the dependence of the EFISH intensity on the thickness of MEH-PPV:PS film with the 1:10 stoichiometric ratio. The EFISH intensity increased approximately linearly with the film thickness. At low film thickness and low dye concentration we expected a quadratic dependence. However, several factors may cause deviation from this dependence: the EFISH light absorption, inhomogeneous electric field distribution, and finally the Maker fringe pattern [13] in thick layers.

In conclusion, the presented experimental data demonstrate the potential of the EFISH generation with interdigitated combs of electrodes as a convenient tool for the characterization of nonlinear optical and other properties of thin molecular films. The EFISH radiation creates an unusual angular interference pattern with the zero intensity in the direction of the directly propagating excitation beam and with maxima in the positions different from diffraction angles of both the fundamental and SH radiation. This unusual angular dependence enables background-free EFISH

measurements, easy separation of the EFISH signal from the ordinary SH generation in non-perfectly centrosymmetric, polycrystalline etc. materials. These properties may also be important to some applications in the light control or other areas of nonlinear optics.

Although manufacturing of the electrode arrays requires high precision technologies, the preparation of samples on already manufactured arrays becomes easy and fast. It is enough to form a thin layer of material on the electrode arrays. This technique is particularly convenient for the solution processed films, which may be formed by using spin coating, dip coating or doctor blade techniques. The comb electrodes may be reused if the organic film can be washed off. It solves the top electrode problem enabling the application of the EFISH technique to monolayer or other ultrathin films. This scheme enables a simple changing of the angle between the light polarization and the external electric field if other polarizability tensor elements are addressed. Moreover, this scheme provides possibilities of additional experimental realizations, which are not possible in "sandwich" samples. For example, molecular films may be oriented parallel or perpendicular to the comb of electrodes using conventional orientation techniques, which would enable the investigation of orientation dependent optical properties and processes.

REFERENCES

- Ch. Bosshard, G. Knöpfle, P. Pretre, and P. Günter. *J. Appl. Phys.* 71, 1594 (1992).
- J. W. Perry. *Nonlinear Optical-Properties of Molecules and Materials, in Materials for Nonlinear Optics*, (edited by S. R. Marder, E. J. Sohn, and G. D. Stucky), American Chemical Society, Washington, D.C., p. 67. (1991).
- T. Manaka, E. Lim, R. Tamura, M. Iwamoto. *Nature Photonics* 1, 581 (2007).
- D. Taguchi, Le Zhang, Jun Li, M. Weis, T. Manaka, M. Iwamoto. *J. Phys. Chem. C*, 114, 15136 (2010).
- D. Taguchi, T. Shino, Le Zhang, Jun Li, M. Weis, T. Manaka, M. Iwamoto. *Appl. Phys. Express* 4, 021602 (2011).
- Y. D. Glinka, T.V. Shahbazyan, I. E. Perakis, N. H. Tolk, X. Liu, Y. Sasaki, and J. K. Furdyna. *Appl. Phys. Lett.* 81, 3717 (2002).
- A. Devižis, A. Serbenta, K. Meerholz, D. Hertel and V. Gulbinas. *Phys. Rev. Lett.* 103, 027404 (2009).
- D. Amarasinghe Vithanage, A. Devižis, V. Abramavičius, Y. Infahsaeng, D. Abramavičius, R.C.I. MacKenzie, P.E. Keivanidis, A. Yartsev, D. Hertel, J. Nelson, V. Sundstrom, V. Gulbinas. *Nature Communications* 4, 2334, (2013).
- E. Adler. *Phys. Rev.* 134, A728 (1964).
- H. Hoshi, T. Yamada, K. Ishikawa, H. Takezoe, A. Fukuda. *Phys. Rev. B* 52, 12355 (1995).
- S. Kielich. *IEEE J. Quantum Electronics* 5, 562 (1969).
- T. Manaka, Cheng-Qun Li, Xiao-Man Cheng, M. Iwamoto. *J. Chem. Phys.* 120, 7725 (2004).
- S. Liu, R. Glaser, P. Sharp, John F. Kauffman. *J. Phys. Chem. A* 101, 7176 (1997).
- R.S. Finn, J.F. Ward. *Phys. Rev. Lett.* 26, 285 (1971).
- X. Yang, L. T. Wood, J. H. Miller. *Appl. Opt.* 40 (31), 5583 (2001).
- X. Yang, M. Aspelmeyer, L. T. Wood, J. H. Miller. *Appl. Opt.* 41(28), 5845 (2002).
- A. Alejo-Molina, K. Hingerl, H. Hardhienata. *J. Opt. Soc. Am B* 32, 562 (2015).
- M. G. Harrison, J. Grüner, and G. C. W. Spencer. *Phys. Rev. B* 55, 7831 (1997).

2

**Carrier photogeneration, drift and recombination in
a semiconducting carbon nanotube network**

Angela Eckstein, Valentas Bertašius, Vidmantas Jašinskas, Imge Namal,
Tobias Hertel, and Vidmantas Gulbinas

Cite this: *Nanoscale*, 2017, 9, 12441

Carrier photogeneration, drift and recombination in a semiconducting carbon nanotube network

A. Eckstein,^a V. Bertašius,^a V. Jašinskas,^a I. Namal,^b T. Hertel^b and V. Gulbinas^{id}*^{a,c}

Charge carrier photogeneration, drift and recombination in thin film networks of polymer-wrapped (6,5)-single-wall carbon nanotubes (SWNTs) blended with phenyl-C61-butyric acid methyl ester (PCBM) have been investigated by using transient photocurrent and time-delayed collection field (TDCF) techniques. Three distinct transient photocurrent components on the nano- and microsecond timescales have been identified. We attribute the dominant (>50% of total extracted charge) ultrashort photocurrent component with a decay time below our experimental time-resolution of 2 ns to the intratube hole motion. The second component on the few microsecond timescale is attributed to the intertube hole transfer, while the slowest component is assigned to the electron drift within the PCBM phase. The hole drift distance appears to be limited by gaps in the nanotube percolation network rather than by hole trapping or recombination. Photocurrent saturation was observed when excitation densities reached more than one charge pair per nanotube; we attribute this to the local electric field screening.

Received 29th May 2017,
Accepted 25th July 2017
DOI: 10.1039/c7nr03813e
rsc.li/nanoscale

Introduction

Their intriguing geometric structure and variety as well as the associated tunability of the electronic properties of single-wall carbon nanotubes (SWNTs) continue to draw interest for their potential use in micro- or nanoelectronics,^{1,2} energy storage,³ or photovoltaics.^{4–7} The fact that SWNTs, depending on the diameter and chirality, may be either metallic or semiconducting is of particular interest to most technological applications. For example, thin film networks of metallic SWNTs were tested for their use as large area transparent conducting layers in organic solar cells⁸ or for electromagnetic shielding.⁹ Furthermore, semiconducting nanotubes have potential to be used as photoactive materials in solar cells or light detectors.⁷ The photoresponse in the infrared (IR) spectral region also makes SWNTs particularly well suited for IR or photothermal detectors^{10,11} and for near-IR light harvesting in solar cells.¹² SWNTs were also tested in organic solar cells to enhance the charge transport,¹³ both as electron acceptors in blends with conjugated polymers^{6,14} and as electron donors in heterojunctions with fullerene derivatives.^{15,16}

The photoconductivity of SWNTs is the key for the performance of SWNT-based optoelectronic devices and it has pre-

viously been investigated by photoelectrical and purely optical methods.^{4,17–19} In one such example, Fujiwara *et al.* reported the photoconductivity of SWNT bundles positioned in-between electrodes separated by 10 μm.¹⁷ The transient photocurrent was observed as a short (<5 ns) peak with unusual temperature dependence and a 10–1000 fold increase of the photoresponse at 13 K. However, the mechanism of the photoresponse remained unclear. Freitag *et al.* observed the photoconductivity of a single carbon nanotube forming a channel of a field-effect transistor.²¹ Lu *et al.* observed the electron transfer from the excited SWNT films to platinum electrodes over distances of several millimetres.¹⁸ They demonstrated that molecular desorption from SWNTs increased the photocurrent and adsorbed molecules were, thus, suggested to act as recombination centres rather than generation centres. They observed that the optical heating of SWNTs increased the photocurrent in contrast to earlier reports,¹⁷ possibly because the authors investigated a slow rather than a fast photocurrent response. Beard *et al.* found that the free carrier yield in SWCNT films did not depend on the excitation energy, and that carrier-dynamics did not depend on the excitation wavelength and the nanotube type (metallic or semiconducting).²² However, later two different photocurrent mechanisms in metallic and semiconducting CNTs have been identified. In metallic CNTs the response was shown to have a photothermoelectric origin due to the gradients in the nanotube Seebeck coefficient near the contacts.^{4,23} In semiconducting CNTs the photovoltaic effect dominates when the photocurrent arises from the electric field.²³

Time-resolved microwave conductivity (TRMC) investigations have recently demonstrated spontaneous carrier photo-

^aCenter for Physical Sciences and Technology, Saulėtekio av. 3, LT-10257 Vilnius, Lithuania. E-mail: vidmantas.gulbinas@ftmc.lt

^bUniversity of Würzburg, Physical Chemistry Department, Am Hubland, 97074 Würzburg, Germany

^cDepartment of General Physics and Spectroscopy, Vilnius University, Saulėtekio 9-III, LT-10222 Vilnius, Lithuania

generation in the suspensions of SWNTs,¹⁹ and at the heterojunctions of SWNTs and fullerene layers.^{24–26} The carrier generation at the heterojunction was attributed to the electron transfer from the excited SWNTs to fullerenes. The photoconductivity signal decayed on a timescale of hundreds of ns. Purely optical transient absorption investigations also revealed spontaneous carrier generation in (6,5) semiconducting SWNTs,²⁰ however, the observed carrier recombination was much faster on a sub-nanosecond timescale. It remains unclear whether both studies probed different processes or the experimental conditions were too different to allow a detailed comparison.

Although these investigations revealed important properties of carrier generation and motion in SWNTs, this information obtained from different samples and different investigation techniques is still insufficient to draw a general photoconductivity picture. In this work, we used conventional transient and steady state photocurrent measurements as well as a time-delayed collection field technique to investigate the charge carrier generation, motion and recombination processes in layers of bundles of (6,5) SWNTs mixed with phenyl-C61-butylric acid methyl ester (PCBM) deposited on interdigitated electrode arrays. PCBM, which is a strong electron acceptor, was demonstrated to facilitate the charge carrier generation by accepting electrons from photoexcited carbon nanotubes. We demonstrate that the photocurrent is composed of very short-lived nanosecond- and longer microsecond components, which we attribute to intratube and intertube hole motions, respectively, the latter being limited at high excitation intensity by the local electric field screening.

Experimental results

Absorption

Fig. 1 shows the absorption spectra of the samples with different PCBM/SWNT mass ratios. Absorption at 1000 nm and

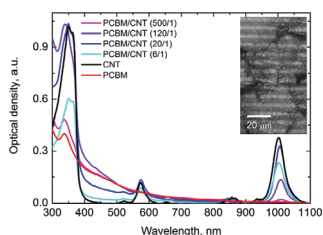


Fig. 1 Absorption spectra of films on the electrode comb with different PCBM to SWNT mass ratios. The comb absorbance was compensated. The insert shows a microscopy view of the PCBM/SWNT(120/1) film with the 120/1 PCBM to SWNT mass ratio. Horizontal lines here show electrodes and gaps between electrodes, while the random dark regions indicate an inhomogeneous distribution of carbon nanotubes.

580 nm corresponds to the two low energy dipole-allowed exciton transitions in (6,5)-SWNTs. The absorbance between 400 nm and 500 nm in samples with high PCBM concentrations is mostly due to PCBM, while both PCBM and (6,5)-SWNTs absorb at 300–400 nm. An observed 7 nm red-shift of the SWNT exciton band in the blends may be due to the increased dielectric screening in SWNTs by PCBM molecules nearby.²⁴

Steady state and transient photoconductivity

For the initial characterization of the photoconductivity properties of the films, we have measured steady-state and transient photocurrents in samples with different PCBM to SWNT mass-ratios. For steady-state measurements, samples were illuminated with an incandescent halogen lamp with band-pass filters serving to select specific excitation wavelength ranges. A sizable photocurrent was observed only under excitation at SWNT bands, while the photocurrent was absent or very low under excitation in-between SWNT exciton bands at about 450 nm and 700 nm. This suggests that the excitation of PCBM produces no or only a very weak photocurrent. For further steady-state investigations and for better comparison of their results with the transient photocurrent measurements performed under 532 nm laser excitation, we thus illuminated samples with a LED in the 520–530 nm range, at the vibronic band of the second electronic transition.

Fig. 2 shows the dependence of the steady state photocurrent on the PCBM/SWNT mass ratio for the excitation intensity of $300 \mu\text{W cm}^{-2}$. The absorbance of samples at the excitation wavelength decreased with the PCBM/SWNT mass ratio, and therefore the photocurrent shown in Fig. 2 is normalized to the absorbed light intensity. The normalized photocurrent was very low in a pure SWNT sample. It increased with the PCBM content, but started to decrease again at a PCBM/SWNT mass ratio exceeding 100.

Pulsed excitation of our samples with 532 nm sub-nanosecond laser pulses at the 5 Hz repetition rate created short

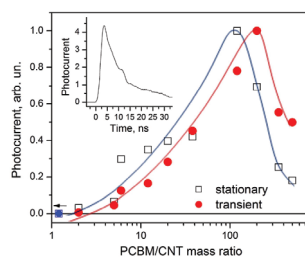


Fig. 2 Dependence of the steady state and transient photocurrent on the relative PCBM/SWNT mass ratio. Blue symbols show photocurrent values in the sample without PCBM. The insert shows typical transient photocurrent kinetics.

photocurrent pulses limited by the time-resolution of our setup (see the insert in Fig. 2) containing a very weak photocurrent tail lasting for tens of nanoseconds. An amplitude of the photocurrent pulse showed a similar dependence on the PCBM/SWNT mass ratio to that observed with the steady excitation. The only difference is the slight shift in the peak position. The non-monotonic photocurrent dependence on the PCBM content suggests that at least two competing processes determine the photocurrent intensity. The increase of the photocurrent with the PCBM content at low concentrations is simple to rationalize; PCBM molecules act as electron acceptors from excited SWNTs and facilitate the charge carrier generation.^{5,26} According to this interpretation the charge carrier generation efficiency is expected to saturate when carbon nanotubes are covered with a sufficient number of PCBM molecules to ensure an efficient electron capture. The small residual photocurrent in samples with no PCBM is probably created by impurities, defects or carrier transfer to metal contacts. The decrease of the photocurrent at a high PCBM content is most likely related to the increase in the dark-state resistance of the samples from ~ 8 k Ω of a pure SWNT film to ~ 200 k Ω of films with the highest PCBM content. This suggests that PCBM molecules covering SWNTs electrically isolate them from metal electrodes and possibly also one from another. A less significant decrease of the transient photocurrent at a high PCBM content (see Fig. 2) in comparison with the CW photocurrent is in line with this explanation; charge carriers moving inside the isolated SWNTs create a displacement photocurrent, which significantly contributes to the transient photoelectrical signal while it does not contribute to the steady-state photocurrent.

To further explore the photoconductivity properties of our samples, we have investigated the photocurrent kinetics using an integrating measurement regime. This regime enables the measurement of very weak photocurrents on long timescales and it has better time resolution. In this case, we used a 1 M Ω oscilloscope input instead of 50 Ω , and measured the voltage kinetics on an integrating capacitor formed by the sample and oscilloscope capacitances. The voltage was proportional to the charge extracted from the sample, while the photocurrent strength can be evaluated as a time derivative of the extracted charge transients. Fig. 3 shows the charge extraction kinetics from the samples with a different PCBM content. The observed charge extraction kinetics have three growth components: the initial ultrafast component shorter than the time resolution of our setup (≈ 2 ns) reveals the presence of the strong but short-lasting photocurrent, the second component present in all samples reveals the photocurrent lasting for several microseconds, while the longest, tens of microseconds component was observed only in samples with a high PCBM content. We attribute this to the electron drift *via* PCBM. PCBM at its high content is likely to form a continuous film enabling the electron drift, while at a low content, PCBM is likely in the form of isolated molecules, probably partly adsorbed to SWNTs, and it forms no continuous path for electrons. The estimation of the PCBM film thickness supports this attribution. The absor-

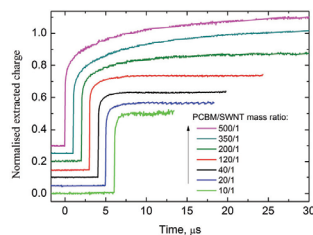


Fig. 3 Charge extraction kinetics from samples with different PCBM to SWNT mass ratios measured under excitation at 1064 nm with $16 \mu\text{J cm}^{-2}$ energy pulses under 2 V applied voltage. The curves are normalized to the equal intensity of the fast growth component and shifted both vertically and horizontally for clarity.

bance of the samples with the highest PCBM content is of about 0.15 OD at 450 nm, which translates to the PCBM layer thickness of about 20 nm. The same estimation for three films with the lowest PCBM content gives their thicknesses below 1 nm, thus insufficient for the continuous film formation. Electron extraction times are also in good agreement with the reported electron mobility values in PCBM ranging from $10^{-1} \text{ cm}^2 \text{ V}^{-1} \text{ s}^{-1}$ to $10^{-3} \text{ cm}^2 \text{ V}^{-1} \text{ s}^{-1}$.^{27–30} This gives the electron extraction time between 1 μs and 100 μs at the applied voltage of 2 V, which is in good agreement with the experimentally obtained slow charge extraction times of tens of μs . In the following we will not analyse the electron motion *via* PCBM in any further detail since it is not related to SWNTs.

The ultrafast and intermediate (several microseconds) photocurrent components are present in all samples, including those with no PCBM, thus they should be attributed to carriers moving inside the SWNT network. Fig. 4 shows the charge extraction kinetics of the PCBM/SWNT(120/1) sample measured under excitation at 1064 nm at different applied voltages (a) and at different excitation intensities (b). Since PCBM does not absorb at 1064 nm, we can unambiguously attribute the photocurrent to the excitation of carbon nanotubes at the low energy wing of the first sub-band exciton. We found that the extracted charge is proportional to the applied voltage, but the shape of the extraction kinetics within the experimental accuracy is independent of the applied voltage. The dependence of the charge extraction kinetics on the excitation intensity presented in Fig. 4b is more complex. The $1.25 \mu\text{J cm}^{-2}$ curve multiplied by 4 coincides with the $5 \mu\text{J cm}^{-2}$ curve, which shows that the extracted charge increases linearly with the excitation intensity and the shape of the charge extraction kinetics does not change up to about $5 \mu\text{J cm}^{-2}$. This suggests that carrier dynamics at low excitation densities is not affected by the nongeminate electron-hole recombination or other nonlinear processes. At higher intensities, the extracted charge starts to saturate. The intermediate component saturates completely starting with the $20 \mu\text{J cm}^{-2}$ intensity, while the ultrafast component does not reach complete saturation. The esti-

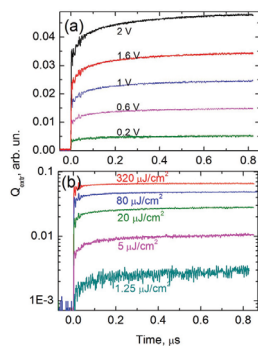


Fig. 4 Charge extraction kinetics from the PCBM/SWNT(120/1) sample measured under excitation at 1064 nm at different applied voltages (a) and at different excitation intensities (b).

mation based on the evaluation of the total SWNT number per square area unit of the film using the published SWNT photo-absorption cross-sections^{31,32} and absorbed photon density suggests that the saturation of the extracted charge starts at an excitation intensity creating approximately one charge pair per nanotube.

Time-delayed collection field (TDCF) measurements

TDCF investigations were done to separate the charge carrier generation and extraction phases as well as to investigate the carrier recombination dynamics. We applied an adjustable generation voltage during the optical sample excitation and after a tuneable delay time we switched on a collection voltage. Fig. 6 shows a typical TDCF carrier extraction transient measured in an integrating mode. Fig. 5 shows the dependence of the total extracted charge (determined from the plateau of the carrier extraction transients) on generation and collection voltages at a collection delay of 300 ns. The total extracted charge increases linearly with the collection voltage, which shows that the carrier extraction is the major factor determining the photocurrent dependence on the applied voltage. The extracted charge shows no saturation indicating that the used voltage was not nearly high enough to extract all photogenerated carriers. On the other hand, the extracted charge, except for some random scattering, was independent of the generation voltage when the collection voltage was maintained at 3 V. This unambiguously shows that the external electric field is not necessary and does not influence the carrier photogeneration, at least up to its strength of about 10^4 V cm⁻¹. This conclusion is in agreement with the conclusion on the spontaneous carrier generation in carbon nanotubes in solutions¹⁹ and at SWNT/fullerene interfaces.^{24–26}

Fig. 6a shows the time-delayed carrier extraction kinetics at different collection delay times. They resemble those obtained

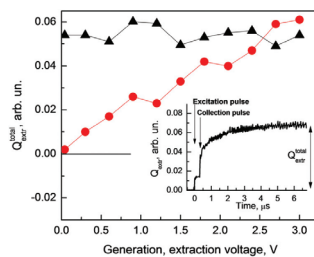


Fig. 5 Dependences of the total extracted charge from the sample PCBM/SWNT(120/1) by the collection voltage of 3 V delayed by 300 ns on the generation voltage (triangles) and on the extraction voltage when the generation voltage was 0 V (circles). The insert shows the TDCF charge extraction transient measured with 1 V generation and 3 V collection voltages.

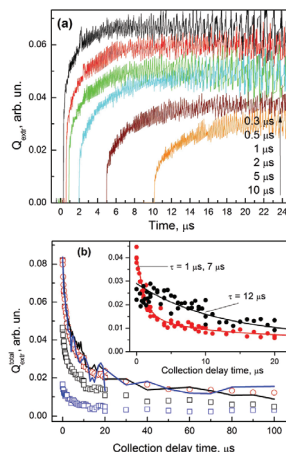


Fig. 6 (a) TDCF charge extraction kinetics at different delay times between optical excitation and electrical collection pulses measured in the PCBM/SWNT(120/1) sample at 0 V generation and 2 V extraction voltages. Zero time corresponds to the optical excitation pulse. (b) Dependence of the total TDCF extracted charge on the extraction delay time, measured in the PCBM/SWNT(120/1) sample at 0 V generation and 2 V extraction voltages at 320 $\mu\text{J cm}^{-2}$, 80 $\mu\text{J cm}^{-2}$ and 20 $\mu\text{J cm}^{-2}$ excitation intensities. Solid lines show normalised kinetics. The insert shows the same dependence for the ultrafast (red symbols) and slow (black symbols) extraction components. The lines in the insert are fits with exponential or biexponential decay functions.

under the steady state applied voltage (see Fig. 3), but the contribution of the ultrafast component is smaller and it decreases with the extraction delay time. The intermediate

component also becomes slower at longer delays. Variation of the carrier extraction kinetics with the collection delay time indicates that besides the decay in carrier density their mobility also decreases, which may be attributed to the carrier localization at low energy sites, typical of disordered materials.³³

Fig. 6b shows the dependence of the total extracted charge on the collection delay time at 0 V generation and 2 V collection voltages. It shows that the charge carrier concentration decreases rapidly during the first several microseconds, but almost stabilizes after several tens of microseconds. By normalising the delay dependence of the carrier extraction kinetics (solid lines in Fig. 6b) we see that their shape remained identical even when the excitation intensity increased by a factor of 16, indicating that the bimolecular charge carrier recombination did not play any important role.

The insert in Fig. 6b shows the dependence of charges extracted during the ultrafast and intermediate phases, which indicate that the concentration of charge carriers responsible for the ultrafast photocurrent phase decays much faster than the one responsible for the intermediate phase.

It should also be noted that the carrier density decay determined from TDCF measurements is much slower than the decay of the photoconductance of SWNT/PCBM systems determined by means of the time-resolved microwave conductivity (TRMC) technique,^{19,24,25} where it was found to be determined by the second order recombination.²⁵ This difference further supports the conclusion that the bimolecular carrier recombination in our systems is insignificant and the carrier decay is determined by the geminate charge pair recombination. Suppression of the bimolecular recombination is most probably related to the structure of our samples: SWNTs form a weakly percolated network, where the carrier migration between nanotubes is slow, the electron migration within the thin disordered PCBM film is also slow and therefore the recombination of non-geminate electrons and holes is inefficient.

Discussion

Our findings presented so far confirm that photocurrents in the polymer-wrapped SWNT/PCBM system are created by spontaneous electron transfer from photoexcited SWNTs to PCBM. We distinguish a fast carrier motion in the SWNT network and a slow one within the PCBM phase. However, the properties and motion peculiarities of the charge carriers inside the SWNT network required further analysis.

To this end, we next compared the charge extraction kinetics measured under the applied constant voltage by using the TDCF technique (Fig. 4a and 6b). TDCF kinetics is determined by the decay of the charge carrier concentration only, while the photocurrent at the constant applied voltage (derivative of the kinetics presented in Fig. 4a) is determined by the product of the carrier concentration and their mobility. Much faster charge extraction kinetics at the constant applied voltage than the TDCF kinetics indicates that the former is mainly determined by the decreasing carrier mobility.

In order to understand the mechanism of the carrier mobility decrease we again considered the spatial structure of our samples. As discussed before, SWNTs and their bundles may be considered as dispersed in the isolating PCBM matrix or air. Under these conditions, the drift distance of the photogenerated holes is limited by the SWNT length, or by dimensions of their bundles forming a percolated pathway. Carrier drifting inside such a SWNT network is expected to have different mobilities depending on the length scale. The mobility is high for the intratube hole motion,³⁴ but it may decrease significantly when carriers reach the ends of the tube where continued drift requires them to jump to another tube. However, this mobility decay mechanism is important only to the one-directional carrier drift, but plays no role in TRMC measurements where carriers move forth and back, or in TDCF investigations where charge carriers move only by diffusion during the delay time before the collection pulse.

The intratube hole drift is also expected to be complex. Charge carriers were suggested to be delocalized inside SWNTs, with the delocalization length of about 100 nm (ref. 35) limited by defects and impurities. Nanotube wrapping with the polymer may cause additional disorder, thus the delocalization length is expected to be shorter. The initial dynamics of carriers inside the delocalization region should be considered as an instantaneous polarization of the hole density distribution causing the displacement current, while carrier localization at low energy sites and jumps over barriers limit the intratube carrier mobility.³⁶ Thus, carrier motion within the SWNT network is also expected to show the following stages: instantaneous hole polarization followed by fast intratube drift and slow intertube jumps.

Very fast (<2 ns) initial carrier extraction and linear scaling of the ultrafast extraction component with the applied voltage suggest that it may happen due to displacement. Then, the photocurrent on the tens of ns timescale might be attributed to the intratube carrier drift limited by barriers and traps, while the photocurrent for several microseconds shall be assigned to the intertube hole motion. However, this assignment is questionable because of the large contribution of the ultrafast component to the total extracted charge. Even for a 100 nm carrier delocalization length, the field-induced displacement of the delocalised hole density distribution may be expected to be of tens of nanometers at most, which is about 100 times shorter than the carrier drift distance along the entire nanotube length. Thus, the contribution of the displacement current to the total extracted charge is expected to be of about 1% or less. It is more likely that the ultrafast carrier extraction phase accounts for the carrier drift inside the entire SWNT length. This drift may also be very fast. Literature data report up to thousands of $\text{cm}^2 \text{V}^{-1} \text{s}^{-1}$ charge carrier mobility within individual SWNTs.^{37–39} Taking into account the applied electric field strength and the SWNT length of several micrometres, the hole drift inside a single SWNT is expected to take place on a picosecond to several nanoseconds timescale. In this case, the intermediate carrier extraction phase at 10–1000

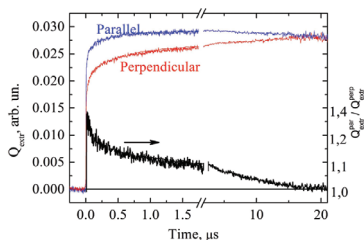


Fig. 7 Charge extraction kinetics from the PCBM/SWNT(120/1) sample under excitation by 1064 nm light polarised parallel and perpendicular to the applied electric field direction. The bottom curve shows their ratio.

ns is attributed to the intertube hole drift within the SWNT bundles. The intertube mobility in polymer wrapped SWNTs has recently been reported to be in the $1\text{--}10\text{ cm}^2\text{ V}^{-1}\text{ s}^{-1}$ range,⁴⁰ which gives intertube hole jump times of tens to hundreds of nanoseconds, in close agreement with this assignment. The weak photocurrent lasting for up to several microseconds is attributed to the hole drift at larger distances within a poorly percolated nanotube network.

This assertion is further supported by the excitation polarization investigations (see Fig. 7). A simple evaluation shows that the extracted charge related to the displacement current shall be about three times larger when the excitation polarization is parallel to the electric field direction than when it is perpendicular (in analogy with the fluorescence anisotropy). The relatively low initial difference between the charge values extracted under different excitation polarizations presented in Fig. 7 shows that holes have already moved to differently oriented nanotube segments during the ultrafast photocurrent phase. Subsequent polarization memory loss during the intermediate charge extraction phase is assigned to the intertube hole jumps.

According to this assignment, the majority of holes remain located on the same SWNTs where they were generated during the ultrafast photocurrent phase. A fraction of holes jump to neighbouring SWNTs creating photocurrent on a nanosecond to several microseconds timescale. Consequently, carrier decay with about $1\text{ }\mu\text{s}$ time constant revealed by TDCF measurements is attributed to the geminate recombination of holes that remain on the same SWNT where they were generated and electrons that are located on PCBM molecules adsorbed onto these SWNTs. At longer delay times, only holes transferred to different SWNTs survive and their recombination takes place for tens to hundreds of microseconds. Charge carrier generation and motion processes are summarized and illustrated schematically in Fig. 8.

Finally, we will briefly discuss the saturation of the extracted charge at high excitation intensities. It may be caused by two types of processes: the nonlinear charge carrier

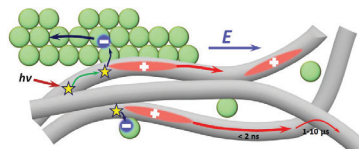


Fig. 8 Photoelectrical processes in the SWNT/PCBM system.

and/or exciton recombination or the electric field screening. The saturation can hardly be caused by the bimolecular carrier recombination because the recombination kinetics determined by using the TDCF technique is identical at excitation intensities differing up to 16 times. Exciton–exciton annihilation, which was shown to be very effective in SWNTs,⁴¹ would cause proportional saturation of both ultrafast and intermediate photocurrent components, which is not the case. Thus, although we cannot completely exclude these processes, their role in the photocurrent saturation is apparently not dominating.

The electric field screening is another common process limiting photocurrents in photoconducting organic layers. In homogeneous materials, space charges created by drifting carriers may screen the electric field in the bulk material and reduce the current. A significant field screening is expected when the photogenerated charge becomes comparable to the charge on electrodes, *i.e.* to the product of the sample capacitance and the applied voltage. In the integrating regime, it causes the voltage drop comparable to the applied voltage. In our samples the voltage drop was more than 10 times lower than the applied voltage even at the highest used excitation intensities, which excludes the total macroscopic field screening. However, the screening mechanism in our samples containing photoconducting SWNTs dispersed in the dielectric PCBM matrix may be more complex. In addition to the macroscopic screening, drifting charge carriers may screen the electric field locally inside individual SWNTs or their bundles when charge carriers accumulate at their edges. This mechanism may cause photocurrent saturation at lower extracted charge values in agreement with the photocurrent dependence on the excitation intensity presented in Fig. 4.

Experimental

SWNTs used for the sample preparation were purified from CoMoCAT type SWNT soot (99.9%, Sigma Aldrich) by means of wrapping with a poly[(9,9-dioctyl uorenyl-2,7-diyl)-*alt*-co(6,6-2,2-bipyridine)] (PFO-Bpy) polymer as described in ref. 40. Chlorobenzene suspensions with polymer-wrapped SWNTs were mixed with PCBM solutions of different concentrations. The resulting mixtures were drop-cast on interdigitated electrode arrays with a total area of 9.6 mm^2 formed by 150 nm

thick Pt electrodes of 5 μm width and 5 μm interelectrode distances. SWNTs in the films were aggregated into bundles forming an entangled-network pattern (the insert of Fig. 1). The PCBM to SWNT-polymer weight ratio x/y in different films is indicated using the designation PCBM/SWNT(x/y). x/y ratios were estimated from the film absorption spectra using published SWNT photo-absorption cross-sections.^{31,32}

The steady state photocurrent was measured using a Keithley 6487 picoammeter. A steady state voltage up to 5 V was applied to interdigitated comb electrodes forming the electric field between neighbouring electrodes. The field strength was position dependent; it was up to about 4 times larger close to electrodes than in the middle between electrodes. The samples were illuminated with a green photodiode with the light intensity of 300 $\mu\text{W cm}^{-2}$. The photocurrent was determined by subtracting the dark current from the current under illumination.

Transient photocurrent investigations were performed with an Agilent Technologies DS05054A oscilloscope and a function generator Tektronex AFG 3101 under the sample illumination with sub-nanosecond laser pulses at 532 nm or 1064 nm wavelength at the 5 Hz repetition rate. The transient photocurrent was measured in current-mode using the 50 Ω input of an oscilloscope and in the integrating regime using the 1 M Ω oscilloscope input when the sample and oscilloscope capacitances served as the integrating capacitor. The extracted charge is defined as: $Q_{\text{ext}}(t) = \int_0^t I(t') dt'$. The time resolution of the current measurements was about 10 ns, mainly determined by the oscilloscope input resistance and the sample capacitance, which depending on the PCBM/SWNT film composition ranged between 3 and 20 nF. The time resolution of the integrating regime of about 2 ns was limited by the non-perfect electrical circuit and was better than that of the current regime. A more convenient measurement of weak currents at long times is another advantage of the integrating regime; therefore it was the main technique used. The integrated kinetics were corrected for the limited recharging time of the integrating capacitor using the procedure described by Kettlitz *et al.*⁴² Otherwise, a decrease of the extracted charge values in tens of microseconds would be observed. In order to improve the accuracy and exclude the influence of some slow sample photomodification processes, data from several tens of laser pulses as well as from several cycles of variation of applied voltage were averaged.

Time-delayed collection field (TDCF) investigations were performed with the same experimental setup. An adjustable voltage was applied to the sample during the optical excitation (generation voltage) and after a tuneable delay time a collection voltage was switched on. Charge extraction kinetics was measured using an integrating measurement mode. The photocurrent in this case appears together with the dark current, and therefore the time-delayed charge extraction kinetics was evaluated as the difference between the charge extraction kinetics with and without the optical excitation. The data were averaged in a similar way to the case of transient photocurrent measurements.

Conclusions

We used a combination of steady state and transient photocurrents with the time-delayed-collection field technique for an investigation of the charge carrier generation, drift and recombination processes in the networks of polyfluorene-wrapped (6,5) SWNTs blended with PCBM, following their optical excitation. The charge carrier generation takes place spontaneously by the electron transfer from excited SWNTs to PCBM. The generated holes create a transient photocurrent in the SWNT network, which is controlled by the morphology of the network rather than by the carrier recombination or extraction. The transient photocurrent shows three characteristic decay regimes. An ultrafast phase, lasting for less than 2 ns, is attributed to the hole transfer within single SWNTs while the hole jumps between SWNTs take a few microseconds. The slowest photocurrent component is observed only at high PCBM concentrations and is attributed to the electron transfer *via* PCBM. Additionally, electrons and holes residing on the same nanotube recombine within about 1 μs . In contrast, carriers located on different SWNTs can survive for hundreds of microseconds.

The clear identification of several photocurrent phases in SWNT systems provides broader perspectives for their application in photoelectrical devices while giving new leads for the optimization of photocurrents. The ultrafast photocurrent component, which may be particularly useful in designing new ultrafast photodetectors may be further optimized by increasing nanotube lengths and by making networks with a higher degree of nanotube alignment orientation. Additional improvements might be achieved if SWNTs are better isolated from one another to prevent intertube carrier jumps. On the other hand, the improvement of the SWNT network percolation is a crucial requirement for the maximization of steady state photocurrents.

Acknowledgements

This research was partly financed by EC *via* the Marie Curie Actions project FP7 ITN "POCAONTAS", Project no.: 316633.

Notes and references

- 1 H. W. Ch. Postma, T. Teepen, Z. Yao, M. Grifoni and C. Dekker, *Science*, 2001, **293**, 76–79.
- 2 F. Bottacchi, L. Petti, F. Späth, I. Namal, G. Tröster, T. Hertel and T. D. Anthopoulos, *Appl. Phys. Lett.*, 2015, **106**, 193302.
- 3 L. Hu, H. Wu, F. La Mantia, Y. Yang and Y. Cui, *ACS Nano*, 2010, **4**, 5843–5848.
- 4 S. Nanot, A. W. Cubmmings, C. L. Pint, A. Ikeuchi, T. Akiho, K. Sueoka, R. H. Hauge, F. Leonard and J. Kono, *Sci. Rep.*, 2013, **3**, 1335.

- 5 C. Li, Y. Chen, Y. Wang, Z. Iqbal, M. Chhowalla and S. Mitra, *J. Mater. Chem.*, 2007, **17**, 2406–2411.
- 6 T. Schuettfort, A. Nish and R. J. Nicholas, *Nano Lett.*, 2009, **9**, 3871–3876.
- 7 M. S. Arnold, J. L. Blackburn, J. J. Crochet, S. K. Doorn, J. G. Dugue, A. Mohite and H. Telg, *Phys. Chem. Chem. Phys.*, 2013, **15**, 14896–14918.
- 8 M. W. Rowell, M. A. Topinka, M. D. McGehee, H.-J. Prall, G. Dennler, N. S. Sariciftci, L. Hu and G. Gruner, *Appl. Phys. Lett.*, 2006, **88**, 233506.
- 9 H. M. Kim, K. Kim, C. Y. Lee, J. Joo, S. J. Cho, H. S. Yoon, D. A. Pejakovi, J. W. Yoo and A. J. Epstein, *Appl. Phys. Lett.*, 2004, **84**, 589–591.
- 10 K. Erikson, X. He, A. A. Talin, B. Mills, R. H. Hauge, T. Iguchi, N. Fujimura, Y. Kawano, J. Kono and F. Léonard, Figure of Merit for Carbon Nanotube Photothermoelectric Detectors, *ACS Nano*, 2015, **9**(12), 11618–11627.
- 11 S. Liang, Z. Ma, G. Wu, N. Wei, L. Huang, H. Huang, H. Liu, S. Wang and L.-M. Peng, *ACS Nano*, 2016, **10**, 6963–6971.
- 12 D. J. Bindl, M.-Y. Wu, F. C. Prehn and M. S. Arnold, *Nano Lett.*, 2011, **11**, 455–460.
- 13 T. Y. Lee, P. S. Alegaonkar and J.-B. Yoo, *Thin Solid Films*, 2007, **515**, 5131–5135.
- 14 M. Lanzani, L. Paganin and D. Caretti, *Polym. J.*, 2008, **49**, 4942–4948.
- 15 D. J. Bindl, A. S. Brewer and M. S. Arnold, *Nano Res.*, 2011, **4**, 1174–1179.
- 16 M. J. Shea and M. S. Arnold, *Appl. Phys. Lett.*, 2013, **102**, 243101.
- 17 A. Fujiwara, Y. Matsuoka, H. Suematsu, N. Ogawa, K. Miyano, H. Kataura, Y. Maniwa, S. Suzuki and Y. Achiba, *Jpn. J. Appl. Phys.*, 2001, **40**, L1229–L1231.
- 18 S. Lu and B. Panchapakesan, *Nanotechnology*, 2006, **17**, 1843–1850.
- 19 J. Park, O. G. Reid, J. L. Blackburn and G. Rumbles, *Nat. Commun.*, 2015, **6**, 8809.
- 20 G. Soavi, F. Scotognella, D. Viola, T. Hefner, T. Hertel, G. Cerullo and G. Lanzani, *Sci. Rep.*, 2015, **5**, 9681.
- 21 M. Freitag, Y. Martin, J. A. Misewich, R. Martel and Ph. Avouris, *Nano Lett.*, 2003, **3**, 1067–1071.
- 22 M. C. Beard, J. L. Blackburn and M. J. Heben, *Nano Lett.*, 2008, **8**, 4238–4242.
- 23 M. Barkelid and V. Zwiller, *Nat. Photonics*, 2014, **8**, 47–51.
- 24 D. J. Bindl, A. J. Ferguson, M.-Y. Wu, N. Kopidakis, J. L. Blackburn and M. S. Arnold, *J. Phys. Chem. Lett.*, 2013, **4**, 3550–3559.
- 25 A. J. Ferguson, A.-M. Dowgiallo, D. J. Bindl, K. S. Mistry, O. G. Reid, N. Kopidakis, M. S. Arnold and J. L. Blackburn, *Phys. Rev. B: Condens. Matter*, 2015, **91**, 245311.
- 26 R. Ihly, K. S. Mistry, A. J. Ferguson, T. T. Clikeman, B. W. Larson, O. Reid, O. V. Boltalina, S. H. Strauss, G. Rumbles and J. L. Blackburn, *Nat. Chem.*, 2016, **8**, 603–609.
- 27 A. Devizis, D. Hertel, K. Meerholz, V. Gulbinas and E. Moser, *Org. Electron.*, 2014, **15**, 3729–3734.
- 28 S. M. Tuladhar, D. Poplavskyy, S. A. Choulis, J. R. Durrant, D. D. Bradley and J. Nelson, *Adv. Funct. Mater.*, 2005, **15**, 1171–1182.
- 29 T. J. Savenije, J. E. Kroeze, M. M. Wienk, J. M. Kroon and J. M. Warman, *Phys. Rev. B: Condens. Matter*, 2004, **69**, 155205.
- 30 C. S. Ponseca Jr., H. Nemeč, N. Vukmirović, S. Fusco, E. Wang, M. R. Andersson, P. Chabera, A. Yartsev and V. Sundström, *J. Phys. Chem. Lett.*, 2012, **3**, 2442–2446.
- 31 F. Schöppler, C. Mann, T. C. Hain, F. M. Neubauer, G. Privitera, F. Bonaccorso, D. Chu, A. C. Ferrari and T. Hertel, *J. Phys. Chem. C*, 2011, **115**, 14682–14686.
- 32 S. R. Sanchez, S. M. Bachilo, Y. Kadria-Vili, C.-W. Lin and R. Bruce Weisman, *Nano Lett.*, 2016, **16**, 6903–6909.
- 33 H. Bässler, *Phys. Status Solidi B*, 1993, **175**, 15–56.
- 34 T. Hertel, S. Himmelein, T. Ackermann, D. Stich and J. Crochet, *ACS Nano*, 2010, **4**, 7161–7168.
- 35 L. Perfetti, T. Kampfrath, F. Schapper, A. Hagen, T. Hertel, C. M. Aguirre, P. Desjardins, R. Martel, C. Frischkorn and M. Wolf, *Phys. Rev. Lett.*, 2006, **96**, 027401.
- 36 C. Gómez-Navarro, P. J. De Pablo, J. Gómez-Herrero, B. Biel, F. J. Garcia-Vidal, A. Rubio and F. Flores, *Nat. Mater.*, 2005, **4**, 534–539.
- 37 X. Zhou, J.-Y. Park, S. Huang, J. Liu and P. L. McEuen, *Phys. Rev. Lett.*, 2005, **95**, 146805.
- 38 S. Rosenblatt, Y. Yaish, J. Park, J. Gore, V. Sazonova and P. L. McEuen, *Nano Lett.*, 2002, **2**, 869–872.
- 39 M. Shim, A. Javey, N. W. S. Kam and H. J. Dai, *J. Am. Chem. Soc.*, 2001, **123**, 11512–11513.
- 40 M. Held, S. P. Schießl, D. Miehler, F. Gannott and J. Zaumseil, *Appl. Phys. Lett.*, 2015, **107**, 083301.
- 41 Y. Z. Ma, L. Valkūnas, S. L. Dexheimer, S. M. Bachilo and G. R. Fleming, *Phys. Rev. Lett.*, 2005, **94**, 157402.
- 42 S. W. Kettlitz, J. Mescher, N. S. Christ, M. Nintz, S. Valouch, A. Colmann and U. Lemmer, Eliminating RC-Effects in Transient Photocurrent Measurements on Organic Photodiodes, *IEEE Photonics Technol. Lett.*, 2013, **25**(7), 682–685.

3

Direct tracking of ultrafast carrier motion dynamics in semiconducting single-wall carbon nanotubes

Vidmantas Jašinskas, Florian Oberndorfer, Vidas Pakštas, Tobias Hertel,
and Vidmantas Gulbinas

Direct Tracking of Ultrafast Carrier Motion Dynamics in Semiconducting Single-Wall Carbon Nanotubes

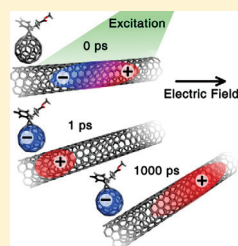
Vidmantas Jašinaskas,[†] Florian Oberndorfer,[‡] Vidas Pakštis,[†] Tobias Hertel,^{‡,§} and Vidmantas Gulbinas^{*,†,§}

[†]Center for Physical Sciences and Technology, Saulėtekio al. 3, LT-10257 Vilnius, Lithuania

[‡]Physical Chemistry Department, University of Würzburg, Am Hubland, 97074 Würzburg, Germany

[§]Institute of Chemical Physics, Vilnius University, Saulėtekio al. 9-III, LT-10222 Vilnius, Lithuania

ABSTRACT: An ultrafast all-optical electric field strength measurement technique based on the electric-field-induced second harmonic generation together with conventional transient photocurrent measurements has been applied for the direct tracking of carrier separation and motion dynamics in semiconducting single-wall carbon nanotubes (SWNTs). Thin films of (6,5)-SWNT-enriched samples were prepared on combs of interdigitated electrodes with different concentrations of fullerene derivative phenyl-C₆₁-butyric acid methyl ester (PCBM) serving as an electron acceptor. Neutral delocalized excitons photogenerated in the samples with high PCBM concentration were found to form localized charge-transfer (CT) states within less than 1 ps with the electron transferred to the PCBM and a hole remaining on the SWNT. The hole's drift along the length of individual nanotubes was found to take ~200–1000 ps and is most likely limited by dissociation of the CT states rather than by the hole's mobility. A fraction of about (30–50)% of generated charge carriers was found to recombine within 3.6 ns measurement interval.



1. INTRODUCTION

Because of their unique structure and unusual electronic properties, carbon nanotubes (CNTs) continue to attract interest and are explored as potentially promising materials for the development of devices based on new operating principles. Devices based on a single nanotube may be a good example paving a way toward nanotechnology-based electronics.¹ Because of strong and spectrally tunable absorption bands in visible and IR spectral regions and related photoconductivity, as well as high carrier mobility, CNTs are also promising for the development of materials with enhanced useful electronic properties for more conventional photoelectronic devices.² They were attempted to use in organic solar cells,^{3–6} light detectors,^{7,8} transistors,^{9,10} and phototransistors.^{11,12}

Photoelectrical applications require a clear understanding of the electronic processes in photoexcited CNTs, including exciton and charge carrier generation and motion, which is still lacking. Several studies have explored the photoconductivity of single CNTs¹ and of thin films^{2,13} without reaching a broader consensus. The mechanism of charge carrier generation is thus still not fully understood and requires further investigation. Initially, CNTs photoconductivity was discussed in terms of excitonic and interband transitions.¹⁴ However, high binding energies of excitons in single-wall carbon nanotubes (SWNTs), reaching hundreds of millielectron volts,^{15,16} called direct carrier photogeneration into question. Nonetheless, spontaneous carrier photogeneration in SWNTs has been reported by several authors,^{17–20} and it remains unclear if the spontaneous carrier generation may also occur in “perfect” nanotubes or if it

requires defects or impurities. Adsorbed oxygen was demonstrated to significantly enhance the photocurrent,² and charge separation was also suggested to occur by electron transfer to metal electrodes.¹³ The local electric field was recently suggested to cause free carrier photogeneration in inhomogeneously doped single semiconducting nanotubes.²¹

Efficient charge photogeneration was also demonstrated to take place at the interfaces between CNTs and fullerenes or fullerene derivatives, raising interest to the potential of such systems for solar cell fabrication.^{3,4,7} In most of these systems, SWNTs and fullerene derivatives form type-II heterojunctions;⁷ thus, the carrier generation mechanism in this case is quite clear. However, the dynamics associated with the charge carrier generation and motion away from their initial generation sites are still largely unexplored. Conventional electrical methods have insufficient time resolution to address initial carrier generation and motion phases. Time-resolved microwave conductivity enabled contactless probing of the carrier motion dynamics and provided valuable information about the carrier trapping and recombination processes.^{20,22} However, its time resolution was also too low to address the generation dynamics. Transient absorption spectroscopy revealed the charge carrier generation by electron transfer between SWNTs and fullerene which is very fast on a femtosecond timescale.^{18,23,24} Electron transfer to conjugated

Received: May 16, 2018

Revised: June 26, 2018

Published: June 27, 2018

polymer (P3HT) was found taking place with the similar rate.²⁵ However, conventional transient absorption was unable to separate between free and localized charge carriers. Attempts to address the carrier dynamics with another ultrafast technique, time-resolved THz spectroscopy, revealed the generation of localized and delocalized charge carriers and their localization during the thermalization process, but the free charge carrier response was not identified.²⁶ The elementary steps following photon absorption leading to the generation of free charge carriers thus still remain somewhat vague, and it is not clear what processes determine carrier generation efficiency, its dependence on the material chemical composition, morphology, and external conditions.

We have recently investigated photoconductivity dynamics in films composed of (6,5)-SWNTs wrapped with polyfluorene-based polymer poly[(9,9-dioctylfluorenyl-2,7-diyl)-*alt*-co-(6,6-2,2-bipyridine)] (PFO-Bpy). Addition of the fullerene derivative PCBM was found to greatly enhance the carrier generation efficiency in such samples.²⁵ Electrical investigations with about 2 ns time resolution revealed two photocurrent phases. The slow phase on a sub-microsecond timescale was attributed to the intertube carrier migration between aggregated nanotubes, whereas the fast phase, which is much faster than the time resolution, was attributed to the intratube carrier generation and motion.

To investigate the ultrafast carrier generation and motion dynamics, here, we use an all-optical technique sensitive to charge carrier motion with a very high time resolution of about 1 ps. The samples were prepared as thin films formed on combs of interdigitated electrodes. We combined the ultrafast measurements with conventional transient photocurrent investigations to address all pathways from photon absorption to final hole motion phases inside individual nanotubes and their aggregates. Investigation of films prepared from fresh nanotube suspension and from aged suspension with a high concentration of more tightly assembled or bundled SWNTs enabled us to additionally confirm attribution of the fast and slow photocurrent phases to the intratube and intertube carrier motion, respectively.

2. EXPERIMENTAL SECTION

Semiconducting (6,5)-SWNTs used for the sample preparation were purified using CNTs synthesized by the CoMoCAT process as a starting material (99.9%, Sigma-Aldrich). The enrichment of (6,5)-SWNTs in our samples was based on ultrasound-assisted wrapping with PFO-Bpy copolymer, centrifugation, and filtration-assisted polymer depletion.²⁷ The PFO-Bpy-stabilized (6,5)-SWNTs were resuspended in chlorobenzene (>98%, Fluka) and then mixed using different mass ratios with a solution of [6,6]-phenyl C₆₁ butyric acid methyl ester (PCBM) (>99.5%, Sigma-Aldrich). The mixtures were then drop-cast on the interdigitated electrodes (ED-IDE3-Pt, Micrux Technologies) and dried in air. Interdigitated Pt electrodes fabricated on glass substrates were formed from 5 μm wide and 150 nm thick stripes with 10 μm pitch. Two types of samples were prepared, from fresh solution and from solution aged more than a year when SWNT aggregation took place. For the sake of simplicity, these samples will be referred to as *fresh* and *aged*, respectively. Scanning electron microscopy (SEM) images of *fresh* and *aged* films on interdigitated electrodes are shown in Figure 1a. *Aged* films contain clearly visible aggregates with densely packed SWNTs, whereas *fresh* films form a netlike structure. Absorption spectra

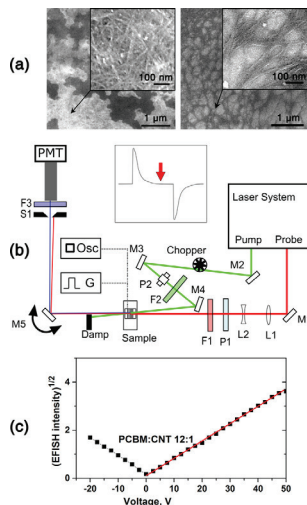


Figure 1. (a) SEM images of aged (left) and fresh (right) samples and (b) schematic illustration of the experimental setup. The inset shows the electric pulse synchronization timing, (c) change of the square root of the EFISH signal with applied voltage. The red line is a linear fit.

of the fresh samples are presented in Figure 3, whereas spectra of *aged* samples are presented in ref26. There is no clear difference between spectra of the two sample types. Relative intensities of polymer and SWNTs absorption bands gave estimate of the SWNTs to PFO-Bpy mass ratios indicated in the sample names.

For investigation of the conventional transient photocurrent kinetics, we worked in the integrating regime, where the cumulated charge of the photocurrent was measured using the voltage drop across an integrating capacitor formed by the sample and oscilloscope capacitances connected in parallel. The samples were excited at 1000 nm by radiation of the optical parametric amplifier Topas-C (Light Conversion Ltd.) pumped by femtosecond Ti:sapphire laser Integra-C from Quamtronix Inc. ($\lambda = 800$ nm, $\tau_{\text{pulse}} = 130$ fs). An Agilent Technologies DS05054A oscilloscope with a 1 M Ω input resistance was used for these measurements. The photocurrent was obtained from the rate at which the cumulated charge increases. This measurement regime ensures better time resolution, not limited by the sample capacitance in comparison with the current measurement regime.

Ultrafast transient absorption investigations were performed by means of a pump-probe spectrometer based on a Pharos femtosecond laser (Light Conversion) generating 1030 nm, 250 fs duration pulses at 5 kHz repetition rate. Parametric generator ORPHEUS (Light Conversion) was used to produce excitation pulses at 1000 nm, and light continuum generated in a sapphire plate was used as a probe light.

The ultrafast carrier motion dynamics was investigated by means of a time-resolved electric-field-induced second harmonic generation (TREFISH) technique. This all-optical

investigation technique has demonstrated its usefulness for investigations of ultrafast carrier motion dynamics in conjugated polymers²⁸ and blends for organic solar cells²⁹ and was described in detail earlier.^{28,30} This pump-probe-type technique is based on the EFISH generation phenomenon, which facilitates the measurement of electric field dynamics directly inside the investigated material. Briefly, an applied voltage charges the sample capacitance prior to optical excitation. When the sample is excited with an ultrashort light pulse, the induced photocurrent reduces the electric field by discharging the sample's capacitance and subsequent probe pulse delayed by a variable delay time probes the electric field kinetics. Specifics of the EFISH generation in a geometry of films deposited on interdigitated electrodes are described in ref 31.

A schematic of the experimental setup for the TREFISH measurements is reproduced in Figure 1b. A femtosecond Ti:sapphire laser equipped with an optical parametric amplifier Topas-C described above was used as a light source. The samples were excited at 1000 nm, and fundamental laser radiation at 800 nm was used as a probe light to probe the second harmonic generation efficiency. To minimize irreversible sample damage from a current breakdown, the voltage was applied in the form of short 20 μ s square pulses (Tektronix AFG 2021 arbitrary function generator equipped with the high-speed high-voltage linear amplifier Falco Systems WMA-320) synchronized with laser pulses (see the inset in Figure 1b). The electric-field-induced second harmonic (EFISH) intensity was measured by the photomultiplier. The electric field strength was determined from the EFISH signal as: $F = F_0(I_{2H}/I_{2H}^0)^{1/2}$, where F_0 is the applied electric field, I_{2H} and I_{2H}^0 are the second harmonic intensities with and without excitation, respectively. Figure 1c shows the square root of the EFISH intensity for the PCBM/CNT 12:1 sample, which depends linearly on the applied voltage, thus enabling a straightforward determination of the electric field strength from the EFISH signal.

3. RESULTS AND DISCUSSION

Figure 2 compares the kinetics of the cumulated charge in films made from fresh and aged solutions of SWNTs with different PCBM to SWNTs mass ratios. All samples exhibit an ultrafast increase of the cumulated charge, indicating that the photocurrent pulse is too fast to be resolved by our setup with the time resolution of about 2 ns. The subsequent kinetics strongly varies from sample to sample. PCBM/CNT 12:1 and CNT/PFO-Bpy films prepared from fresh solutions show only a fast growth of the cumulated charge, and subsequent slow decay caused by recharging of the sample capacitance with its rate being determined by the sample resistance.

The photoconductivity of SWNT/PCBM blends was previously attributed to charge carrier generation by electron transfer from photoexcited SWNTs to adjacent PCBM molecules.^{7,32} Despite relatively high content of PFO-Bpy polymer in our samples, PCBM molecules apparently made close complexes with SWNTs enabling efficient electron transfer. In contrast, oxygen or other impurities were suggested to play the role of electron acceptor in samples without PCBM.² The photocurrent was shown to be dominated by the hole motion within the SWNTs network. Thus, the hole drift in PCBM/CNT 12:1 and CNT/PFO-Bpy films continues for less than 2 ns.

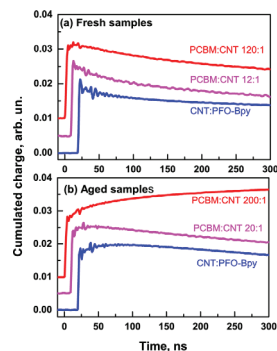


Figure 2. Kinetics of the cumulated charge for fresh (a) and aged (b) samples with different CNT to PCBM mass ratios measured at 5 V applied voltage. For better presentation, the curves are offset vertically and horizontally. Decay on a hundreds of nanosecond timescale is caused by the sample recharging.

The PCBM/CNT 120:1 sample prepared from fresh solution shows an additional weak increase of the cumulated charge during tens of nanoseconds. This increase is more expressed for all films prepared from aged solutions. The tens of nanoseconds component was previously attributed to intertube carrier migration within aggregates.²⁶ The relative intensity and the decay rate of this photocurrent component vary somewhat from sample to sample, which is not surprising, taking into account that drop-casting is prone to the variability of the film microstructure, thus causing different percolations between SWNTs. The absence of this component in some films made from fresh SWNTs solutions suggests that SWNTs in these films are less aggregated and thus less percolated, which is in agreement with the SEM images presented in Figure 1. These observations are in agreement with the earlier conclusion that the carrier generation and drift inside individual nanotubes take less than 2 ns at the electric field strengths used here. The PCBM/CNT 200:1 film also shows a weak, hundreds of nanoseconds component. This component is probably also present in the PCBM/CNT 120:1 sample only upstaged by the sample recharging. This slow photocurrent component observed in samples with a high PCBM content was attributed to the electron motion within PCBM.²⁶

To address the kinetics of carrier motion inside individual nanotubes that cannot be resolved by conventional transient photocurrent measurements, we used the all-optical TREFISH technique.²⁸ These investigations were combined with another ultrafast technique—transient absorption, giving additional information about the excited-state dynamics. Figure 3 shows the absorption bleaching relaxation measured for the fresh samples with and without PCBM at the maximum of the S_{11} absorption band (1000 nm) under excitation at 1000 nm. The excitation relaxation kinetics is very similar to that reported previously.^{23,33} The dominating exciton decay in the film without PCBM takes place during tens of picoseconds. A weak long-living component shall be attributed to low efficiency generation of free charge carriers responsible for a weak photoconductivity of this film.¹⁸ A fresh PCBM/CNT 120:1 film shows only partial relaxation on a subnanosecond—

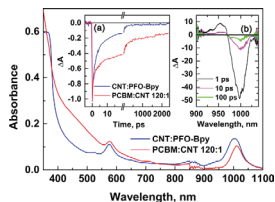


Figure 3. Steady-state absorption spectra of fresh CNT/PFO-Bpy and PCBM/CNT 120:1 samples. Inset (a) shows absorption bleaching kinetics measured at 1000 nm for both samples, and inset (b) shows the transient differential absorption spectra of the CNT/PFO-Bpy sample at different delay times. The excitation wavelength was 1000 nm.

nanosecond timescale. The strong long-living component shall be unambiguously attributed to the efficient ultrafast electron transfer from excited CNT to PCBM and generation of free charge carriers preventing complete recovery of the CNT absorption.²³ The partial relaxation of the absorption bleaching on a subnanosecond–nanosecond timescale shall be attributed to the charge carrier recombination, which, according to the model described below, is likely being geminate.

Figure 4 shows the dependences of the electric field strength on the delay time between the excitation and probe pulses in

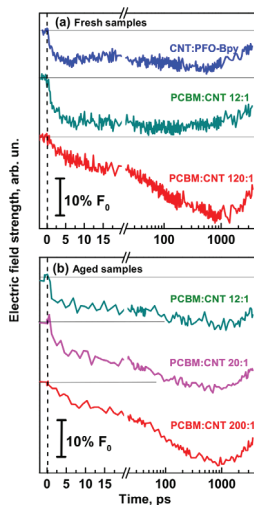


Figure 4. Electric field kinetics for fresh (a) and aged (b) samples measured at an applied voltage of 40 V after excitation at 1000 nm. Horizontal lines show EFISH intensity before sample excitation. Vertical dashed lines show excitation time. Bars indicate values of the electric field changes relatively to the applied electric field (because of the different optical densities of the samples and their spatial inhomogeneity, the changes in the electric field strength in each sample should not be compared directly).

aged and in fresh samples with different PCBM concentrations measured by the TREFISH technique.

To analyze the ultrafast electric field kinetics, we consider four excited-state species, which may be created by photoexcitation in the SWNT/PCBM system: neutral excitons, charge-transfer (CT) states with a hole located in a SWNT, and an electron in the adjacent PCBM, as well as free electrons in the PCBM phase with holes in the SWNTs. All of these species contribute to displacement or conductivity currents and, thus, change the applied electric field. We can describe the change of the electric field as

$$\Delta F(t) = \frac{F_0}{2\epsilon\epsilon_0} [n_{\text{ex}}(t)\Delta\alpha_{\text{ex}} + n_{\text{CT}}(t)\Delta\alpha_{\text{CT}}] + \frac{e}{\epsilon\epsilon_0} [n_{\text{el}}(t)l_{\text{el}}(t) + n_{\text{h}}(t)l_{\text{h}}(t)]$$

where the first and second terms describe electric field changes caused by the displacement current from photogenerated neutral and CT excitons, whereas the third and fourth terms describe changes created by the drift of photogenerated electrons and holes, respectively. Here, $n_{\text{ex}}(t)$, $n_{\text{CT}}(t)$, $n_{\text{el}}(t)$, and $n_{\text{h}}(t)$ are densities of the species described above, $\Delta\alpha_{\text{ex}}$ and $\Delta\alpha_{\text{CT}}$ are differences between polarizabilities of related excitons and neutral SWNT segments, e is the electron charge, and $l_{\text{el}}(t)$ and $l_{\text{h}}(t)$ are the electron and hole drift distances.

According to the transient absorption investigations, only neutral excitons and low concentration of charge carriers are generated in samples without PCBM. Neutral and CT excitons usually have higher polarizabilities than corresponding non-excited species; therefore, they reduce the electric field inside the investigated material by increasing its dielectric constant and consequent capacity of the charged sample. Neutral excitons, which are generated during the excitation pulse duration, get polarized by the electric field instantaneously and screen the electric field practically instantaneously. We observe such ultrafast electric field drop in samples without or with low PCBM concentration. The electric field is expected to recover again when excitons relax on tens of picosecond timescale. We observe such partial recovery of the electric field in the CNT/PFO-Bpy sample during 5–20 ps. At longer times, the recovery is apparently compensated by the photocurrent created by the photogenerated charge carriers.

As determined from the transient photocurrent measurements, PCBM increases the carrier generation efficiency and it is larger by over an order of magnitude in samples with a high PCBM content if compared to the samples without PCBM.²⁶ Therefore, charge carrier contribution to the electric field dynamics in samples with PCBM is much larger overwhelming the electric field dynamics caused by the exciton decay. Surprisingly, we also do not see any instantaneous electric field drop in samples with a very high PCBM content (120:1 and 200:1). It suggests that neutral excitons responsible for the ultrafast field drop are not generated or are very rapidly quenched in these samples. Such rapid quenching by electron transfer from excited CNTs to fullerenes is in agreement with the transient photocurrent measurements and was also observed in similar systems taking place during hundreds of femtoseconds.²³ The absence of the fast electric field drop also suggests that polarizability of the CT excitons created by electron transfer to PCBM is low, much lower than that of neutral excitons. The low polarizability is expected because electrons in CT states are localized on comparatively small

PCBM molecules, whereas the Coulomb interaction also causes localization of a hole. Similar carrier localization was discussed for AuCl₃-doped SWNTs.^{34,35}

The subsequent electric field dynamics on the picosecond timescale is determined by the free carrier generation and motion processes. In cells with the highest PCBM content, where exciton contribution is insignificant, these processes completely determine the field dynamics during initial nanosecond. Unfortunately, carrier generation and motion processes cannot be separated one from another in our experiments—the slower one limits the field decrease rate. We can, thus, only establish upper limits for the either one being about 200–1000 ps. Assuming carrier motion is the rate-limiting process, we can estimate the intratube hole mobility of about 10 cm²/V s. This value is about 2 orders of magnitude lower than the intratube mobility values reported in the prior literature^{36–39} and thus hardly can be correct. On the other hand, PCBM molecules adsorbed to CNTs may disturb carrier delocalization and change intratube mobility. However, electric field kinetics (Figure 4) show no clear differences between the carrier drift dynamics in samples with low, high PCBM concentration and without it. It suggests that electrically neutral PCBM molecules do not significantly influence carrier motion in CNTs. Consequently, more likely that the electric field decay is limited by carrier generation, that is, splitting of CT states into free charge carriers, which lasts for about 1000 ps.

It is important to note that we do not see any significant differences between the ultrafast electric field dynamics in films made from fresh and aged SWNT solutions. This is in contrast to the different photocurrent kinetics on a nanosecond timescale, attributed to different sample morphologies causing different intertube carrier motions (see Figure 2b). Therefore, we attribute the ultrafast electric field dynamics to electronic processes within individual nanotubes. This also confirms the earlier conclusion that intertube hole motion takes place on a nanosecond timescale.²⁶

The electric field slightly recovers again during several nanoseconds after optical excitation. We attribute this recovery to the geminate charge carrier recombination observed also in transient absorption measurements. Similar recombination rate was also determined for charge carriers generated at the SWNT/C₆₀ interface.²³ This process is most likely dominated by carriers generated in SWNTs oriented nearly perpendicular to the direction of the electric field, where diffusion of holes against the electric field back to electrons located on PCBM is associated with only a small energy barrier. This recovery is slightly weaker in aged films. We attribute this difference to a manifestation of intertube carrier motion: some carriers, which would have recombined in isolated SWNTs, may jump to neighboring nanotubes and avoid geminate recombination.

It should be also noted that the neutral excitons do not contribute to the transient photocurrent measured by an oscilloscope. This is because of limited time resolution of the oscilloscope, which cannot detect species with lifetimes of tens of picoseconds. On the other hand, we do not observe any signatures of the electron motion in ultrafast TREFISH investigations. The electron motion gives a sizable contribution to the photocurrent at very high PCBM concentration, and this contribution is associated with a photocurrent on a much slower, sub-microsecond timescale. Thus, we can ignore the electron contribution considering picosecond electric field dynamics.

Last, we here report the dependence of the electric field kinetics on the excitation light polarization, which provides additional information about charge carrier motion. Figure 5

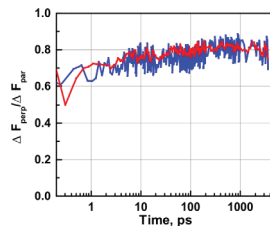


Figure 5. Time dependence of the ratio of the excitation-induced EFISH drop under parallel and perpendicular to the electric field direction excitation pulse polarizations for the samples prepared from fresh solutions without PCBM (blue) and PCBM/CNT 12:1 (red).

presents data for fresh samples without PCBM and PCBM/CNT 12:1. The ratio between the electric field drops created by excitation light polarized perpendicularly and in parallel to the electric field direction equals to about 0.6 at the initial time and increases to about 0.8 at a long time. The influence of the excitation light polarization on the EFISH signal value shall be identical to the influence of the excitation light polarization on the value of the transient absorption signal in polarized transient absorption measurements and to the anisotropy of fluorescence created by linearly polarized light. From this analogy, we expect this ratio being equal to 0.33 for randomly oriented linear stick-like particles if intertube exciton and carrier migrations do not take place. Because the initial electric field drop in these samples is mainly caused by neutral excitons, the larger ratio of about 0.6 is apparently caused by depolarization of excitons because of their diffusion along bent SWNTs to slightly differently oriented SWNT segments or to neighboring SWNTs faster than the time resolution of our measurements. Additional depolarization on a subnanosecond timescale reflects slower exciton migration phase and probably also hole motion along bent SWNTs. Within experimental accuracy, the depolarization kinetics for samples without and with PCBM are identical, which confirms that PCBM is essential for the charge carrier generation but does not influence the motion of generated holes. The depolarization kinetics for the samples prepared from aged samples were within experimental accuracy identical, therefore not presented.

The scheme in Figure 6 summarizes all of the above-discussed processes. Four photoinduced processes were found to take place on an ultrafast (picoseconds to several nanoseconds) timescale in individual SWNTs: first, electron transfer from photoexcited SWNT to PCBM or impurity creating CT state; second, CT state dissociation; third, hole drift, and fourth, recombination of a fraction of photo-generated charge carriers. Intertube hole motion in SWNT aggregates was found to be much slower, dominantly happening during several microseconds.

4. CONCLUSIONS

Combination of several experimental techniques—conventional transient photocurrent, time-resolved TREFISH gen-

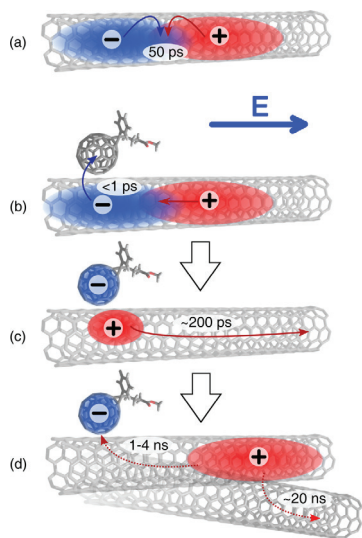


Figure 6. Schematic illustration of the processes in excited SWNTs. (a) Relaxation of neutral exciton in isolated SWNT, (b) creation of CT exciton by electron transfer to PCBM and simultaneous hole localization next to electron, (c) dissociation of CT exciton to free charge carriers, and (d) recombination of fraction of carriers and eventual interchain hole transfer.

eration, and transient absorption—enabled us to directly track the carrier generation and motion in individual wrapped by polymer SWNTs and their aggregates. Our investigations revealed that directly photogenerated delocalized neutral excitons feature high polarizability and significantly screen applied electric field. The neutral excitons are quenched on a femtosecond timescale by electron transfer to adjacent PCBM creating strongly localized weakly polarizable CT states. The CT states dissociate into free charge carriers during hundreds of picoseconds and limit the photocurrent dynamics, whereas hole transfer along individual nanotubes is much faster. A much slower intertube hole motion in SWNT aggregates takes place during tens of nanoseconds. These findings based on direct tracking of ultrafast electronic processes in photoexcited SWNTs give explicit information about carrier generation and motion mechanisms necessary for their control in the development of more efficient CNT-based systems and devices.

■ AUTHOR INFORMATION

Corresponding Author

*E-mail: vidmantas.gulbinas@ftmc.lt.

ORCID

Vidmantas Jašinaskas: 0000-0001-5982-8214

Tobias Hertel: 0000-0001-7907-4341

Notes

The authors declare no competing financial interest.

■ ACKNOWLEDGMENTS

This work was financially supported by the Research Council of Lithuania via grant no. LAT-07/2016.

■ REFERENCES

- (1) Freitag, M.; Martin, Y.; Misewich, J. A.; Martel, R.; Avouris, P. Photoconductivity of Single Carbon Nanotubes. *Nano Lett.* **2003**, *3*, 1067–1071.
- (2) Levitsky, I. A.; Euler, W. B. Photoconductivity of Single-Wall Carbon Nanotubes under Continuous-Wave near-Infrared Illumination. *Appl. Phys. Lett.* **2003**, *83*, 1857–1859.
- (3) Shea, M. J.; Arnold, M. S. 1% Solar Cells Derived from Ultrathin Carbon Nanotube Photoabsorbing Films. *Appl. Phys. Lett.* **2013**, *102*, 243101.
- (4) Bindl, D. J.; Wu, M.-Y.; Prehn, F. C.; Arnold, M. S. Efficiently Harvesting Excitons from Electronic Type-Controlled Semiconducting Carbon Nanotube Films. *Nano Lett.* **2011**, *11*, 455–460.
- (5) Ramuz, M. P.; Vosguerichian, M.; Wei, P.; Wang, C.; Gao, Y.; Wu, Y.; Chen, Y.; Bao, Z. Evaluation of Solution-Processable Carbon-Based Electrodes for All-Carbon Solar Cells. *ACS Nano* **2012**, *6*, 10384–10395.
- (6) Lanzi, M.; Paganin, L.; Caretti, D. New Photoactive Oligo- and Poly-Alkylthiophenes. *Polymer* **2008**, *49*, 4942–4948.
- (7) Arnold, M. S.; Zimmerman, J. D.; Renshaw, C. K.; Xu, X.; Lunt, R. R.; Austin, C. M.; Forrest, S. R. Broad Spectral Response Using Carbon Nanotube/Organic Semiconductor/C60 Photodetectors. *Nano Lett.* **2009**, *9*, 3354–3358.
- (8) Liang, S.; Ma, Z.; Wu, G.; Wei, N.; Huang, L.; Huang, H.; Liu, H.; Wang, S.; Peng, L.-M. Microcavity-Integrated Carbon Nanotube Photodetectors. *ACS Nano* **2016**, *10*, 6963–6971.
- (9) Park, R. S.; Shulaker, M. M.; Hills, G.; Liyanage, L. S.; Lee, S.; Tang, A.; Mitra, S.; Wong, H.-S. P. Hysteresis in Carbon Nanotube Transistors: Measurement and Analysis of Trap Density, Energy Level, and Spatial Distribution. *ACS Nano* **2016**, *10*, 4599–4608.
- (10) Qiu, C.; Zhang, Z.; Xiao, M.; Yang, Y.; Zhong, D.; Peng, L.-M. Scaling Carbon Nanotube Complementary Transistors to 5-Nm Gate Lengths. *Science* **2017**, *355*, 271–276.
- (11) Biswas, C.; Jeong, H.; Jeong, M. S.; Yu, W. J.; Pribat, D.; Lee, Y. H. Quantum Dot–Carbon Nanotube Hybrid Phototransistor with an Enhanced Optical Stark Effect. *Adv. Funct. Mater.* **2013**, *23*, 3653–3660.
- (12) Spina, M.; Náfrádi, B.; Tóháti, H. M.; Kamarás, K.; Bonvin, E.; Gaal, R.; Forró, L.; Horváth, E. Ultrasensitive 1D Field-Effect Phototransistors: CH₃NH₃ PBI 3 Nanowire Sensitized Individual Carbon Nanotubes. *Nanoscale* **2016**, *8*, 4888–4893.
- (13) Lu, S.; Panchapakesan, B. Photoconductivity in Single Wall Carbon Nanotube Sheets. *Nanotechnology* **2006**, *17*, 1843.
- (14) Fujiwara, A.; Matsuoka, Y.; Suematsu, H.; Ogawa, N.; Miyano, K.; Kataura, H.; Maniwa, Y.; Suzuki, S.; Achiba, Y. Photoconductivity in Semiconducting Single-Walled Carbon Nanotubes. *Jpn. J. Appl. Phys.* **2001**, *40*, L1229.
- (15) Wang, F.; Dukovic, G.; Brus, L. E.; Heinz, T. F. The Optical Resonances in Carbon Nanotubes Arise from Excitons. *Science* **2005**, *308*, 838–841.
- (16) Maulttsch, J.; Pomraenke, R.; Reich, S.; Chang, E.; Prezzi, D.; Ruini, A.; Molinari, E.; Strano, M. S.; Thomsen, C.; Lienau, C. Exciton Binding Energies in Carbon Nanotubes from Two-Photon Photoluminescence. *Phys. Rev. B: Condens. Matter Phys.* **2005**, *72*, 241402.
- (17) Beard, M. C.; Blackburn, J. L.; Heben, M. J. Photogenerated Free Carrier Dynamics in Metal and Semiconductor Single-Walled Carbon Nanotube Films. *Nano Lett.* **2008**, *8*, 4238–4242.
- (18) Soavi, G.; Scotognella, F.; Brida, D.; Hefner, T.; Späth, F.; Antognazza, M. R.; Hertel, T.; Lanzani, G.; Cerullo, G. Ultrafast Charge Photogeneration in Semiconducting Carbon Nanotubes. *J. Phys. Chem. C* **2013**, *117*, 10849–10855.

16429

DOI: 10.1021/acs.jpcc.8b04672
J. Phys. Chem. C **2018**, *122*, 16424–16430

Reprinted with permission from The Journal of Physical Chemistry C 122(28), 16424-16430 (2018).

DOI: 10.1021/acs.jpcc.8b04672. Copyright 2018 American Chemical Society

- (19) Kumamoto, Y.; Yoshida, M.; Ishii, A.; Yokoyama, A.; Shimada, T.; Kato, Y. K. Spontaneous Exciton Dissociation in Carbon Nanotubes. *Phys. Rev. Lett.* **2014**, *112*, 117401.
- (20) Park, J.; Reid, O. G.; Blackburn, J. L.; Rumbles, G. Photoinduced Spontaneous Free-Carrier Generation in Semiconducting Single-Walled Carbon Nanotubes. *Nat. Commun.* **2015**, *6*, 8809.
- (21) Barkelid, M.; Zwiller, V. Photocurrent Generation in Semiconducting and Metallic Carbon Nanotubes. *Nat. Photonics* **2014**, *8*, 47–51.
- (22) Ferguson, A. J.; Dowgiallo, A.-M.; Bindl, D. J.; Mistry, K. S.; Reid, O. G.; Kopidakis, N.; Arnold, M. S.; Blackburn, J. L. Trap-Limited Carrier Recombination in Single-Walled Carbon Nanotube Heterojunctions with Fullerene Acceptor Layers. *Phys. Rev. B: Condens. Matter Mater. Phys.* **2015**, *91*, 245311.
- (23) Dowgiallo, A.-M.; Mistry, K. S.; Johnson, J. C.; Blackburn, J. L. Ultrafast Spectroscopic Signature of Charge Transfer between Single-Walled Carbon Nanotubes and C₆₀. *ACS Nano* **2014**, *8*, 8573–8581.
- (24) Stranks, S. D.; Weisspfennig, C.; Parkinson, P.; Johnston, M. B.; Herz, L. M.; Nicholas, R. J. Ultrafast Charge Separation at a Polymer–Single-Walled Carbon Nanotube Molecular Junction. *Nano Lett.* **2011**, *11*, 66–72.
- (25) Perfetti, L.; Kampfrath, T.; Schapper, F.; Hagen, A.; Hertel, T.; Aguirre, C. M.; Desjardins, P.; Martel, R.; Frischkorn, C.; Wolf, M. Ultrafast Dynamics of Delocalized and Localized Electrons in Carbon Nanotubes. *Phys. Rev. Lett.* **2006**, *96*, 027401.
- (26) Eckstein, A.; Bertasius, V.; Jašinskas, V.; Namal, I.; Hertel, T.; Gulbinas, V. Carrier Photogeneration, Drift and Recombination in a Semiconducting Carbon Nanotube Network. *Nanoscale* **2017**, *9*, 12441–12448.
- (27) Ozawa, H.; Ide, N.; Fujigaya, T.; Niidome, Y.; Nakashima, N. One-Pot Separation of Highly Enriched (6,5)-Single-Walled Carbon Nanotubes Using a Fluorene-Based Copolymer. *Chem. Lett.* **2011**, *40*, 239–241.
- (28) Devizis, A.; Serbenta, A.; Meerholz, K.; Hertel, D.; Gulbinas, V. Ultrafast Dynamics of Carrier Mobility in a Conjugated Polymer Probed at Molecular and Microscopic Length Scales. *Phys. Rev. Lett.* **2009**, *103*, 027404.
- (29) Vithanage, D. A.; Devizis, A.; Abramavičius, V.; Infahsaeng, Y.; Abramavičius, D.; MacKenzie, R. C. I.; Keivanidis, P. E.; Yartsev, A.; Hertel, D.; Nelson, J.; et al. Visualizing Charge Separation in Bulk Heterojunction Organic Solar Cells. *Nat. Commun.* **2013**, *4*, 2334.
- (30) Devizis, A.; Meerholz, K.; Hertel, D.; Gulbinas, V. Ultrafast Charge Carrier Mobility Dynamics in Poly(Spirofluorene-co-Benzothiadiazole): Influence of Temperature on Initial Transport. *Phys. Rev. B: Condens. Matter Mater. Phys.* **2010**, *82*, 155204.
- (31) Jašinskas, V.; Gedvilas, M.; Račiukaitis, G.; Gulbinas, V. Background-Free Electric Field-Induced Second Harmonic Generation with Interdigitated Combs of Electrodes. *Opt. Lett.* **2016**, *41*, 2759–2762.
- (32) Isborn, C. M.; Tang, C.; Martini, A.; Johnson, E. R.; Otero-de-la-Roza, A.; Tung, V. C. Carbon Nanotube Chirality Determines Efficiency of Electron Transfer to Fullerene in All-Carbon Photovoltaics. *J. Phys. Chem. Lett.* **2013**, *4*, 2914–2918.
- (33) Styers-Barnett, D. J.; Ellison, S. P.; Mehl, B. P.; Westlake, B. C.; House, R. L.; Park, C.; Wise, K. E.; Papanikolas, J. M. Exciton Dynamics and Biexciton Formation in Single-Walled Carbon Nanotubes Studied with Femtosecond Transient Absorption Spectroscopy. *J. Phys. Chem. C* **2008**, *112*, 4507–4516.
- (34) Eckstein, K. H.; Hartleb, H.; Achsnich, M. M.; Schöppler, F.; Hertel, T. Localized Charges Control Exciton Energetics and Energy Dissipation in Doped Carbon Nanotubes. *ACS Nano* **2017**, *11*, 10401–10408.
- (35) Kim, S. M.; Kim, K. K.; Jo, Y. W.; Park, M. H.; Chae, S. J.; Duong, D. L.; Yang, C. W.; Kong, J.; Lee, Y. H. Role of Anions in the AuCl₃-Doping of Carbon Nanotubes. *ACS Nano* **2011**, *5*, 1236–1242.
- (36) Fu, W.; Xu, Z.; Bai, X.; Gu, C.; Wang, E. Intrinsic Memory Function of Carbon Nanotube-Based Ferroelectric Field-Effect Transistor. *Nano Lett.* **2009**, *9*, 921–925.
- (37) Zhou, X.; Park, J.-Y.; Huang, S.; Liu, J.; McEuen, P. L. Band Structure, Phonon Scattering, and the Performance Limit of Single-Walled Carbon Nanotube Transistors. *Phys. Rev. Lett.* **2005**, *95*, 146805.
- (38) Pennington, G.; Goldsman, N. Semiclassical Transport and Phonon Scattering of Electrons in Semiconducting Carbon Nanotubes. *Phys. Rev. B: Condens. Matter Mater. Phys.* **2003**, *68*, 045426.
- (39) Dürkop, T.; Kim, B. M.; Fuhrer, M. S. Properties and Applications of High-Mobility Semiconducting Nanotubes. *J. Phys.: Condens. Matter* **2004**, *16*, R553.

4

Electronic and ionic electric field screening and persistent built-in electric field in carbon nanotube/PCBM films

Vidmantas Jašinskas, Florian Oberndorfer, Tobias Hertel,
and Vidmantas Gulbinas

Electronic and Ionic Electric Field Screening and Persistent Built-In Electric Field in Carbon Nanotube/PCBM Films

Vidmantas Jašinaskas, Florian Oberdorfer, Tobias Hertel, and Vidmantas Gulbinas*

The application of carbon nanotubes in electronic devices requires detailed knowledge of their electrical properties. Herein, the long-lasting electric field-induced polarization of single-wall carbon nanotube (SWCNT) networks is demonstrated. It is found that electric voltage applied to the films of SWCNTs and their blends with [6,6]-phenyl-C₆₁-butyric acid methyl ester (PCBM) creates persistent polarization that partly screens the external electric field and creates a built-in electric field of the opposite direction remaining for several days. The built-in electric field has caused the appearance of an open-circuit photovoltage and a short-circuit photocurrent under the sample illumination at zero applied voltage. The built-in field showed a clearly bicomponential decay. The short tens of microseconds component is attributed to the electronic polarization, while the long-lived component, which decreases at low temperatures, is attributed to the temperature-assisted motion of ions.

1. Introduction

Due to their unique mechanical, electronic and optical properties, carbon nanotubes are interesting materials for many technological applications. Two main structural groups of carbon nanotubes exist: single-wall and multiwall. An additional structural property is their chirality, defining the symmetry of their arrangement. Depending on chirality, carbon nanotubes may exhibit metallic or semiconductor properties. From all types of carbon nanotubes, semiconducting single-wall carbon nanotubes (SWCNTs) stand out as being particularly interesting for electronic applications. They have been tested in organic solar cells as both electron acceptors^[1] and electron donors.^[2] In addition, functionalized carbon nanotubes were applied in cell biology for probing of some molecular functions.^[3] Photoresponse in the infrared spectral region also makes SWCNTs well suited for wavelength-selective infrared light detectors.^[4]

Application of these nanomaterials in electronic devices requires clear understanding of their various physical properties,


especially charge transport properties, which are particularly important for any electronic material. Charge transport through the bundles of SWCNTs^[5–10] as well as its dependence on the temperature,^[5,6] doping,^[7] and intertube interactions^[6,8] have been addressed in a number of publications. Charge carrier photogeneration and their transport through the SWCNT network can be considered as very fast or ultrafast process.^[9,10] Intratube charge carrier mobility reaches thousands of cm² (Vs)⁻¹,^[11–13] which makes them interesting for fast electronics. However, charge carrier motion in carbon nanotube films is extremely dispersive. The intratube carrier transport takes place on a picosecond timescale, while intertube carrier jumps are much slower occurring on a timescale of tens of microseconds.^[9] Gadermaier et al. reported an effective lifetime of 43 ms of the trapped charges in SWCNTs.^[14]

Much slower electronic processes in carbon nanotube films were also reported. Gravity-induced self-charging of article-like carbon nanotube–polyaniline supercapacitors lasting for hours was reported by Gao et al. and attributed to the motion of electrolyte ions.^[15] Slow processes also cause a well-known persistent photoconductivity phenomenon. It was observed in a number of materials^[16,17] including carbon nanotube structures.^[18–20] Persistent photoconductivity of modified carbon nanotube film lasting for more than 30 min was reported by Khairoutdinov et al.^[19] The slow processes were attributed to the photoinduced electron transfer from attached molecular substituents to carbon nanotubes. Allen et al. have demonstrated that the slow processes lasting for tens of minutes influence carrier mobility in a nanotube field-effect transistor.^[21]

Herein, we investigate slow electronic processes in films of (6,5)-SWCNT networks and their blends with fullerene derivative [6,6]-phenyl-C₆₁-butyric acid methyl ester (PCBM). PCBM is an efficient electron acceptor widely used in organic solar cells. PCBM also strongly enhances the photoconductivity of SWCNT films by accepting electrons from the photoexcited SWCNT.^[9] Such SWCNT/PCBM blend has been tested for application as active solar cell material.^[22] The films were deposited on interdigitated comb-like electrodes which enable simple preparation of samples convenient for investigation of carrier motion in lateral geometry. We demonstrate that an external voltage applied to the carbon nanotube and the blend films creates a built-in electric field lasting for hours to days. Such electrically poled films show photocurrent and photovoltage without applied external voltage. The persistent built-in electric field may be an interesting

V. Jašinaskas, Prof. V. Gulbinas
Center for Physical Sciences and Technology
Saulėtekio al. 3, LT-10257 Vilnius, Lithuania
E-mail: vidmantas.gulbinas@ftmc.lt

F. Oberdorfer, Prof. T. Hertel
Physical Chemistry Department
University of Würzburg
Am Hubland, 97074 Würzburg, Germany

 The ORCID identification number(s) for the author(s) of this article can be found under <https://doi.org/10.1002/pssa.201900673>.

DOI: 10.1002/pssa.201900673

phenomenon for application of carbon nanotubes systems as memory elements or for photodetectors operating without applied voltage.

2. Results and Discussion

The persistent built-in electric field was formed by poling the samples using a relatively high voltage applied to the sample. The poling of the samples used for steady-state investigations was performed by applying the steady-state voltage (up to 7 V) or 20 μ s voltage pulses (up to 40 V) at 1 kHz repetition rate. Steady-state electrical and photoelectrical properties of pristine and poled SWCNT films were investigated by measuring current-voltage characteristics (I - V curves) under application of a small external voltage, which does not change substantially the sample poling. Figure 1 shows I - V curves measured in the dark and under 1 Sun ($\approx 0.1 \text{ W cm}^{-2}$) illumination for the nonpoled SWCNT/PCBM(1/120) sample and that poled for 20 min

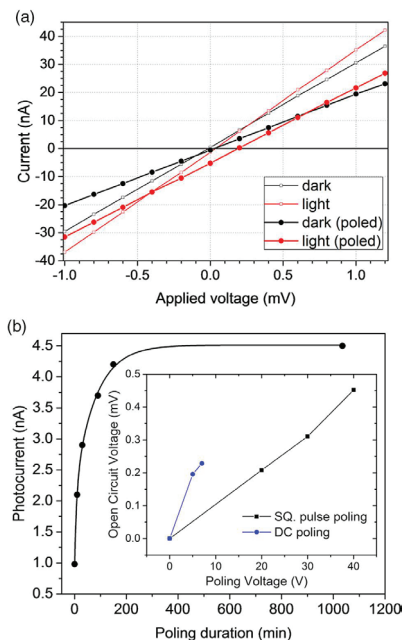


Figure 1. a) I - V curves measured in dark and under illumination by about 0.1 W cm^{-2} white light for nonpoled SWCNT/PCBM(1/120) sample and that poled for 20 min by the steady-state voltage of 5 V. b) Dependence of the closed-circuit photocurrent on the poling time (20 μ s square-pulsed voltage of 20 μ s duration at 1 kHz repetition rate). Inset: A built-in voltage created by 10 min poling using constant or pulsed voltage.

by steady-state voltage of 5 V. As expected, the dark I - V curves for the nonpoled sample cross the (0,0) point. The I - V curve for the poled sample measured in the dark is less steep, indicating that the poling reduces the sample conductivity. However, sample illumination increases steepness of I - V curves almost identically for both poled and nonpoled samples, showing that photoconductivity of the films does not change substantially with the sample poling. It suggests that poling reduces mobility of equilibrium carriers, while carriers, photogenerated after the termination of the poling voltage, are not affected. Illumination of the poled sample also shifts the I - V curve down revealing the photocurrent at zero applied voltage (close-circuit current) and a built-in open-circuit voltage of about 0.2 mV.

Inset in Figure 1b shows the dependences of the built-in voltage on the constant or pulsed voltage used for the sample poling. In the case of the sample poling by pulsed voltage, the investigated parameters show nearly linear voltage dependences in the whole examined voltage range. In the case of the constant poling voltage, the curve starts to saturate at approximately 6 V, while further voltage increase usually caused sample degradation due to sample heating and thus irreversible changes. Square 20 μ s, 20 V pulses at 1 kHz repetition rate created approximately equivalent sample poling as steady-state voltage of 0.2 mV, but pulsed voltage caused no sample degradation up to 40 V. Therefore, in further experiments, the sample poling was performed by 20 μ s pulses at 1 kHz repetition rate. Figure 1b shows the dependence of the close-circuit photocurrent on the poling duration. Initially, the photocurrent increases rapidly with the poling time, but the full saturation of the photocurrent was reached after several hours.

We further investigated the poling dynamics and decay of the created built-in field. To address fast phases of the built-in field formation and decay, the samples were similarly poled by the train of 20 μ s electrical pulses at 1 kHz repetition rate, but to avoid the effect of the slow poling component, every second pulse was of the opposite polarity. Thus, the time-averaged sample poling was absent, and the poling by any individual pulse was identical to that created by a single pulse (see inset in Figure 2). We probed the dynamics of the internal electric field by measuring photocurrent which was created by 130 fs, 1000 nm optical pulses synchronized with the electrical poling pulses. The photoresponse kinetics was obtained from multiple pulses by changing optical probing time relatively to the rising front of the electrical pulse. The optical probing time was varied during the entire electrical pulse and during the interval between electrical pulses which allowed to probe both polarization formation and its decay. The optical excitation created pulses of photocurrent lasting for less than 10 ns, but we considered only their peak values that we termed photoresponses.

The curves in Figure 2 show the photoresponse dependences on the probing time for different samples. The upper inset schematically shows the investigated samples. The photoresponse dependences were qualitatively similar for all investigated samples. The zero time corresponds to the probing immediately after the application of the electrical pulse. The photoresponse then was maximal and decreased with the probing delay, indicating that the created polarization screened the applied electric field. After termination of the electrical pulse, the photoresponse changed its polarity and initially was approximately equal to the

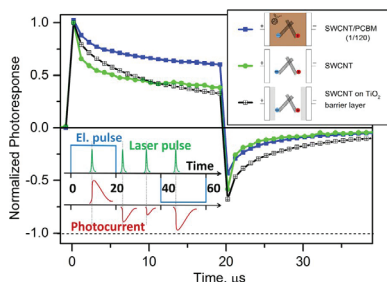


Figure 2. Photoresponse as the function of the delay time between the rising front of the electrical poling pulse (20 V) and photoexcitation pulse. Inset: The synchronization scheme of the electrical pulses, laser pulses, and measured photoresponses.

drop of the photoresponse during the electrical pulse action. Moreover, the decay kinetics of the photoresponse during the electrical pulse action and after its termination was very similar. It shows that the negative photoresponse observed after the termination of the electrical pulse originates from the built-in internal electric field of the opposite direction created by the sample polarization, which is also responsible for the screening of the applied electric field. The electric field kinetics resembles that of sample connected in series with capacitor. However, sample capacitance and external load give RC time constant of several nanoseconds only, which shows that internal processes in SWCNT film are responsible for the observed dynamics.

For the SWCNT/PCBM(1/120) film, the photoresponse decreased by about 40% during the 20 μ s electrical pulse action. For a pure SWCNT film, the photoresponse decrease was even stronger, by about 60%. The built-in field was also correspondingly stronger. Films with other SWCNT to PCBM ratio were also investigated. The tendency of the decrease in the built-in field in samples with larger PCBM content was observed; however, a clear dependence was not established because of the weak differences and of the limited sample fabrication reproducibility. It should be also noted that the absolute photoresponse values for the pure SWCNT films were more than 10 times lower than for the blends with PCBM because of the less efficient charge carrier photogeneration. The absolute photoresponse value was not important for probing of the built-in field values relatively to the applied field; however, samples with PCBM were more convenient for investigation of the weak built-in fields.

To verify the role of internal processes, the electrodes comb was also covered with TiO₂ layer forming additional capacitor connected in series with the SWCNT film. The thin TiO₂ layer did not block the charge transport completely, but sample resistance increased more than 10 times to tens or even hundreds of kilohms. As Figure 2 shows, the sample with TiO₂ layer showed a qualitatively similar electric field dynamics to these without it. The electric field screening and the residual built-in field were of similar values confirming that the internal processes within a SWCNT film were mainly responsible for the built-in field.

The large additional resistance slightly slowed down formation and relaxation of the built-in field.

We further examined the built-in field decay on a minutes and hours timescale. But the photoresponse created by a single electrical pulse was too weak at long delay times. Therefore, we have examined the decay of the photoresponse created by a train of 20 μ s electrical pulses of the same polarity applied at 1 kHz repetition rate for 10 min. The slow polarization decay component lasting for hours was observed in all investigated samples.

We chose the SWCNT/PCBM(1/120) film for a more detail investigation of the built-in field decay because of its stronger photoresponse. We examined the decay kinetics both on short and long timescales at different temperatures. Figure 3 shows the merged data for both decay components on a wide timescale in a log-log representation. The photoresponse values created by a single pulse and by a train of pulses were appropriately normalized. We clearly observe two polarization decay phases.

The fast decay phase continues for hundreds of microseconds, and the photoresponse drops almost by two orders of magnitude during this time. As the inset in Figure 3 shows, the fast phase is also strongly nonexponential, and polarization decreases several times during the initial several microseconds. This decay phase closely resembles the recombination kinetics of photogenerated charge carriers determined by the time-delayed collection field (TDCF) technique reported in ref. [9]. Therefore, this phase should be attributed to the motion of equilibrium charge carriers present in a SWCNT layer. The carrier motion is limited by inter-tube jumps in a disordered SWCNT network causing a strongly nonexponential decay. The fast phase shows a very weak temperature dependence, similarly as the transient photocurrent (see inset in Figure 4). It indicates that the initial carrier motion is governed by the carrier tunneling between carbon nanotubes and their clusters, rather than by thermally activated jumps.

The slow polarization component is about 100 times weaker than the fast one. It starts to dominate at about 1 ms and its relaxation continues for hours. This phase shows a strong temperature dependence.

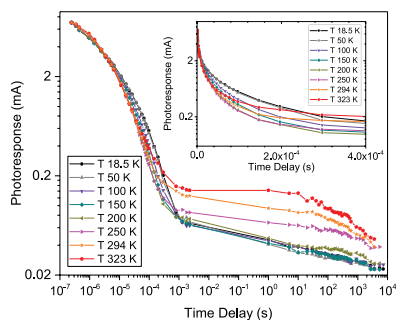


Figure 3. Kinetics of the photoresponse decay after termination of the electrical poling pulse on a wide log-log scale measured for the SWCNT/PCBM(1/120) blend film at different temperatures. Inset: The fast decay phase.

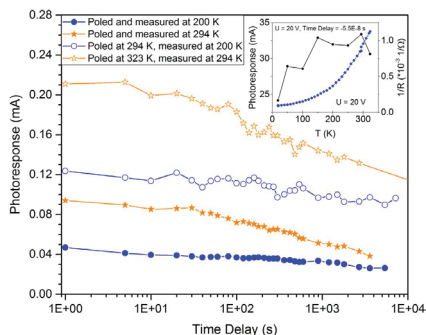


Figure 4. Slow phase of the photoresponse decay kinetics for SWCNT/PCBM(1/120) sample at frozen and non-frozen poling conditions. Inset: The dependences on the temperature of the steady-state sample conductivity (blue) and of the photoresponses while 20 V poling voltage is applied (black).

The polarization decay shows a complex temperature dependence. The fast polarization phase and its decay during the initial several microseconds are insensitive to temperature. The decay slightly slows down at low temperature on a timescale of tens of microseconds. The slow polarization component is also almost independent of temperature below 200 K, but increases more than 3 times in the 200–323 K range. Such weak temperature dependence is surprising considering that the dark conductivity of the film decreases more than 10 times at low temperatures (see inset in Figure 4).

We can further increase the slow polarization component at some particular temperature by performing the film poling at a higher temperature. The samples were heated to the desired poling temperature, and then the poling voltage was applied. After some poling time, the samples were cooled down still keeping the poling voltage applied until the desired measurement temperature was reached. Then the poling voltage was disconnected and the photoresponse decay kinetics was measured. As Figure 4 shows, only the polarization intensity increases by the sample poling at higher temperature, while its decay kinetics remains approximately unchanged.

The two phases of photoresponse decay should be attributed to different processes. The field screening may be caused by charge carriers as well as by ions. Most likely SWCNT films possess equilibrium holes, because SWCNTs in the ambient atmosphere become p-doped because of adsorbed oxygen molecules, which withdraw electrons.^[23–25] The SWCNT films are composed of single SWCNTs and their bundles, which are partly interconnected, but pathways for charge transport apparently contain dead ends. Under applied electric field a fraction of drifting charge carriers stack on the dead ends of their pathways causing the appearance of electrical dipoles created by the stacked holes and the immobile negatively charged oxygen molecules. The created dipoles cause the screening of the applied external

electric field. After the voltage cutoff, created dipoles gradually decay when charge carriers drift back to their initial positions. Consequently, screening of the electric field and decay of the built-in field reveal very slow charge carrier drift tails, which contribute to the current very little, and therefore cannot be observed, for example, by investigating transient photocurrent kinetics. As mentioned before, this dynamics resembles recombination dynamics of photogenerated charge carriers measured by TDCF technique. Indeed, these processes are expected to be similar because both of them are determined by carriers traveling back to their countercharges at zero applied electric field. Electrons and holes can hardly cause processes lasting for hours and days; therefore, we attribute the long-lasting built-in electric field to the motion of ions. A similar attribution was made analyzing the environmental influence on the electrical conductivity of SWCNT films where such long-lasting processes were assigned to adsorbed oxygen.^[26] As the temperature dependences in Figure 3 show, this motion requires thermal assistance of about 200 K (16 meV), which, according to Arrhenius equation, converts into 5–10 meV activation energy.

To obtain additional information about the properties of the built-in electric field, we attempted to compensate it by applying an external voltage. To better reveal a weak photocurrent at long times, we performed these investigations in the integrating regime using a high load resistance of 100 k Ω . In these measurements, the sample capacitance served as an integrating capacitor and the measured voltage was proportional to the integrated photocurrent.

Figure 5 shows the integrated photocurrent kinetics at different applied voltages for the poled sample. We were unable to compensate the transient photocurrent during the entire time range. At high applied voltage (100 mV), when the applied field strongly dominated over the built-in field, the voltage growth was relatively slow and continued for more than 1 μ s. While at zero applied voltage, when only the built-in electric field was present, the voltage drop was faster than could be resolved by our measurements. It shows that the photocurrent created by the built-in field endures much shorter than the photocurrent created by an external applied voltage.

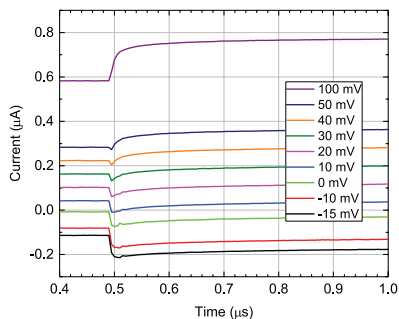


Figure 5. Transient integrated photocurrent kinetics of the SWCNT/PCBM(1/120) blend film at small applied voltages.

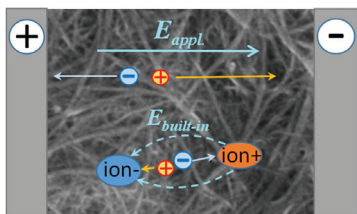


Figure 6. Carrier motion model in poled SWCNT films.

When the applied and built-in fields were of similar strength but of opposite directions, the photocurrent kinetics was more complex, apparently determined by the competition of the two photocurrent components. Such curve shape suggests that the internal net electric field, in this case, was inhomogeneous and even of different directions in different spatial regions: regions in the vicinities of poling-induced dipoles with dominating built-in field were surrounded by the regions weakly affected by the induced dipoles, where the electric field created by applied voltage was dominating (see **Figure 6**). Charge carriers photogenerated in the vicinity of induced dipoles moved only over short distances toward charges forming the induced dipoles, thus creating only short photocurrent pulse. However, charge carriers photogenerated in the regions dominated by the external electric field moved over larger distances and correspondingly longer time.

3. Conclusions

We have found that the voltage applied to SWCNT and SWCNT/PCBM blend films deposited on interdigitated electrodes induces the formation of persistent electric dipoles in SWCNT clusters. As a result, the applied electric field is screened, which causes persistent photoconductivity lasting for hours and days after the voltage was switched off. The fast ($\approx 10 \mu\text{s}$) component of the decay of the persistent photoconductivity was attributed to the charge carrier displacement, while the slow component lasting for several days is likely to result from the displacement of ions. The slow component becomes weaker at low temperatures, indicating that the field-induced ion displacement requires thermal activation. Samples with PCBM show weaker electric field screening and weaker residual built-in field, but the photoresponse after the termination of the applied voltage may be even stronger because of higher carrier generation efficiency. The built-in internal electric field, which we discovered, may play an important role in SWCNT-based electrical and photoelectrical devices because it may screen the applied electric field, reducing its strength by several times and causing long-lasting memory effects.

4. Experimental Section

Purification of semiconducting (6,5)-SWCNTs from the commercial chemical (99.9%; Sigma-Aldrich) and the sample preparation were described in ref. [10] Briefly, enrichment of (6,5)-SWCNTs was achieved through

ultrasound-assisted SWCNT wrapping with poly[(9,9-dioctylfluorenyl-2,7-diy)-alt-co(6,6-2,2-bipyridine)] (PFO-Bpy) copolymer, centrifugation, and filtration-assisted polymer depletion.^[17] The obtained chlorobenzene suspensions with polymer-wrapped SWCNTs were used for preparation of neat (6,5)-SWCNT samples, or PCBM solution was added to the SWCNT suspension for preparation of SWCNT/PCBM (x/y) films (x/y here indicates the SWCNT to PCBM mass ratio in the solution used for sample preparation). The obtained mixtures were drop-cast on the interdigitated comb-like electrodes (ED-IDE3-Pt; Micruz Technologies) with $5 \mu\text{m}$ inter-electrode distances and dried in the air. Morphology and photoelectrical properties of the obtained samples were described in Ref. [10]. Typical thickness of the samples was about 700 nm. The TiO_2 intermediate layer of about 200 nm thickness was prepared by repetitive spray pyrolysis using 5.2 mL ethanol solution containing 0.12 mL titanium diisopropoxide bis(acetylacetonate) solution (75% in 2-propanol; Sigma-Aldrich) and 0.08 mL acetylacetonate at 450°C in air.^[28]

Sample poling was performed by using arbitrary function generator Tektronix AFG2021 with high-voltage amplifier Falco Systems WMA-320. Steady-state photocurrent and photovoltage investigations were performed using a picoammpermeter-voltage source Keithley 6487 and a halogen lamp as a light source (illumination approximately equal to 1 Sun ($\approx 0.1 \text{ W cm}^{-2}$)). For the transient photocurrent investigations, the samples were excited at $\lambda = 1000 \text{ nm}$ by radiation of the optical parametric amplifier Topas-C (Light Conversion Ltd.) pumped by femto-second Ti:Sapphire laser (Integra-C from Quantronix Inc.; $\lambda = 800 \text{ nm}$, $\tau_{\text{pulse}} = 130 \text{ fs}$). An Agilent Technologies DSO 5054A oscilloscope was also used for measurements of transient photocurrent.

Conflict of Interest

The authors declare no conflict of interest.

Keywords

built-in field, carbon nanotubes, PCBM, photocurrent

Received: August 16, 2019

Revised: January 3, 2020

Published online:

- [1] M. Lanzi, L. Paganin, D. Caretti, *Polymer* **2008**, *49*, 4942.
- [2] M. J. Shea, M. S. Arnold, *Appl. Phys. Lett.* **2013**, *102*, 243101.
- [3] C. Ménard-Moyon, K. Kostarelos, M. Prato, A. Bianco, *Chem. Biol.* **2010**, *17*, 107.
- [4] Q. Zeng, S. Wang, L. Yang, Z. Wang, T. Pei, Z. Zhang, L.-M. Peng, W. Zhou, J. Liu, W. Zhou, S. Xie, *Opt. Mater. Express* **2012**, *2*, 839.
- [5] M. Salvato, M. Cirillo, M. Lucci, S. Orlanducci, I. Ottaviani, M. L. Terranova, F. Toschi, *Phys. Rev. Lett.* **2008**, *101*, 246804.
- [6] B. Gao, D. C. Clattli, B. Plaças, A. Bachtold, *Phys. Rev. B* **2006**, *74*, 085410.
- [7] R. S. Lee, H. J. Kim, J. E. Fischer, A. Thess, R. E. Smalley, *Nature* **1997**, *388*, 255.
- [8] T. Kim, G. Kim, W. I. Choi, Y.-K. Kwon, J.-M. Zuo, *Appl. Phys. Lett.* **2010**, *96*, 173107.
- [9] A. Eckstein, V. Bertašius, V. Jašinskas, I. Namil, T. Hertel, V. Gulbins, *Nanoscale* **2017**, *9*, 12441.
- [10] V. Jašinskas, F. Oberndorfer, V. Pakštas, T. Hertel, V. Gulbins, *J. Phys. Chem. C* **2018**, *122*, 16424.
- [11] X. Zhou, J.-Y. Park, S. Huang, J. Liu, P. L. McEuen, *Phys. Rev. Lett.* **2005**, *95*, 146805.
- [12] S. Rosenblatt, Y. Yaish, J. Park, J. Gore, V. Sazonova, P. L. McEuen, *Nano Lett.* **2002**, *2*, 869.

- [13] M. Shirm, A. Javey, N. W. Shi Kam, H. Dai, *J. Am. Chem. Soc.* **2001**, 123, 11512.
- [14] C. Gadermaier, E. Menna, M. Meneghetti, W. J. Kennedy, Z. V. Vardeny, G. Lanzani, *Nano Lett.* **2006**, 6, 301.
- [15] D. Gao, R. Liu, W. Yu, Z. Luo, C. Liu, S. Fan, *J. Phys. Chem. C* **2019**, 123, 5249.
- [16] H. J. Queisser, D. E. Theodorou, *Phys. Rev. B* **1986**, 33, 4027.
- [17] N. B. Pendyala, K. S. R. K. Rao, *Solid State Commun.* **2009**, 149, 1928.
- [18] I. A. Levitsky, W. B. Euler, *Appl. Phys. Lett.* **2003**, 83, 1857.
- [19] R. F. Khairoutdinov, L. V. Doubova, R. C. Haddon, L. Saraf, *J. Phys. Chem. B* **2004**, 108, 19976.
- [20] J.-L. Zhu, G. Zhang, J. Wei, J.-L. Sun, *Appl. Phys. Lett.* **2012**, 101, 123117.
- [21] C. S. Allen, G. Liu, Y. Chen, A. W. Robertson, K. He, K. Porfyrakis, J. Zhang, G. A. D. Briggs, J. H. Warner, *Nanoscale* **2013**, 6, 572.
- [22] C. Li, Y. Chen, Y. Wang, Z. Iqbal, M. Chhowalla, S. Mitra, *J. Mater. Chem.* **2007**, 17, 2406.
- [23] J. Zhao, A. Buldum, J. Han, J. P. Lu, *Nanotechnology* **2002**, 13, 195.
- [24] D. Kang, N. Park, J. Ko, E. Bae, W. Park, *Nanotechnology* **2005**, 16, 1048.
- [25] S.-H. Jhi, S. G. Louie, M. L. Cohen, *Phys. Rev. Lett.* **2000**, 85, 1710.
- [26] A. Roch, M. Greifzu, E. R. Talens, L. Stepien, T. Roch, J. Hege, N. Van Nong, T. Schmiel, I. Dani, C. Leyens, O. Jost, A. Leson, *Carbon* **2015**, 95, 347.
- [27] H. Ozawa, N. Ide, T. Fujigaya, Y. Niidome, N. Nakashima, *Chem. Lett.* **2011**, 40, 239.
- [28] R. Gegevičius, M. Treideris, V. Pakštas, M. Franckevičius, V. Gulbinas, *Adv. Electron. Mater.* **2018**, 4, 1800114.

NOTES

NOTES

Vilniaus universiteto leidykla
Saulėtekio al. 9, III rūmai, LT-10222 Vilnius
El. p. info@leidykla.vu.lt, www.leidykla.vu.lt
Tiražas 20 egz.